

2000-11

# Applied Computational Electromagnetics Society Journal, Special Issue on Computational Electromagnetic Techniques in Mobile Wireless Communications / Volume 15,

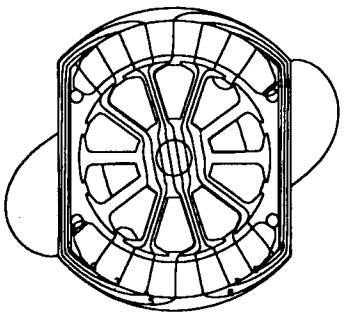

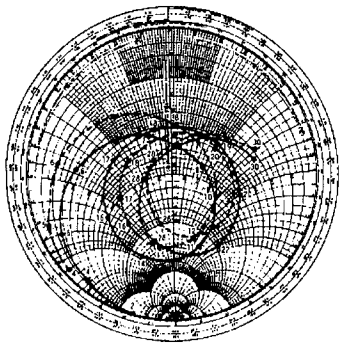

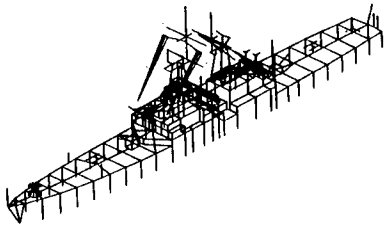

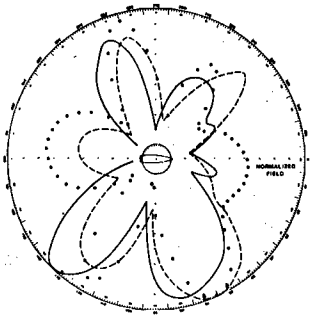

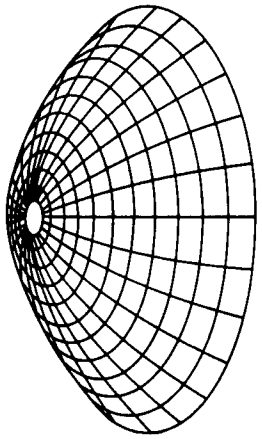

# APPLIED COMPUTATIONAL ELECTROMAGNETICS SOCIETY JOURNAL

## SPECIAL ISSUE

ON

## COMPUTATIONAL ELECTROMAGNETIC TECHNIQUES IN MOBILE WIRELESS COMMUNICATIONS

GUEST EDITORS
RAY PEREZ
AND
CHRIS HOLLOWAY

2000
Vol. 15 No. 3

ISSN 1054-4887

**GENERAL PURPOSE AND SCOPE.** The Applied Computational Electromagnetics Society Journal hereinafter known as the ***ACES Journal*** is devoted to the exchange of information in computational electromagnetics, to the advancement of the state-of-the-art, and to the promotion of related technical activities. A primary objective of the information exchange is the elimination of the need to "re-invent the wheel" to solve a previously-solved computational problem in electrical engineering, physics, or related fields of study. The technical activities promoted by this publication include code validation, performance analysis, and input/output standardization; code or technique optimization and error minimization; innovations in solution technique or in data input/output; identification of new applications for electromagnetics modeling codes and techniques; integration of computational electromagnetics techniques with new computer architectures; and correlation of computational parameters with physical mechanisms.

**SUBMISSIONS.** The ***ACES Journal*** welcomes original, previously unpublished papers, relating to **applied computational electromagnetics.**

Typical papers will represent the computational electromagnetics aspects of research in electrical engineering, physics, or related disciplines. However, papers which represent research in **applied computational electromagnetics** itself are equally acceptable.

Contributions may be sent to the Editors-in-Chief, Dr. Ahmed Kishk or Dr. Allen Glisson

Department of EE
University of Mississippi
University, MS, 38677 USA
Phone: 601-232-5385 (Ahmed)
Phone: 601-232-5353 (Allen)
Fax: 601-232-7231
email:ahmed@olemiss.edu
email:aglisson@mail.olemiss.edu. See "Information for Authors" on inside of back cover.

**SUBSCRIPTIONS.** All members of the Applied Computational Electromagnetics Society (**ACES**) who have paid their subscription fees are entitled to receive the ***ACES Journal*** with a minimum of three issues per calendar year.

**Visit us on line at: www.emclab.umr.edu/aces, and http://aces.ee.olemiss.edu**

**Back issues**, when available, are $15.00 each. Subscriptions to **ACES**, orders for back issues of the ***ACES Journal*** and changes of addresses should be sent to:

Dr. Richard W. Adler
ACES Executive Officer
ECE Department, Code ECAB
Naval Postgraduate School
833 Dyer Road, Room 437
Monterey, CA 93943-5121 USA

Allow four week's advance notice for change of address. Claims for missing issues will not be honored because of insufficient notice or address change or loss in mail unless the secretary is notified within 60 days for USA and Canadian subscribers or 90 days for subscribers in other countries, from the last day of the month of publication. For information regarding reprints of individual papers or other materials, see "Information for Authors".

**LIABILITY.** Neither ACES or the ***ACES Journal*** editors are responsible for any consequence of misinformation or claims, express or implied, in any published material in an ***ACES Journal*** issue. This also applies to advertising, for which only camera-ready copies are accepted. Authors are responsible for information contained in their papers. If any material submitted for publication includes material which has already been published elsewhere, it is the author's responsibility to obtain written permission to reproduce such material.

# APPLIED COMPUTATIONAL ELECTROMAGNETICS SOCIETY Journal

November 2000
Vol. 15 No. 3

ISSN 1054-4887

The ACES Journal is abstracted in INSPEC, in Engineering Index, and in DTIC.

The second, third, fourth, and fifth illustrations on the front cover have been obtained from Lawrence Livermore National laboratory.

The first illustration on the front cover has been obtained from FLUX2D software, CEDRAT S.S. France, MAGSOFT Corporation, New York.

# THE APPLIED COMPUTATIONAL ELECTROMAGNETICS SOCIETY

## JOURNAL EDITORS

## ACKNOWLEDGMENT

We would like to express our thanks to guest reviewers of this special issue. The reviewers have done a great job and have taken time out of their own busy schedule to serve ACES. Our appreciation and acknowledgment.

Bruce Archambeault, IBM
Edmund K. Miller, Los Alamos National Lab
Ray Perez, JPL
Chris Holloway, NIST
Quirino Balzano, Motorola
Robert Paknys, Concordia University
Keth J. Balmain, Univ. of Toronto
Andrew L. Drozd, Andro Consulting Services
Pat. R. Foster, Microwave and Antenna Systems
The "Review Team" at NIST, Boulder Colorado

# THE APPLIED COMPUTATIONAL ELECTROMAGNETICS SOCIETY

## JOURNAL

## SPECIAL ISSUE ON COMPUTATIONAL ELECTROMAGNETIC TECHNIQUES IN MOBILE WIRELESS COMMUNICATIONS

Vol. 15 No. 3 November 2000

### TABLE OF CONTENTS

# A random-phase-assisted ray-tracing technique for wireless channel modeling

Houtao Zhu[1], Jun-ichi Takada[1], Kiyomichi Araki[2], and Takehiko Kobayashi[3]

[1]Department of Electrical and Electronic Engineering, Tokyo Institute of Technology
2-12-1 O-okayama, Meguro-ku, Tokyo 152-8552, JAPAN
[3]YRP Mobile Telecommunications Key Technology Research Laboratories Co., Ltd

*Abstract*— **A random-phase-assisted ray-tracing technique for predicting spatio-temporal wireless channel parameters is presented. A two dimensional-three dimensional (2D-3D) hybrid ray-tracing algorithm is implemented in code for the prediction of channel parameters in outdoor micro- and pico-cellular urban environments. Meanwhile, a Random Phase Approach (RPA) is applied in the ray-tracing algorithm. The application of the RPA is intended for two purposes: 1) to account for the effects of inaccurate antenna positions; 2) to predict the range of short-term fading fluctuation. Several measurements carried out in pico-cell environments confirm the calculation accuracy of this technique. It was found that measured fluctuation of path-loss and delay profiles are almost fully confined within the 90% confidence interval, proving that the approach can account for the effects mentioned above. In addition, the conventional verification of path-loss and delay profiles predicted by ray tracing was extended to include the verification of angle-of-arrival (AOA). The demonstrated calculation accuracy in spatial and temporal domain confirms the applicability of authors' technique to analyze system performance in real environments.**

## I. Introduction

Recently, ray-tracing methods have become popular approaches applied in prediction of cell coverage in wireless networks [1]–[3] and even proposed for deterministic channel modeling [4]. In fact, ray tracing combines computer graphics techniques and numerical electromagnetic computation techniques (e.g., Uniform Theory of Diffraction (UTD)) together. Current ray-tracing methods mainly focus on predicting path loss or delay spread in microcell and picocell environments [1]–[3][5]–[9]. However, the fast progress of spatio-temporal signal processing techniques (e.g., smart antenna) for next-generation wireless systems has demanded an accurate prediction of channel parameters not only temporally but also spatially for system performance evaluation. Verification of predicting spatio-temporal channel parameters from ray tracing, however, has not been fully completed. There are few verifications reported in the literature. In addition, a number of disadvantages inherent in existing ray-tracing methods frustrate people who use them. For example, although 3D ray-launching methods [1][5][7] launch rays from an icosahedron, they are launched with unequal separating angles that can cause deterioration in the accuracy of a calculation. Alternatively, image methods [3][6][8][9] normally require a substantial amount of memory to establish high-order image sources. A disadvantage of ray tracing is that phases of rays can not be correctly predicted due to inaccurate coordinates of buildings and antenna positions. These phase errors can cause inaccurate results when the rays are summed in vector forms [1].

Therefore, the RPA [10][11] is applied in authors' code to address the phase-error problem by assuming the rays have random phases. With this assumption, the statistical distribution of signal strength at each location (for path-loss prediction) and at each sampling instant (for delay-profile prediction) can be derived analytically. With this distribution, the phase-error problem can be mitigated by choosing a local mean value obtained from the distribution. Besides this effect, it was also found that the fluctuation range of fast-fading signal levels and delay profiles can be accurately predicted with the RPA. This range is impossible to predict with the conventional ray-tracing codes. In this paper, the RPA is incorporated with a 2D-3D hybrid ray-tracing method [12] to be proposed for predicting spatio-temporal channel parameters in outdoor micro- and pico-cellular environments.

The organization of this paper is as follows: Section 2 presents the detailed ray-tracing algorithm and the RPA. Section 3 describes the measurement and comparison of ray-tracing results with measurement data in: 1) path-loss, 2) delay profiles and 3) azimuth-delay profiles. Finally, section 4 draws conclusions on this ray-tracing technique.

## II. 2D-3D Hybrid Ray-Tracing Method

The purpose of the authors' ray-tracing code is to predict spatio-temporal channel parameters in micro- and pico-cellular environments. The following assumptions are made :

- Transmitting antenna heights are below the rooftops of surrounding buildings
- The ground is smooth and flat.
- Walls of buildings are perpendicular to the ground.

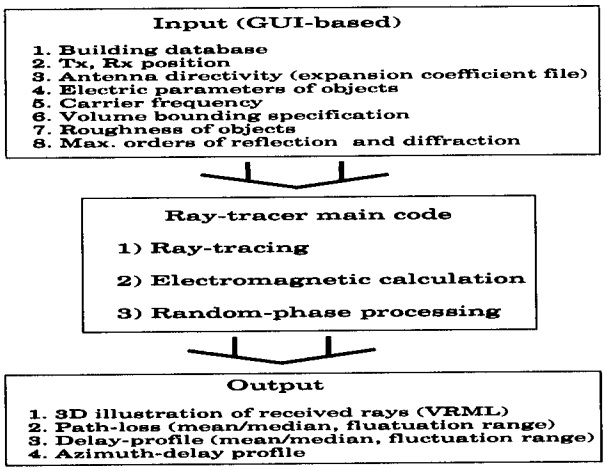


Fig. 1. Block diagram of the authors' ray-tracing code

The main body of the authors' 2D-3D hybrid ray-tracing code can be divided into three parts: 1) Ray tracing, 2) Electromagnetic wave calculation, and 3) Random-phase processing (Fig. 1). Ray tracing traces rays from transmitter to receiver as efficiently as possible to find detailed ray paths. Electromagnetic wave calculation uses electromagnetic wave theory to calculate theoretical values in a realistic environment. The RPA is then applied to calculate the local mean or median value and a confidence interval which corresponds to the fluctuation range of fading.

### *A. Ray-Tracing Formulation*

The 2D-3D hybrid ray-tracing method [12] is based on the ray-launching idea [5], which regards the transmitter as being a point source that launches rays in every direction. In the authors' approach, rays are launched in a 2-dimensional horizontal plane with equal angle separation. The location of the reflection and diffraction points and the formulation of reflected and diffracted rays are carried out based on Geometrical Optics (GO), Snell's Law of Reflection, and Keller's Law of Diffraction[13].

#### 1.1 Determination of the ray path

When vertical walls are only considered, 2D tracing gives correct 3D results. The locations of reflection points are determined by simple line and line intersection in a 2-dimensional coordinate system. Since the incident angle should be equal to the reflection angle (the Law of Reflection), the reflected ray vector is determined by the following simple vector calculation [14]:

$$\hat{\boldsymbol{k}}_r = \hat{\boldsymbol{k}}_i - 2\,(\hat{\boldsymbol{n}} \cdot \hat{\boldsymbol{k}}_i)\,\hat{\boldsymbol{n}} \tag{1}$$

where

$\hat{\boldsymbol{k}}_i$ : unit vector of the incident ray
$\hat{\boldsymbol{n}}$ : unit vector of the surface normal
$\hat{\boldsymbol{k}}_r$ : unit vector of the reflected ray

Building corners are checked by setting up capture circles to determine diffraction points [5]. As the incident angle (the angle between the incident ray and the edge of a building wall) is equal to the diffraction angle (the angle between the diffracted ray and the edge of a building wall), if we virtually unfold the incident plane and diffraction plane into one plane, the incident ray and the diffracted ray are actually in a straight line. After determining the intersection points, the ray paths are established by geometrically calculating the heights of intersection points. The height $h_k$ of the $k$th reflection or diffraction point is obtained as:

$$h_k = \frac{L_{tk} \cdot h_r + h_t \cdot (L_{tr} - L_{tk})}{L_{tr}} \tag{2}$$

where

$L_{tk}$ : 2D ray path length from the transmitter to the intersection point
$L_{tr}$ : 2D ray path length from the transmitter to the receiver
$h_t$ : the height of the transmitter
$h_r$ : the height of the receiver

As each ray path generates a pair of rays (one with ground-reflection and one without), ground-reflected rays are formed by searching the ground-reflection point in the previous ray path. The ray path length from the transmitter to the ground-reflection point $L_{tg}$ is calculated by:

$$L_{tg} = \frac{h_t \cdot L_{tr}}{h_t + h_r} \tag{3}$$

The ground-reflection point is formed along the ray path, and the heights of other intersection points are adjusted by the Eq. (3). Finally, the heights of intersection points are compared with the heights of the buildings. If one of the intersection points is higher than the building, the ray path does not exist.

The capture circle [5] is set up to determine whether the ray reaches each building corner and receiving point or not. The circle radius is defined as $0.5 \cdot \alpha \cdot L$, where $\alpha$ is the angle separation, and $L$ is the whole length of the ray path between the source and the capture circle. Although calculation accuracy is improved when launching-angle separation is smaller, computational time increases. There is a tradeoff between accuracy and computational time with regard to launching-angle separation. In the authors' experiences, a 0.1° to 1° launching angle separation is sufficient for pico-cells (0.1°— 0.5° for $60 \times 60$ m$^2$) and micro-cells (0.5°— 1° for $600 \times 600$ m$^2$). In addition to the ray reaching the receiving point, ray tracing is terminated if one of the following three conditions is met:

1. The signal level of the ray is below the threshold value,

2. The intersection order of the ray exceeds the user-specified maximum reflection and diffraction number,
3. The ray leaves the whole area.

1.2 Application of ray-acceleration techniques

To decrease computational time, a series of ray-acceleration techniques [14] is used in the authors' ray-tracing code. These are:

1. Back-face Culling
   Since most of the computational time is spent on intersection checks, the authors' main intention is to reduce intersection-check times. The dot product of the normal vector of a surface (building wall) with the launching ray vector is used to determine if the wall is invisible to the launching ray (back-face). If the dot product is greater than zero, the building face is invisible to the launching ray and it does not need to be checked for an intersection.
2. Volume Bounding
   The volume bounding technique is used to reduce the number of buildings required for an intersection-check. An area is divided into several rectangular sub-areas (bounding volume) and users specify the size of the bounding volume. When the bounding volume intersected by the ray is determined, the buildings in that volume are checked for an intersection. Without this technique, every building in the area would have to be checked. Computational time would then be dramatically increased.
3. Partition Vector
   The authors propose Partition Vector (PV) as a simple but effective technique for ray-acceleration. The ray vector is bounded with two partition vectors: unit vectors that start from the end point of the current ray vector and can be directed along positive/negative $x$ or $y$-axis direction. A bounding area formed by using two partition vectors in one bounding volume is shown in Fig. 2. If the coordinates of one of the building's corners are confined in the bounding area, this building then qualifies for an intersection check.

*B. Theoretical Calculation*

The authors' ray-tracing code allows the user to specify the positions of the transmitter and the receiver, the electrical parameters (conductivity and permittivity) of every building and ground plane, and carrier frequency and the vector field directivity of antennas. Since in real environments building walls may not be smooth, the roughness of reflecting surfaces can be specified by the standard deviation of the surface height with respect to the mean surface height. The randomness of the surface height is assumed to be modeled by a Gaussian distribution.

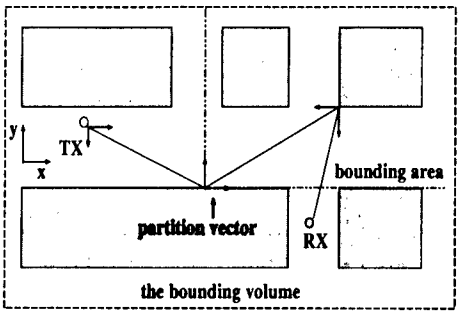


Fig. 2. Application of partition vectors in one bounding volume

2.1 Field calculation

The rotation of the polarization vector is considered for each reflection and diffraction event. The dyadic reflection and diffraction coefficients [15] are used for the field calculation. At reflection and diffraction points, the electric field components in the global coordinate system $E_{x,y,z}$ are first resolved into parallel and perpendicular components (with respect to the incidence plane) and multiplied by corresponding reflection/diffraction coefficients. After the calculation, the polarization components are resolved again to $E_{x,y,z}$ in the global Cartesian coordinate system. The average rough-surface reflection coefficient [16] and the heuristic dielectric wedge diffraction coefficient [17] from UTD are used for the calculation of reflection and diffraction loss.

The received electric field at the receiving antenna is therefore calculated by the following formulas:
Direct ray

$$\boldsymbol{E}_{\mathrm{LOS}} = \frac{\boldsymbol{E}_0}{d} e^{-jkd} \tag{4}$$

Reflected rays

$$\boldsymbol{E}_{\mathrm{R}} = \frac{\boldsymbol{E}_0}{d} \cdot \overline{\boldsymbol{R}}_{rough} e^{-jkd} \tag{5}$$

Once-diffracted rays

$$\boldsymbol{E}_{\mathrm{D}} = \frac{\boldsymbol{E}_0}{s'} \cdot \overline{\boldsymbol{R}}_{rough} \cdot \overline{\boldsymbol{D}} \sqrt{\frac{s'}{s(s'+s)}} e^{-jk(s+s')} \tag{6}$$

Twice-diffracted rays[1]

$$\boldsymbol{E}_{\mathrm{DD}} = \frac{\boldsymbol{E}_0}{s'} \cdot \overline{\boldsymbol{R}}_{rough} \cdot \overline{\boldsymbol{D}}_1 \cdot \overline{\boldsymbol{D}}_2 \sqrt{\frac{s'}{ss''(s'+s+s'')}} e^{-jk(s+s'+s'')} \tag{7}$$

where

$\boldsymbol{E}_0$ : emitted electric field observed at the unit distance
$d$ : propagation path length

$s'$ : path length from the source to the first diffracting wedge
$s$ : path length from the first diffracting wedge to the receiver (for once-diffracted rays) or to the second diffracting wedge (for twice-diffracted rays)
$s''$ : path length from the second diffracting wedge to the receiver
$\overline{\boldsymbol{R}}_{rough}$ : dyadic reflection coefficient of the rough surface
$\overline{\boldsymbol{D}}$ : dyadic diffraction coefficient of the dielectric wedge

The total field strength at any receiving point is contributed by reflected, diffracted and multiple reflected/-diffracted signals due to the multipath phenomena. This is calculated by the deterministic linear superposition of all single contributions as follows:

$$\boldsymbol{E}_{total} = \sum_{i=1}^{k} \boldsymbol{E}_i = \sum_{i=1}^{k} E_i \hat{\boldsymbol{e}} \cdot e^{j\phi_i} \tag{8}$$

where

$\hat{e}$ : unit vector of polarization for $i$-th arrival ray
$E_i$ : amplitude of $i$-th arrival ray ($|E_i|$)
$\phi_i$ : phase of $i$-th arrival ray

and $\phi_i$ is given as follows:

$$\phi_i = \psi_i - kd_i \tag{9}$$

where

$\psi_i$ : phase shift caused by interaction with obstacles
$d_i$ : propagation path length of $i$-th arrival ray

In the authors' approach, $\phi_i$ is assumed to be random. A statistical superposition of single contributions to calculate the total field strength is therefore adopted.

### 2.2 Calculation of the vector antenna pattern

Normally, the antenna radiation pattern used in ray tracing is approximated by the E and H plane patterns [18] or applied by a 3D radiation pattern stored in the computer [6]. The former is accurate only near the antenna main beam. The latter wastes computer memory. In the authors' approach, far-field pattern functions $\boldsymbol{K}_{smn}(\theta, \phi)$ and the expansion coefficient $Q_{smn}$ [19] express the field directivity pattern of the antenna. The index $s$ distinguishes the two modes: $s = 1$ denotes TE mode and $s = 2$ denotes TM mode. The indices $m$ and $n$ indicate the mode numbers of the wave functions in the $\phi$ and $\theta$ directions respectively.

Since the radiating power of the antenna is given by:

$$P = \frac{1}{2} \sum_{smn} |Q_{smn}|^2 \tag{10}$$

the transmitting power can be normalized to a 0 dB gain and the vector directivity function is obtained as:

$$\boldsymbol{D}(\theta, \phi) = \frac{\sum_{smn} Q_{smn} \boldsymbol{K}_{smn}(\theta, \phi)}{\sqrt{\sum_{smn} |Q_{smn}|^2}} \tag{11}$$

Therefore, if the field pattern of an arbitrary antenna is given, the expansion coefficient is obtained by the following equation:

$$Q_{smn} = \oint_{\Omega} \boldsymbol{E} \cdot \boldsymbol{K}^*_{smn} d\Omega \tag{12}$$

The expansion coefficient is stored as a look-up table in the computer. Finally, the emitted field is calculated according to the Eq. (11) and resolved into $E_{x,y,z}$ components from spherical coordinates in the global coordinate system. The use of the far-field pattern function has some advantages. First, it strictly satisfies Maxwell's equations and is therefore widely used in spherical near-field antenna measurements [19]. Second, the mode number of the function, sufficient to the expansion, is limited and proportional to the antenna size. This can reduce the need for computer memory to store antenna patterns.

### *C. Random-Phase Processing*

The conventional power-summing approach [20] sums up the power of each individual ray to obtain the total signal level by assuming that the incoming rays are incoherent. However, this approach can not indicate the fluctuation range of the signal level or demonstrate the fading phenomena. Alternatively, the phase-summing approach [20] calculates the total signal level from the sum of individual complex rays. Fast variation (multipath fading) of the signal can be observed in the total signal level. However, the calculation is quite possibly corrupted by the phase errors of some rays. This approach requires a sufficiently large observation window to obtain the statistical parameters of the signal fluctuation [20]. Since the statistical parameters are calculated from a number of sampling points inside this window, it is definitely a time-consuming approach. In the authors' approach, the idea of random phase ray-tracing [10][11] is adopted to model the level of fluctuation due to the coherent interaction among different rays.

Since the building database and the positions of the antennas may not be accurate in the order of wavelength, a phase error is introduced into each ray. This may dramatically deteriorate the accuracy of the ray-tracing results. As the total field at the receiving point is expressed in Eq. (8), the amplitude $A_i$ is predicted deterministically from ray tracing and the phase $\phi_i$ is then assumed to be random. The cumulative probability of the total field strength (fading statistics) at the receiving point can be derived by the characteristic function method and is

given as [21]:

$$P(|E|) = \frac{2|E|}{R} \sum_{n=1}^{\infty} \frac{\Phi(\gamma_n/R)}{\gamma_n J_1^2(\gamma_n)} J_1\left(\frac{\gamma_n |E|}{R}\right) \qquad (13)$$

where

$\gamma_n$ : the $n$-th root of zeroth-order Bessel function $J_0(.)$
$J_1(.)$ : the first order Bessel function.

and

$$\Phi(x) = \exp\left(-\frac{\sigma^2 x^2}{2}\right) \cdot \prod_{i=1}^{k} J_0(A_i x) \qquad (14)$$

where

$\sigma^2$ : receiver noise power
$A_i$ : the amplitude of the $i$th ray

and $R$ is an upper limit parameter, as sufficiently large as possible and chosen as [22]:

$$R = \sum_{i=1}^{k} A_i + 5\sigma \qquad (15)$$

With the amplitudes of received rays predicted from ray tracing, the cumulative probability and the corresponding amplitude $|E|$ can be determined from above equations. The total field strength corresponding to the cumulative probability from 5% to 95% is selected as the confidence interval. The prediction error of ray-tracing approaches, caused by incorrect phases, can be improved by using the local mean calculated by the RPA. By incorporating the RPA into the ray-tracing method, it provides an insight into the fading mechanism and also a specific range, within which the signal level will fluctuate.

The RPA can also be applied to predict the fluctuation range of delay profiles [23]. The band-limited delay profiles are obtained by convolving the channel impulse response predicted from ray tracing with a channel filter. In fact, these delay profiles are sampled and the sampling interval is decided by the system bandwidth. At each sampling instant, the interaction between different impulses occurs due to convolution, which can be represented as:

$$h(nT_s) = \sum_{i=1}^{n} A_i e^{j\phi_i} P(\tau_i - nTs) \qquad (16)$$

where

$T_s$ : symbol duration or chip duration
$P(t)$ : impulse response of the channel filter

Correspondingly, the RPA can be applied here by assuming $\phi_i$ is random.

## III. Field Measurement and Comparison Results

This ray-tracing code is designed in object oriented programming paradigm and implemented by using the C++ computer language. In order to help the user to enter parameters, a user-friendly Graphic User Interface (GUI) is also implemented with the Tcl/Tk computer language as seen in Fig 3. After calculation, the incoming rays at the desired receiving point are illustrated in 3D graphics by using the Virtual Reality Modeling Language (VRML) as seen in Fig. 4. The program was compiled by using the GCC public domain C++ compiler and then run at a Sun Ultra-Sparc workstation. It can also work on a Intel Pentium processor running at 166 MHz and equipped with 32 MByte memory. Borland C++ is used to compile the program on the PC.

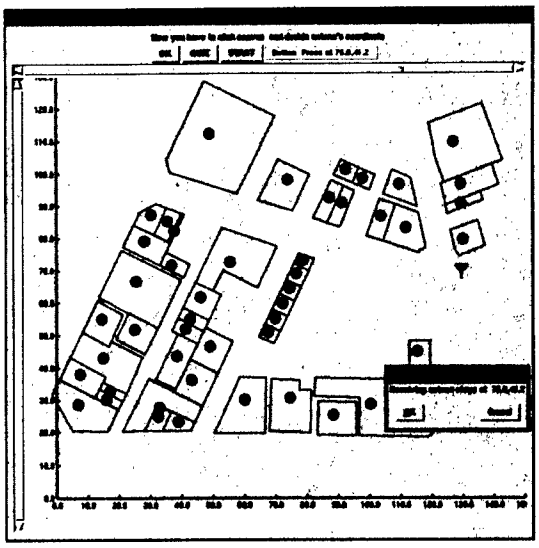

Fig. 3. GUI interface of the ray-tracing code

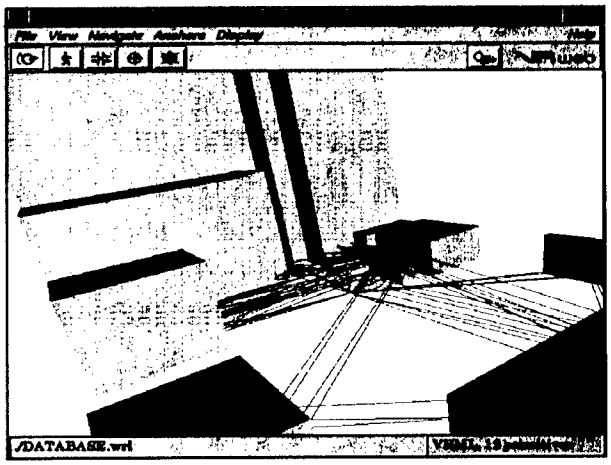


Fig. 4. 3D illustration of the received rays in VRML

The accuracy of the code is verified by comparing the calculation result with measurement. The measuring environments are shown in Fig. 5 and Fig. 6. Both measurement sites are typical pico-cell cases with areas under 60 × 60 square meters. Since it is very difficult to verify the calculation accuracy of ray tracing in AOA, a good starting point is to compare ray-tracing results with measurement in pico-cell environments. The Tokyo Institute of Technol-

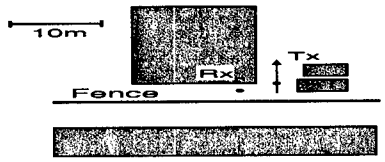


Fig. 5. Path-loss measurement environment in TIT

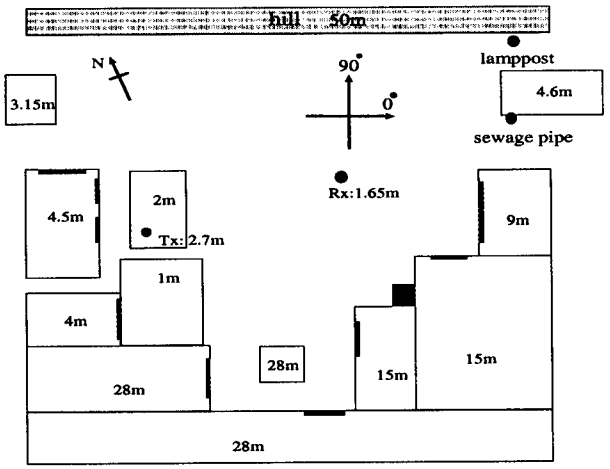


Fig. 6. Delay-profile measurement environment in YRP

ogy (TIT) measurement environment is rather simple and the Yokosuka Research Park (YRP) measurement environment is quite complex with mixed heights of buildings and a nearby hill. A metal pillar and doors are indicated by a square black box and thin black boxes. The heights of a car, buildings and antennas are also shown in the figure. The electrical parameters [24] used for the calculation of ray-tracing in all environments are listed in Table I.

The other simulation parameters are listed in Table II. In different environments the results were checked iteratively by changing the order of reflections and diffractions. It was found that the results converged with the above order of reflections and diffractions in different environments. The measurements of path loss, delay profile, and AOA were carried out and compared with the ray-tracing results.

TABLE I
ELECTRICAL PARAMETERS USED IN RAY-TRACING

| | $\epsilon_r$ | $\sigma$ [S/m] |
|---|---|---|
| building wall | 5.5 | 0.023 |
| ground plane | 15.0 | 0.005 |
| metal | - | $\infty$ |
| hill | 3.5 | 0.01 |

TABLE II
SIMULATION PARAMETERS USED IN RAY-TRACING

| | TIT | YRP |
|---|---|---|
| Carrier frequency [Hz] | 1.28 G | 8.45 G |
| Tx height [m] | 1.45 | 2.7 |
| Rx height [m] | 1.45 | 1.65 |
| Reflection no. | 4 | 6 |
| Diffraction no. | 1 | 1 |
| Antenna | V-polarized 0.5$\lambda$ dipole | |

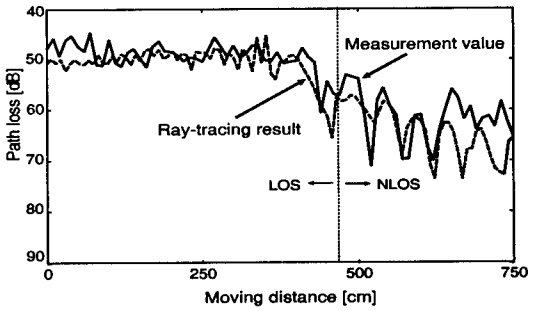


Fig. 7. Comparison of fast-fading variation of signal level between ray tracing and measurement

## A. Path Loss

During the measurement, the transmitter moved from the line-of-sight (LOS) area to the non-LOS (NLOS) area while the receiver was put in a fixed position. The transmitter antenna was connected to a signal generator and 1.28 GHz CW signal of 10 dBm transmitted. A spectrum analyzer measured the received signal level. The whole moving range was 7.5 m and the transmitter moved at a step of 10 cm, which was nearly equal to 0.5$\lambda$ of the CW signal.

Figure 7 shows the measured fast-fading pattern of signal level with the calculated ray-tracing result. The level deviation of the fast-fading signal can be observed at around 15 dB in the NLOS region. Figure 8 shows a local mean calculated over 1-meter range with the moving-average method for comparison. The local mean predicted from the RPA is also shown there. The improvement of accuracy by using the RPA can be seen in the NLOS region. That is because the result is more sensitive to phase-errors in the NLOS region. The underestimated result in the NLOS due to phase-errors can be improved by using local mean predicted from the RPA. Meanwhile, with the RPA, a 90% confidence interval is calculated as seen in Fig. 9. Almost all of the measurement data fell into this confidence interval. That proves that the RPA can predict the fluctuation range of the fast-fading signal.

## B. Delay Profile

The delay profile measurement is carried out in another pico-cellular environment as shown in Fig. 6. A delay profile measurement system utilizing pseudo noise (PN) code [25] is used here. A 8.45 GHz spread-spectrum signal with the rate of 50 Mchips/s was transmitted. The whole dynamic range is above 60 dB (2047 chips of PN length) and the whole bandwidth of this system is 100 MHz. The receiving antenna is moved at $8 \times 8$ grid points with a 0.4$\lambda$ sep-

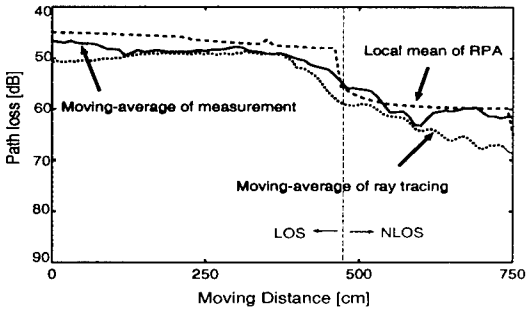


Fig. 8. Comparison of mean signal level between ray tracing and measurement

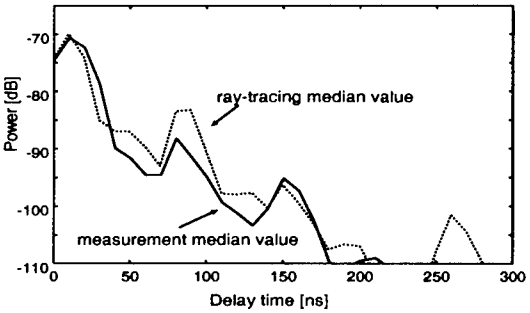


Fig. 10. Comparison of median delay profile between ray tracing and measurement

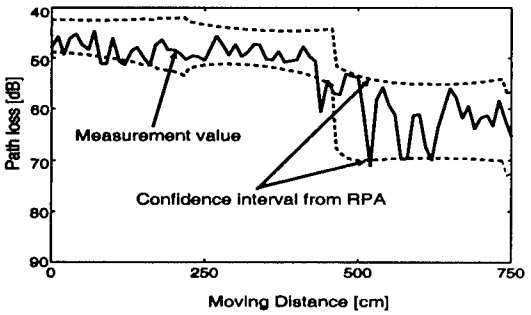


Fig. 9. Comparison of fading-fluctuation range between ray tracing and measurement

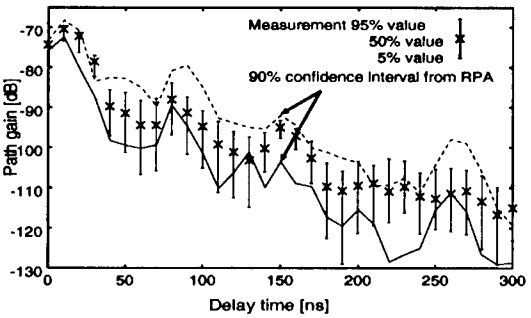


Fig. 11. Comparison of fluctuated delay profiles between ray tracing and measurement

aration distance between grids. Since the scattering effects of a small hill near the receiving point can not be neglected, it is modeled as a tall rectangular obstacle. The effects of metal doors and pillars are also modeled in the ray-tracing process.

The delay profiles corresponding to 5%, 50% and 95% cumulative probabilities are extracted from all 64 measured delay profiles. Alternatively, the delay profiles corresponding to 5%, 50% and 95% cumulative probabilities derived from the random phase approach are then compared with measurement results. Figure 10 shows a high level of agreement between the median delay profiles of ray tracing and measurement. Especially, there is an almost 100% overlap of the peaks of direct wave, second arrival waves, third arrival waves in the graph. The over-estimation of ray tracing is observed at around 260 ns. This may be caused by inaccurate approximation of electrical parameters because the signal level is still strong enough after the ray traveled 78 meters. Figure 11 shows that the fluctuation range of measured delay profiles in this small area (about $4\lambda \times 4\lambda$) are almost totally confined within the 90% confidence interval calculated by the RPA. It proves that the RPA can predict an accurate short-term fluctuation range of delay profiles. In other words, the effects of inaccurate antenna positions ($4\lambda$ in this case) can be also addressed.

### C. Azimuth-Delay Profile

In this measurement, the measurement setup is the same as that described in the section III-2. To obtain a synthetic aperture, the receiving antenna is moved at $8 \times 8$ grid points with a $0.4\lambda$ separation distance of grids. A $8 \times 8$ 2-dimensional array antenna system is therefore simulated. An azimuth-delay power profile (beam-forming pattern) of this antenna system is calculated and compared with the corresponding ray-tracing result. The ray-tracing result is first transformed into the band-limited response in the delay domain and then convolved with the antenna pattern to generate the beam-forming pattern.

These azimuth-delay profiles are plotted in contour figures. Figure 12 plots the measurement data. Figure 13 shows the ray-tracing result. From these two graphs, a good agreement can be observed at direct waves (at around 200 degrees) and back-reflection waves (at 340 degrees). At these directions, the first, the second and the third arrival waves (for 200 degrees only) are all separated around 70 ns. Some angle deviations of the second and third arrival waves are also observed. These phenomena are all accurately predicted by ray tracing. However, the arrival waves between 40 degrees to 120 degrees are not predicted by ray tracing. Among these directions, there is almost an open space, because the hill is quite far away. Since they almost arrived at the same delay time as the direct waves, they can be understood as the local scattered waves by the nearby equipments.

Overall, the authors' ray-tracing tool showed a high level of accuracy and was fully verified with regard to the path loss, the delay profiles and the angle of arrival.

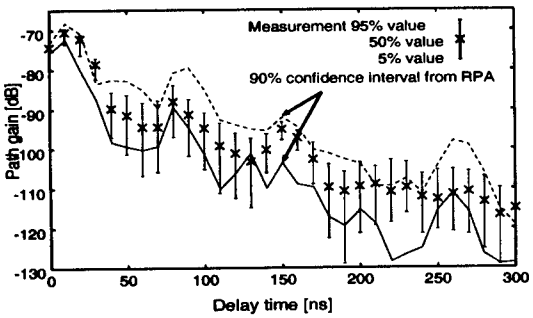


Fig. 12. Contour plot of the measured azimuth-delay profile

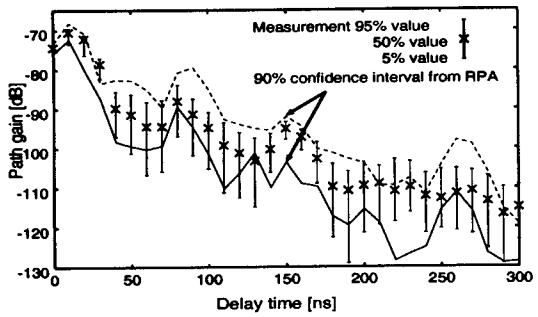


Fig. 13. Contour plot of the predicted azimuth-delay profile from ray tracing

## IV. Conclusion

This paper described a random-phase-assisted ray-tracing technique, which is designed for predicting spatio-temporal channel parameters. The main purpose of this technique is to provide an accurate prediction tool for deterministic wireless channel modeling. The RPA is applied in ray-tracing to give statistically correct results in the calculation of path loss and delay profiles. It was also found that the RPA could predict an accurate fading-fluctuation range of signal level and delay profiles. These advantages can not be achieved with the conventional ray-tracing codes. In addition to those, the authors also verified the prediction accuracy of the ray-tracing method with respect to angles. The further verification of this technique in micro-cellular environments has been continued [26] and will be submitted as another paper. The authors are continuing their efforts to launch a full-functional ray-tracing code both for channel modeling and network planning.

## V. Acknowledgments

The authors thanks K. Takiishi, J. Fu, N. Abe, N. Sakai, and K. Sakaguchi of Tokyo Institute of Technology, H. Masui, H. Shimizu, M. Ishii and K. Sakawa of YRP Key Tech Labs for their help in this work. This work is partly supported by the Scientific Grant in Aid from Japanese Society of Promotion of Science.

## References

[1] V. Erceg, S. J. Fortune, J. Ling, A. J. Rustako, Jr., and R. A. Valenzuela, "Comparisons of a computer-based propagation prediction tool with experimental data collected in urban microcellular environments," *IEEE J. Selected Areas Commun.*, vol. 15, no. 4, pp. 677–684, May 1997.

[2] R. P. Torres, L. Valle, M. Domingo, S. Loredo and M. C. Diez, "CINDOOR: An engineering tool for planning and design of wireless systems in enclosed spaces," *IEEE Ant. & Prop. Mag.*, vol. 41, no. 4, pp. 11–22, Aug. 1999.

[3] Cátedra, M., J. Pérez, F. Saez de Adana, and O. Gutierrez, "Efficient ray-tracing techniques for three-dimensional analyses of propagation in mobile communications: application to picocell and microcell scenarios," *IEEE Ant. & Prop. Mag.*, vol. 40, no. 2, pp. 15–27, April 1998.

[4] T. Kurner, D. J. Cichon, and W. Wiesbeck, "Evaluation and verification of the VHF/UHF propagation channel based on a 3-D-Wave propagation model," *IEEE Trans. Ant. & Prop.*, vol. 44, no. 3, pp. 393–404, Mar. 1996.

[5] S. Y. Seidel, and T. S. Rappaport, "Site-specific propagation prediction for wireless in-building personal communication system design," *IEEE Trans. Veh. Tech.*, vol. 43, no. 4, pp. 879–891, Nov. 1994.

[6] G. Athanasiadou, A. Nix, J. McGeehan, "Comparison of predictions from a ray tracing microcellular model with narrowband measurements," at 47th IEEE Vehicular Technology Conference, pp. 800–804, Phoenix, May 1997.

[7] G. Durgin, N. Patwari, T.S., Rappaport, "An advanced 3D ray launching method for wireless propagation prediction," at 47th IEEE Vehicular Technology Conference, pp. 785–789, Phoenix, May 1997.

[8] K. Rizk, J. Wagen, and F. Gardiol, "Two-dimensional ray-tracing modeling for propagation prediction in microcellular environments," *IEEE Trans. Veh. Tech.*, vol. 46, no. 2, pp. 508–517, May 1997.

[9] A. G. Kanatas, I. D. Kountouris, G. B. Kostaras, and P. Constantinou, "A UTD propagation model in urban microcellular environments," *IEEE Trans. Veh. Tech.*, vol. 46, no. 1, pp. 185–193, 1997.

[10] S. Takahashi, Y. Yamada and K. Ogura, "Propagation-loss prediction using ray tracing with a random-phase technique," *IEICE Trans. Fundamentals*, vol. E81-A, no. 7, pp. 855–859, Jul. 1998.

[11] H. Zhu, J. Takada, and K. Araki, "The implementation of a 3D ray-tracing method for the spatio-temporal channel modeling," in the 433th URSI-F Japanese Committee meeting, April 1999.

[12] H. Zhu, J. Takada, and K. Araki, "Ray-tracing-based spatio-temporal channel modeling for multimedia mobile access communication systems (MMAC)," Int. Symp. on Personal, Indoor and Mobile Radio Comm. (PIMRC'99), pp. 116–120, Osaka, Sept. 1999.

[13] J. B. Keller, Geometric theory of diffraction, *J. Opt. Soc. Amer., 52,* pp. 116–130, 1962.

[14] J. D. Foley, A. van Dam, S. K. Feiner, J. F. Hughes, *Computer Graphics Principles and Practice*, pp. 660–663, Addison–Wesley, New York, 1997.

[15] C. Balanis, *Advanced Engineering Electromagnetics*, John Wiley & Sons, NewYork, 1989.

[16] O. Landron, M. J. Feuerstein and T. S. Rappaport, "A comparison of theoretical and empirical reflection coefficients for typical exterior wall surfaces in a mobile radio environment," *IEEE Trans. Ant. & Prop.*, vol. 44, no. 3, pp. 341–351, March 1996.

[17] R. J. Luebbers, "Finite conductivity uniform GTD versus knife edge diffraction in prediction of propagation path loss," *IEEE Trans. Ant. & Prop.*, vol. AP-32, no. 1, pp. 70–76, Jan. 1984

[18] A. Hammoudeh, M. Sánchez, and E. Grindrod, "Experimental analysis of propagation at 62 GHz in suburban mobile radio microcells," *IEEE Trans. Veh. Tech.*, vol. 48, no. 2, pp. 576–587, Mar. 1999.

[19] J. E. Hansen, *Spherical Near-Field Antenna Measurements*, pp. 312-342, IEE, London, 1988.

[20] V. Erceg, A. J. Rustako, Jr., and R. S. Roman, "Diffraction around corners and its effects on the microcell

coverage area in urban and suburban environments at 900 MHz, 2 GHz, and 6 GHz," *IEEE Trans. Veh. Tech.*, vol. 43, no. 3, pp. 762–766, Aug. 1994.

[21] R. Barakat, "First-order statistics of combined random sinusoidal waves with applications to laser speckle patterns," *Optica Acta,* vol. 21, no. 11, pp. 903–921, 1974.

[22] J. K. Jao, and M. Elbaum, "First-order statistics of a non-Rayleigh fading signal and its detection," *Proc. IEEE,* vol. 66, no. 7, pp. 781–789, 1978.

[23] H. Zhu, J. Takada, K. Araki, H. Masui, M. Ishii, K. Sakawa, H. Shimizu, and T. Kobayashi, "Ray-tracing modeling and experimental verification of the spatio-temporal channel characteristics in a pico-cellular environment," *IEICE Tech. Rep.,* SST99-62/ITS99-58A/AP99-184/RCS99-204/MW99-224, Feb. 2000.

[24] CCIR Rec. 527-2, Electrical characteristics of the surface of the Earth, *Recommendations and Reports of the CCIR,* Vol. V, ITU, Geneva, 1991.

[25] H. Masui, K. Takahashi, S. Takahashi, K. Kage and T. Kobayashi, "Delay profile measurement system for microwave broadband transmission and analysis of delay characteristics in an urban environment," *IEICE Trans. Electron.,* no. 7, pp. 1287–1292, 1999.

[26] H. Zhu, J. Fu, J. Takada, K. Araki, H. Masui, M. Ishii, K. Sakawa, H. Shimizu, and T. Kobayashi, "An investigation of the spatio-temporal channel model in a suburban micro-cellular environment," *IEICE Tech. Rep.,* SST99-63/ITS99-59A/AP99-185/RCS99-205/MW99-225, Feb. 2000.

# NANOCELLS INTRASYSTEM INTERFERENCE REALISTIC WORST CASE ANALYSIS FOR OPEN SITE PERSONAL COMMUNICATION SCENARIOS

**J. Gavan, Fellow IEEE**
E-mail : gavan @ barley cteh ac.il
**U. Mahlab IEEE Member**

**Holon Academic Institute of Technology,**
**POB 305, Holon 58102, Israel**

## ABSTRACT

The exponential growth in mobile communications is followed by the development of new generations of Personal Communication Systems (PCS). Numerous research activities and papers have been published on PCS but only a few deal with the Electromagnetic Interference (EMI) affecting those systems. This paper presents a realistic worst case analysis and computation of the PCS intrasystem interference effects on open site nanocell scenarios. The operation range is up to 200m, usually under Line of Sight (LOS) propagation conditions where intrasystem interfering signals are maximum. Analysis and computation results are provided for a typical second generation cordless PCS CT-2 telephone (telepoint) operating in the 900 MHz frequency band. The computations show that for most cases of nanocell open site, intrasystem interference can be neglected, except for a few cases of single tone spurious. The good performances is due to PCS advanced Digital Signal Processing (DSP) technology advantages using Adaptive Power Control (APC) to optimize transmitter power requirements and to Dynamic Channel Assignment (DCA) electing the best signal to noise and interference channel available.

## I. Introduction

The exponential growth in mobile communications has led to the development of numerous new Short Range Distance (SRD) systems which are coming into widespread commercial use [1]. The interest in investigating the Personal Communication System immunity to interference, especially for spectrum utilization purposes has increased significantly [2]. Thus this paper investigates the intrasystem mutual interference effects in PCS cells operating in open sites (outdoor conditions). A nanocell network represents a cell under open site propagation conditions with a maximum operation range of 200 meters, in comparison with the significantly wider operation ranges of common cellular radio systems [3,4].

Figure 1 shows an open site nanocell radio system, where some wireless users operate simultaneously at a radius of up to 200m from a common base station connected by wires to a central telephone network. Hence, the problem of mutual radio intrasystem interference between the users' and the base stations' radio becomes an important issue [5,6]. Improving PCS system operation quality requires an analysis and computation of Signal to Noise and of Interference to Noise Ratios (SNR), (SIR) and bit error rate probability for the influent mutual interference sources. This analysis is important especially for PCS open site scenarios where the base and handset antennas are usually in Line of Sight (LOS) Free Space

(FS) propagation conditions, [7] and the interfering power levels are significantly higher than for indoor situations [3;8].

The analysis and computation method described provides a means to reduce interference effects by improving site management criteria and system mitigation techniques. Quantitative computations introduced for the expected desired signal and interference power levels are correct for CT-2 PCS systems operating under an open site nanocell scenario. A CT-2 Common Air Interface (CAI) telepoint system was used as an example, which represents a typical PCS of the second generation [9]. The CT-2 is one of the earliest digital PCS systems introduced using efficient DSP techniques discussed in the following chapters. However, the CT-2 system, first introduced in the United Kingdom, is still very popular in several Far East countries. For instance, the September 1998 (P.161) edition of the IEEE Communication Magazine mention that for South Korea , in spite of the great success of CDMA technology, there are still more than 400,000 subscribers using the CT-2 system in the frequency range of 910 to 914 MHz. The analysis and computation method presented for intra-system interference can also be applied to the Digital European Cordless Telecommunication (DECT) system which is used extensively in Europe and in several other countries in the world or any present or future PCS under nano-cell propagation conditions. In this paper the desired received power level computation for an outdoor nanocell system is introduced in Section. II, followed by the main intrasystem mutual interference sources analysis and computation given in Section III. Section IV and Appendix A provide the main conclusions of the investigations.

## II. Nanocell system receiver desired power levels

A CT-2 PCS telepoint system, was chosen for demonstrating the receiver desired power level computation method [3, 4, 5, 7] required to achieve the desired signal to noise and interference ratio and error probability. The desired power level at the victim receiver preamplifier following the antenna input as shown in (Figure 2) is calculated using the well known Friis equation for Line of Sight (LOS) Free Space (FS) Propagation conditions.

$$P_r = P_t.G_t.G_r.\left(\frac{\lambda}{4\pi d}\right)^2.\frac{1}{A_b} \tag{1}$$

where

$$\lambda = \frac{c}{f_0} \tag{2}$$

and

$$A_{fs} = \left(\frac{4\pi d}{\lambda}\right)^2 \tag{3}$$

or more convenient for radio system specialists in logarithmic units,

$$P_R = P_T + G_T - A_B + G_R - A_{FS} \tag{4}$$

where

$P_R$ - is the received input power level in dBm
$P_T$ - is the transmitter output power level in dBm
$A_B$ - is the additional equipment front end losses including the human body (1 to 2 dB) in the 900 MHz frequency band
h - is the headset height (about 1.5m)
$G_T$ - is the transmitter antenna gain (appx. 3 dBi maximum)
$G_R$ - is the receiver antenna gain in dBi (appx. 2 dBi maximum
$A_{FS}$ - is the free space propagation dispersion loss in dB [7] and is computed as

$$A_{FS} = 10 \cdot \log\left(\frac{4\pi d f_0}{c}\right)^2 = -27.5 + 20\log f_0 + 20\log d \qquad (5)$$

where c is the velocity of light , $f_0$ is the carrier frequency in MHz and d is the separation distance in meters between the system transmitter and receiver antennas as shown in Fig. 2. Required system transmitter and receiver parameters are presented in Appendix A. The scenario for free space propagation loss conditions is introduced in Figure 2. In the case of line of sight conditions, no complex near field propagation effects will occur. For our scenario, the minimum distance ***d*** between all system handset antennas and the base station is $d_f \geq 3\lambda$, which exceeds 3m, and for the non-directive monopulse or heliax antennas that are used for headsets, the distance is less than 1m at of 900MHz. Therefore, for a distance of $d_f \geq 3$m, simple far field propagation conditions are certainly valid [11; 12].
Flat earth approximation is applied and if LOS path clearance occurs, the free space propagation equation is valid. The path clearance depends on the 1st Fresnel zone clearance or obstruction as shown in Figure 2. From propagation principles the classical Friis equation can be applied when dispersion attenuation is proportional to the square of the distance if more than 60% of the 1st Fresnel zone ellipsoid is clear of obstacles [7;13].

The 1st Fresnel zone radius $F_{ZR_{(1)}}$ is given by

$$F_{ZR_{(1)}} = 17.3\sqrt{\frac{d}{4f_0}}. \qquad (6)$$

where the distances d, and $F_{ZR_{(1)}}$, are in meters and the frequency, $f_0$, is in MHz. The maximum radius of the 1st Fresnel zone is located at $\frac{d}{2}$ and $h_m$ is the antenna height at half distance between the base and handset positions as shown in Figure 2. Most cases of open site nanocell PCS under LOS propagation conditions, will be characterized by the clearance of more than 60 % of the 1st Fresnel zone [7]. Therefore for our scenario the free space propagation equation usually applies resulting in a propagation loss, $A_{FS}$ [8].

For $f_0 = 900$ MHz, equation (5) yields :

$$A_{FS} \approx 31.6 + 20\log(d) \qquad (7)$$

The propagation dispersion loss shown in equation (7) for different operation distances and antenna height are presented in Table 1; $\mathbf{h_b}$ and $\mathbf{h_h}$ are the median height of the base station and the portable CT-2 antennas, respectively. The results of $P_R$ in dBm for $P_T$ = 10 dBm, are also included. At distances less than 100 m the applied Adaptive Power Control (APC) mechanism decreases $P_T$ to less than 4 dBm [4]. For the quasi LOS open site nanocell scenario the desired receiver power is Rician statistically distributed and the initial SNR is high [15,16]. The received signal level must exceed the receiver input noise level in order to achieve an acceptable error probability.

**Table 1 : Worst case desired power levels and path clearance for typical open site scenarios ($f_0$ = 900 MHz)**

| $h_b$ (m) | $h_h$ (m) | d (m) | $h_m$ (m) | $F_{ZR_{(1)}}$ (m) | Path clearance of the 1st Fresnel zone | $A_{FS}$ (dB) | $P_R$ (dBm) |
|---|---|---|---|---|---|---|---|
| 3 | 1.2 | 200 | 2.10 | 4.1 | more than 60% | 77.5 | -65 |
| 5 | 1.5 | 200 | 3.25 | 4.1 | more than 80% | 77.5 | -65 |
| 7 | 1.8 | 200 | 4.40 | 4.1 | complete clearance | 77.5 | -65 |
| 3 | 1.2 | 100 | 2.10 | 2.9 | more than 80% | 71.5 | -59 |
| 5 | 1.5 | 100 | 3.25 | 2.9 | complete clearance | 71.5 | -59 |
| 3 | 1.2 | 50 | 2.10 | 2.05 | complete clearance | 65.5 | -53 |

The equivalent receiver input noise $P_n$ at ambient temperature conditions is:

$$P_n = K \cdot T_a \cdot B_r \cdot F_r \tag{8}$$

where $KT_a \simeq -174(\text{dBm/Hz})$ at room ambient temperature, $B_r$ is the receiver IF bandwidth in Hz, the specified receiver internal noise figure $F_r$ (worst case of 10 dB [5]), and $B_n = 84\,\text{kHz}$. Thus, the receiver input noise power level in logarithmic units is:

$$P_n = -174(\text{dBm/Hz}) + 10\log(84 \cdot 10^3) + 10 = -114.8\text{dBm} \tag{9}$$

Median values of the average ambient noise figure $F_a$ above the $K \cdot T_a \cdot B_r$ power level expected near the ground as function of the radio frequency range can be obtained from Consultative Committee International Radio (CCIR) graphs [17]. For 900 MHz , in suburban areas, we obtain $F_A \simeq 1dB$ and in urban areas $F_A \simeq 15dB$ or $F_A$= antilog 1.5 $\simeq$31.6 [7;17].

The equivalent system noise figure is equal to:

$$F_{eq} = F_r + s_a F_a \tag{10}$$

where $s_a$ represents the antenna efficiency, which is around 0.5 [20]. Hence, $F_{Eq} \approx F_R \approx 10dB$ in suburban areas, and in urban areas $F_{Eq} = 10\log(10 + 0.5 \cdot 31.6) \simeq 14.1\text{dB}$. Using a Non-coherent Binary Frequency Shift Keying (NCFSK) modulation technique, a BER of $10^{-3}$ or less required a SNR $\geq$11dB and when fading is added a SNR$\geq$16dB [11; 18]. Thus, the received power level input $P_R$ required to achieve BER$\leq 10^{-3}$ is, from equations 9 and 10, $P_R \geqq$ - 98 dBm in suburban areas and $P_R \geqq$ 94 dBm in urban areas [18].

## III. Main intrasystem mutual interference sources

The main mutual intrasystem interference sources shown in Figure 3 affecting the PCS system are : adjacent linear interference, receiver and transmitter intermodulation (IM), single tone spurious (STS) and desensitization. A discussion and computation of these interference sources effects are presented in this section.

## 1. Intrasystem adjacent linear interference effects

For several handsets operating simultaneously at the same PCS site, cochannel and adjacent channel interference is excluded due to the system receiver dynamic channel selection process [6;9]. When a handset operates on a frequency, $f_0$, a proximate adjacent channel $f_0 \pm \Delta f$ cannot be attributed to a new handset if the new base receiver spurious input power, $P_{R_s}$ exceeds –89 dBm. As the signal from the operating handset transmitter contributes to $P_{R_1}$, several adjacent channels will not be allocated. The number can be obtained from the system transmitter power spectrum response, presented in Figure 4 and from the distance d between the operating handset transceiver and the base station antennas.

## 2. Receiver intermodulation (IM) power level

IM product frequencies may penetrate the selective Intermediate Frequency (IF) filters and disturb PCS system operation [14]. Any 2nd or other even order IM products at frequencies $|f_1 \pm f_2|$ cannot affect the system receivers due to the PCS system selectivity and the narrow frequency band from 891 to 895 MHz. If the interfering frequencies are $f_1$= 892 MHz and $f_2$= 893 MHz, the 2nd order IM frequencies are 1 MHz, and 1785 MHz which are not in the receiver passband. The 3rd order IM products, however, may affect the receiver. A realistic worst case scenario for 3rd order receiver IM is when the victim receiver is tuned to $f_0 = 894.0MHz$, for instance. At distances for $d \geq 3m$ when two handsets are transmitting simultaneously at adjacent channel frequencies $f_1 = (f_0 - \Delta f)$ and $f_2 = (f_0 - 2\Delta f)$, the preamplifier nearest 3rd IM output frequency products are equal to the desired frequency

$$f_{IM_{31}} = 2f_1 - f_2 = f_0 \quad (11)$$

$$f_{IM32} = 2f_2 - f_1 = f_0 - 3\Delta f \quad (12)$$

This interfering signal will reach the detector stage directly without any filtering frequency dependant attenuation. The scenario results in a most proximate IM adjacent channel frequency of $\Delta f = 0.3$MHz due to the system dynamic channel selection process. The interfering preamplifier power level input $P_{Ri}$ in logarithmic units, is equal to

$$P_{R_i} = P_{T_i}. + G_T - A_{FS} + G_R - A_s, \quad (13)$$

if we refer to equation (4) where

$$A_s = A_B + A_{\Delta f}. \quad (14)$$

Thus, the frequency of worst case interfering signal near to the base station is where $P_T \leq 0$dBm due to the system DSP power control process. $A_{FS} \simeq 41dB$ from equations (4) and (7), as $d_{min}$ = 3m, $A_B = 2dB$, $G_T + G_R = 5dBi$ and $A_{\Delta f} = 5dB$. Therefore the realistic worst case receiver pre-selector filter circuit input power level obtained is $P_{Ri1} \leq -43dBm$.

The second worst case interfering frequency is: $f_2 = (f_0 - 0.6)\ MHz$ and $P_{Ri2} = -58dBm$ because of the filter attenuation $A_{(2\Delta f)} \approx 15dB$ at the second adjacent channel for a 0.6 MHz frequency interval.

The 3rd order IM product highest power level at the preamplifier stage output can be computed from the following equation [10;20].

$$P_{IM_{3h}} = 3P_{f1} - 2P_{IP_3} - \Delta P_i \quad (15)$$

where $P_{f1} = P_{Ri1}$ and $P_{f2} = P_{Ri2}$ represent the two interfering worst case power levels at the input of the victim receiver. $\Delta P_i = P_{f1} - P_{f2}$ and $P_{IP_3} = -22\,\text{dBm}$ is the receiver specified 3rd order intercept point power level [6,7]. Thus, the computed interfering $P_{IM_{3h}} \simeq -100dBm$ and $P_{IM3\ell} \simeq$-115 dBm are significantly lower than the desired power level around –65 dBm as shown in Table 1. Therefore the $P_{IM_3}$ products will not disturb the CT-2 receiver operation and only can cause tedious, not real, interference when the desired signal is absent. The higher odd order IM products that can produce in-band IM interference to the victim Rx, especially the 5th order, generate significantly less $P_{IM5}$ power level than the 3rd order. Thus, their interfering effects can also be neglected [14].

### 3. Transmitter intermodulation product power levels

Transmitter IM products are due to the simultaneous operation of two or more transmitters. Signals radiated by the two transmitters' antennas may cause co-channel or adjacent channel interference to a system receiver tuned to the IM product frequencies generated in the transmitters [14]. A typical transmitter IM scenario is presented in Figure 5.

For the realistic worst case scenario of a base station transmitter Tx radiating at frequency $f_1$ simultaneously with a mobile handset transmitter at frequency $f_2$. The minimal distance between the two handset transmitter antennas is also $d_r = 3\text{m}$ and the minimal frequency interval $\Delta f$ between the two transmitters exceeds 0.3 MHz. If, for realistic worst case conditions we choose the base and the handset frequencies $f_1 = 893.0\text{MHz}$ and $f_2 = 893.3\,\text{MHz}$, using equation (11) and (12), the 3rd power IM product frequencies in the base station transmitter are $f_{1M_h} = 892.7$ MHz at a higher power level and $f_{1M\ell} = 893.6MHz$ at a lower power level.

From the transmitter IM scenario shown in Figure 5 $P_{f_1} = P_{f_2} = 0dBm$ due to the base adaptive power control process $A_{FS} = 41dB$ at $d = 3\text{m}$ from the handset as shown from equation 7 when $P_{f1,2} \leqq -41dBm$ and the specified power amplifier 3rd order intercept point $P_{IP_3} = 30\text{dBm}$. We can compute the 3rd order IM products at the power amplifier output of the 1st base station transmitter [16;19] using the following equations [7, 14].

$$P_{IM_{3h}} = 2\left(P_{f_1} - P_{IP_3}\right) + P_{f_{1,2}} \tag{16}$$

and

$$P_{IM_{3\ell}} = 2\left(P_{f_{1,2}} - P_{IP_3}\right) + P_{f_2} \tag{17}$$

Therefore $P_{IM_{3h}} \leqq -101dBm \leqq$ and $P_{IM_{3\ell}} = -142dBm$. These low power levels are still further attenuated by the transmitter Tx output antenna filter and adaptative circuits and their interfering effects are negligible. A second worst case scenario occurs when two handsets are operating far from the base antenna but at a distance $d \leq 200\text{m}$ and a minimal distance of $d_r = 3\text{m}$ between the handsets' antennas as shown in Figure 6. In this case $P_T = 10\text{dBm}$ due to the large distance from the base station.

$P_{f1,2} = P_{f2} = 10mW, P_{f12} = 10 - 41 \simeq -31dBm$ and from equations 16 and 17, $P_{IM3h} \leq$ -71dBm and $P_{IM3\ell} \leqq$ -112 dBm at the transmitter output. The worst case co-channel interference to a neighboring receiver with a minimum $A_{FS}$=41 dB and $P_{Ril} \leq$-153dBm, which effect can also be neglected, will result in $P_{Rih} \leq$-112 dBm. The transmitter 2nd and higher order IM products can all be neglected due to the selectivity of the transmitter output circuits described in Figure 4 [14]. Therefore transmitter IM product interference will not affect the open site nanocell CT-2 system.

## 4. Single tone spurious effects

Single Tone Spurious (STS) effects are inherent in superheterodyne receivers because of the nonlinear behavior of the mixers and frequency converters, where output frequency mixing includes the difference and the sum of the RF input frequency $f_0$ with the LO frequency $f_L$ and the N harmonic spurious products of $f_0$ beating with the $|M|$ harmonic products of $f_L$ where:

$$f_{mixing} = |\pm Mf_L + Nf_0| \tag{18}$$

If the spurious power levels generated exceed the receiver sensitivity threshold-to-interference level, disturbances may occur. Disturbances can, therefore, occur from each external interfering signal or its harmonics which reach the receiver mixer and result in a beating product frequency that is not sufficiently attenuated by the selective IF filters [7].

Receiver front-end selective circuits, also contribute in attenuating part of the STS interfering signals, especially the disturbing image frequency to a reduced power level sufficiently below the receiver detection sensitivity threshold [21]. A prohibited list that includes all potentially disturbing input signal frequencies to avoid can be obtained from the receiver front end circuits parameters and the system operational scenarios [7], by using a special computer program [21].

In the absence of desired transmitter signals, mixing products from an interfering STS signal may cause tedious disturbances which will not degrade performances but may be annoying to system users only because it will not affect significantly the $S/N+I$ when the desired received signal is present [7, 10].

## 5. Desensitization effects computation

The minimal realistic distance between the handset transmitter and the base receiver antennas is $d = 3m$. Thus from equation (4) the propagation dispersion loss is only , $A_{FS} = 41dB$ as shown previously. The handset transmitter power level is very low $P_T \le 0dBm$, due to the Common Air Interface (CAI) dynamic adaptive power control [5].

From equation 10 when the specified system Rx threshold power level is $P_{Rs} = -89dBm$, the required $A_s$ is around

$$A_s \ge P_T + G_T - A_{FS} + G_R - P_{RS} \tag{19}$$

Therefore in the realistic worst case $A_s \ge 53dB$ and the most proximate adjacent channel which provide sufficient frequency attenuation A is from the Transmitter spectrum response of Figure 4, $(f_0 \pm 0.3)MHz$.

At this frequency interval , the low interfering power level $P_{RS}$ at the victim Rx is not sufficient to desensitize the preamplifier (characterized by $P_{1dBG_c} \approx -35dBm$) and the following active stages [7]. Therefore the victim base receiver will operate in linear characteristics conditions. The interfering signal will not affect the receiver selective IF circuits due to an additional frequency attenuation $A_f$ exceeding 40 dB. Thus, direct adjacent channel interference effects are negligible [12]. From the reciprocal principle which can be applied in case of linear systems [16;21] the second transmitter interference effects to the operating receiver are also negligible. A second worst case scenario occurs when two handsets are operating far from the base antenna but at a distance $d \le 200m$ and a minimal distance of $d_r = 3m$ between the handsets' antennas as shown in Figure 6. In this case $P_T = 10dBm$ due to the large distance from the base station. From Table 1 results, the base station receiver power input level is

$P_r \approx -65\text{dBm}$. From equation (13) $A_s \geq 24\text{dB}$ and the base Rx dynamic channel selection process may choose in this case even the 1st adjacent channel at frequency $(f_0 \pm 0.1)MHz$. The worst case path is between the two handset antennas where the adjacent channel spurious interference power level $P_{RS}$ at the second handset receiver can be computed from equations (16) and (17). Using the scenario parameters $P_T = 10dBm$, $A_{FS} = 41dB$, $A_s \approx 36dB$, $A_{\Delta_f} \approx 2dB$ and $G_T = G_R \simeq 0dBi$ [7] we obtain $P_{RS} \simeq -68dBm$.

In this realistic worst case scenario the victim handset receiver will not be desensitized at all at these relatively low power levels and the receiver frequency attenuation to the 1st adjacent frequency signal is exceeding $30dB$. The result is an interfering power level $P_{RS}$ less than –98 dBm which is significantly lower than the desired power level of $-65dBm$ shown in Table 1. Therefore even for these realistic worst case conditions the transmitter power level will not desensitize the receiver front end active stages. These interfering signals are strongly attenuated by the receiver IF selective filters and therefore will have no effect on the CT-2 outdoor system operation.

## 6. Additional intrasystem mutual interference sources

Effects of the additional co-channel mutual interference sources, shown in Figure 3, can be neglected due to the system transmitter harmonics and receiver local oscillator (LO) spurious signals frequencies that fall outside the band of 891 to 895 MHz. The receiver is always operated in its linear characteristics zone excited by input power level below the $P_{1dBc}$ upper dynamic range limit. Thus, AM to PM distortion effects can be neglected due to sufficient linearity of the transmitter and receiver described previously [6;21].

The transmitter non-harmonic broadband noise power level $P_{BN}$ is specified as less than $-70\text{dBc}$ [5]. The worst case interfering distance of 3m produces a minimum dispersion loss of $A_{FS_{min}} = 41\text{dB}$ between the antennas. Therefore, even for the highest interfering transmitter output power level ($P_{T\max} = 10\text{dBm}$), the broadband noise power level $P_{BN_r}$ at the victim receiver input will be around -101 dBm just below the $-100\text{dBm}$, threshold limit which will not affect the desired signal reception. Thus, the transmitter non-harmonic broadband $P_{BN}$ effects and the other minor sources of intrasystem interference presented in Figure 3 can always be neglected. In the analyses of the system intrasystem interference effects two handset were considered . The assumption is based on the fact that the total number of available channels is only 40, without considering the frequency reuse effect from neighboring CT-2 nanocells, in order to avoid harmful cochannel interference between cells. The probability that more than 2 persons are using their headset simultaneously at an LOS distance of less than 3 m is very low. Furthermore, under LOS propagation condition between handsets, if a third or more simultaneous users are operating at a distance further than 10 m, the dispersion attenuation will be at least $20\log(10/3) \simeq 11dB$ higher without considering the filtering effect of the victim receiver on the remote interfering signal. Dynamic channel allocation via DSP techniques can add at least 36 dB more attenuation from the frequency differences of additional users.

## IV. Conclusions

In this paper the intrasystem interference effects for an outdoor nanocell CT-2 system have been analyzed and computed and the equations presented can be included in a computer program for simulation of interference power levels compared to the desired signals in order to predict system performance.

The main conclusions are:

1. System CAI adaptive power control [5,10] enables operation at very low transmitter power levels of $-10\text{dBm}$ to 0 dBm for horizontal distances of about 70 m from the base station antenna. This can increase to a maximum of $10\text{dBm}$ at a cell maximum operational distance of 200 m. This power control mechanism significantly decreases the risk and effects of non-linear intrasystem interference.
2. The PCS system receiver dynamic channel selection process [7,10] reduces harmful linear cochannel and adjacent channel interference effects, even in case of near collocation situations.
3. Realistic worst case receiver IM power levels [20] are very low and their effects can be neglected due to cosited low transmitter power levels and relatively high system receiver dynamic range. Even the most harmful receiver 3rd order IM power level of $P_{IM3_h} \leq -95dBm$, as computed in section III.2, can be neglected.
4. Realistic worst case transmitter 3rd order IM power levels of ($P_{IM_{3h}} \leq -101dBm$) [12] are still lower than receiver IM. This is due to the linearity and high intercept point power level of the power amplifier stage. This IM product and all other IM products of lower power levels generated in the transmitter can also be neglected.
5. There is no risk of receiver desensitization [13,20], even for a realistic worst case distance separation of 3 m between two handsets as computed in section III.5.
6. The effects of all non-linear cochannel, adjacent channel and out of band intrasystem interference sources, presented in Figure 4, can be neglected except the Single Tone Spurious (STS) effects discussed in section III.4.
7. STS interference frequencies and realistic worst case power levels can be computed using semi-empirical methods [21]. The number of potentially disturbing frequencies in the list are very few for the CT-2 system, which is useful for frequency management purposes. A list of forbidden STS spurious spot frequency which are potentially harmfully to the system receiver can be provided. These interference effects can still be significantly reduced or even avoided by modifying receiver front end parameters using simple semi-empirical optimization and simulation methods, but this solution may be practical only for the next generation of PCS receivers [20].

The pico-cell PCS indoor interference effects analysis and computation are different than those of outdoor scenarios [22] and will be presented in a following paper. However, due to indoor obstructions and shadowing, the effect of intrasystem interference will be reduced. The effects of intersystem interference on nano-cell and pico-cell will also be presented in a following paper.

## References


1. Hardt, E., "Telecommunications: A Pillar of Social Evolution", Communications Week International, 6th July 1992. Siemens Supplement, pp. 3-4.
2. ITU Radio-Communication Study Group, "Short Range Communication Systems", Doc 1A/Temp/13-E. Sept. 1993, pp. 1-2.
3. Padgett, J.E., Gunther, C.G., Hattori, T., "Overview of Wireless Personal Communications", IEEE Communications Magazine, January 1995, pp. 28-41.
4. Steele, R., "The Cellular Environment of Lightweight Handheld Portables", IEEE Communications Magazine, July 1989, pp. 20-29.
5. CAI Specifications for the Interworking MPT 1375 between Cordless Telephone Apparatus, May 1989.
6. RF Parameters for CT2 defined in MPT-1334 Dec. 1987 and British Standard BS-69833, Parts 1,2, 1989.
7. Perez, R., Editor, "EMC Handbook", Academic Press, 1995, Chapters 19,20.
8. Parsons, J.D., "The Mobile Radio Propagation Channel", Pentech Press, London 1992, Chapters 1,2,5.
9. Evans, M.W., "CT2 Common Air Interface", British Telecom Eng., Vol. 9, July 1990, pp.103-111.
10. Gavan, J., "Radio System Interference Effects between Two Collocated Vehicular Transceivers: Analysis, Computation and Mitigation Methods", IEEE Trans. on Vehicular Technology, August 1994, pp.447-456.
11. Hess, G.C., "Land mobile Radio System Engineering" Artech House, 1998.
12. Gavan, J., Shulman, M.B., "Effects of Desensitization on Mobile Radio Systems Performance, Part II Quantitative Analysis", IEEE Transactions on Vehicular Technology, Vol.VT-33, No. 4, Nov. 1984, pp. 291-300.
13. Jakes, W.C., "Microwave Mobile Communications", Wiley 1996, Chapters 1,2,3.
14. Gavan, J., "Main Effect of Mutual Interference in Radio Communication Systems using Broadband Transmitters", IEEE Trans. on Electromagnetic Compatibility, Vol. EMC-28, No. 4, Nov. 1986, pp. 211-220.
15. Yao, Y.D., Sheikh, A.V., "Outage Probability Analysis for Microcell Mobile Radio Systems with Cochannel Interferences in a Rician/Rayleigh Fading Environment", Electronics Letters, 21st June 1990, Vol. 26, No. 13, pp. 864-866.
16. Prasad, R., Kegel, A., De Vos, A., "Performance of Microcellular Mobile Radio in a Cochannel Interference, Natural and Man Made Noise Environment", IEEE Trans. on Vehicular Technology, VT-42, No. 1, February 1993, pp. 33-40.
17. ITU-R "Propagation in non-Ionized Media" ITU-R Geneva 1995 P370,452, 523, Recom.63 433-3, 508. CCIR Geneva Switzerland, 1990.
18. Draft Revision of Recom. CCIR PI.372-5 "Radio Noise", 23rd Sept. 1993, pp. 22-25.
19. Gavan, J., Joffe, E.B., "An Investigation of the Desensitizing Effects by High Power HF Broadcast Transmitters on HF Airborne Receivers, IEEE Trans. on Electromagnetic Compatibility, Vol. 34, No. 54, May 1992, pp. 61-73.
20. Gavan, J., "Interference Intrasystem Effects for Nano- and Pico-cell Personal Communications", 11th International Zurich Symposium on EMC, Zurich, March 1995, pp. 159-166.
21. Gavan, J., "Analysis of Single Tone Spurious Effects in Non-desensitized Radio Communication Systems", IEEE Trans. on Electromagnetic Compatibility, May 1991, pp. 77-89.
22. Gavan, J., "Interference Effects for Pico-cell Indoor Personal Communication Systems" EMC International Symposium in Beijing China, May 1997 pp. 25-28.

# APPENDIX

**Table 2: Required CT-2 transmitter's and receiver's specified parameters**

| ***Tx parameters*** | ***Typical values*** |
|---|---|
| Frequency Band | $f_{o=}$ (891-895) MHz |
| Channel spacing<br>Bandwith | Δf=100 kHz<br>Bn=84 kHz |
| Maximum Power level | $P_T$ =10 mW |
| Power Control Variation | $-10 < P_T \leq 10dBm$ |
| Encoding Technique | ADPCM (32kbit/s) |
| Frequency peak deviation | (14.4-25.2) kHz |
| Output frequency response<br>(see figure 4) | $P_T \leq \begin{cases} -36dBm & \lvert\Delta f\rvert \geq 100kHz \\ -70dBm & \lvert\Delta f\rvert \geq 500kHz \end{cases}$ |
| Power Amplifier Linearity<br>Power Amplifier Intercept. Point | Class A linear amplifier.<br>$P_{IP3}$ =30 dBm |
| ***Receiver parameters*** | ***Typical values*** |
| Sensitivity | $P_{sen_m} \geq -109dBm$<br>$P_{sen} = -94dBm$ for BER of $10^{-3}$ |
| Noise Figure | $F_R$ = 9 dB; for worst case 10 dB |
| Front End Third Order Intercept Point | $P_{IP3} = -22dBm$ |
| Desensitization power level | $P_{des} \leq -35dBm$ |
| Antenna characteristics &<br>dimensions | Headset whip $1.2 \leq h_{handset} \leq 1.8$m<br>Base station: Vertical monopole<br>$3 \leq h_{base} \leq 7$m |

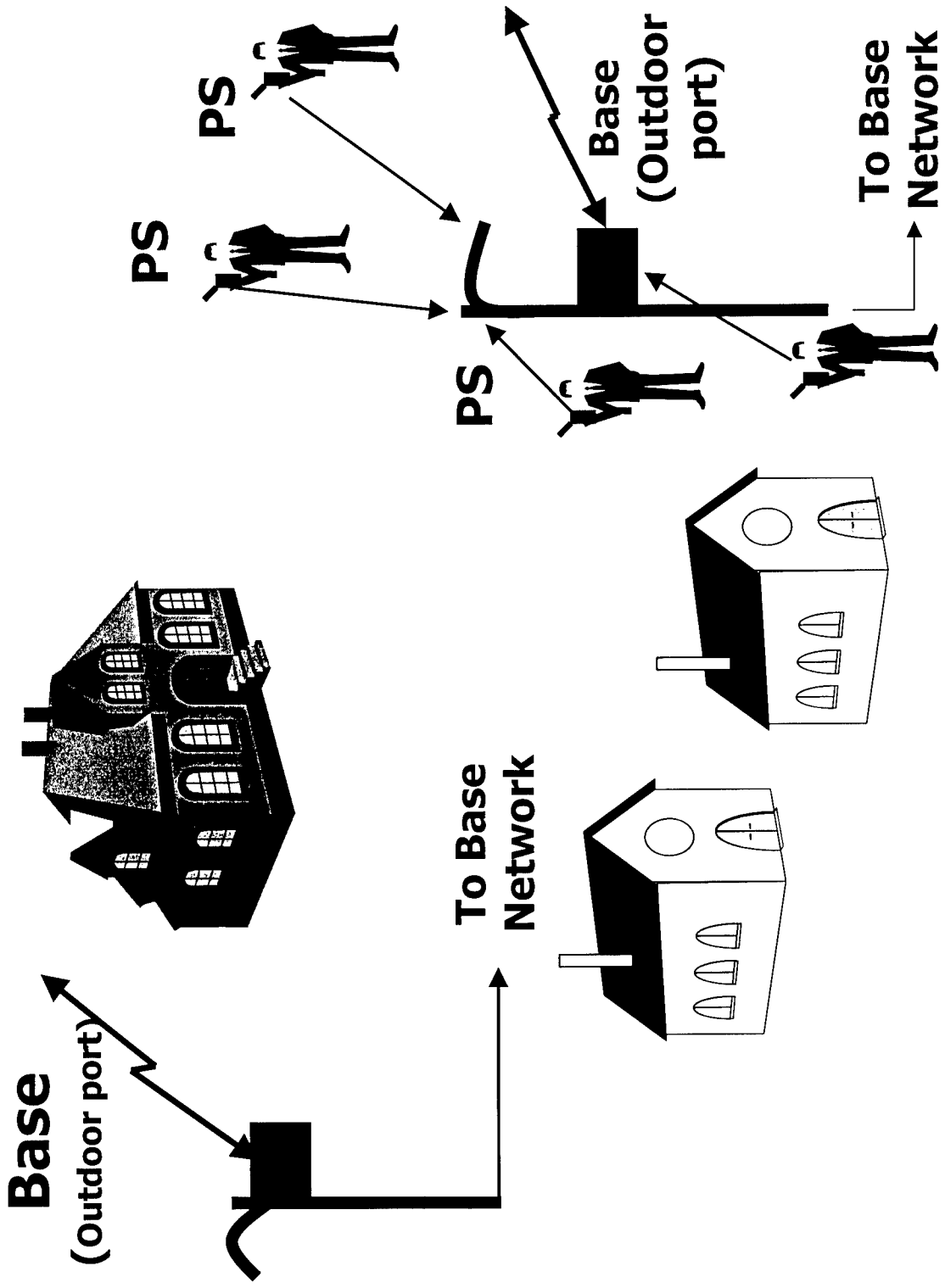


**Figure 1 : Open site outdoor personal communication operation scenario**

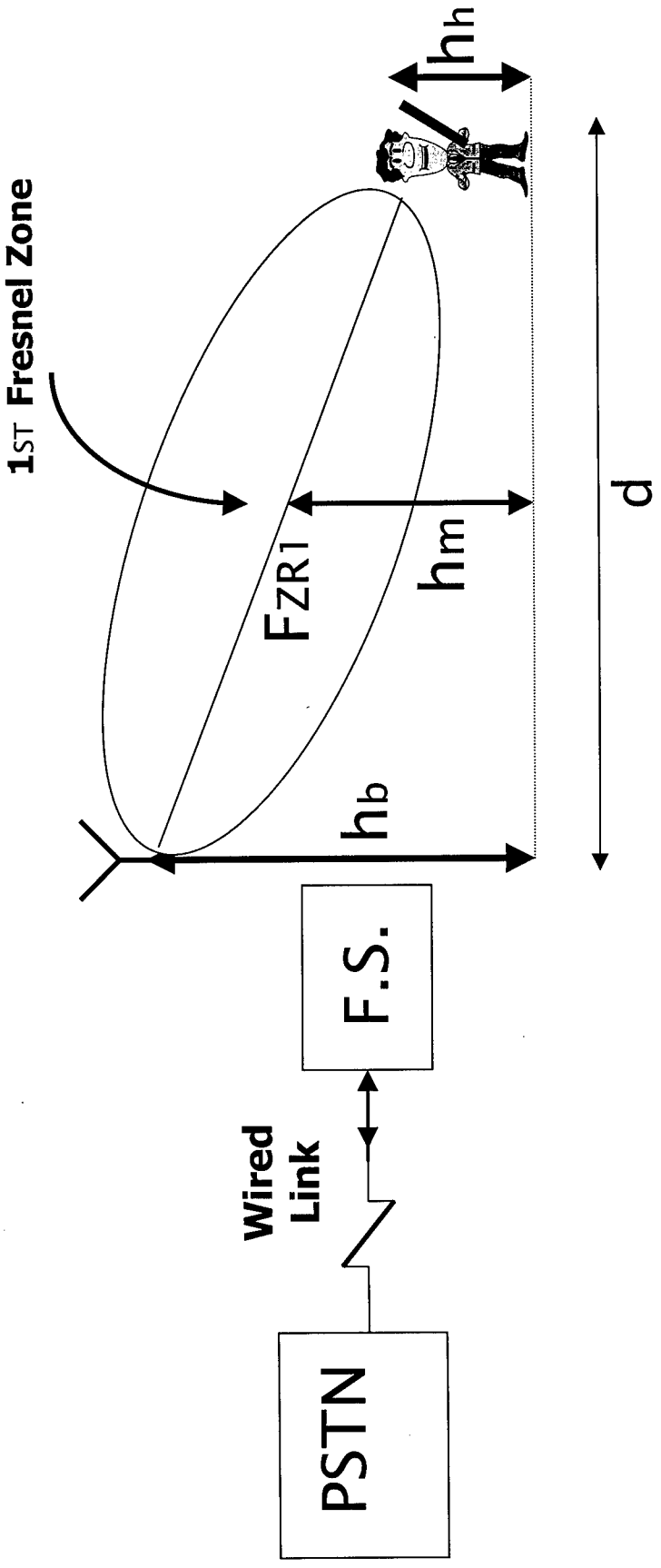


**Figure 2 : Outdoor (open site) personal communication LOS operation conditions using first Fresnel Zone ellopsoid criteria**

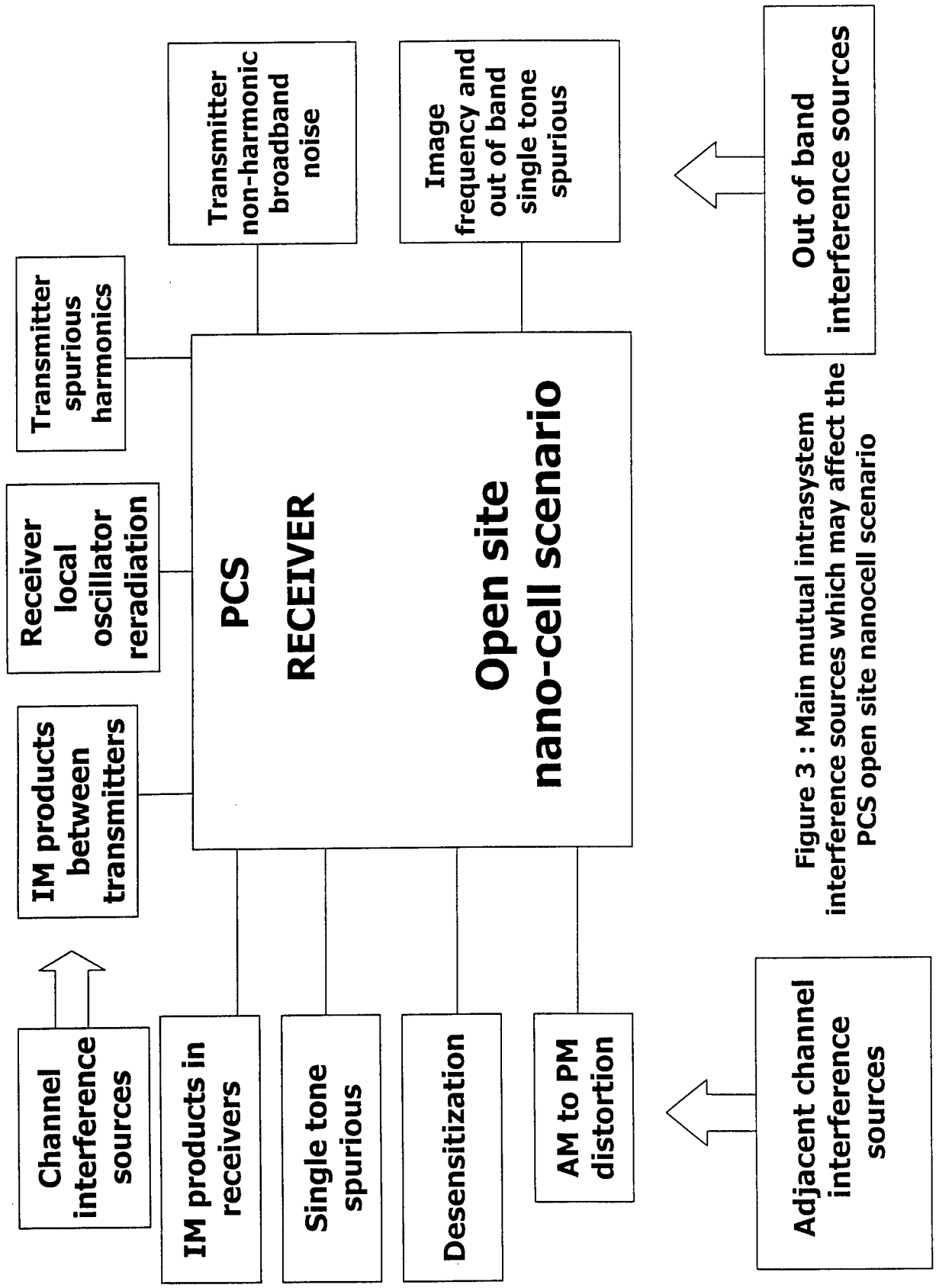


Figure 3 : Main mutual intrasystem interference sources which may affect the PCS open site nanocell scenario

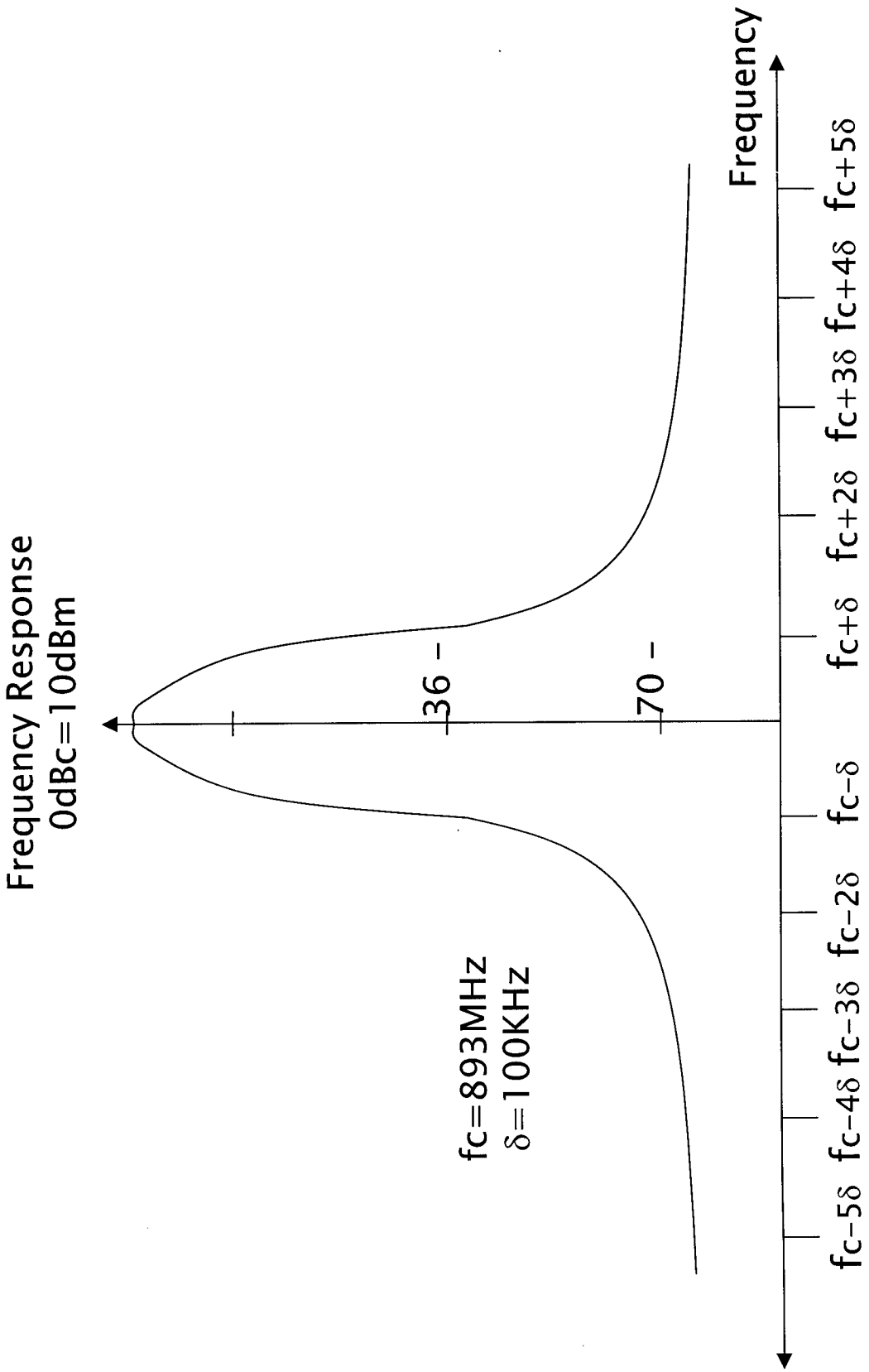


**Figure 4 : PCS-CT-2 Spectrum of the transmitted signal**

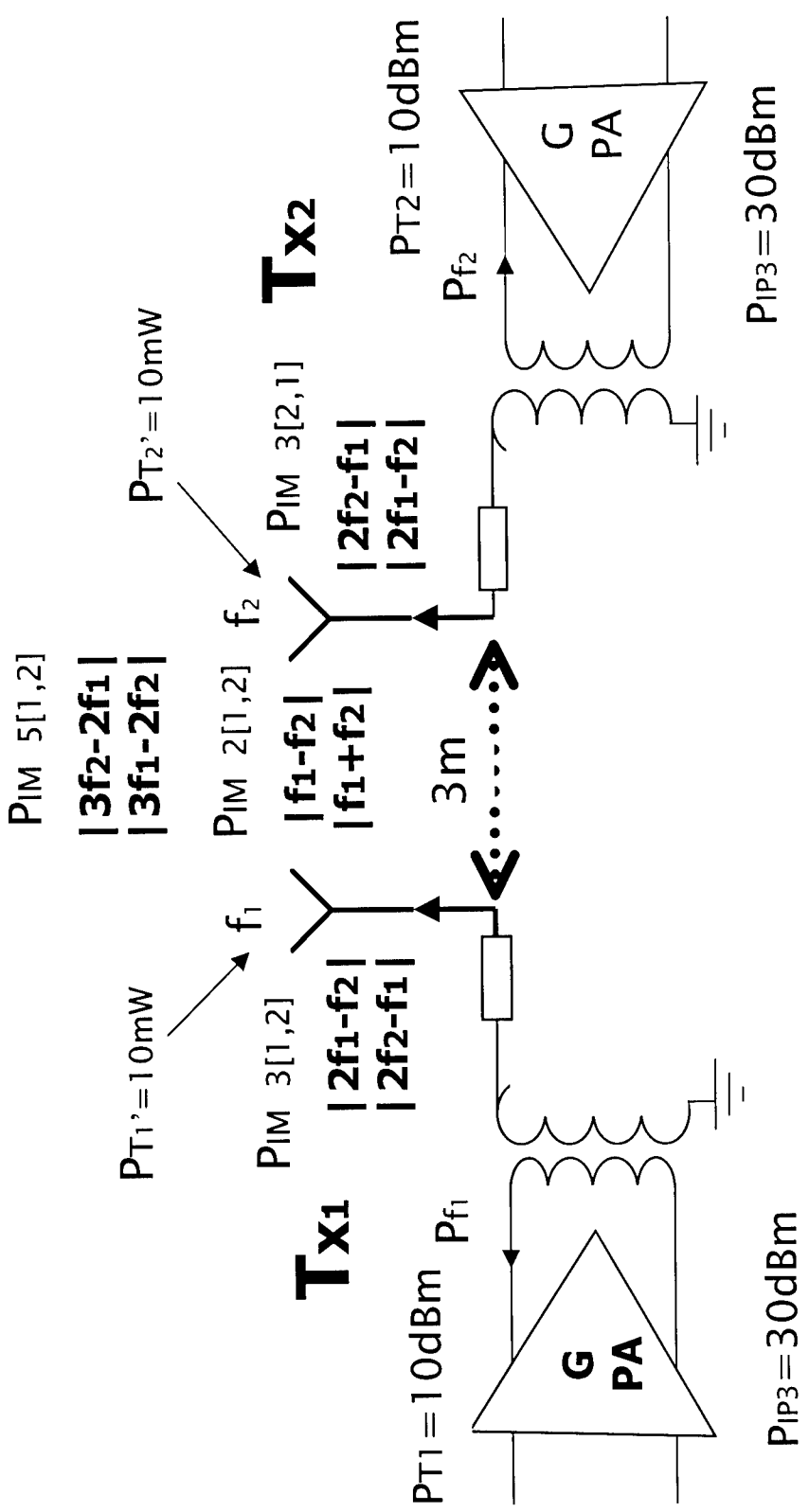


**Figure 5 : Schematic of final stage of PCS transmitter presenting the intermodulation product power level computational method**

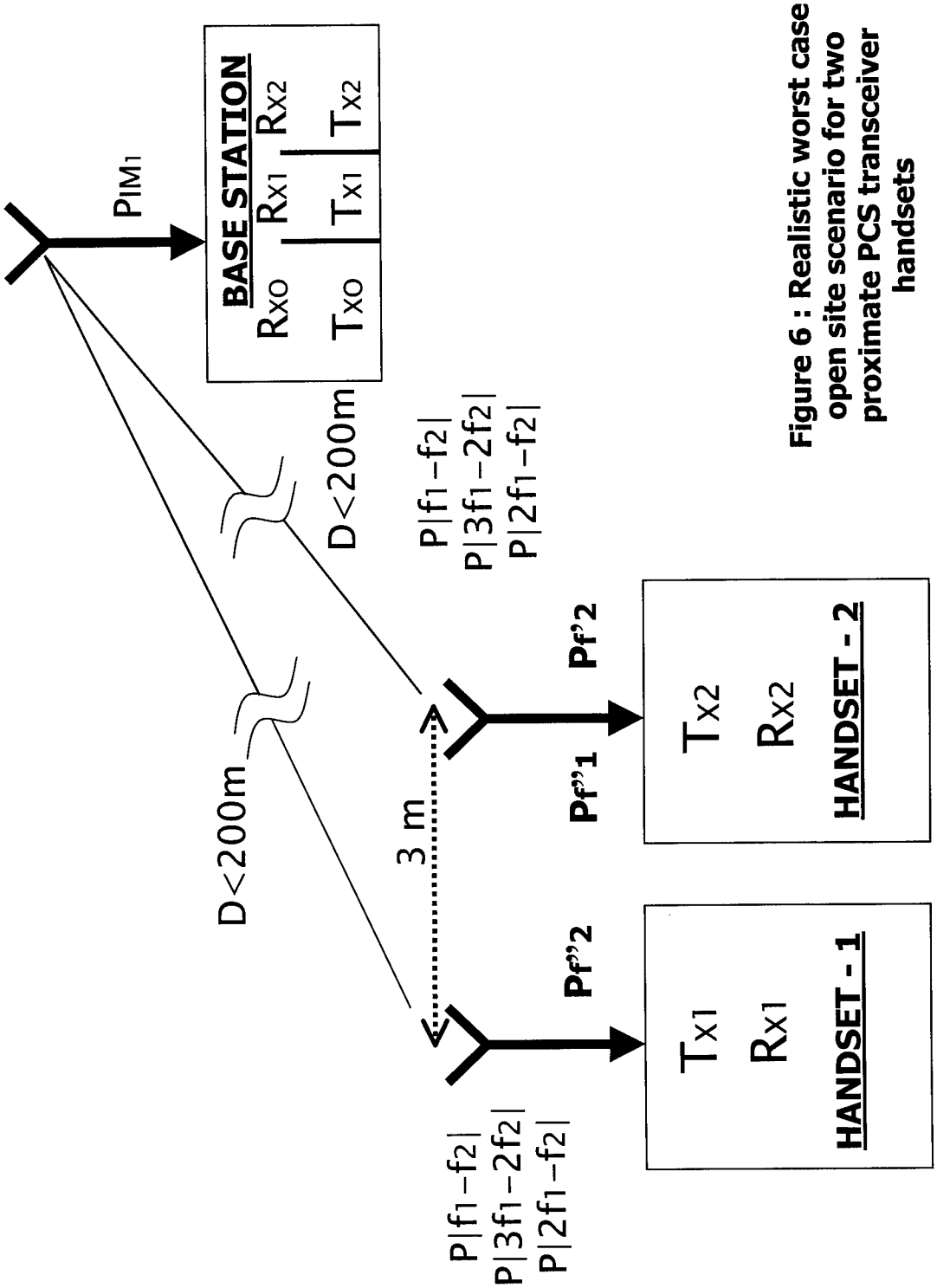


**Figure 6 : Realistic worst case open site scenario for two proximate PCS transceiver handsets**

# Designing Embedded Antennas for Bluetooth Protocol

Ray Perez
Jet Propulsion Laboratory
California Institute of Technology

## Abstract

In the near future, all kinds of portable devices ranging from laptops, PDAs, to cellular phones will be capable of communicating and inter-operate with each other using a new wireless technology networking protocol known as bluetooth. There are however, several hurdles that must be overcomed . One of these hurdles is to provide a communication link that mostly interference free. The design of an appropriate antenna is important in providing a good communication between devices. In this paper we present the outline of an embedded antenna using the method of moments. This work is also extended to address generally other design issues in bluetooth technology that can be address using computational electromagnetic.

## Introduction.

One of the hottest technologies in the wireless world in bluetooth [1-2]. The bluetooth standard was created by the Swedish telecommunications equipment manufacturer Ericsson. Named after the Danish King Harald II, who received the nickname "bluetooth" when he unified Denmark and Norway in the $10^{th}$ century. The bluetooth standard is pose to be the standard for inter-device communications for short-range RF networking in the wireless medium. About 1800 companies are already members of the bluetooth consortium, with more to follow. Bluetooth is intended to provide an energy saving, safe (i.e no known adverse bioelectromagnetic effects), and low cost RF technology in order to eliminate wire connection over short distances. Bluetooth can be integrated in almost all kinds of electronic data-communications devices and can communicate among each other without a line-of-sight connection.

A bluetooth devices consists of a baseband controller and an RF section. The controller has an interface to the host system (e.g. laptop, PDA, cellular phone, desktop PC...). Bluetooth works in the industrial, scientific, and medical (ISM) frequency band between 2.402 and 2.480 GHz and uses a frequency hopping mechanism, where 1600 frequency changes occur every second. A single bluetooth connection uses 79 different frequencies with a channel separation of 1 MHz. The frequency hopping of bluetooth is necessary to provide a higher level of security against eavesdropping and to minimize interference. Interference is an issue because the bluetooth operating frequencies fall within that of microwave oven and other radio services close to the ISM band. Bluetooth also uses forward correction which limits the impact of random noise on long distance links. Whenever interference occur on a specific frequency, this frequency isn't assigned during frequency hopping, and hence a minimization of interference effects. In most cases for such situations, the antenna will be implemented by assigning a short segment of conducting track on a PC board.

The maximum transmission for bluetooth is 1 mW which is enough to communicate up to a distance of 10 m. Most likely however, consumers envision communication at much larger distances. An output of power of about 100 mW is needed to communicate up to 100 m. In the receiving end, the bluetooth describes a sensitivity of –70 dBm working with an IF of 1 MHz. The bluetooth architecture can handle up to 8 devices and can communicate using what is called the "Piconet". Within 2 seconds, individual bluetooth controllers inside the Piconet identify themselves by using a unique 48-bit serial number. The first device that has been identified takes control of the master function. Several Piconets operating with individual hopping algorithms can communicate within a larger multiple Piconet environment known as a scatternet. Bluetooth works with shorter data packets. The full duplex data rate within a scatternet that has 10 fully loaded independent Piconets is more than 6 Mbits/s.

The baseband controller prepares the data for transmission and also controls the entire procedure. When voice data is transmitted, bluetooth works with a transmission rate of 64 kbits/s in a synchronous mode. Every single data packet is transmitted at another hopping frequency and a data packet is assigned to a single time slot. Data can be transmitted asynchronously at net data rates of 721 kbits/s upstream and 57.6 kbits/s downstream, or synchronously at 432.6 kbits/s in both directions. Bluetooth supports the transmission on one synchronous data channel and three synchronous voice channels. Furthermore, it can support one asynchronous data and one synchronous voice audio data within a single channel. Voice channels use the continuous variable slope delta modulation voice coding scheme which is highly robust.

Bluetooth at Work.

The entire connection is mastered by the link controller (see Figure 1) which is an integral part of the baseband IC. The controller takes cares of the protocol and link access routines. Every 1.28 seconds the Piconet "listen" for any signal. If a signal is detected, the bluetooth module will look for the communication partner on 32 individual assigned frequencies. The next step is assigning the master module by using a page message if the address of the communications partner is known. If the communications partners is not known, an address inquiry is followed by a page message that will be sent out. At the beginning of the paging mode, the master sends out 16 identical page telegrams on 16 different hopping frequencies. If no answer is received, then the master resends its page telegrams. The telegrams will sent 16 different hopping frequencies. The maximum time delay a master needs in order to finally contact is about 2.56 sec.

The inquiry telegram is used in order to identify bluetooth devices which are nearby and with known addresses. The inquiry message is very similar to a page message. However, it can demand an additional routine whenever answers from several devices need to be collected. If no data is transmitted, a Piconet master can assign its slaves to operate in the "hold" mode to conserve energy. In this mode an internal timer circuits keeps on working. The master can assign all slaves to operate in the hold mode when it wants to set up a scatternet with an adjacent Piconet. On the side, slaves can request the master to

allow them to change to the hold mode. When any kind of data communications is needed the master wakes up the relevant slave.

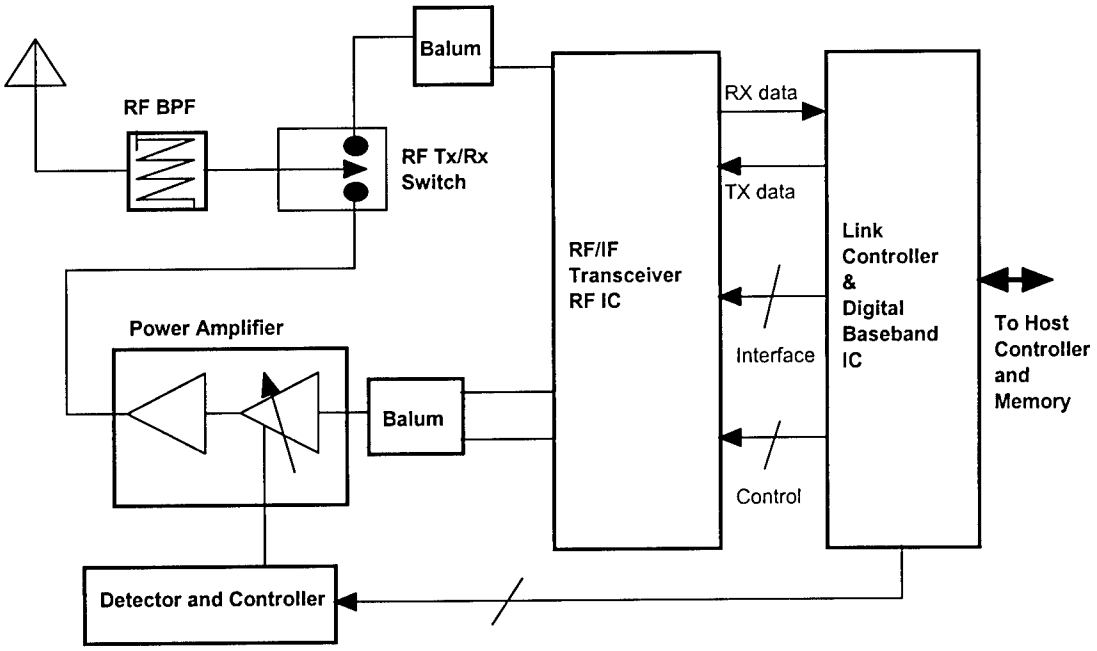


Figure 1. The Bluetooth Sample Architecture.

In Figure 2 the design is more advanced since we have integrated the power amp and baseband processing within a single RF IC and the link controller is implemented using digital signal processing (DSP).

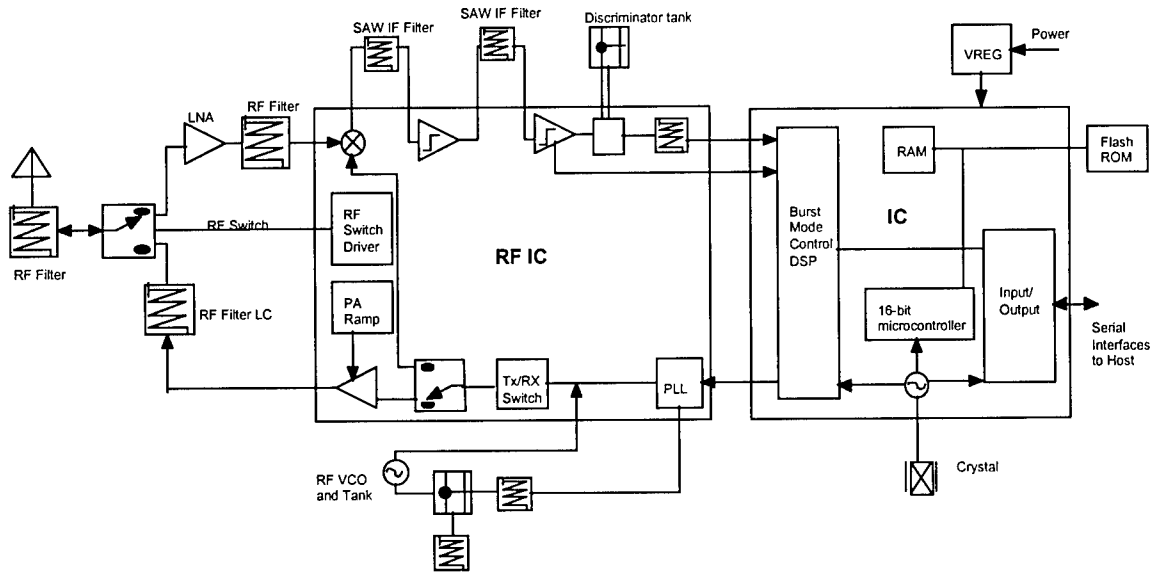


Figure 2. Advance Bluetooth Architecture

Antenna Design for Bluetooth Technology.

An important component in the bluetooth technology is the design of the antenna. Bluetooth is intended for many kinds of devices such as portable devices (PDA, cellular/PCS phones, laptops) and desk top devices (PC, printers, ..etc) which means that antennas must come in different shapes and sizes to accommodate the type of technology. For example, in a cellular phone the bluetooth antenna must be small (smaller than the whip antenna used in most cellular phones) and inserted within the electronics of the phone in order to minimize the complexity of dealing with dual antennas and dual electronics for the phone. In larger devices, such as in a PC, a bluetooth antenna can be easily inserted externally at many possible locations.

Another important characteristic on bluetooth antennas is that an effort must be made to provide an omnidirectional azimuth pattern, since a communication link must often been establish among devices that are not on a direct line of sight (e.g one device can be in the kitchen and the other can be in the living room of a home). In residential homes, doppler and delay spread of the signals are minimal and can be considered as a slowly varying Rician flat-fading channel where all effective multipaths arrive within the information signal [3].

In this paper we address an embedded bluetooth antenna for small portable devices. We have extended the design to include not only an antenna for bluetooth electronics but also for a PCS (1.85 –1.99 GHz) mobile device electronics. The design in shown in Figure 3. The antennas are microstrip dipoles embedded in a dielectric substrate. The dipoles are $\lambda/4$ antennas. The dielectric is of low loss with $\varepsilon_r$ =2.42 and a very low loss-tangent. The embedded antennas within the dielectric frame form a "chip" that can be "plugged-in" into a metal ground plane as shown in the figure. The ground plane should also be around $\lambda/4$ as a minimum. If it is too large, the radiation pattern becomes somewhat multi-lobe, but that is not necessarily a bad thing for an omnidirectional antenna. If the ground plane is much smaller than $\lambda/4$, then the tuning becomes more difficult and the overall performance of the antenna decreases. For example, that is indeed the case with pager antennas. Pager antennas are very much inefficient since the size of pagers are significantly smaller than their operational wavelength. Pager companies make up for this inefficiency by increasing the base station power.

It was decided to make the ground plane somewhat higher than the $\lambda/4$. The bluetooth electronics with its own antenna and ground plane can then be "fitted" within another wireless device such as a PCS device as illustrated in Figure 3. The ground plane of the PCS wireless device (not necessarily a phone) can either be separate or connected to the bluetooth ground plane. In some cases it may be OK to use one large ground plane for both the PCS and bluetooth electronics and antennas.

The analysis and design for both, the PCS and Bluetooth antennas was done using the method of moments in the code NEC. The microstrip design of the dipoles was converted into equivalent round wires with the same surface areas using well known analytical

expressions. The modeling rules of NEC for properly using the method of moments in wire antenna design were faithfully abided by.

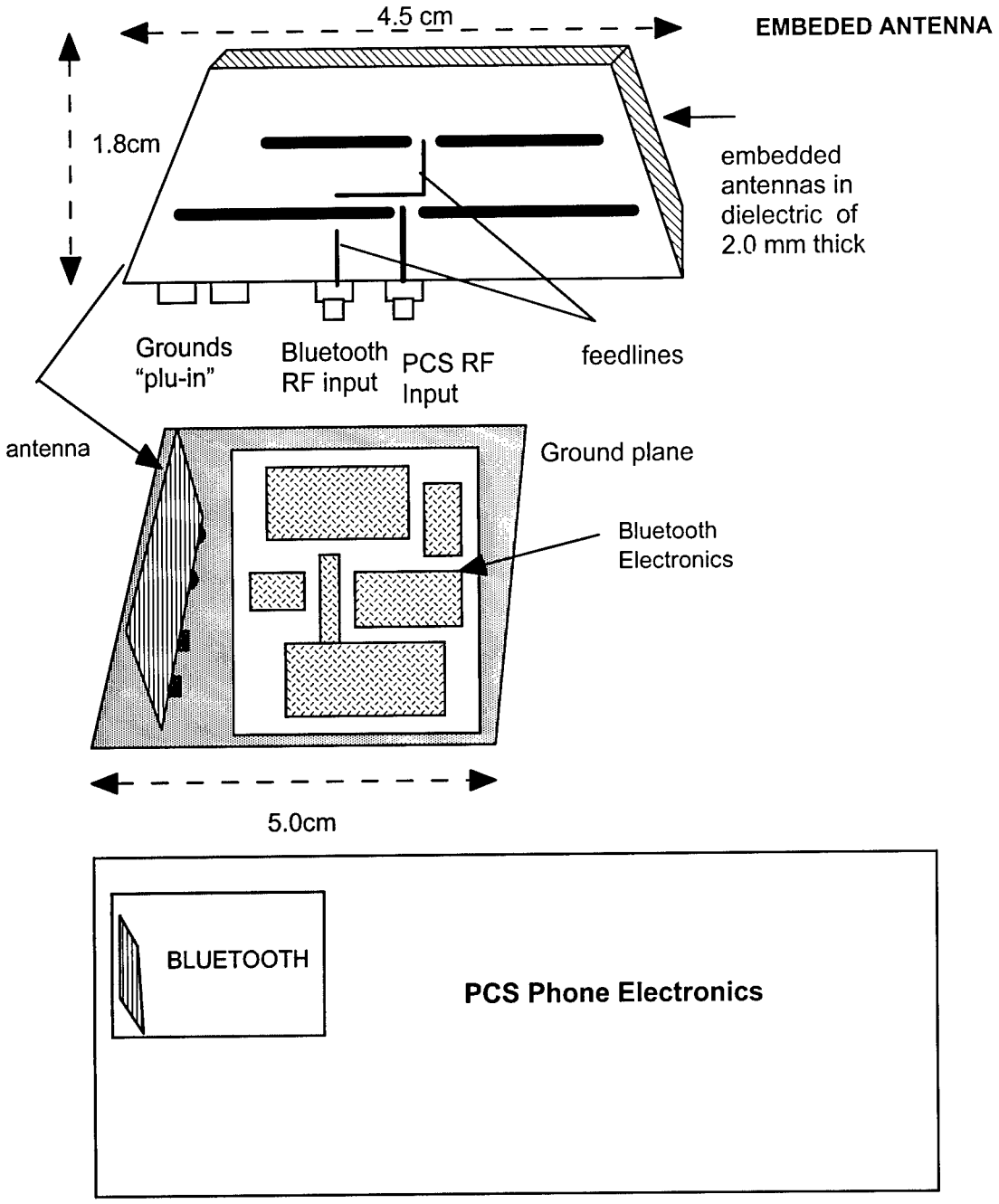


Figure 3. Design of bluetooth and PCS embedded antennas for personal wireless devices

The dielectric material was not ignored, even though it was a low-loss dielectric. The dielectric material was accounted for by putting a "sleeve" of the dielectric around the round wire. The thickness of the sleeve of dielectric was obtained by known equivalence

transformations of a dielectric slab into a cylinder. The ground plane was also modeled in NEC using perfectly conducting patch surfaces.

The calculation of the electric fields were performed in an azimuth manner and normalized at 1 meter so as to calculate the antenna patterns. The results of these calculations are shown in Figure 4. Figure 4 also shows some measured results using an antenna chamber.

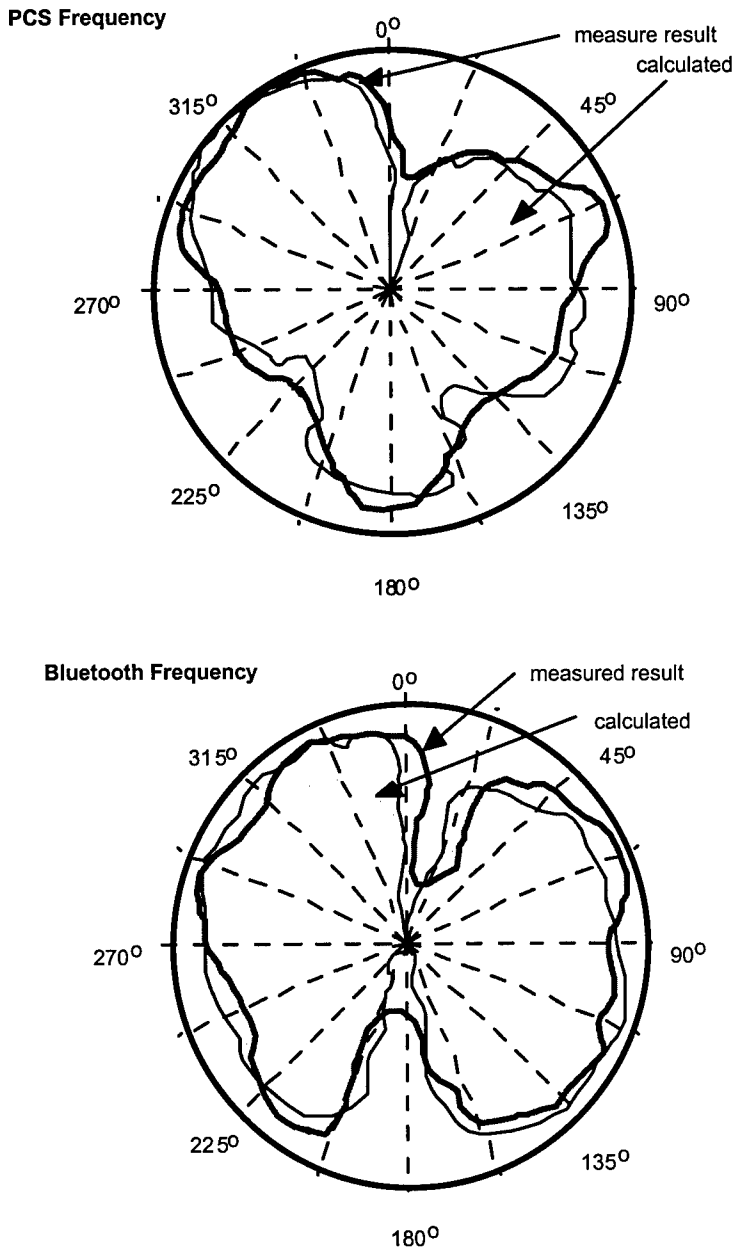


Figure 4. Antenna pattern for PCS and bluetooth antennas, both measured and calculated

Some measured VSWR is shown in Figure 5.

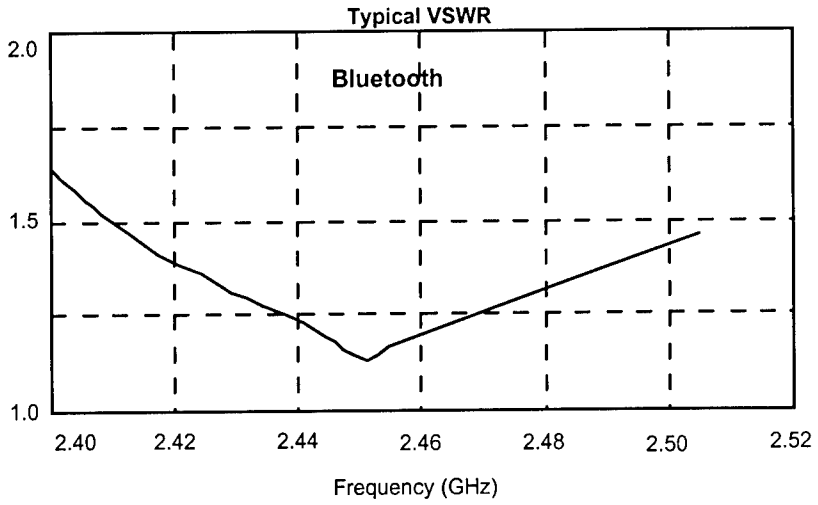


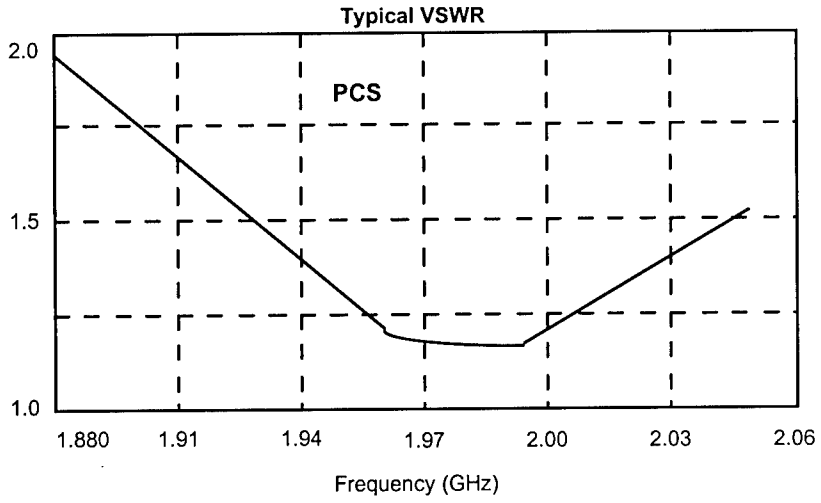


References.

[1] Alan Conrad, and Jack Browne, "Tracking the latest bluetooth developments," Wireless System Design, August 2000.

[2] Ernest, Rejman, "Bluetooth puts bite on mobile communications," Microwave Journal, July 2000.

[3] W.Roberts Nichols II, Moeness G. Amin,"Modeling systems based on bluetooth wireless connectivity," Microwaves and RF, August 2000.

# ANALYSIS AND DESIGN OF TAPERED MEANDER LINE ANTENNAS FOR MOBILE COMMUNICATIONS

**Chun-Wen Paul Huang, Atef Z. Elsherbeni, and Charles E. Smith**

**Electrical Engineering Department, The University of Mississippi**
**University, MS 38677**

*Abstract* - **Small printed antennas are becoming one of the most popular designs in personal wireless communications systems. In this paper, the characterization and design of a novel printed tapered meander line antenna are presented using the finite difference time domain technique. Experimental verifications are applied to ensure the effectiveness of the numerical model, and excellent agreement is found between numerical analysis and prototype measurements. A new design of this antenna features an operating frequency of 2.55 GHz with a 230 MHz bandwidth, which supports future generations of mobile communication systems.**

## I. Introduction

With the advancements of modern integrated circuit technologies, personal communication systems (PCS) feature light weight, small size, high frequency operation, and high transmission efficiency. Mobile antenna design is one of the major tasks in PCS designs, which requires easy integration with the interior circuitry. One of the most widely used wireless communications systems is the global system for mobile (GSM) communications, which operates at 890-915 MHz for uplink and 935-960 MHz for downlink [12]. The new generation of personal communication systems, such as digital communication systems (DCS) 1800 [12], operates at 1.710-1.785 GHz for uplink and 1.805-1.880 GHz for downlink. Another widely adopted telecommunication system for PCS is the code division multiple access (CDMA) system, which operates at 1.8 to 2.0 GHz. Furthermore, recent designs of indoor cordless phones and modems for wireless local area networks (WLAN), operating at 2.4 GHz of the industrial, scientific, and medical (ISM) band applications, are also available in the market. Therefore, antennas for current and future generation of personal communication systems are designed to operate at a single or dual frequencies in the range from 0.9 GHz to 2.5 GHz. New types of printed meander line antennas have been recently investigated by several authors [1-7]. Detailed studies and empirical formulae of the effects of trace width, segment lengths, and ground plane size of meander line antennas can be found in [8 and 9].

In this paper, studies of the characteristics of a novel tapered meander line antenna [7], using the finite difference time domain (FDTD) [10] techniques with Berenger's perfectly matched layers (PML) [11] absorbing boundaries are presented. The presented designs of the antenna shown in Figure 1, feature small dimensions (32 x 25 x 3.17 $mm^3$), and approximately 50 Ω input impedance with a dual printed sleeve tuner. The antenna is designed to operate at a single frequency within the 0.9-3.0 GHz range on a comparably small ground plane (59 x 25.4 $mm^2$). The validation of the numerical analysis used in this investigation is made by computing the return loss of the tapered antenna and comparing it with measurements. Very good agreement is found using the developed FDTD code. Analysis and design based on this numerical model are thus performed. A wideband design is achieved by using a dual sleeve tuner [2, 6]. The antenna operating bandwidth is centered at 2.5 GHz with 230 MHz of bandwidth. This optimal design can be used for future generation of wireless phones or other current wireless applications operating around this frequency.

## II. Design Approach

The antennas considered in this study are shown in Figure 1. In Figure 1(a), a tapered meander line trace is printed on a 25-mm wide dielectric slab sitting on a 59 x 25.4 $mm^2$ perfectly conducting ground plane and 1 mm trace width. The parameters e1 and e2 represent the lengths of the vertical and horizontal printed traces, respectively. The vertical segment length e1 = 2 mm, and the horizontal segment length e2 starts from 4 mm and ends at 15 mm (5 turns) or 17 mm (7 turns) with a 1 mm increment for each horizontal segment. The corresponding vertical length $L_{ax}$ of the antennas are 25 and 29 mm for 5 turns and 7 turns of tapered meander line traces, respectively. The distance between the edge of the dielectric slab and the edge of the ending segment of the meander line is set equal to e1. The reason for modeling the meander line antenna on a small ground plane (59 x 25.4 $mm^2$) is to simulate its performance when this antenna is placed on top of a PCS handset or in other wireless appliances with a

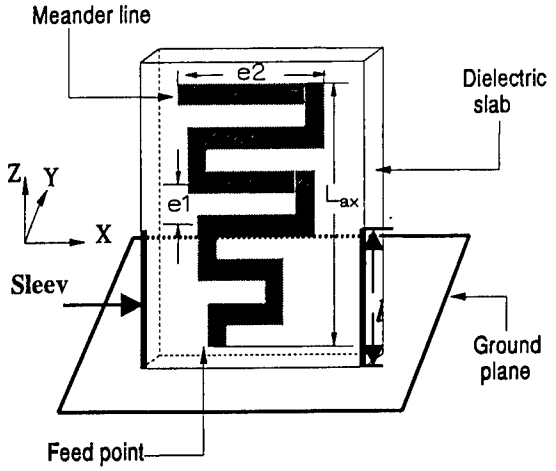


**Figure 1(a) An ascendant tapered meander line monopole with dual sleeves on a small ground plane.**

small effective ground plane. The main objective of this research is to design a meander line antenna with 50 Ω input impedance at an operating frequency within 0.9 to 3.0 GHz. The frequency range under study is extended from 0.9-3.0 GHz to 0.001-10.0 GHz for clearer observations of the resonance behavior of the antenna.

### A. FDTD Analysis

The finite difference time domain (FDTD) technique is applied to model the antenna inside a 3-dimensional air chamber terminated with the artificial boundaries of Berenger's perfectly matched layers (PML) [11]. The PML is adopted to reduce the numerical reflection from the truncated boundaries of the finite problem space, which resembles an anechoic chamber for antenna measurements. Eight layers of PML are used in our numerical simulations. An array of voltage sources with a Gaussian waveform is placed between the ground plane and the edge of the first vertical segment of the trace line for excitation. In the numerical simulations, the maximum amplitude of the waveform was set to 1 Volt and the internal resistance of the source was 50 Ω. The width of the Gaussian waveform pulse is selected to provide reliable results up to 18 GHz. The simulations are performed for 16,364 time steps with the time increment satisfying the Courant condition. The voltage is sampled between the antenna feed and ground plane, while the current is calculated by applying Ampere's law around the antenna feed, expressed as follows.

$$V(t) = -\int \vec{E}(i,j,k,t)\cdot d\vec{l} \cong -\sum \vec{E}(i,j,k,t)\cdot d\vec{l} \quad \textbf{(1.a)}$$

$$I(t) = -\oint \vec{H}(i,j,k,t)\cdot d\vec{l} \cong -\sum \vec{H}(i,j,k,t)\cdot d\vec{l} \quad \textbf{(1.b)}$$

After the transient voltages and currents are sampled, their frequency domain representation are calculated using discrete Fourier transform. Hence, the input impedance is obtained by applying

$$Z(f) = \frac{V(f)}{I(f)} \quad (2)$$

The corresponding reflection coefficient of the antenna can be calculated as

$$\Gamma(f) = \frac{Z(f) - R_c}{Z(f) + R_c} \quad (3)$$

$R_c$ is the characteristic impedance of a transmission line, and is always chosen as 50 Ω in most RF and wireless communications systems. The return loss of the antenna is calculated using 20 *log* $|\Gamma(f)|$. The radiation intensity and directive gain of an antenna are defined by equations (4) and (5), respectively.

$$U(\theta,\phi) \cong \frac{\left|E_\theta(\theta,\phi)\right|^2 + \left|E_\phi(\theta,\phi)\right|^2}{2\eta_o} \quad (4)$$

$$D(\theta,\phi) = 4\pi \frac{U(\theta,\phi)}{\int_0^{2\pi}\int_0^{\pi} U(\theta,\phi)\sin\theta\, d\theta\, d\phi} \quad (5)$$

After the characteristics of the tapered meander monopole are analyzed, dual printed sleeves are employed in the design to enlarge the bandwidth and tune the input impedance toward 50 Ω. Another tuning method using dual floating printed sleeves is studied, which can be also used to model the behavior of the dual sleeves that are not well grounded.

### B. Realization

In order to verify the designs obtained from the numerical simulations, tapered meander line antennas with and without dual-sleeve tuners (as shown in Fig. 2) are built and measured. The thickness of the PCB used in building the prototypes of these antennas is one half of that used in the simulations for the optimal design. However, the experimental data based on these prototypes are compared with the simulation results of the same antenna configuration. To prevent bending of this thin dielectric substrate, the width is increased 2 mm more on each side than the width specified in the previous section. The performance of this antenna is measured on a 1.5 x 2-$m^2$ ground plane to avoid the influence of the scattered fields from surrounding

objects. This ground plane is effective to simulate a semi-infinite ground plane in the frequency range of interest. The test is done using HP 8510C network analyzer, by measuring the return loss over a frequency

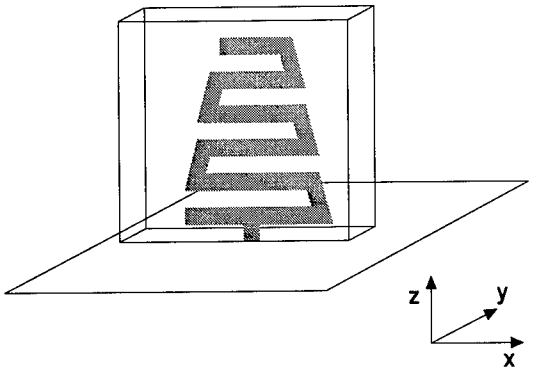


1(b)

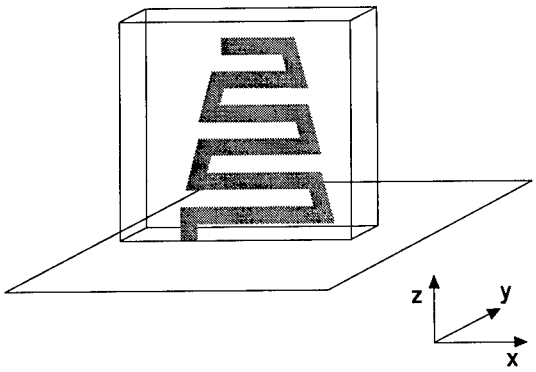


1(c)

**Figure 1 Descendant tapered meander line antenna fed (b) centrally and (c) laterally.**

range up to 10 GHz. As shown in Fig. 2, there is a 43-mm coaxial cable connected to the fixture of the antenna that serves as an antenna feed. This coaxial cable is excluded in measurement results by applying port extension to compensate for the electrical length of the cable to establish a reference plane at the antenna feed, as determined by time domain reflectometry (TDR).

After calibration, the analyzer is switched to time domain mode, and the antenna characterizations are measured in the time domain. To locate the starting plane of the antenna trace, the antenna is shorted to the ground at the feed point, which results in total reflection with 180 degrees out of phase. Therefore, by locating the reflection with magnitude of 1 and by measuring the time difference between this reflection spike and analyzer's reference plane, the information to translate the network analyzer reference to the apparent antenna reference plane is obtained. Therefore, the actual electrical delay can be determined by using one half of the time difference between the analyzer reference plane and the total reflection spike, which is 212.5 picosecond for this antenna model. The one half factor is required because the analyzer presents time domain

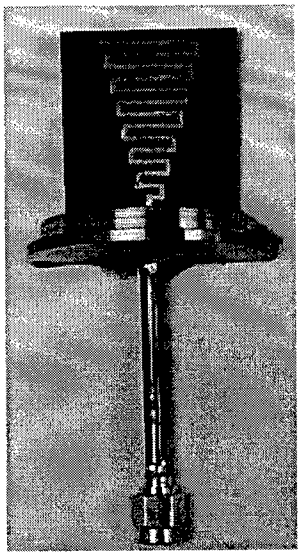

**Figure 2 (a) The prototype of a tapered meander line monopole with e1 = 2 mm, e2 ranges from 3 mm to 17 mm, and a dielectric substrate width of 29 mm.**

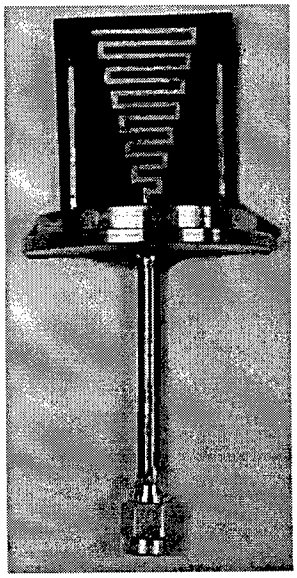

**Figure 2(b) The prototype of a dual-sleeve tapered meander line monopole with e1 = 2 mm, e2 ranges from 3 mm to 17 mm, and a dielectric substrate width of 29 mm.**

reflectometry (TDR) data for twice the traveling time between source and load to detect this total reflection. The computed impedance for the taper meander line antenna placed on a semi-infinite ground plane can be obtained by computing half of the meander line dipole configuration impedance, which is analyzed using a cell size of 0.5 mm with 2 cells for modeling the source.

## III. Results

The study begins with different ways of tapered meander line layouts. In addition to the tapered line in Figure 1(a), the other tapered meander line layout, descendant tapered meander line antennas, are shown in Figure 1(b) and (c), which are fed centrally and laterally, respectively. The return losses of these three different types of 5-turn taped meander line antennas are computed and plotted in Figure 3. From Figure 3, the ascendant type of taper meander monopole has a more desirable wideband characteristic and a better return loss as the frequency increases. Although the side-fed descendant meander line has a very wideband mode, the frequency is too high for PCS applications. Therefore, ascendant tapered meander line antennas are analyzed in this paper and simply referred to tapered meander line antennas.

The first parameter of tapered meander line antennas under study is the effect of the vertical height $L_{ax}$ (or number of turns) on the operating modes. Antennas with 5 and 7 turns of tapered meander traces are analyzed and results are plotted in Figure 4(a). From Figure 4(a), the first and third resonance of the 5-turn tapered meander line antenna occur at 1.9 GHz and 3.98, respectively, which are too high for PCS dual band application. In addition, the resonant impedance is also too small. However, the 7-turn tapered meander line antenna has the first and the third resonance at 1.2 GHz and 2.7 GHz, respectively, which may be tuned as a 50-Ω input impedance antenna for current wireless applications. Therefore, more turns of tapered meander line traces will reduce the operating frequency of the fundamental mode. As observed in Figure 4(a), the operating modes have not only wider bandwidth but also better return loss values as the frequency increases. This 7-turn tapered meander line antenna is also compared with two other types of trace configurations with the same trace length, a printed monopole and equal e2 (10-mm for the first 4 turns and 11-mm for the last 3 turns) meander line antenna. The reason to adopt the same trace length (161-mm) for all three antennas is to study the resonant characteristics caused by different ways of trace bending. As shown in Figure 4(b), the non-tapered meander line does not have the wideband characteristics like the tapered meander line. In addition, the printed monopole has a repetitive resonant pattern, but all the operation modes are narrow-band.

To simplify the tuning design, the dual-sleeve method [2, 6] is adopted to improve the input impedance. Because the tapered line is not a uniform segment ratio trace, the optimal sleeve length $l$ is not necessarily ½ of

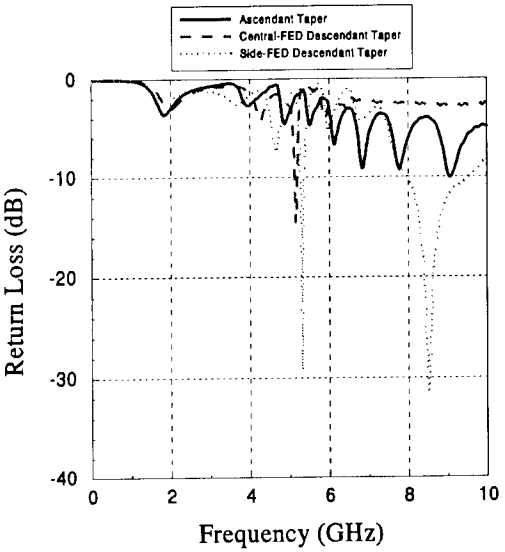


**Figure 3 The return losses of ascendant and descendant tapered meander line monopoles.**

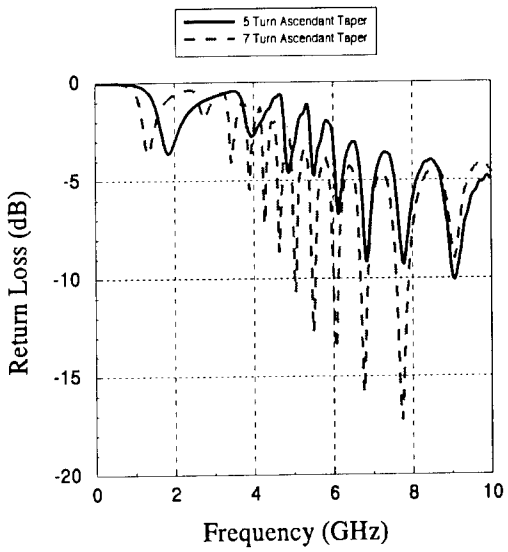


**Figure 4(a) The return losses of 5-turn and 7-turn ascendant tapered meander line monopole**

$L_{ax}$, as suggested in [2]. Choosing a spacing of 1mm away from the longest horizontal segment, the effects of different sleeve length is observed in Figure 5(a). From Figure 5(a), the optimal sleeve length for the

lower frequency end is found when the sleeve is 24 mm, 83 % of $L_{ax}$. Since the optimal sleeve length is determined for the current antenna configuration, the following analysis is made to determine the best location for dual-sleeves. From Figure 5(b), the optimal return loss is found when the spacing between the longest segment and a sleeve is 3 mm (i.e., at the edge of the substrate. For this case the antenna operates at 2.55 GHz with 230 MHz bandwidth, which is appropriate for future wideband mobile phones and current wireless ISM applications in the vicinity of this frequency. The input impedance at the operating frequency band of this optimal design is shown in Figure 5(c). Small reactance and 50-Ω resistance centered at 2.5 GHz within the operational bandwidth

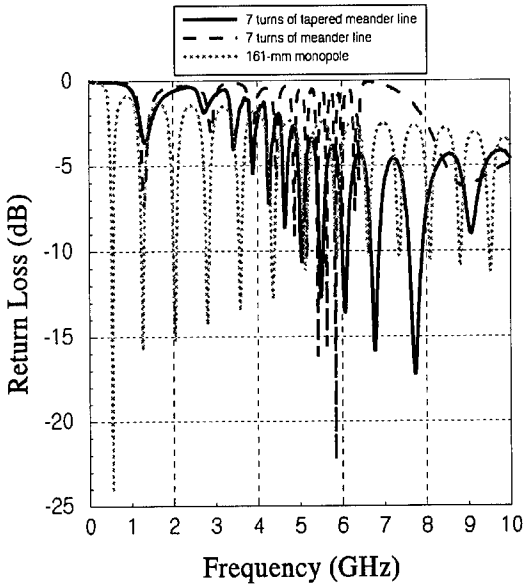


**Figure 4(b) The return loss comparisons of a meander line, a tapered meander line, and a monopole antenna with the same trace length (161mm).**

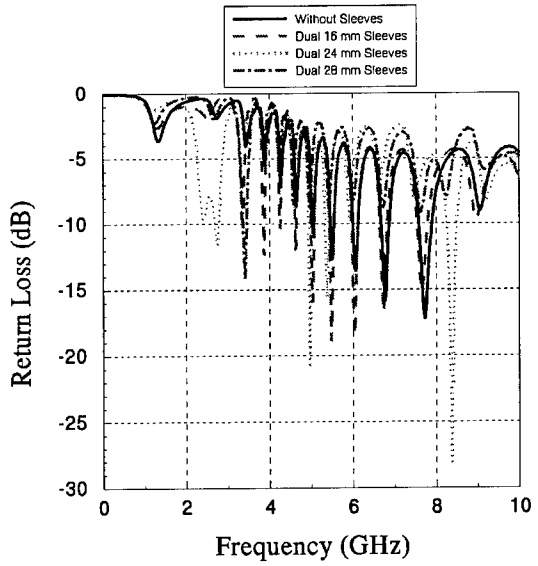


**Figure 5(a) Return loss of the tapered meander line monopole versus sleeve length.**

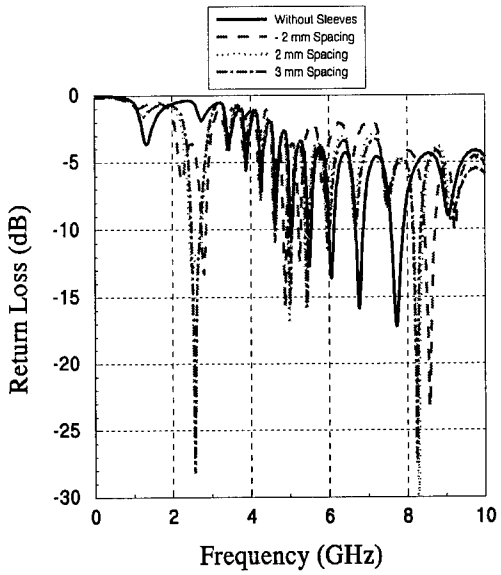


**Figure 5(b) Return loss of the tapered meander line monopole versus sleeve spacing.**

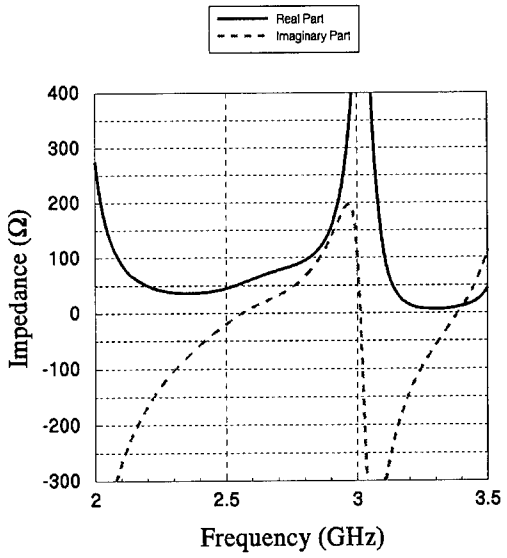


**Figure 5(c) Input impedance of the optimal tapered meander line monopole design with 24-mm sleeve and 3-mm away from the longest segment.**

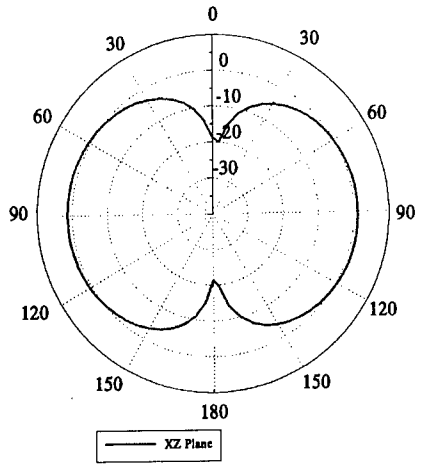


(a)

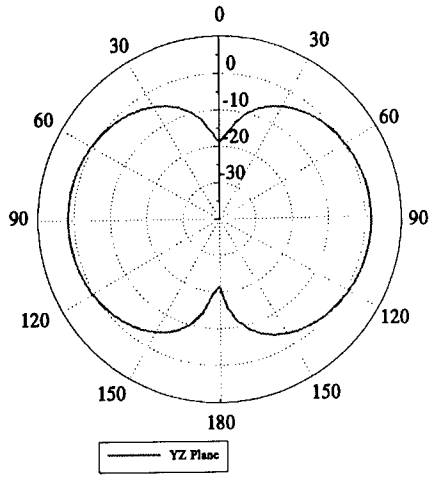


(b)

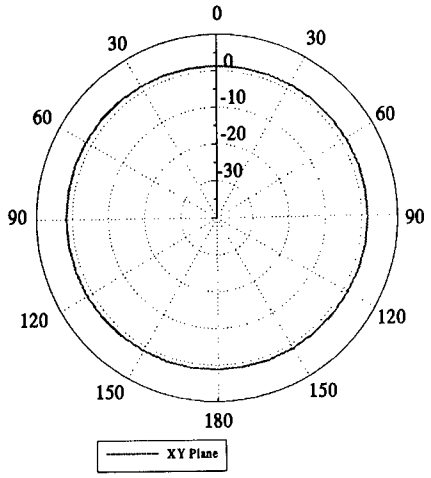


(c)

**Figure 6 The radiation directive gain on (a) xz plane (b) yz plane (c) xy plane at 2.55 GHz.**

are observed. The directive gain f this antenna is also computed and patterns in three different planes are shown in Figure 6. From Figure 6, this design has an omni-directional radiation pattern in the xy plane, which is very similar to that of a monopole antenna. From the results in Figures 5(b) and 6, this tapered meander line with dual 24-mm sleeves may be an optimal design for current wireless application.

To analyze the case when the sleeve tuners are not connected to the ground, another study is conducted for dual floating printed lines, as shown in Figure 7(a). The lines are simulated by printed traces at the center of the tapered meander line trace. From Figure 7(b), the effects of floating traces are found to be trivial at frequencies below 5 GHz, but detectable above 5 GHz. From this study, the results indicate that the tuning effectiveness for this application is greatly reduced when the dual sleeves are not well grounded.

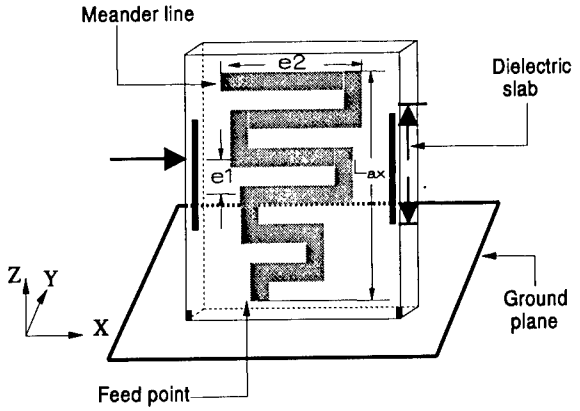


**Figure 7(a) Tapered meander line monopole with dual floating lines.**

The designs of a tapered meander line antenna with and without dual 24-mm sleeves, as shown in Figure 2, are fabricated and measured. As shown in Figures 8 and 9, agreements are observed up to 10 GHz between the numerical and experimental results. The slight frequency shift in magnitude and phase differences at higher frequencies are mainly accounted by the different feeds used in the numerical and experimental methods and the conductor and dielectric losses at higher frequencies which are not considered in the FDTD simulation. From comparisons of results in Figures 8 and 9, the effectiveness of the numerical model and analyses are reassured.

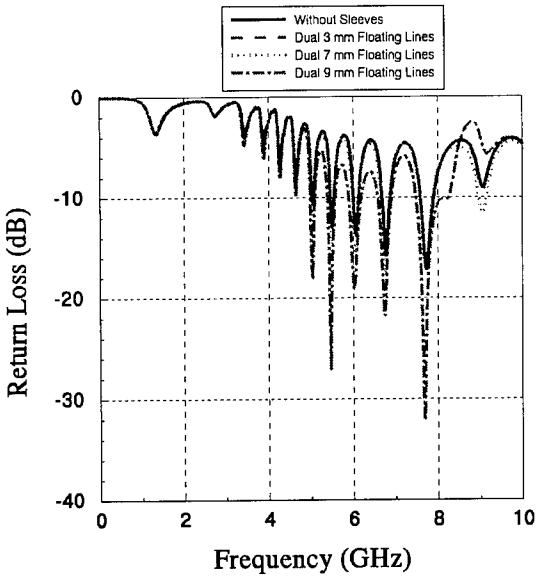


**Figure 7(b) Return loss of the tapered meander line monopole versus floating line length.**

## IV. Conclusions

The reliability of the numerical analyses in this study is demonstrated by comparing FDTD simulations with test results of the prototype antennas. A detailed investigation for optimizing the operating frequncy and input impedance of a tapered meander line monopole antenna for wireless communication has been presented. The presented tapered meander line monopoles can be tuned for a broad bandwidth of 230 MHz, operation at 2.55 GHz, and for a 50 Ω input impedance using printed tuning sleeves, which is appropriate for support of current and future generations of wideband wireless communication systems. Optimal results for lower frequency applications, between 1 and 2 GHz, may be achieved by increasing the meander line trace segments or by employing other tuning methods. Future studies will be focused on finding simple tuning methods to tune the lower frequncy modes and the optimization of the radiation pattern parameters of the current design.

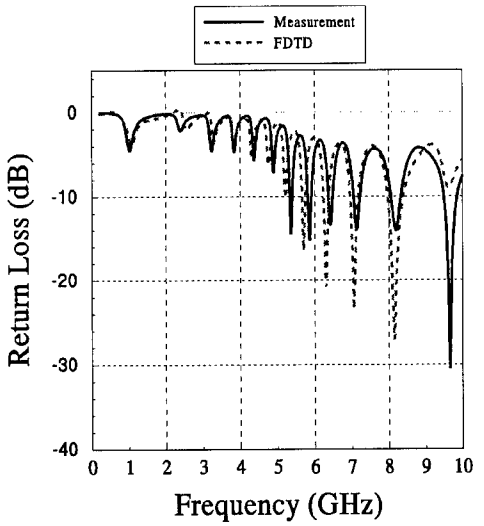


(a)

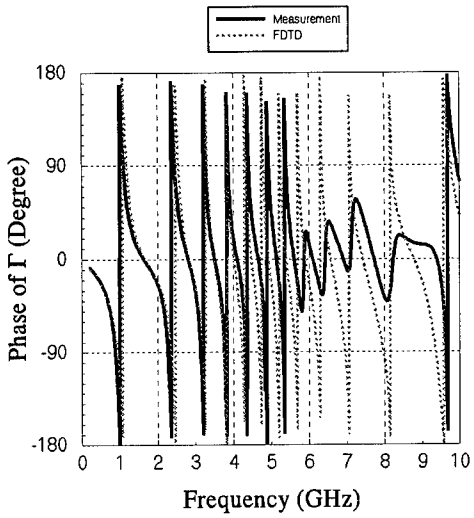


(b)

**Figure 8 Comparison of the computed and measured (a) return loss (b) phase of the reflection coefficient of the prototyped tapered meander line monopole.**

## V. Acknowledgement

The authors would like to express their appreciation to Dr. Wen-Liang Wu for his helpful discussions and to Mr. Joon Shin for providing MATLAB programs to vizualize the FDTD modelings. In addition, the authors also would like to thank Mr. Po-Leng Chin, Mr. Maqsud Alam, and Mr. Martye Hickman for their efforts on the fabrication of the antenna prototypes.

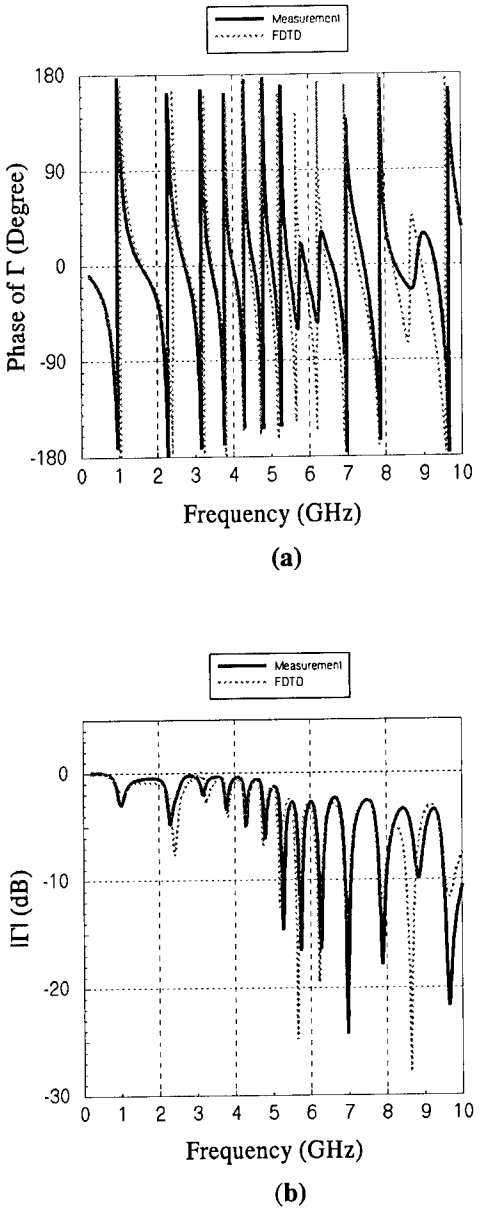


**Figure 9 Comparison of measured and FDTD simulation of (a) return loss (b) phase of the reflection coefficient of the dual-sleeve tapered meander line monopole.**

## REFERENCES

[1] K. Noguchi, M. Mizusawa, T. Yamaguchi, and Y. Okumura, "Numerical analysis of the radiation characteristics of the meander line antennas consisting of two strips," *IEEE AP-S Digest,* pp. 1598-1601, 1996.

[2] M. Ali, S. S. Stuchly, and K. Caputa, "A wide-band dual meander-sleeve antenna," *Journal of Electromagnetic Waves and Applications,* vol. 10, no. 9, pp. 1223-1236, 1996.

[3] A. Z. Elsherbeni, J. Chen, C. E. Smith, and Y. Rahmatt-Sami, "FDTD analysis of meander line antennas for personal communication applications," Progress in Electromagnetics Research Symposium (*PIERS*), Cambridge, MA, 1997.

[4] M. Ali, S. S. Stuchly, and M. Okoniewski, "Characterization of planar printed meander line antennas using the finite difference time domain technique," *IEEE AP-S Dig.*, pp. 1546-1549, 1997.

[5] H. Y. Wang and M. J. Lancaster, "Aperture-coupled thin-film superconducting meander line antennas," *IEEE Trans. Antennas Propagat.*, vol. 47, no.5, pp. 829-836, May 1999.

[6] C. P. Huang, A. Z. Elsherbeni, J. J. Chen, and C. E. Smith, "FDTD characterization of meander line antennas for RF and wireless communications," Progress in Electromagnetics Research Symposium (*PIERS*), vol. 24, pp. 185-200, 1999.

[7] C. P. Huang, A. Z. Elsherbeni, and C. E. Smith, "FDTD analysis of tapered meander line antennas for RF and wireless communications," the 16th Annual Review of Progress in Applied Computational Electromagnetics (*ACES*), March, 2000.

[8] C. P. Huang, "Analysis and design of printed antennas for wireless communications using finite difference time domain technique, " Ph.D. dissertation, Dept. Electrical Engineering, Univ. of Mississippi, Dec. 1999.

[9] A. Z. Elsherbeni, C. P. Huang, and C. E. Smith, "Finite difference time domain analysis of printed meander line antennas for personal wireless communications, "Dept. Electrical Engineering, Univ. of Mississippi, technical report No. TR 001, Jan. 2000.

[10] K. S. Yee, "Numerical solution of initial boundary value problems involving Maxwell's equations in isotropic media," *IEEE Trans. Antennas Propagat.*, vol. 14, pp. 202-307, 1966.

[11] J. P. Berenger, "A perfectly matched layer for the absorption of electromagnetic waves," *J. Computat. Phys.*, Oct. 1994.

[12] K. D. Katsibas, C. A. Balanis, P. A. Tirkas, and C. R. Birtcher, "Folded loop antenna for mobile hand-held units," *IEEE Trans. Antennas Propagat.*, vol. 46, no. 2, pp. 260-266, Feb.1998

# A COLE-COLE DIAGRAM REPRESENTATION OF MICROSTRIP STRUCTURE

S. Malisuwan
Department of Electrical Engineering
Chulachomklao Royal Military Academy
Nakhon-Nayok, Thailand

P.S. Neelakanta and V. Ungvichian
Department of Electrical Engineering
Florida Atlantic University
Boca Raton, FL 33432, USA.

**Abatract**—A method for analyzing the performance of a microstrip line using the concept of Cole-Cole diagram, is proposed. Analogous to dielectric relaxation considerations of Cole-Cole diagrams as applied to dielectric materials, a "reactive relaxation" concept is introduced to represent the frequency-dependent characteristics of a microstrip. Also, included in the algorithm are relevant considerations pertinent to the substrate dielectric and strip-line conductor losses. The dynamic permittivity of the microstrip structure (deduced via Cole-Cole diagram) leads to a convenient and modified Smith-chart representation that includes the frequency-dependent influence of the fringing field and the lossy characteristics of the line cohesively. The efficacy of the model is illustrated with an example concerning a microstrip patch antenna in ISM band. Relevant algorithms are useful in computer-aided designs (CADs).

**Indexing Terms**—Cole-Cole diagram, Microstrip structure, Microstrip patch antenna, Modified Smith chart, CAD.

## 1. INTRODUCTION

The microstrip line is one of the most popular types of planar transmission lines, primarily because it is easily integrated with other passive and active microwave devices. Relevant design equations in closed-form using semi-empirical strategies specifying the frequency-dependent, effective dielectric permittivity concept and dispersion characteristics of a microstrip line have been derived in the existing literature [1]-[7]. Although many computer-aided design (CAD) systems have been developed using such algorithms with built-in microstrip design capabilities, simple calculation methods for microstrip line parameters by hand-calculator and/or by personal computer are needed for preliminary design purposes, and/or for quick circuit evaluation purposes. Moreover, designers may need to observe the physical considerations of microstrip circuits on step-by-step basis. Therefore, many researchers are in search of simple methods, which are at the same time and sufficient to explain the physical aspects of microstrip circuits, precisely.

In this research an approach that uses the Debye relation [8] is introduced to develop an "equivalent relaxation diagram" (analogous to the Cole-Cole diagram) that represents the frequency-dependent, lossy and lossless capacitive characteristics of a microstrip line structure. Further, the frequency-dependent, lossy characteristics of microstrip lines are addressed via Smith chart representation. Results based on the proposed model are compared with the available data in the literature in respect of a microstrip patch antenna.

## 2. MICROSTRIP-BASED EQUIVALENT RELAXATION PROCESS

The Debye relation on the relative complex permittivity of a material depicting the dielectric relaxation can be written as [9]:

$$\varepsilon_m^*(\omega) = \varepsilon_\infty + \frac{\varepsilon_s - \varepsilon_\infty}{1 + j2\pi(\omega/\omega_r)} \tag{1a}$$

$$\text{or } \varepsilon_m^*(\omega) = \left[\varepsilon_\infty + \frac{\varepsilon_s - \varepsilon_\infty}{1+4\pi^2(\omega/\omega_r)^2}\right] - j\left[(\varepsilon_s - \varepsilon_\infty)\frac{2\pi(\omega/\omega_r)}{1+4\pi^2(\omega/\omega_r)^2}\right] \tag{1b}$$

where $\omega = 2\pi f$; f is the applied frequency; and, $f_r = 1/\tau_r$ where $\tau_r$ is the characteristic relaxation time of the dielectric material. Further, $\varepsilon_\infty$ and $\varepsilon_s$ are the relative permittivities of the material at very high ($f \to \infty$) and quasi-static ($f \to 0$) frequencies.

The concept of dielectric relaxation can be analogously applied to characterize the frequency-dependent performance of a microstrip line. Hence, Kirschning and Jansen' frequency-dependent effective permittivity deduced for a microstrip [5] can be written in a Debye relation form as follows:

$$\varepsilon_u'(\omega) = \varepsilon_{eff}(\omega) = \left[\varepsilon_r + \frac{\varepsilon_{eff}(0,u) - \varepsilon_r}{1+Q(\omega,u)}\right] \equiv \text{Re}\left[\varepsilon_r + \frac{\varepsilon_{eff}(0,u) - \varepsilon_r}{1+j(1/2\pi)(\omega_o/\omega)}\right] \tag{2}$$

where u is the line-width to substrate-thickness ratio, $(w/\lambda)/(h/\lambda)$; $\varepsilon_r$ is the dielectric constant of the substrate; $\varepsilon_{eff}(0, u)$ is the equivalent (relative) static permittivity; and $Q(\omega, u)$ is a dimension-dependent factor [5] and $\lambda$ is the wavelength of operation.

The frequency-dependent effective permittivity in Eqn. (2), it can be equated to the real part of Eqn. (1b) as follows.

$$\varepsilon_r + \frac{\varepsilon_{eff}(0,u) - \varepsilon_r}{1+Q(\omega,u)} = \varepsilon_\infty + \frac{\varepsilon_s - \varepsilon_\infty}{1+4\pi^2(\omega/\omega_r)^2} \tag{3}$$

This gives,

$$\varepsilon_r = \varepsilon_\infty \tag{4}$$

$$\varepsilon_{eff}(0,u) = \varepsilon_s \tag{5}$$

$$\tau_o = \frac{\sqrt{Q(\omega,u)}}{\omega} \tag{6}$$

Now, an "imaginary part" of the equivalent permittivity of a microstrip system can be obtained by applying Eqns. (4)-(6) into the imaginary part of Eqn. (1b). Hence, the imaginary part of Cole-Cole expression for a microstrip system can be written as

$$\varepsilon_u''(\omega) = \left[\frac{(\varepsilon_{eff}(0,u) - \varepsilon_r)\sqrt{Q(\omega)}}{1+Q(\omega)}\right] \tag{7}$$

Hence, the complex permittivity of microstrip system in compact form can be written as:

$$\varepsilon_u^*(\omega) = \varepsilon_r + \frac{\varepsilon_{eff}(0) - \varepsilon_r}{1 + j(1/2\pi)(\omega_o/\omega)} \tag{8}$$

By illustrating the relevant Debye relations via Cole-Cole diagrams, a lateral inversion as shown in Eqns. (1a) and (8) can be noticed. That is, the material-based and microstrip-based Cole-Cole diagrams are laterally inverted in a mirror-image fashion as shown in Figs. 1 and 2.

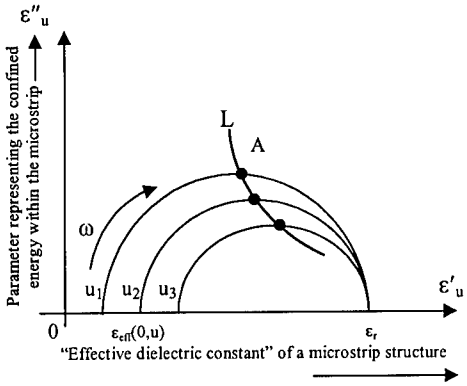


**Fig. 1** Cole-Cole representation of reactive relaxation of a microstrip structure with u = (w/λ)/(h/λ) and u1 < u2 < u3

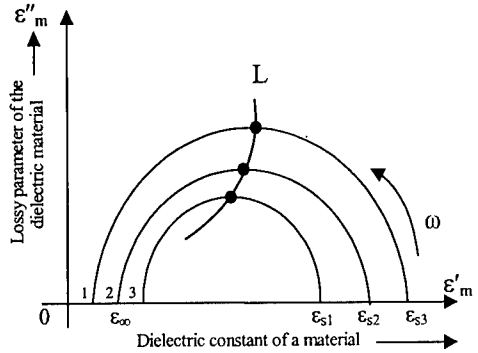


**Fig. 2** Cole-Cole diagram of Debye relaxation in a dielectric material with $\varepsilon_{s1} < \varepsilon_{s2} < \varepsilon_{s3}$ and $\tau_r(\varepsilon_{s1}) < \tau_r(\varepsilon_{s2}) < \tau_r(\varepsilon_{s3})$

Further, the maximum points of semi-circles in the Cole-Cole patterns correspond to maximum Debye loss in a lossy dielectric material; but, in respect of a microstrip system, these points can be regarded as to depict the maximum reactive (capacitive) energy confined within the microstrip structure. That is, pertinent to these maximum value points (A) in Fig. 1, it can be considered that the microstrip geometry holds the field within itself, rather letting it to fringe out. In material-based diagram (Fig. 2), it can be observed that loss in the material increases with dielectric constant. In contrast, in the microstrip-based diagram (Fig. 1), there is a reduction in the extent of energy confined when u = (w/λ)/(h/λ) ratio is increased. That is because, an increase in fringing field results in with decreasing substrate thickness.

Considering the equivalent Cole-Cole diagram of the test microstrip depicted in Fig. 3, the simulation results reveal that the nonfringing part of the reactive energy in the microstrip reduces when the (w/λ)/(h/λ) ratio increases. For example, about 10% reduction of this nonfringing energy is observed when the (w/λ)/(h/λ) ratio is increased from 1.0 to 2.0 for both dielectric materials. The results also indicate that the extent of the energy confined within microstrip line without proliferation as fringe fields increases with the dielectric constant of the substrate.

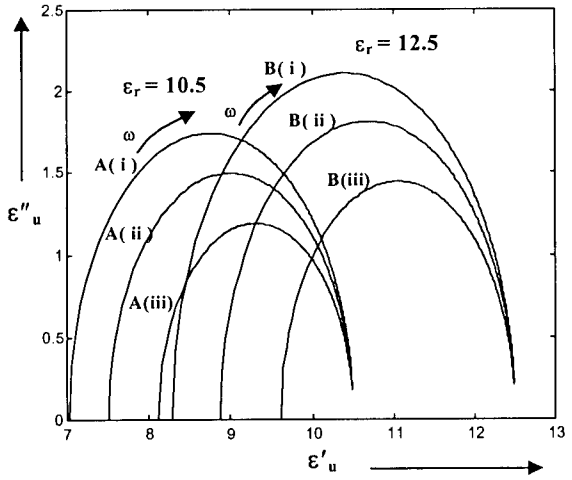


**Fig. 3** Cole-Cole diagram for the test microstrip structures
curves A: alumina ($\varepsilon_r = 10.5$)
curves B: gallium arsenide ($\varepsilon_r = 12.5$)
( i ) (w/λ)/(h/λ)= 1.0 ( ii ) (w/λ)/(h/λ) = 2.0
( iii ) (w/λ)/(h/λ) = 4.0

The equivalent Cole-Cole diagram for the microstrip line (Fig. 1) can be further modified to include the lossy attributions. That is, in the event that the stripline has a lossy substrate and/or when the metallic strip poses a conduction loss, the relevant considerations can be appropriately included in the Cole-Cole representation of Fig. 1.

The conductor loss of the strip can be added as a lossy component into the imaginary part of the equivalent permittivity of the microstrip system. Considering the attenuation (in Np/m) due to the transmission along a microstrip conductor as specified in [3]:

$$\alpha_c \cong \sqrt{\pi f \mu_o \sigma_{eff}} \cong \frac{\sqrt{\varepsilon_{eff}(0,u)}\exp\left[-1.2\left(Z_0(0)/\eta_o\right)^{0.7}\right]\sqrt{\pi f \mu_o}}{Z_0(0) w \sqrt{\sigma_c}} \tag{9}$$

where $\sigma_{eff}$ represents the effective loss constituent of the microstrip conductor and $Z_0(0)$ is the quasi-static characteristic impedance of the microstrip line in a homogeneous medium. Further, w is the line-width; $\sigma_c$ is the conductivity of the microstrip line; $\eta_o$ is the intrinsic impedance of free-space (377 Ω); and $\mu_o$ is the permeability of free-space ($4\pi\times10^{-7}$ H/m).

This conductor-loss can be added as a lossy component into the imaginary part of the equivalent complex permittivity of the microstrip system. The attenuation (in Np/m) due to the transmission along the microstrip conductor can be specified as:

$$\alpha_c \cong \sqrt{\pi f \mu_o \sigma_{c,eff}} \tag{10}$$

where $\sigma_{c,eff}$ represents the effective loss constituent of the microstrip conductor. Equating Eqns. (9) and (10), this

effective conductivity ($\sigma_{c,eff}$) of the microstrip can be deduced as:

$$\sigma_{c,eff} = \frac{\varepsilon_{eff}(0,u)\exp\left[-2.4(Z_0(0)/\eta_o)^{0.7}\right]}{Z_0^2(0)w^2\sigma_c} \quad (11)$$

In corporating Eqn. (11) in the Cole-Cole expression, an imaginary part of the effective permittivity of the microstrip ($-j\varepsilon''_c(\omega)$) can be written as:

$$-j\varepsilon_c''(\omega) = -j\frac{\varepsilon_{eff}(0,u)\exp\left[-2.4(Z_0(0)/\eta_o)^{0.7}\right]}{\omega\varepsilon_o\varepsilon_u'(\omega)Z_0^2(0)w^2\sigma_c} \quad (12)$$

Lastly, the substrate loss ($-j\varepsilon''_d(\omega)$) can be specified as $-j\varepsilon''_d(\omega) = -j\sigma_d/\omega\varepsilon_o\varepsilon_r$ where $\sigma_d$ is the conductivity of the lossy substrate. Hence, the resultant equivalent Cole-Cole diagram representation of the microstrip system can be written as,

$$\varepsilon^*(\omega) = \varepsilon_u'(\omega) - j\varepsilon_u''(\omega) - j\varepsilon_c''(\omega) - j\varepsilon_d''(\omega) \quad (13)$$

Considering the equivalent Cole-Cole diagram of the test microstrip depicted in Fig. 4, the simulation results reveal that the nonfringing part of the reactive energy in the microstrip reduces as the $(w/\lambda)/(h/\lambda)$ ratio increases. For example, about 8% reduction of this nonfringing energy is observed when the $(w/\lambda)/(h/\lambda)$ ratio is increased from 0.5 to 1.0 for both dielectric substrate materials considered. As expected, the results also indicate that the extent of the energy confined within microstrip line (without proliferating as fringe fields) increases with the dielectric constant of the substrate; and, the reduction of energy can be observed when the substrate and conductor losses are included in the calculation.

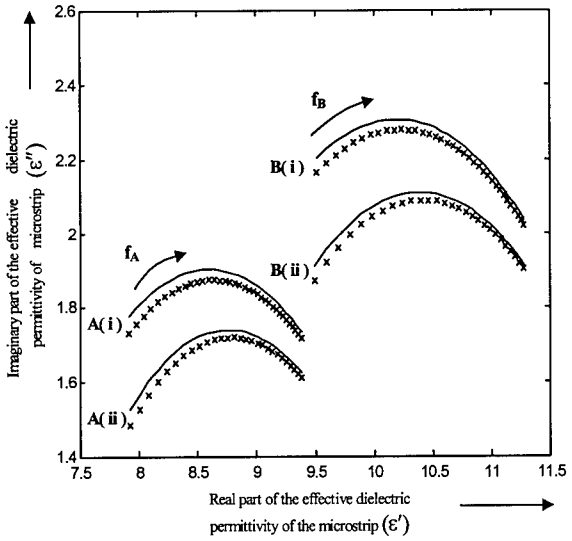


**Fig. 4** Cole-Cole diagrams of test microstrip structures
$\sigma_d$ = 0.5 S/m
Curves A: Alumina ($\varepsilon_r$ = 10.5)
Curves B: Gallium arsenide ($\varepsilon_r$ = 12.5)
( i ) u = $(w/\lambda)/(h/\lambda)$= 0.5; ( ii ) u = $(w/\lambda)/(h/\lambda)$ = 1.0
$f_A$: 20-60 GHz and $f_B$: 20-80 GHz
—— Lossless
×××× Lossy

## 3. FREQUENCY-DEPENDENT (LOSSY) MICROSTRIP LINE PERFORMANCE: COLE-COLE DIAGRAM BASED SMITH-CHART REPRESENTATION

The Smith-chart is an impedance representation in a complex plane depicting a set of circles of constant resistance and partial circles of constant reactance. The standard Smith-chart is based on the static characteristic impedance ($Z_0$) and does not include the frequency-dependent aspects of $Z_0$. However, it can be modified to include lossy (frequency-dependent) considerations. In this section, the concept of microstrip-based Cole-Cole diagram (developed in the last section) is applied to construct a frequency-dependent (lossy) Smith-chart to analyze microstrip line characteristics.

Before deriving the frequency-dependent Smith-chart relations, the capacitance parameter in microstrip-line system can be considered. The classical paralell-plate capacitor is shown in Fig. 5. From the geometry shown in Fig. 5, the capacitance per unit length of the structure can be expressed as [10]:

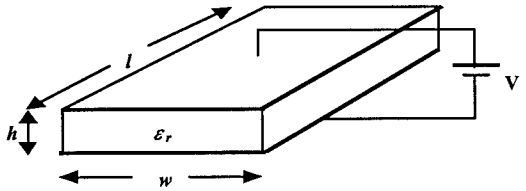


**Fig. 5** A parallel-plate capacitor

$$C = \varepsilon\frac{w}{h} \quad (14)$$

A simple frequency-dependent capacitance of the parallel-plate capacitor can be modeled in terms of any frequency-dependent attributes of $\varepsilon$. That is,

$$C(\omega) = \varepsilon_o\varepsilon^*(\omega)\frac{w}{h} \quad (15)$$

where $\varepsilon^*(\omega)$ is a complex permittivity equal to $\varepsilon'(\omega) - j\varepsilon''(\omega)$.

Therefore,

$$C(\omega) = \varepsilon_o\varepsilon'(\omega)\frac{w}{h} - j\varepsilon_o\varepsilon''(\omega)\frac{w}{h} \quad (16)$$

Referring to the equivalent Cole-Cole diagram deduced for a parallel-plate microstrip line in Eqn. (13) is substituted into Eqn. (16). Hence,

$$C(\omega) = C\left(\frac{1}{1+Q(\omega)}\left[Q(\omega)+\frac{\varepsilon_{eff}(0)}{\varepsilon_r}\right]\right) - j\frac{C}{\varepsilon_r}\left[\varepsilon_u''(\omega)+\varepsilon_c''(\omega)+\varepsilon_d''(\omega)\right] \quad (17)$$

where $C = \varepsilon_o\varepsilon_r(w/h)$.

For simplicity, the coefficients of Eqn. (17) are defined as follows:

$$A(\omega) = \frac{1}{1+Q(\omega)}\left[Q(\omega)+\frac{\varepsilon_{eff}(0)}{\varepsilon_r}\right] \quad (18)$$

$$B(\omega) = \frac{1}{\varepsilon_r}\left[\varepsilon_u''(\omega)+\varepsilon_c''(\omega)+\varepsilon_d''(\omega)\right] \quad (19)$$

In general, the characteristic impedance of a transmission line is given by

$$Z_0 = \sqrt{\frac{R + j\omega L}{G + j\omega C}} \tag{20}$$

where R, L, G, C are per unit length quantities defined as follows:

R = resistance per unit length in Ω/m.
L = inductance per unit length in H/m.
G = conductance per unit length in S/m.
C = capacitance per unit length in F/m.

If G and C are neglected, the characteristic impedance can be written as:

$$Z_0 = \sqrt{\frac{L}{C}} \tag{21}$$

To obtain the frequency-dependent characteristic impedance ($Z_0'(\omega)$), the frequency-dependent capacitance ($C(\omega)$) of Eqn. (17) is substituted into the capacitance (C) in Eqn. (21). The resulting frequency-dependent characteristic impedance is then given by:

$$Z_0'(\omega) = \sqrt{\frac{L}{C[A(\omega) - jB(\omega)]}} = \frac{Z_0}{\sqrt{A(\omega) - jB(\omega)}} \tag{22}$$

Now, the frequency-dependent (lossy) Smith-chart can be constructed by applying $Z_0'(\omega)$ in Eqn. (22) into the normalized terminal impedance expression following the procedure as that for a standard Smith-chart [11]. Hence, the resulting normalized terminal impedance $z'_L$ is given by

$$z'_L = \frac{Z_L}{Z_0'(\omega)} = br + jbx \qquad \text{(Dimensionless)} \tag{23}$$

where r and x are the normalized resistance and normalized reactance, respectively, and $b = \sqrt{A(\omega) - jB(\omega)}$.

Corresponding, the voltage reflection coefficient of present Smith chart can be expressed as:

$$\Gamma' = \Gamma'_r + j\Gamma'_i = \frac{z'_L - 1}{z'_L + 1} \tag{24}$$

or

$$z'_L = \frac{Z_L}{Z_0'(\omega)} = br + jbx = \frac{(1 + \Gamma'_r) + j\Gamma'_i}{(1 - \Gamma'_r) - j\Gamma'_i} \tag{25}$$

Now, the desired set of equations depicting the modified Smith-chart are:

$$\left(\Gamma'_r - \frac{br}{1 + br}\right)^2 + \Gamma'^2_i = \frac{1}{(1 + br)^2} \tag{26}$$

and

$$(\Gamma'_r - 1)^2 + \left(\Gamma'_i - \frac{1}{bx}\right)^2 = \left(\frac{1}{bx}\right)^2 \tag{27}$$

To illustrate the construction of the proposed frequency-dependent Smith-chart, a lossy microstrip structure is considered. It consists of a gallium arsenide substrate ($\varepsilon_r$ = 12.5) with a 1.0 mm substrate-thickness (h), 0.75 mm line-width (w) and design parameter $(l/\lambda)/(h/\lambda)$ = 10.0. The proposed Smith-chart simulated is compared with a standard Smith-chart in Fig. 6. It can be seen that when the lossy characteristics (substrate loss, conductor loss, and frequency-dependent characteristic impedance of the microstrip line) are included in the calculation, the Smith-chart takes the form of a spiral. As well known in lossy transmission line theory that, when attenuation as a function of line-length is plotted on the Smith chart, it also takes the form of a spiral.

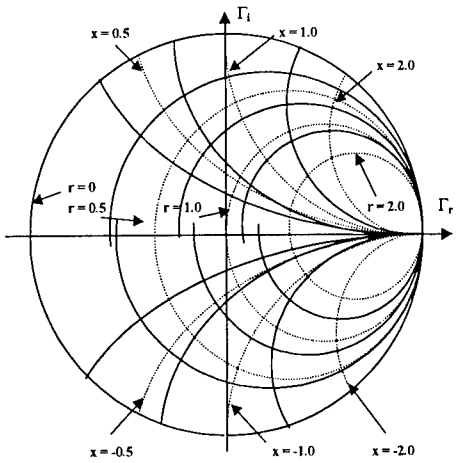


**Fig. 6** The frequency-dependent (lossy) Smith chart with $\varepsilon_r$ = 12.5; h = 1 mm, w = 0.75 mm, $\sigma_d$ = 0.05 S/m, $(l/\lambda)/(h/\lambda)$ = 10.0
——— Proposed Smith chart
····· Standard Smith chart

## 4. APPLICATION OF THE FREQUENCY-DEPENDENT SMITH-CHART CONSTRUCTED ON THE BASIS OF COLE-COLE DIAGRAM

This chapter is devoted to illustrate the use of frequency-dependent Smith-chart considerations deduced (on the basis of Cole-Cole diagram principle) in characterizing microstrip lines. A microstrip patch antenna is considered as a test structure for analysis.

A rectangular microstrip antenna shown in Fig. 7 is considered presently to study the frequency-dependent Smith-chart application deduced in the last section. The rectangular patch antenna in Fig. 7(a) is fed from a microstrip transmission line.

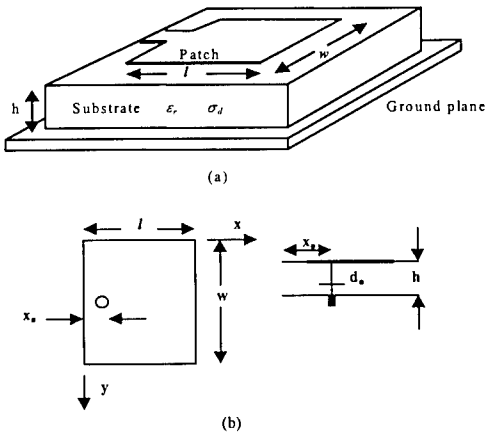


**Fig. 7** Rectangular microstrip patch antenna
(a) Direct feed
(b) Coax-feed

A microstrip antenna may be excited or 'fed' by different types of transmission lines, for example coaxial (Fig. 7(b)), microstrip, or coplanar. The radiating elements may be fed directly, with electrical continuity between the conductor of the transmission line and the conducting patch. On the other hand, the microstrip patch antenna fed by a transmission line behaves as a complex impedance $Z_{in} = (R + jX)$, which depends mainly on the geometry of the coupling between the transmission line and the antenna. For direct feed (Fig. 6.1(a)), the input impedance depends strongly on the point of contact with the patch. The input impedance expressions of the microstrip patch antenna used are from Abboud's model [12].

The input impedance of the structure shown in Fig. 6.1 is given by [12]

$$Z(f) = \frac{R}{1+Q_T^2[f/f_R - f_R/f]^2} + j\left[X_L - \frac{RQ_T[f/f_R - f_R/f]}{1+Q_T^2[f/f_R - f_R/f]^2}\right] \quad (28)$$

where $R$ is the resonant resistance including the influence of the fringing field at the edges of the patch; $Q_T$ is the quality factor associated with system losses; $f$ is the operating frequency; and $f_R$ is the resonant frequency. It can be written as [12]:

$$R = \frac{Q_T h}{\pi f_R \varepsilon_{dyn} \varepsilon_o lw} \cos^2\left(\frac{\pi x_o}{l}\right) \quad (29)$$

where $\varepsilon_{dyn}$ is the dynamic permittivity.

To take the effect of coax-feed probe (Fig. 7(b)) into account, it is necessary to modify the input impedance by an inductive reactance term [13], given by

$$X_L = \frac{377}{c_o} \ln\left(\frac{c_o}{\pi f d_o \sqrt{\varepsilon_r}}\right) \quad (30)$$

where $c_o$ is the velocity of light in vacuum and $d_o$ is the diameter of the probe.The detail in Eqn. (28) can be found in [12].

The flowchart of the method to calculate the input impedance of the rectangular microstrip antenna by utilizing the proposed model is shown in Fig. 8.

Fig. 9 shows the input impedance for a patch antenna operating at about 2.22 GHz. The proposed model results are compared with the computed results in [12] and measured data of [14]. The results indicate that the proposed model gives results close to the experimental data. It can also be observed that the present results are better than those predicted in [12] especially at the higher frequency range. Also, at 2.22 GHz, the result from the proposed model is closer to the measured result [12] than that calculated by [12]. The reason is that, in the proposed model, the frequency-dependent characteristic impedance is more comprehensively addressed included in the algorithm so that possible errors in the high frequency are reduced.

## 5. AN ANTENNA SYSTEM IN WIRELESS COMMUNICATION APPLICATIONS (2.45 GHz ISM BAND): DESIGN CONSIDERATIONS

The Industrial, Scientific and Medical (ISM) frequency bands governed by Federal Communications Commission (FCC) Part 15 specifications have seen dramatic growth in recent years, particularly the 2.4000 to 2.4835 GHz (ISM-2400) band.

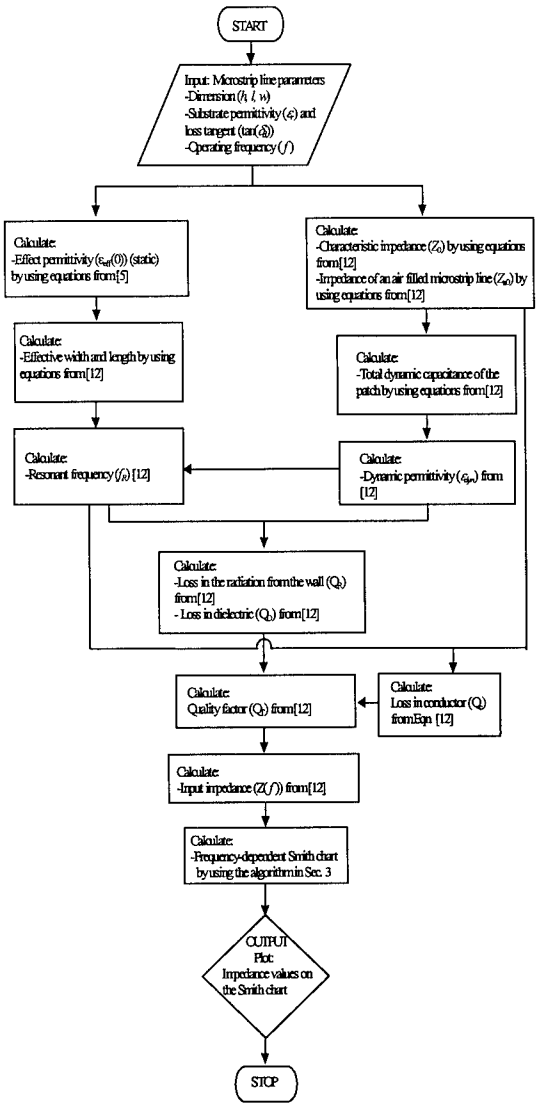


**Fig. 8** Flowchart of input impedance calculation by using the proposed model

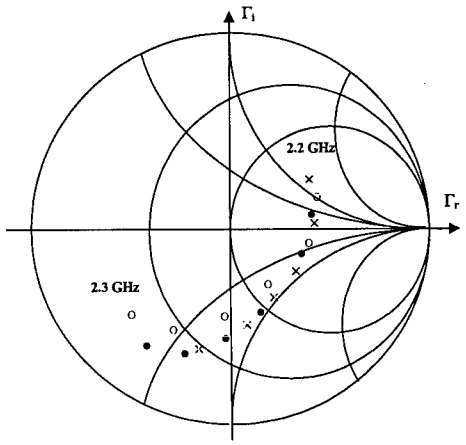


**Fig. 9** Input impedance of coax-fed microstrip patch antenna
$\varepsilon_r = 2.5$; Loss tangent = 0.002; h = 1.524 mm; $d_o = 1.27$ mm; $Z_0 = 50$ Ω; w = 68.58 mm; l = 41.40 mm; $x_o = 0.0$; mode (m = 0, n = 1)
O Measured [14] × Calculated [12] • Proposed model

The present effort addresses the design of an antenna system for wireless communication applications, which operates in the 2.45 GHz (ISM) band. The input impedance of the antenna is based upon the proposed model in the Section 4. The design of the matching section for the antenna is followed the procedure in [15].

For the present design, the rectangular microstrip antenna has a substrate with dielectric constant ($\varepsilon_r$) of 2.5 and the antenna is a direct-feed type. The size of the patch is 4.10 cm ($w$) × 4.14 cm ( $l$ ) ($w = 0.3350\lambda$; $l = 0.3382\lambda$ at $f =$ 2.45 GHz) and a thickness of $h = 0.1524$ cm ($h = 0.0125\lambda$ at $f$ = 2.45 GHz). Fig. 10 shows the input impedances calculated as per the present model and that by the Abboud's model [12] for the patch operating at 2.45 GHz. The design of the matching section for the antenna will be the next step and is discussed in the following sections.

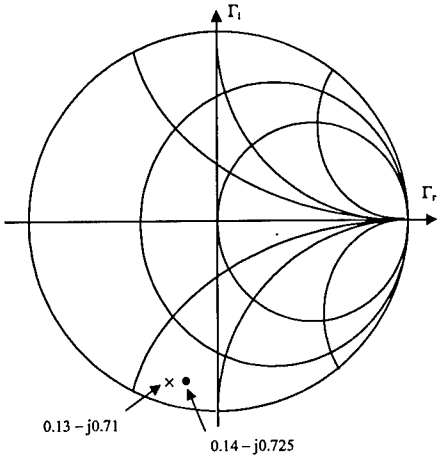


**Fig. 10** The input impedance for a patch operating at 2.45 GHz
• Proposed model
× Calculate [12]

The quarter-wave transformer is a simple structure compatible for matching a real load impedance to a transmission line. An additional feature of the quarter-wave transformer is that it can be extended to multisection designs for broader bandwidths. A complex load impedance such as that indicated in Fig. 10 can always be transformed to a real part by using an appropriate length of transmission line between the load and the transformer as illustrated in Fig. 11. For the example under discussion, the line-length required to transform the complex impedance to the real values are 1.236 cm ($0.101\lambda$ at $f = 2.45$ GHz) and 1.102 cm ($0.09\lambda$ at $f$ = 2.45 GHz) for the proposed model and the Abboud's model, respectively.

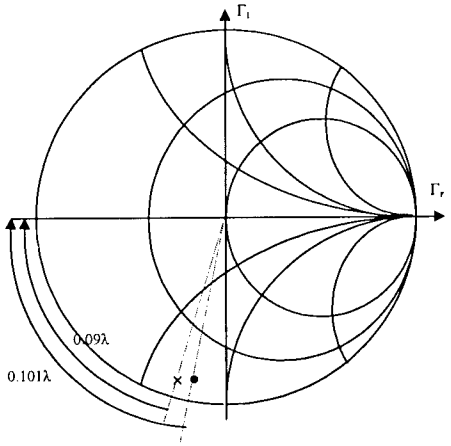


**Fig. 11** Moving complex load impedance to a real impedance
• Proposed model
× Calculate [12]

The broadband design can be achieved by using a set of cascaded quarter-wave transformer sections. Assuming, that two or more quarter-wave sections are connected in cascade to transform $R_R$ to $R_{in}$ (Fig. 12), the problem is then to determine $R'_o$, $R''_o$, $R'''_o$, namely, the characteristic impedances of these sections. A number of approaches have been proposed in the literature for this purpose. For example, Everitt [15] has suggested that the use of common logarithms of the impedance ratios at the junctions in the system with the coefficients of the binomial expansion $(a+b)^n$, as indicated below:

| *No. of* λ/4 *sections, n* | *Logarithm of impedance ratio* |
|---|---|
| 2 | 1 2 1 |
| 3 | 1 3 3 1 |
| 4 | 1 4 6 4 1 |

For the present application, consider the design of a two-quarter-wave-section system. Reading from left to right in the inset of Fig. 12, the impedance ratios at the junctions are $R_R/R'_o$, $R'_o/R''_o$, and $R''_o/R_o$. Since the number of sections, $n$, is equal to 2,

$$\log\left(\frac{R'_o}{R''_o}\right) = 2\log\left(\frac{R''_o}{R_o}\right) = 2\log\left(\frac{R_R}{R_o}\right) \tag{31}$$

That is, from left to right, the logarithms of the impedance ratios follow the rule 1 2 1 in accordance with the above table. Then, taking antilogarithms,

$$\frac{R'_o}{R''_o} = \left(\frac{R''_o}{R_o}\right)^2 = \left(\frac{R_R}{R'_o}\right)^2 \tag{32}$$

Solving for $R'_o$ and $R''_o$ in terms of $R_o$ and $R_R$,

$$R'_o = \frac{R_o R_R}{R''_o} \quad \text{or} \quad R'_o = \sqrt[4]{R_R^3 R_o} \tag{33}$$

$$R''_o = \frac{R_o R_R}{R'_o} \tag{34}$$

The impedance at the junction of the two quarter-wave sections is

$$R_j = \sqrt{R_R R_o} \tag{35}$$

This transformation will now be used to design a double-section system for an over-all transformation ratio of $R_R : R_o$.

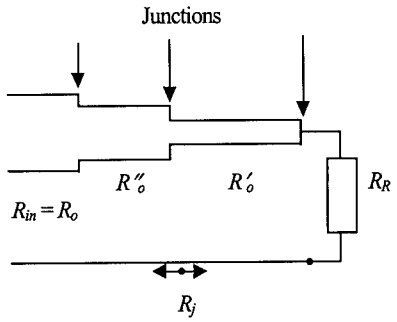


**Fig. 12** Two cascaded quarter-wave transformers terminated in a constant resistive load

Consider the right-hand section, and normalized $R_R$ with respect to $R'_o$:

$$r'_r = \frac{R_R}{R'_o} \tag{36a}$$

By Eqn. (35) the normalized input impedance should be

$$r'_j = \frac{R_j}{R'_o} \tag{36b}$$

Following the method of the last section, enter $r'_r$ value on the Smith chart diagram, and rotate on a circle of constant $S'$ the appropriate fraction of a wavelength at each frequency. The values of $z'_j$ are tabulated in Table 1.

Now, $Z_j$ is the termination for the left-hand quarter-wave transformer in Fig. 12. To handle this section on the Smith-diagram, all quantities should be normalized with respect to $R''_o$. The double prime will indicate these quantities; thus,

$$z''_j = \frac{Z_j}{R''_o} = \frac{Z_j}{R'_o}\frac{R'_o}{R''_o} = \frac{R'_o}{R''_o} z'_j \tag{37}$$

Since $z''_j$ at each frequency and rotating toward the generator on a circle of constant $S''$ the appropriate distance indicated in the table. $Z_{in}$ is determined by,

$$z_{in} = \frac{Z_{in}}{R_o} = \frac{Z_{in}}{R''_o}\frac{R''_o}{R_o} = \frac{R''_o}{R_o} z''_{in} \tag{38}$$

**Table 1** Calculation of $z_{in}$ for a quarter-wave transformer (Proposed model)

$f_o = 2.45$ GHz, $r'_r = 0.61$, $r'_j = 1.64$, $r''_j = 0.37\, r'_j$

| $f/f_o$ | $l/\lambda$ | $z'_j$ | $z''_j$ | $z''_{in}$ | $z_{in}$ proposed model |
|---|---|---|---|---|---|
| 1.5 | 0.375 | 0.88 – j 0.46 | 0.33– j 0.17 | 0.91 – j 1.16 | 0.54 + j 0.66 |
| 1.4 | 0.350 | 1.03 – j 0.51 | 0.38 – j 0.19 | 1.47 – j 1.15 | 0.88 + j 0.67 |
| 1.3 | 0.325 | 1.20 – j 0.51 | 0.44 – j 0.19 | 1.94 – j 0.70 | 1.14 + j 0.39 |
| 1.2 | 0.300 | 1.42 – j 0.44 | 0.53 – j 0.16 | 1.90 – j 0.20 | 1.12 + j 0.12 |
| 1.1 | 0.275 | 1.60 – j 0.25 | 0.59 – j 0.09 | 1.70 – j 0.02 | 1.02 + j 0.02 |
| 1.0 | 0.250 | 1.68 | 0.62 | 1.64 | 0.95 |
| 0.9 | 0.225 | 1.60 + j 0.25 | 0.59 + j 0.09 | 1.70 + j 0.02 | 1.00+ j 0.01 |
| 0.8 | 0.200 | 1.42 + j0.44 | 0.53 + j 0.16 | 1.90 + j 0.20 | 1.10 + j 0.10 |
| 0.7 | 0.175 | 1.20 + j 0.51 | 0.44 + j 0.19 | 1.94 + j 0.70 | 1.15 + j 0.37 |
| 0.6 | 0.150 | 1.03 + j 0.51 | 0.38 + j 0.19 | 1.47 + j 1.15 | 0.87 + j 0.66 |
| 0.5 | 0.125 | 0.88 + j 0.46 | 0.33 + j 0.17 | 0.91 + j 1.16 | 0.54 + j 0.68 |

From Fig. 13, it can be seen that, when the maximum standing wave ratio is stipulated as 2, the allowable bandwidth of the proposed model shows a greater value than that of the Abboud's model [12], to an extent of about 10%. A possible explanation is that $\Delta f / f$ (bandwidth) is directly proportional to the loss of the system [16]. Therefore, when the frequency-dependent characteristic impedance is taken into the calculation, it is reflected in an increase of bandwidth calculated (using proposed model). The structure and dimension of the designed antenna is obtained in Fig. 14 and Table 2.

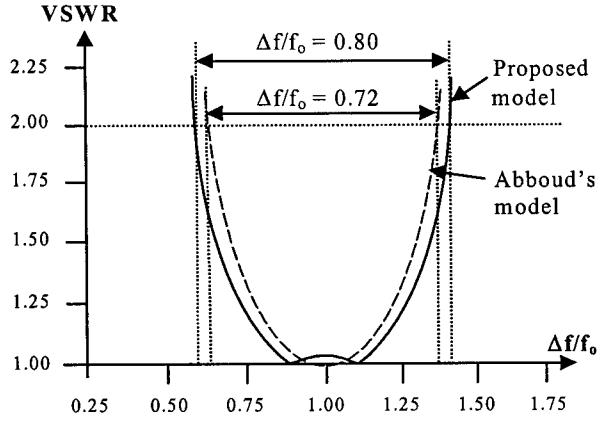


**Fig. 13** Comparison bandwidth between Abboud's model and proposed model with VSWR ≤ 2.0

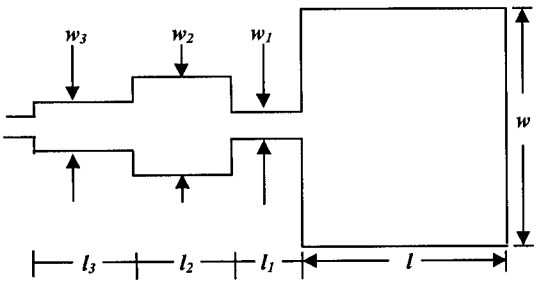


**Fig. 14** Antenna structure and double-wave-transformer

**Table 2** Comparison between Abboud's model and proposed model ($f_o$ = 2.45 GHz)

| Model | Abboud's model | Proposed model | Δ(% difference) |
|---|---|---|---|
| $w_1$ | 0.435 cm ($0.0355\lambda_o$) | 0.435 cm ($0.0355\lambda_o$) | 0 |
| $w_2$ | 2.950 cm ($0.2410\lambda_o$) | 2.785 cm ($0.2275\lambda_o$) | 5.59 |
| $w_3$ | 0.880 cm ($0.0719\lambda_o$) | 0.884 cm ($0.0722\lambda_o$) | 0.45 |
| $l_1$ | 1.102 cm ($0.0900\lambda_o$) | 1.236 cm ($0.1010\lambda_o$) | 10.84 |
| $l_2$ | 3.060 cm ($0.2500\lambda_o$) | 3.060 cm ($0.2500\lambda_o$) | 0 |
| $l_3$ | 3.060 cm ($0.2500\lambda_o$) | 3.060 cm ($0.2500\lambda_o$) | 0 |
| Bandwidth (GHz) | 1.764 | 1.960 | 10.00 |

## 6. CONCLUSIONS

The use of frequency-dependent Smith-chart deduced via microstrip-based Cole-Cole diagram representation is proved to be a method representing the frequency-dependent characteristics of microstrip lines. The present study demonstrates the feasibility of a cohesive presentation of the dispersion (lossy and lossless) characteristics of a microstrip structure via Cole-Cole diagram format, which is compatible for CAD efforts.

In summary, the technique described in this chapter offers a strategy of portraying the frequency-dependent characteristics of microstrip structures via a modified Smith-chart representation. Further, as far as the author knows of, this is the first attempt in depicting the dispersion characteristics of a microstrip line via Cole-Cole diagram format.

## REFERENCES

[1] M. Kobayashi, "A dispersion formula satisfying recent requirement in microstrip CAD," vol. 36, pp. 1246-1250, Aug. 1988.

[2] P. Pramanick and P. Bhartia, "An accurate description of dispersion in microstrip," Microwave J., vol. 26, no. 12, pp. 89-92, Dec. 1983.

[3] E. hammerstad and O. Jensen, "Accurate models for microstrip computer aided design," IEEE MTT-S Int. Microwave Symp. Dig., New York, NY, June 1980, pp. 407-409.

[4] E. Yamashita, K. Atsuki, and T. Veda, "An accurate dispersion formula of microstrip line for computer-aided design of microwave integrated circuits," IEEE Trans. Microwave Theory Tech., vol. MTT-27, pp. 1036-1038, Dec. 1979.

[5] M. Kirschning and R. H. Jansen, "Accurate model for effective dielectric constant with validity up to millimeter-wave frequency," Electron. Lett., vol. 18, pp. 272-273, Jan. 1982.

[6] A. K. Verma and R. Kumar, "New empirical unified dispersion model for shielded-, suspended-, and composite-substrate microstrip line for microwave and mm-wave applications," IEEE Trans. Microwave Theory Tech., vol. MTT-46, pp. 1187-1192, Aug. 1998.

[7] A. K. Verma and R. Kumar, "A new dispersion model for microstrip line," IEEE Trans. Microwave Theory Tech., vol. MTT-46, pp. 1183-1187, Aug. 1998.

[8] E. Riande and E. Saiz, Dipole Moments and Birefringence of Polymers, New Jersey: Prentice Hall, 1992.

[9] R. Coelho, Physics of dielectrics for engineer. Netherlands: Elsevier, 1979.

[10] C. S. Walker, Capacitance, Inductance and Crosstalk Analysis. Norwood, MA: Artech House, 1990.

[11] J. C. Freeman, Fundamentals of Microwave Transmission Lines, John Wiley & Sons, Inc., NewYork, 1995.

[12] F. Abboud, J. P. Damiano, and A. Papiernik, "Simple model for the input impedance of coax-fed rectangular microstrip patch antenna for CAD", IEE Proc. H, Microwaves, Antenna & Progag., vol. 135, pp. 323-326, 1988.

[13] M. D. Deshpande and M. C. Bailey, "Input impedance of microstrip antenna," IEEE Trans. Antennas Propagat., vol. 30, pp. 645-650, Dec. 1982.

[14] K. R. Carver and E. L. Coffey, "Theoretical investigation of the microstrip antenna," Technical Report 00929. Physical Science Laboratory, New Mexico State University, Las Cruces (New Mexico),

[15] Everitt and Anner, Communication Engineering, 3rd edition , Mcgraw-Hill, 1956.

[16] S. Drabowitch, A. Papiernik, H. Griffiths, and J. Encinas, Printed antenna, Ch. 6 in Modern Antennas, Chapman & Hall, Cambridge, 1998.

# Enhancement of Numerical Computation Methods Useful for Radio Communication Antenna Systems

H. Matzner*, N. Amir*, U. Mahlab*and J. Gavan*, Fellow IEEE

**Abstract**

The radiation from a flanged parallel-plate waveguide is solved efficiently by the moment method, where the expansion functions contain the correct edge behavior of the fields. This computation method can be useful to optimize radiation of microwave transmitters and efficiency of receiver antenna and front end circuits. It is shown that three appropriate expansion functions are sufficient for an excellent accuracy and convergence rate of the solution.

## 1 Introduction

Several radio communication microwave systems use aperture antennas as waveguide apertures, slot arrays, horns, etc. The moment method (MM) is one of the most popular method for the calculation of the radiation related to this kind of antennas. In this paper we present an efficient selection of the MM expansion functions in order to investigate the accuracy of the required parameters necessary to improve efficiency of such antennas. We achieve a first step for accurate computation by solving the simple example of the radiation from a flanged parallel-plate waveguide. An accurate solution for the waveguide electromagnetic field components and reflection coefficient will enable optimum adaptation and efficiency with minimum of cut and try steps.

The problem of radiation from a flanged parallel-plate waveguide has been solved by many authors [1-15]. An efficient MM solution has been offered by

*Holon Academic Institute of Technology, 52 Golomb St., P.O.B. 305, Holon, Israel.

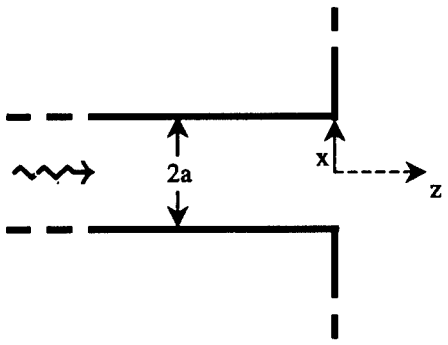


Figure 1: The geometry of the problem. A TEM wave is propagating in the $\hat{\mathbf{z}}$ direction inside the flanged parallel-plate waveguide and scattered by the discontinuity.

[15] ,where the dominant edge behavior of the fields is included in the MM expansion functions. It has been shown by [16], [17] that applying the MM with expansion functions that include the *correct* edge behavior of the fields improves the accuracy and convergence rate of the solution. In this paper we solve the problem of the transverse electromagnetic (TEM) case for the radiation from a flanged parallel-plate waveguide by applying the method used in [16], [17]. We compare also the results with the case where only the dominant behavior of the fields near the edges of the waveguide are included in the MM expansion functions [15].

# 2 Formulation of the Problem

## 2.1 The Relevant Field Components

The geometry of the waveguide is given in Fig. 1

The distance between the plates is $2a$ and the center of the gap is at the coordinates origin. The TEM incident field is expressed by

$$E_x = \exp(-jk_0 z) \tag{1}$$

$$H_y = \frac{1}{\eta}\exp(-jk_0 z) \tag{2}$$

where $\eta = 120\pi$ ohms and $k_0$ is the wave number. The TEM and transverse magnetic (TM) backward transverse fields are well known, and can be

expressed by [18]

$$E_x = \frac{1}{k_0}\sum_{n=0}^{\infty}\beta_n A_n \cos\left(\frac{n\pi x}{a}\right)\exp(j\beta_n z) \tag{3}$$

$$H_y = -\frac{1}{\eta}\sum_{n=0}^{\infty} A_n \cos\left(\frac{n\pi x}{a}\right)\exp(j\beta_n z) \tag{4}$$

where

$$\beta_n = \begin{cases} \sqrt{k_0^2-(n\pi/a)^2}, & k_0 \geq n\pi/a \\ -j\sqrt{(n\pi/a)^2-k_0^2}, & n\pi/a > k_0 \end{cases} \tag{5}$$

where the $n = 0$ term is connected to the TEM mode. The electric field above the flange is given by

$$E_x^{II} = \int_{-\infty}^{\infty}\tilde{A}(k_x)\exp(-jk_x x)\exp(-j\gamma z)dk_x \tag{6}$$

where

$$\gamma = \begin{cases} \sqrt{k_0^2-k_x^2}, & k_0 \geq k_x \\ -j\sqrt{k_x^2-k_0^2}, & k_x > k_0 \end{cases} \tag{7}$$

Using

$$\mathbf{H} = \frac{j}{\omega\mu}\boldsymbol{\nabla}\times\mathbf{E} \tag{8}$$

we get

$$\begin{aligned} H_y^{II} &= \frac{1}{\omega\mu}\int_{-\infty}^{\infty}(\gamma+\frac{k_x^2}{\gamma})\tilde{A}(k_x)\exp(-jk_x x)\exp(-j\gamma z)dk_x \\ &= \frac{1}{\eta}\int_{-\infty}^{\infty}\frac{k_0}{\gamma}\tilde{A}(k_x)\exp(-jk_x x)\exp(-j\gamma z)dk_x \end{aligned} \tag{9}$$

## 2.2 Moment Method Solution

The tangential electric field on the gap is given by the moment expansion

$$E_x^{III} = \sum_{j=1}^{N} a_j e_j(x) \tag{10}$$

where $N$ is the number of expansion function taken to the calculation, and

$$e_j(x) = \cos^{\alpha_j}\left(\frac{\pi x}{2a}\right), \qquad \alpha_j = \{-1/3, 1/3, 5/3, ...\} \tag{11}$$

It was shown in [16] ,[17] that the correct edge behavior of $E_x$ near a similar 2-dimensional 90° conducting edge is given by $\alpha_1 r^{-1/3} + \alpha_2 r^{1/3} + \alpha_3 r^{5/3} +$ ...where $r$ is the distance of the field point from the edge and $\alpha_i$ are arbitrary constants. It also has been shown that these $e_j(x)$ expansion functions exactly contain this edge power series behavior, that is, $e_j(x)$ contain all the terms of the edge power series, and do not contain terms which do not belong to the edge power series. We apply now the Galerkin MM version, that is, the set of the test functions the same as the set of the expansion functions.

In order to write the final equation, the $A_m$'s and $\tilde{A}(k_x)$ terms are extracted in terms of the $a_j$'s , and next we apply the boundary condition for the tangential magnetic field on the gap. Thus, the $A_n$'s terms are extracted by

$$1 + \frac{1}{k_0} \sum_{n=0}^{\infty} \beta_n A_n \cos \frac{n\pi x}{a} = \sum_{j=1}^{N} a_j e_j(x) \tag{12}$$

using the orthogonality relation

$$2a + 2aA_0 = \sum_{j=1}^{N} a_j \overline{e}_{j0} \tag{13}$$

where

$$\overline{e}_{j0} = \int_{-a}^{a} e_j(x) dx \tag{14}$$

hence

$$A_0 = \frac{1}{2a} \sum_{j=1}^{N} a_j \overline{e}_{j0} - 1 \tag{15}$$

and

$$aA_n \frac{\beta_n}{k_0} = \sum_{j=1}^{N} a_j \overline{e}_{jn} \tag{16}$$

where

$$\overline{e}_{jn} = \int_{-a}^{a} e_j(x) \cos\left(\frac{n\pi x}{a}\right) dx \tag{17}$$

For the external field we obtain

$$\int_{-\infty}^{\infty} \tilde{A}(k_x) \exp(-jk_x x) dk_x = \sum_{j=1}^{N} a_j e_j(x) \tag{18}$$

hence

$$2\pi \tilde{A}(k_x) = \sum_{j=1}^{N} a_j \tilde{e}_j(k_x) \tag{19}$$

where

$$\tilde{e}_j(k_x) = \int_{-a}^{a} e_j(x) \exp(jk_x x) dx \tag{20}$$

The MM equation now obtained by equating $H_y$ on the gap

$$1 - \sum_{n=0}^{\infty} A_n \cos\left(\frac{n\pi x}{a}\right) = \int_{-\infty}^{\infty} \frac{k_0}{\gamma} \tilde{A}(k_x) \exp(-jk_x x) dk_x \tag{21}$$

Multiply each side by $e_i(x)$ and integrate over the aperture, we obtain

$$(1 - A_0)\overline{e}_{i0} - \sum_{n=1}^{\infty} A_n \overline{e}_{in} = k_0 \int_{-\infty}^{\infty} \frac{1}{\gamma} \tilde{A}(k_x) \tilde{e}_i^*(k_x) dk_x, \qquad i = 1, 2, ..N \tag{22}$$

or

$$\left\{1 - \left[\frac{1}{2a}\left(\sum_{j=1}^{N} a_j \overline{e}_{j0}\right) - 1\right]\right\} \overline{e}_{i0} - \sum_{n=1}^{\infty} \left(\frac{k_0}{a\beta_n} \sum_{j=1}^{N} a_j \overline{e}_{jn}\right) \overline{e}_{in} \tag{23}$$

$$= k_0 \int_{-\infty}^{\infty} \frac{1}{\gamma} \left[\frac{1}{2\pi} \sum_{j=1}^{N} a_j \tilde{e}_j(k_x)\right] \tilde{e}_i(k_x) dk_x$$

Finally, the MM linear system of eqautions is given by

$$\sum_{j=1}^{N} A_{ij} \beta_j = B_i, \qquad i = 1, 2, ..N \tag{24}$$

where

$$A_{ij} = \frac{k_0}{\pi} \int_0^{\infty} \frac{1}{\gamma} \tilde{e}_j(k_x) \tilde{e}_i(k_x) dk_x + \frac{k_0}{2a} \sum_{n=0}^{\infty} \frac{\epsilon_n}{\beta_n} \overline{e}_{jn} \overline{e}_{in}, \tag{25}$$

$$\epsilon_n = \begin{cases} 1, & n = 0 \\ 2 & n \neq 0 \end{cases} \tag{26}$$

$$B_i = 2\overline{e}_{i0} \tag{27}$$

# 3 Main Results

We present here the results for the reflection coefficient

$$\Gamma = \frac{1}{2a} \sum_{j=1}^{N} a_j \overline{e}_{j0} - 1 \tag{28}$$

in comparison with the results of [15]. For a single frequency point $2a/\lambda = 0.8$ we present the following table:

| # funcs. | $\|\Gamma\|$ [15] | arg ($\Gamma$) [deg][15] | $\|\Gamma\|$ (*) | arg ($\Gamma$) [deg] (*) |
|---|---|---|---|---|
| 1 | 0.1463 | 112.01 | 0.167271 | 109.801 |
| 2 | 0.0643 | 75.82 | 0.0644 | 75.7013 |
| 3 | 0.06433 | 75.73 | 0.064322 | 75.7072 |
| 4 | 0.06433 | 75.71 | 0.064322 | 75.7072 |
| 5 | 0.06433 | 75.71 | | |

Table 1: Comparison between the results of [15] (columns 2,3) for the amplitude and phase of the reflection coefficient, for $2a/\lambda = 0.8$, and our results (*) in columns 4,5. Column 1 is for the number of the expansion functions taken to the calculation.

It is shown that the rate of convergence of the amplitude of the reflection coefficient in [15] is slightly better, but the rate of convergence of the phase and the overall rate of convergence is slightly better in our results.

Now we show a graph (Fig. 2) of the amplitude of the reflection coefficient for $a/\lambda$ from zero to one, applying 3 expansion functions, in comparison to the results of [15]. It is shown that both results are in very good agreement.

Finally a graph of the phase of the amplitude of the reflection coefficient is presented (Fig. 3), for $a/\lambda$ from zero to one, 3 expansion functions where applyed, and compared to the results of [15]. A very good agreement is observed.

# 4 Conclusions

The problem of the scattering of a TEM wave from the end of a flanged parallel-plate waveguide has been solved, where the MM expansion functions obey the correct edge behavior near the waveguide corners. It has been shown that the specific choice of the MM expansion functions in our work improves the accuracy and the rate of convergence of the solution, when compared to MM solutions for which the expansion functions only contain the dominant behavior of the field near the edges. The investigated computation method enable us to compute with accuracy the field components and the reflection coefficient required for antenna adaptation.

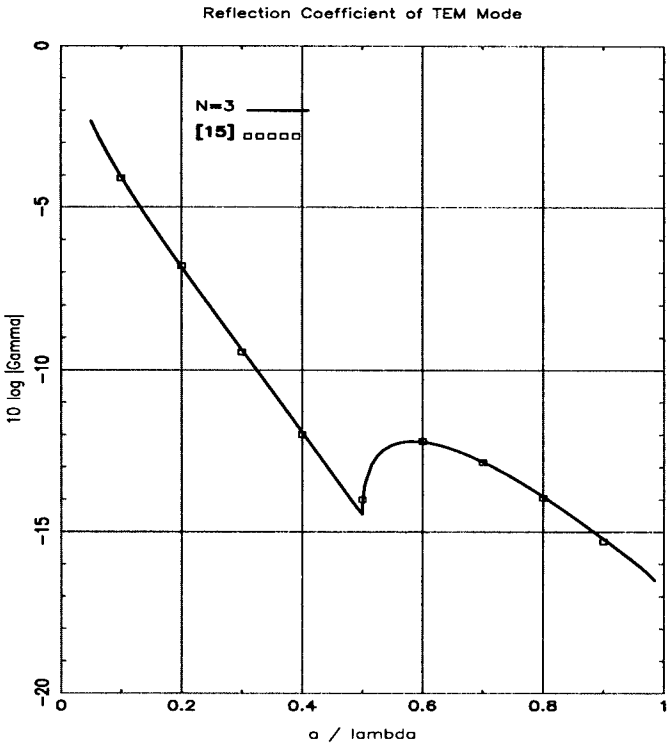


Figure 2: Amplitude of the reflection coefficient [dB] as a function of $a/\lambda$, where $2a$ is the distance between the planes of the waveguide and $\lambda$ is the wavelength. Solid line - our results with 3 MM expansion functions, squares - result of ref. [15].

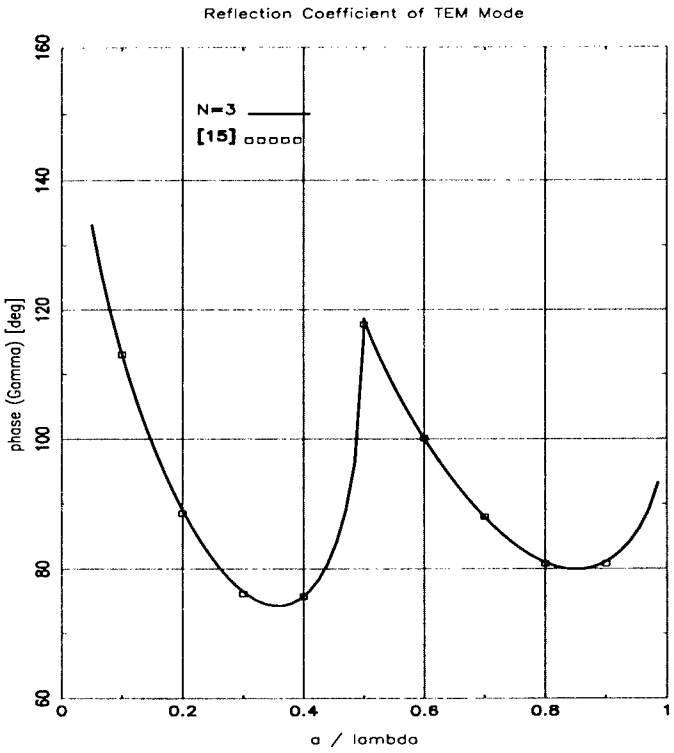


Figure 3: Phase of the reflection coefficient [deg] as a function of $a/\lambda$, where $2a$ is the distance between the planes of the waveguide and $\lambda$ is the wavelength. Solid line - our results with 3 MM expansion functions, squares - result of ref. [15].

# 5 Appendix

$e_{j0}$ is given by

$$e_{j0} = \int_{-a}^{a} e_j(x)dx = 2\int_0^a \cos^{\alpha_j}(\frac{\pi x}{2a})dx = 2\frac{a\Gamma\left[(1+\alpha_j)/2\right]}{\sqrt{\pi}\Gamma\left(1+\alpha_j/2\right)} \tag{29}$$

$\overline{e}_{jm}$ is given by

$$\begin{aligned} \overline{e}_{jn} &= \int_{-a}^{a} e_j(x)\cos\frac{n\pi x}{a}dx = 2\int_0^a \cos^{\alpha_j}(\frac{\pi x}{2a})\cos\frac{n\pi x}{a}dx \\ &= 4\frac{a}{\pi}\int_0^{\pi/2}\cos^{\alpha_j}(t)\cos(2nt)dt = 4\frac{a}{\pi}I_c(\alpha_j, 2n) \end{aligned} \tag{30}$$

$\widetilde{e}_j(k_x)$ is given by

$$\begin{aligned} \widetilde{e}_j(k_x) &= \int_{-a}^{a} e_j(x)\exp(-jk_x x)dx = 2\int_0^a \cos^{\alpha_j}(\frac{\pi x}{2a})\cos(k_x x)dx \\ &= 4\frac{a}{\pi}\int_0^{\pi/2}\cos^{\alpha_j}(t)\cos(k_x\frac{2a}{\pi}t)dt = 4\frac{a}{\pi}I_c(\alpha_j, k_x\frac{2a}{\pi}) \end{aligned} \tag{31}$$

and $I_c(a,k)$ is defined by

$$I_c(a,k) = \int_0^{\pi/2}\cos^a(t)\cos(kt)dt = \frac{2^{-1-a}\pi\Gamma(1+a)}{\Gamma\left(\frac{2+a-k}{2}\right)\Gamma\left(\frac{2+a+k}{2}\right)} \tag{32}$$

[19].

# 6 Acknowledgements

We thank Prof. S. Shtrikman from the Electronics Department of the Weizmann Institute of Science for his great help and fruitfull discussions.

# References

[1] N. Markuvitz, "Waveguide Handbook", pp. 183-184, 187-191, McGraw-Hill, 1951.

[2] R. H. Macphie and A. I. Zaghloul, "Radiation from a rectanuglar waveguide with infinite flanged-exact solution by the correlation matrix method", IEEE Trans.,AP-28, pp. 497 - 503, 1980.

[3] S. W. Lee and L. Grun, "Radiation from flanged waveguide: Comparison of solutions', IEEE Trans., AP-30, pp. 147-148, 1982.

[4] R. F. Harrington, "Time-harmonic Electromagnetic Fields", McGraw-Hill, 1961, pp. 180-186.

[5] V. P. Lyapin, V. S. Mikhalevsky and G. P. Sinyavsky, "Taking Into Account the Edge Condition in the Problem of Diffraction Waves on Step Discontinuity in Plate Waveguide", IEEE Trans., 1982, MTT-30, pp.1107-1109.

[6] J. D. Hunter, "The Displaced Rectangular Waveguide Junction and its Use as an Adjustable Reference Reflection", IEEE Trans., 1982, MTT-32, pp. 387-394.

[7] S. W. Lee, "Ray Theory of Diffraction by Open-Ended Waveguide, Part I", J. Math Phys, 1970, 11, pp. 2830-2850.

[8] T. Itoh and R. Mittra, "A New Method of Solution for Radiation from a Flanged Waveguide", Proc. IEEE, 1971, 59, pp. 1131-1133.

[9] K. Hongo, Y. Ogawa, Y. , T. Itoh and K. Ogusu, "Field Distribution in a Flanged Parallel-Plate Waveguide", IEEE Trans., 1975, AP-23, pp. 558-560.

[10] K. C. Rudduck and D. C. F. Wu, "Slope Diffraction Analysis of TEM Parallel-Plate Guide Radiation Patterns",IEEE Trans., 1969, AP-17, pp. 797-799.

[11] D. C. F. Wu, R. C. Rudduck and E. L. Pelton, "Application of a Surface Integration Technique to Parallel-Plate Waveguide Radiation Pattern Analysis", IEEE Trans., AP-17, pp. 280-285.

[12] H. M. Nussenzveig, "Solution of a Diffraction Problem", Phil. Trans. Roy. Soc. London, A, 1959, 252, pp. 1-51.

[13] C. M. D. Amarald and J. W. B. Vidal, "Evanescent-Mode Effects in the Double Wedge Problem", Appl. Sci Res. B. 1963, 11, pp. 1-25.

[14] A. Q. Howard, "One the Mathematical Theory of Electromagnetic Radiation from Flanged Waveguide", J. Math. Phys., 1972, 13, pp. 482-490.

[15] M. S. Leong and P. S. Kooi, "Radiation from a flanged parallel-plate waveguide: solution by moment method with inclusion of edge condition", IEE Proceedings, Vol. 135, Pt. H, No 4, 1988.

[16] H. Matzner and S. Shtrikman, "The Westmijze Head - an In-Depth Study", Current Topics in Magnet. Res., 1, pp. 145-158, 1984.

[17] H. Matzner and S. Shtrikman, "Some Improved Formulas for the Westmijze Head", IEEE Trans. on Mag., Vol. 33, pp. 820, 1997.

[18] U. S. Inan and A. S. Inan, "Engineering Electromagnetics", Addison-Wesley, 1999, pp. 742.

[19] I. S. Gradshteyn and I. M. Ryzhik, "Table of Integrals, Series and Products", pp. 372, Academic Press, 1980.

# TIME AND FREQUENCY DOMAIN WAVE PROPAGATORS

**Funda Akleman**[1] **Levent Sevgi**[2,3]

[1]*ITU Electronics and Communication Engineering Department,*
80626 Maslak / Istanbul, TURKEY
[2]*ITU Institute of Science and Technology, Defense Technologies,*
80626 Maslak / Istanbul, TURKEY
[3]*TUBITAK-Marmara Research Center, Electronic Systems Department*
*Gebze / Kocaeli TURKEY*

**Abstract** - *In this paper, a new time-domain wave propagator (TDWP) that was recently introduced, is compared against a frequency-domain one that has been in use for more than a decade. The new time-domain wave propagator is built by a two-dimensional (2D) finite-difference time-domain (FDTD) algorithm. The frequency-domain wave propagator is the Split-step Parabolic Equation (SSPE), which is the solution of (one-way) wave equation in parabolic form. These two techniques can be both used for different kinds of 2D propagation problems. In this paper, ground wave problems, which are difficult to solve, have been taken into consideration in order to compare the methods and show their power. Assuming an azimuthal symmetry, ground wave propagation and surface and/or elevated ducts may be represented via transverse and/or longitudinal refractivity and boundary perturbations in 2D space. The 2D propagation space extends from $x=0$ (bottom) to $x\rightarrow\infty$ (top), vertically and from $z\rightarrow -\infty$ (left) to $z\rightarrow \infty$ (right), horizontally. Pulse propagation is simulated in TDWP and while a moving window escorts the transmitted waveform from one end to the other end within the FDTD computation space, time histories are accumulated at chosen observation points. Any vertical and/or horizontal field profile at a desired frequency is extracted by applying off-line discrete Fourier transformation (DFT). On the other hand, a given vertical field profile is longitudinally propagated by moving back and forth between the transverse spatial and wavenumber domains in SSPE. The results of TDWP and SSPE are compared on different ducting and anti-ducting refractivity profiles and their agreement is presented.*

## I. Introduction

Today's communication systems as well as radars are mostly used within multi-area, multi-sensor, land-based, maritime and/or air-based integrated complex systems (such as an integrated maritime surveillance system or integrated early warning system against tactical ballistic missiles, etc.). The research towards development and, then, to the performance evaluations of such systems require powerful computer simulation tools and can only be done via these simulators. Some requirements related to current integrated system simulations are as follows:

- Modeling of propagation characteristics and path loss predictions in integrated surveillance systems, where microwave as well as HF (high-frequency) radars are used,
- Service planning, in rural and urban locations for mobile communication systems using both 900MHz and 1.8GHz systems
- Knowledge of propagation characteristics to overcome problems related to emerging radar technologies (HF and VHF radars).

1054-4887 © 2000 ACES

All these simulations require the simulation of ground wave propagation through atmosphere over a 3D regional digitized terrain map. A service planner, site-engineer or the leader of a small military ground contingent needs to have access in real time to the propagation characteristics between any two selected points (e.g., a communication transmitter and receiver) including terrain profile, vegetation and atmospheric effects. It has been a continuing challenge to prepare a general chart or computer code to satisfy such requirements.

Although all physical propagation problems are in three dimensions (3D), two dimensional (2D) approximations can be used if symmetry in one of the three dimensions exists or is assumed to exist. It is well accepted to solve atmospheric propagation problems in 2D for a broad frequency range because of the approximate azimuthal symmetry of earth. It is also common to use 2D solutions in some optical propagation problems (e.g. slab waveguide propagation solutions). Here, communication problems that involve atmospheric propagation are taken into account.

Long range communication, which includes both ground and sky waves, is one of the most difficult and important propagation problems. Sky wave is mostly affected by the upper atmosphere (ionosphere), while ground wave propagation changes due to the lower and middle atmosphere (troposphere) characteristics as well as ground effects. In this paper, ground wave propagation that can be solved by split step parabolic equation (SSPE) and time domain wave propagator (TDWP), is taken into consideration.

Ground waves have three components: direct waves, ground-reflected waves and surface waves. The model environment is a spherical earth with various ground characteristics, above which exists a radially inhomogeneous atmosphere. Having an excitation and observer anywhere on or above the ground, this model has served as a canonical problem. This problem is very complex and a full-wave, numerically computable analytical solution has not appeared yet. The physical characteristics of the propagation depend on many parameters, such as the operating frequency, medium parameters, transmitter and receiver locations and the geometry (boundary conditions, BC) between them. For example, the propagation is limited by the line-of-sight at microwaves because surface waves are almost negligible at these frequencies. On the other hand, beyond the horizon propagation is possible at HF (3-30MHz) and lower frequencies, because surface waves may reach ranges up to hundreds of kilometers in diffraction region.

Ground wave propagation problem and available analytical approximate solutions have been outlined in [1] together with the hybridization of ray and mode methods. Some of analytical-numerical and pure numerical techniques have also been summarized in [1]. Surface and/or elevated-ducting effects of various transverse as well as longitudinal refractivity profiles have been investigated either analytically [2-5], or numerically [6-8].

Here, two different wave propagators, which simulate wave propagation in time and frequency domains, are taken into account. The first one, TDWP, has been recently introduced and is a general technique that can be applied to broad range of propagation problems [9]. It is based on a two-dimensional (2D) finite-difference time-domain [10] (FDTD) algorithm, where broad band pulse propagation is simulated and traced over long distances by a virtual rectangular window that circulates the FDTD space longitudinally back and forth until the range of interest is reached. The second one, SSPE, is the well-known split step parabolic equation technique, which is the solution of one-way wave equation in parabolic form [6-8]. In

Sec.II, FDTD based TDWP is briefly summarized. The classical SSPE wave propagator is outlined in Sec.III. Numerical examples are chosen to be the simulations of wave propagation through surface guiding and anti-guiding ducts and are presented in Sec.IV, where results of the two techniques are compared. Finally, the conclusions and future implementations that are needed are given in Sec.V.

## II. The Time-domain Wave Propagator (TDWP)

The 2D-FDTD wave propagation region and the FDTD computation space are pictured in Fig.1. The structure is assumed to have an azimuthal symmetry. The transverse (x) and longitudinal (z) field components are $E_x$, $H_y$ and $E_z$, respectively, which models the classical 2D $TM_z$ ground wave propagation over earth's surface, representing a vertical polarization problem.

FDTD is based on the discretization of Maxwell' s two curl equations directly in time and spatial domains and dividing the volume of interest into very small identical blocks called Yee cells [10]. In 3D-FDTD, there are three electric and three magnetic field components in each Yee cell distinguished by (i,j,k) label. The time and spatial discretization steps are $\Delta t$ and $\Delta x$, $\Delta y$, $\Delta z$, respectively. Although field components in each cell are labeled with the same (i,j,k) numbers (such as $E_x(i,j,k)$ or $H_z(i,j,k)$), their locations are different. There is also a $\Delta t/2$ time difference between E and H field components in the Yee cell. Any object may be simulated by the medium parameters permittivity $\varepsilon$ [F/m], permeability $\mu$ [H/m] and conductivity $\sigma$ [S/m]. Although electric and magnetic field components are updated during the time simulation, voltages and currents in (i,j,k) cell may be obtained directly from Gauss and Faraday laws. Narrow and broad band responses may be readily obtained via FDTD simulations. Since its first introduction, other algorithms, such as free-space simulations (i.e., absorbing boundary simulations) and near-to-far field transformations have supported FDTD. Now, FDTD can be applied to variety of complex electromagnetic problems including radar cross-section (RCS) prediction and antenna simulations [11,12], biomedical modeling [13] and planar microwave network analysis and electromagnetic compatibility (EMC) simulations [14].

In TDWP, the related iterative FDTD equations are

$$E_x^n(i,k) = \frac{\varepsilon}{\varepsilon + \sigma\Delta t} E_x^{n-1}(i,k) - \frac{\Delta t}{(\varepsilon + \sigma\Delta t)\Delta z}\left[H_y^{n-1/2}(i,k) - H_y^{n-1/2}(i,k-1)\right] \quad (1)$$

$$E_z^n(i,k) = \frac{\varepsilon}{\varepsilon + \sigma\Delta t} E_z^{n-1}(i,k) + \frac{\Delta t}{(\varepsilon + \sigma\Delta t)\Delta x}\left[H_y^{n-1/2}(i,k) - H_y^{n-1/2}(i-1,k)\right] \quad (2)$$

$$H_y^{n+1/2}(i,k) = H_y^{n-1/2}(i,k) - \frac{\Delta t}{\mu_0 \Delta z}\left[E_x^{n-1}(i,k+1) - E_x^{n-1}(i,k)\right] + \frac{\Delta t}{\mu_0 \Delta x}\left[E_z^{n-1}(i+1,k) - E_z^{n-1}(i,k)\right] \quad (3)$$

where i and k are the cell numbers in the x and z coordinates, respectively, and n tags the time step

The time domain ground wave propagation over earth's surface is simulated in TDWP as follows:

- The propagation region (see Fig.1a) is much larger than the FDTD computation space. Therefore, the FDTD computation space covers this region like a moving computation sub-region.
- An $N_x$ by $N_z$ (number of transverse and longitudinal cells, respectively) FDTD computation space is terminated by perfectly matched layer (PML) blocks [15,16] from left ($z\rightarrow-\infty$), right ($z\rightarrow\infty$) and ($x\rightarrow\infty$) top. Any boundary condition (BC) can be simulated at x=0. For example, a perfectly electrical conductor (PEC) or a lossy ground termination may be used at the bottom.
- Taking $N_x$ = 500 and $N_z$ = 500 (total of 250,000 FDTD cells) corresponds to a $50\lambda_{min} \times 50\lambda_{min}$ ($\lambda_{min}$: minimum wavelength) space with a typical $\lambda_{min}/10$ spatial discretization.
- A source with a chosen spatial height distribution, and temporally pulsed so that it furnishes broadband information with a single simulation, is injected through the relevant field components.
- One-way propagation is traced via a 2D rectangular window as shown in Fig.1b. The content of this propagation window is the pulse, which carries information related to the three wave components; direct, ground-reflected and surface waves.
- This virtual propagation window moves from left to right in FDTD computation space and circulates back to the left when reaches the right most-end, which is the initial profile of the next FDTD computation space. The process and FDTD simulations repeat until the wave longitudinally propagates to a desired range.
- Keeping in mind the number of FDTD cells traced during the circulation of the propagation window, the transverse and/or longitudinal propagation characteristics are obtained.

Since TDWP is based on sliding the rectangular FDTD window along the propagation direction, it is defined for the flattened earth. But, the effects of the earth's curvature may easily be added via the relative permittivity $\varepsilon_r=n^2(x,z)$, as done in analytical approximate formulations [1], by modifying the refractivity profile. The earth's curvature can be included by defining the height profile of refractive index at a given range as $n=n_0+x/a$ (where $a=6378km$ is the earth's radius and $n_0$ is the refractive index value at the ground). This is valid when refractive index is constant. In real world, refractive index above the ground changes with both height and range. The change of refractive index with height is mostly dominant, since changes with range are relatively much slower. Therefore, only vertical refractive index profiles are of interest for most of the propagation cases.

Because of the closeness of n to unity, it is customary to use the refractivity N defined as

$$N = (n(x) - 1) \times 10^6 . \tag{4}$$

N is dimensionless, but is measured in "N units" for convenience. N depends on the pressure $P$ (mbar), the absolute temperature $T$ (°K) and the partial pressure of water vapor $e$ (mbar) as [17],

$$N = 77.6\frac{P}{T} + 3.73 \times 10^5 \frac{e}{T^2} \tag{5}$$

which is valid in earth-troposphere waveguides and can be used in ground wave propagation modeling. Depending on the variation of $P$, $T$ and $e$, various vertical refractivity profiles are defined. It has been found that refractivity gradient with respect to height is around -40Nunit/km (i.e., $\partial N / \partial x$ =-40Nunit/km)

after long period of measurements and observations around the world. This is accepted as *standard atmosphere* profile.

If the refractive index were constant, radio waves would propagate in straight lines. Since n decreases with height (e.g., as in the standard atmosphere case), radio waves are bent downward towards the earth, so that the radio horizon lies further away than the optical horizon.

In TDWP (and also in other wave propagators, such as SSPE) it is easy to include both the earth's curvature and the standard atmosphere condition at once by using $n=n_0+x/a_e$, where $a_e=4a/3=8504$km is the effective earth's radius.

In summary, n is either defined as n=n(x)+x/a, in order to take into account the effects of earth's curvature for all variations of atmospheric refractivity index, or equivalent fictitious medium is introduced, where N as defined in (4) is replaced by the modified refractivity M

$$M = N + \frac{x}{a} \times 10^6 = \mathrm{N} + 157\mathrm{x} \qquad (6)$$

with the height x given in kilometers [17]. N decreases by about 40Nunit/km while M increases by about 117Nunit/km for standard atmosphere. Sub-refraction (super-refraction) occurs when the rate of change in N with respect to height (i.e., $\partial N / \partial x$) is less (more) than 40Nunit/km.

The direct, ground-reflected and surface waves are traced in time domain, where wave fronts and their interferences (wave maxima and minima) appear as 2D images. A typical example is given in Fig.2 for a bilinear refractivity profile. Here, equi-amplitude contours are plotted as height versus range. A Gaussian altitude profile is fed as the initial field distribution inside a 500×500 FDTD computation space corresponding to 50m×50m physical space. The initial field distribution has a pulse character in time (i.e., first derivative of a Gaussian function with 200MHz bandwidth at 100MHz center frequency). A 500×250 virtual window circulates 20 times as if the longitudinal number of cells in FDTD computation space is 5000. Instant snapshots are taken at different simulation times and are plotted as the field profiles at different ranges. As shown in the figure, the wave propagates towards the ground and reflects back. The interference of direct and ground reflected waves as well as the surface waves are clearly observed in the figure.

Time histories of the pulse propagation in Fig.2, accumulated at different ranges and along the source height (i.e., 25m above the ground) is shown in Fig.3. The four plots, arranged in two vertical columns, correspond to the 94ns time histories (i.e., signal vs. time) at four different ranges (noted on the top right of each plot). These plots also correspond to the signal accumulation at four ranges inside nine FDTD propagation windows. Since the scale in each plot is normalized to its maximum value in order to reveal the detailed pulse shapes along the entire trajectory, relative field strengths with respect to the first window are also included as dB values inside the boxes. At $z=Z_1=24$m, only the initial pulse appears inside the 94ns FDTD propagation window because the delay of the signal caused by the path difference $R_1$-$R_2$ exceeds the window length. As the distance increases the path difference $R_1$-$R_2$ decreases and the ground-reflected pulse also appears inside the 94ns FDTD propagation window (see Figs.3b and 3c). Inside the last FDTD window (at $Z_4=223$m) the direct and ground-reflected pulses are almost indistinguishable. The signal in the last window is 13dB weaker than the signal in the first window.

Frequency domain characteristics can easily be obtained from the FDTD simulations. For example, an altitude field distribution at a given range can be obtained as follows:

- FDTD simulation is performed as explained above and propagation of waves is traced with the sliding rectangular window until the desired range.
- Time domain propagation data is accumulated at a number of altitude points (L) at the desired range (as given in Fig.3). A 2D array is used to accumulate the transient responses for all altitude points at the desired range.
- The accumulation continues until all the transients disappear at all altitude points and L different plots (each of which looks like the one shown in one of the windows of Fig.3) are obtained.
- After the FDTD simulation, altitude field distribution at any frequency (within the content of the pulse) is obtained by applying off-line DFT analysis to time histories at each altitude point.

Modeling ground wave propagation with TDWP needs careful parameter selection. First of all applying PML absorbing boundary simulators for backward as well as upward propagated waves is a challenging signal processing problem. Effective absorption within PML blocks depend on the number of PML layers and artificial PML medium parameters, which in turn depend on the wave phenomena inside the moving FDTD window. For a chosen number of PML blocks and artificial medium parameters, different degrees of absorption are obtained for surface guided, anti-guided, elevated ducted and/or rough surface scattered wave components. Therefore, one should be aware of possible induced wave components before the application of TDWP. This can also be obtained by visualizing the time domain propagation within the chosen scenario and by observing the real time pulse propagation. It should also be noted that, for long-range with dominant forward scattered propagation, the wave turns out to be plane (as expected in the far field), where the direction of propagation is parallel to the PML blocks, which is the worst case for PML absorbing boundary simulations and is a challenging problem. Nevertheless, TDWP with well-chosen PML parameters is an effective propagation simulator as presented in this paper.

Secondly, the numerical dispersion effects should be taken into account when dealing with long-range propagation scenarios. The longer the range the more spatial dispersion. Since TDWP is based on the application of 2D moving FDTD window, simulation of two-way propagation together with surface-scattered waves is possible. Therefore, there are forward, backward and/or upward propagated wave components inside the sliding FDTD window. This requires an intelligent separation of forward propagated pulse from the backward and upward propagated pulses. This separation and spatial dispersion can be controlled by applying a dynamic FDTD window size instead of a fixed-one.

## III. The Frequency-domain Wave Propagator (SSPE)

SSPE is a frequency domain wave propagator, which is the solution of a parabolic type (PE) wave equation [6-8]. If the propagation medium is assumed to be homogeneous with the refractive index $n$, field components satisfy the 2D scalar wave equation. This is useful for mostly propagation in troposphere where the range and height variations of $n$ is slow on the scale of wavelength. In order to solve 2D wave equation, a field function $\varphi(z,x)$, which varies slowly in range for energy propagating at angles close to the paraxial direction, is taken into consideration [18].

$$u(z,x) = e^{-ikz}\varphi(z,x) \tag{7}$$

where $x$ and $z$ are the height and range variables, respectively, and k is the free-space wavenumber. Then the 2D wave equation can be split into backward and forward propagating waves as

$$\frac{\partial u}{\partial z} = -ik(1+Q)u \qquad \text{(backward)} \tag{8}$$

$$\frac{\partial u}{\partial z} = -ik(1-Q)u \qquad \text{(forward)} \tag{9}$$

where

$$Q = \sqrt{\frac{1}{k^2}\frac{\partial^2}{\partial x^2} + n^2(z,x)} \tag{10}$$

is the pseudo-differential operator. The standard parabolic equation for forward propagation can be derived using first-order Taylor expansions of the square root and exponential functions [18],

$$\frac{\partial^2 u}{\partial x^2} + 2ik\frac{\partial^2 u}{\partial z} + k^2(n^2-1)u = 0 \ . \tag{11}$$

The solution of (11) with the help of Fourier transform is called SSPE, which is a one-way propagator that is valid under paraxial approximation (i.e., under weak longitudinal refractivity dependence or near axial propagation), where backscatter effects are omitted. The general solution of the SSPE technique is given as;

$$u(z,x) = \exp\left[i\frac{k}{2}(n^2-1)\Delta z\right] FFT^{-1}\left[\exp\left[-i\frac{k_x{}^2\Delta z}{2k}\right] FFT\{u(z_0,x)\}\right] \tag{12}$$

where $\Delta z = z - z_0$, $k_x$, FFT and $FFT^{-1}$ correspond to range step size, transverse wavenumber, discrete (fast) Fourier and inverse discrete (fast) Fourier transforms, respectively. The standard PE technique is a narrow-angle propagation approximation because the error caused by using first-order Taylor expansions is based on the angle of the wave from the horizontal. Since higher order polynomial expansions of the square root results in instability [19,20], other types of approximations, which include Padé-(1,1) expansion are used in order to solve wide-angle propagation problems [21]. In this paper, standard PE solution, which is satisfactory for the examples, has been used.

Since PE is an initial value problem, an initial transverse field distribution, $u(z_0,x)$ is injected and is longitudinally propagated through a medium defined by its refractive index profile $n(z,x)$; then the transverse field profile $u(z_0+\Delta z,x)$ at the next range step, is obtained. By multi-moving back and forth

between x and $k_x$ domains via FFT and inverse FFT the transverse field profile at any range may be obtained.

The 2D SSPE propagation space is pictured in Fig.4. The implementation of the SSPE algorithm is as follows:

- An altitude profile is injected into the SSPE wave propagator. A 1D complex array is used to built the initial profile $u(z_0,x_i)$, where $x_i$ (i=1, .., L, L is number of altitude points). This array contains amplitude and phase of the fields at each altitude (see Fig.4a).
- SSPE can not handle the BC at the surface by itself. Dirichlet or Neumann type BCs can be satisfied by either extending initial vertical profile from [0-$X_{max}$] to [-$X_{max}$, $X_{max}$], odd or even symmetric, or by applying SINE or COSINE FFT, respectively (see Fig.4b). In this paper, we use Neumann type BC that is required for a vertical polarization problem.
- This initial profile is longitudinally propagated from $z_0$ to $z_0+\Delta z$ via eq.(12). The same complex array is used to store the altitude profile at the next range step.
- Using the new altitude profile as the initial profile for the next step and applying SSPE propagator for the second time yield the altitude profile at the second range step $z_0+2\Delta z$ (see Fig.4c).
- The procedure is applied repeatedly until the propagator reaches the desired range $z_{last}$.
- The transverse and longitudinal step sizes ($\Delta$x and $\Delta$z, respectively) and maximum altitude $X_{max}$ are determined from the wave content and wavenumber requirements as well as sampling necessities and aliasing effects[6-8].

Two typical transverse refractivity profiles and SSPE propagation simulations through the ducts formed by these refractivity profiles are pictured in Fig.5. On top of the figure, a surface duct (i.e., a standard linearly decreasing refractivity over flat earth) and propagation of transmitted signal, which has a Gaussian height profile, is plotted. At the bottom, an elevated duct formed by a tri-linear vertical refractivity (over spherical earth) and its effect on propagation is plotted. As long as trapped within paraxial region, propagation through any duct formed by any transverse and/or longitudinal refractivity variation can be modeled via the SSPE propagator.

Terrain implementation, which is important for propagation prediction, is not very difficult for SSPE algorithm. There are different types of terrain modeling and it is possible to choose the appropriate one for the problem. One of them is called as conformal mapping [18,22], which depends on the change of variables due to terrain height. If the terrain function is known, it is easy to apply this conformal mapping to the SSPE algorithm since only the second derivative of the function is required for terrain inclusion in refractive index. Generally, it is not possible to know the terrain function, instead, the ground height difference with range can be measured, therefore there exist only the terrain height for each range step. With the help of this knowledge, terrain can be represented as a sequence of linear segments. Then, the second derivative can be determined using second-order central difference formula with the range interval corresponding to the PE range step for the SSPE algorithm [18,22].

Another simple way of terrain modeling is called as staircase terrain modeling [18], where slope values are not required, only the terrain height for each range is needed. For staircase terrain, the field is propagated in the usual way on each segment of constant height, applying the boundary condition at the ground. When the terrain height changes, corner diffraction is ignored since paraxial approximation neglects backscatter so the field is simply set to zero on vertical terrain facets, which is suitable for the assumption that the ground does not support propagation [18]. Since the computation height is not

changed due to the terrain, there is no need for the modification of refractivity index gradient, therefore it is also easy to implement the staircase terrain modeling into the SSPE algorithm.

## IV. Numerical Applications

To check the validity of the new time-domain wave propagator and to make comparisons between TDWP and SSPE, a surface duct problem is taken into account. A linearly decreasing refractivity altitude profile (e.g., standard atmosphere without earth's curvature) corresponds to a surface duct over planar earth's surface. The earth's curvature may also be included as a perturbation in refractivity as explained in Section II.

First, one-way propagation through a strongly trapping surface duct over flat earth is simulated with both TDWP and SSPE and the results are compared against each other. Same transverse (spatial) initial profile is fed into both TDWP and SSPE algorithms and the propagators are run for 500m. The TDWP is used once and broad band results are obtained. The SSPE propagator needs to be run separately for each frequency. Vertical field profiles at 500m away from the transmitter, which are obtained with both techniques are plotted in Fig.6 as propagation factors ($|E/E_0|$) vs. height. A similar procedure is applied to calculate the propagation factor in both TDWP and SSPE techniques. Both algorithms are run twice. In the first runs, propagation over PEC ground is simulated. In the second runs, they are repeated in free-space and the propagation factors are obtained. A good agreement between the results of time and frequency domain wave propagators is clearly seen from the figure.

A similar comparison is given in Fig.7 for range variation of vertical electric field component at a fixed altitude. In this case, time histories of propagation at various observation ranges at 25m fixed altitude are accumulated in TDWP and off-line DFT is then applied. SSPE calculates fields at all altitudes of all ranges, therefore, the calculation procedure does not change. In fact, higher range steps can be used in SSPE, but small steps are chosen for the comparison of range variations. The results agree quite well for both 100MHz (bottom) and 150MHz (top) frequency calculations. As seen from both Figs.6 and 7, interaction of direct and ground reflected wave components increases as the frequency increases.

First calculations and comparisons presented above belong to surface duct over flat earth. The calculations are repeated when earth's curvature is taken into account. In both TDWP and SSPE techniques, propagation over spherical earth's surface can be modeled as a modification in vertical refractivity profile. Guiding over flat earth's surface is modeled by a negative vertical refractivity gradient. On the other hand, it becomes a positive refractivity gradient when the curvature is included. While waves are trapped over surface with negative vertical refractivity gradient, energy detaches from the surface (i.e., wave divergence occurs) for positive vertical refractivity gradient.

In Fig.8, two typical SSPE results are pictured. Again, equi-amplitude contours are plotted as height versus range. The initial field profiles are normal modes [3,5] at 3MHz and 10MHz, where field maxima point the surface. They are the eigensolutions of 2D scalar Helmholtz wave equation with Neumann type BC at the surface (surface modes). Therefore, initial profiles simulate the surface coupling of transmitter energy. As SSPE proceeds, the detachment of the energy from the surface occurs, which is clearly observed in the figure. Although most of the energy detaches from the surface significant energy still follows the curvature of the earth through the shadow region up to 500km. Surface wave propagation at 3MHz is more significant than at 10MHz.

This anti-guiding problem is also modeled via TDWP and similar detachment is observed in time domain. Time domain propagation over spherical earth's surface is plotted in Fig.9. As TDWP proceeds, the pulse detaches from the surface and energy over the surface diminishes with range.

The results of TDWP and SSPE for this anti-guiding model are compared in Fig.10. Here, propagation factor vs. height at three different frequencies at 500m range are shown. As clearly seen from the figure, the higher the frequency the stronger the wave detachment from the surface. The propagation factor just above the surface at 500m range is –22dB at 100MHz and reduces to –33dB at 200MHz. This means, when the frequency increases from 100MHz to 200MHz field amplitude just above the surface at the same range reduces by 11dB.

Finally, the terrain effects at HF frequencies are shown in Fig.11 for three frequencies. At the top, a typical terrain model that can be accepted as two mountains with a valley in between is shown. At the bottom, range variations of the propagation factor are plotted for 5,15 and 30MHz. Here, to calculate the propagation factor SSPE is run twice and in the first run, propagation over PEC terrain is simulated. In the second run, it is repeated for PEC ground without terrain and the propagation factor, which includes only the terrain effects, is obtained. In fact, in order to simulate propagation for terrain at HF frequencies, mixed boundary conditions for ground should be applied. Here, Neumann boundary condition is used since our aim is to show only the terrain effect variations at different HF frequencies. As it is seen from the figure, the terrain affects propagation much more while frequency increases.

The TDWP is computationally expensive, when compared to the SSPE propagator. Although the TDWP simulation time is much more than the other, the SSPE algorithm must be repeated for hundreds of times to give the broad band propagation information obtained with one TDWP run. It should be noted that, no parameter optimization or algorithmic arrangement has yet been done in TDWP algorithm. Its memory requirements and computation time will drastically be decreased when optimization is done and when the sliding window size is dynamically controlled.

## V. Conclusions

Two powerful propagators are taken into account in this paper. The SSPE has been in use for more than a decade and has successfully been applied to many one-way propagation problems including acoustics, electromagnetics and optics. On the other hand, TDWP has just been introduced [9] and applied to various electromagnetic ducting problems. A very similar FDTD based technique has also been used in analyzing VLF and LF propagation through earth – ionosphere waveguides [23].

The new time domain wave propagator, TDWP is very promising in dealing with various complex propagation problems. Since not restricted within paraxial region, TDWP seems to have more potential than SSPE in modeling propagation problems. Terrain effects and surface roughness as well as ground losses [24-25] can be modeled, where any kind of transverse and/or longitudinal refractivity profiles can be taken into account [26,27]. The technique may also be applied to vertical propagation [28] or any other waveguiding structures [29].

Although short-range calculations are performed in the numerical examples presented here, theoretically there is no altitude or range limitations or BC restrictions at the surface in TDWP applications. Long

computation times may be required for long range propagation simulations, which may be overcomed by using some intelligent algorithmic and/or parallel processing techniques. It should be noted that, signal processing aspects during TDWP application are very important. One should be aware of the necessity of:

- monitoring the forward propagated and/or upward wave components and controlling its dispersion both in time and spatial domains,
- separation and absorbing of the backward and/or upward propagated or scattered wave components,
- absorbing surface scattered and/or anti-guiding or anti-ducting wave components,
- taking care of numerical dispersion effects when long propagation regions are of interest,
- extra caution in applying PML absorbing boundary simulations when long range propagation with dominant forward scattered wave component is of interest.

Nevertheless, by adding decision-makers and parallel processing routines, TDWP may be able to simulate not only 2D but also 3D pulsed propagation, utilizing digital terrain data, which may include surface impedance variations.

## References

[1] L. Sevgi & L. B. Felsen, "A new Algorithm for Ground Wave Propagation Based on a Hybrid Ray-Mode Approach", *Int. J. of Numerical Modeling*, Vol 11, No 2, pp.87-103, 1998

[2] L. B. Felsen & L. Sevgi, "Adiabatic and Intrinsic Modes for Wave Propagation in Guiding Environments with Longitudinal and Transverse Variations: Formulation and Canonical Test", *IEEE Transactions on Antennas and Propagat.* Vol 39 No 8, pp.1130-1136, 1991

[3] L. B. Felsen & L. Sevgi, "Adiabatic and Intrinsic Modes for Wave Propagation in Guiding Environments with Longitudinal and Transverse Variations: Continuously Refracting Media", *IEEE Transactions on Antennas and Propagat.* Vol.39 No.8, pp.1137-1143, 1991

[4] B. Polat, E. Topuz & L. Sevgi, "Wave Propagation Through Linearly Tapered Homogeneous Dielectric Slab Waveguides", *AEU, Int. J. of Electronics and Communication*, Vol.52, No.2, pp.105-108, March 1998

[5] L. Sevgi, S. Paker & E. Topuz, "Intrinsic Mode (IM) Formalism and Its Asymptotical Evaluations in 3D Non-Homogeneous Environments", *AEU, Int. J. of Electronics and Communication*, V.50, No.3, pp.201-207, May 1996

[6] G. D. Dockery, " Modeling Electromagnetic Wave Propagation in the Troposphere Using Parabolic Wave Equation", *IEEE Transactions on Antennas and Propagat.* Vol.36, pp.1464-1470, 1988

[7] A. E. Barrios, " Parabolic Equation Modeling in Horizontally inhomogeneous Environments", *IEEE Transactions on Antennas and Propagat.* Vol 40, pp.791-797, 1992

[8] L. Sevgi "Split Step Parabolic Equation Solutions in Surface Duct-to-Elevated Duct Transition", *Turkish J. of Physics*, Vol 19, No 3, pp. 541-551, 1995

[9] F. Akleman & L. Sevgi, "A Novel Finite-Difference Time-Domain Wave Propagator", *IEEE Transaction on Antennas and Propagat*, Vol. 48, No 5, pp.839-841, May 2000

[10] K. S. Yee, "Numerical solution of initial boundary value problems involving Maxwell's equations" *IEEE Transactions on Antennas and Propagat*, V-14, no. 3, pp. 302-307, 1966

[11] L. Sevgi & S. Paker, "FDTD Based RCS Calculations and Antenna Simulations", *AEU, International J. of Electronics and Commun.,* Vol.52, No.2, pp.65-75, March 1998

[12] F. Akleman & L. Sevgi, "Radar Cross Section and Antenna Modeling with FDTD Method", *Proc. of JINA'98, 10th Int. Symposium on Antennas*, November 17-19, 1998, France

[13] F. Akleman & L. Sevgi, "FDTD Analysis of Human Head – Mobile Phone Interaction in Terms of Specific Absorption Rate (SAR) Calculations and Antenna Design", *Proc. of IEEE-APS, Conference on Antennas & Propagation for Wireless Comm.*, pp. 85-88, November 2-4, 1998, Waltham, MA, USA

[14] M. Orhan Ozyalcin & L. Sevgi, "Comparisons of FDTD and TLM methods in Shielding effect analysis", *Proc. of IEEE CEFC'98 the Eight Biennial IEEE Conference on Electromagnetic field Computation*, June 1-3, Tuscon, Arizona, USA

[15] J. P. Berenger, "A Perfectly Matched Layer for the Absorption of Electromagnetic Waves", J. Comput. Phys., Vol.114, pp. 185-200, 1994

[16] F. Akleman & L. Sevgi, "A Novel Implementation of Berenger's PML for FDTD Applications", *IEEE Microwaves and Guided Wave Letters*, Vol.8, No 10, pp.324-327, 1998

[17] M. P. M. Hall, L. W. Barclay, M. T. Hewitt (ed), *Propagation of Radiowaves*, IEE Press, London, 1996

[18] M. Levy, *Parabolic equation methods for electromagnetic wave propagation*, Institution of Electrical Engineers, 2000

[19] A. Bambenger, B. Engquist, L. Halpern and P. Joly, "Parabolic Wave Equation Approximations in Heteregeneous Media", *SIAM J. Appl. Math.*, vol. 48, pp. 99-128, 1988

[20] A. Bambenger, B. Engquist, L. Halpern and P. Joly, "Higher Order Paraxial Wave Equation Approximations in Heteregeneous Media", *SIAM J. Appl. Math.*, vol. 48, pp. 129-154, 1988

[21] J. F. Claerbout, *Fundamentals of Geophysical Data Processing with Application to Petroleum Prospect,* McGraw-Hill, New York, 1976

[22] A. E. Barrios "A Terrain Parabolic Equation Model for Propagation in the Troposphere", *IEEE Transactions on Antennas and Propagat.*, Vol. 42, No.1, pp.90-98, 1994

[23] J. P. Berenger, "Finite Difference Computation of VLF-LF Propagation in the Earth – Ionosphere Waveguide", *Proc. Of URSI XXVI General Assembly*, pp. 464,Toronto, 1999

[24] G. D. Dockery and J. R. Kuttler, "An Improved Impedance Boundary Algorithm for Fourier Split Step Solutions of the Parabolic Wave Equations", *IEEE Transactions on Antennas and Propagat.* Vol 44, No 12, pp.1592-1599, 1996

[25] S. H. Marcus, "A Hybrid (finite difference-surface Green's function) Method for Computing Transmission Losses in an Inhomogeneous Atmosphere over irregular terrain", *IEEE Transactions on Antennas and Propagat.* Vol 40, No 12, pp.1451-1458, 1992

[26] F. Akleman & L. Sevgi, "Realistic Surface Modeling in a Time-domain Wave Propagator ", *IEEE Transactions on Antennas and Propagation*, (submitted) July 2000

[27] L. Sevgi, F. Akleman & L. B. Felsen, "Ground Wave Propagation Modeling: Problem-matched Analytical Formulations and Direct Numerical Techniques", *IEEE Antennas and Propagation Magazine*, (submitted) Sep. 2000

[28] M. F. Levy, "Horizontal Parabolic Equation Solution of Radio Wave Propagation Problems on Large Domains", *IEEE Transactions on Antennas and Propagat*, V-43, no. 2, pp. 137-144, 1995

[29] L. Sevgi & E. Topuz, "Split step Parabolic Equation Analysis of Coupled Dielectric Waveguides", *ELEKTRIK, Turkish J. of Electronics and Communication*, Vol. 3, No 2-3, pp. 85-92, 1995

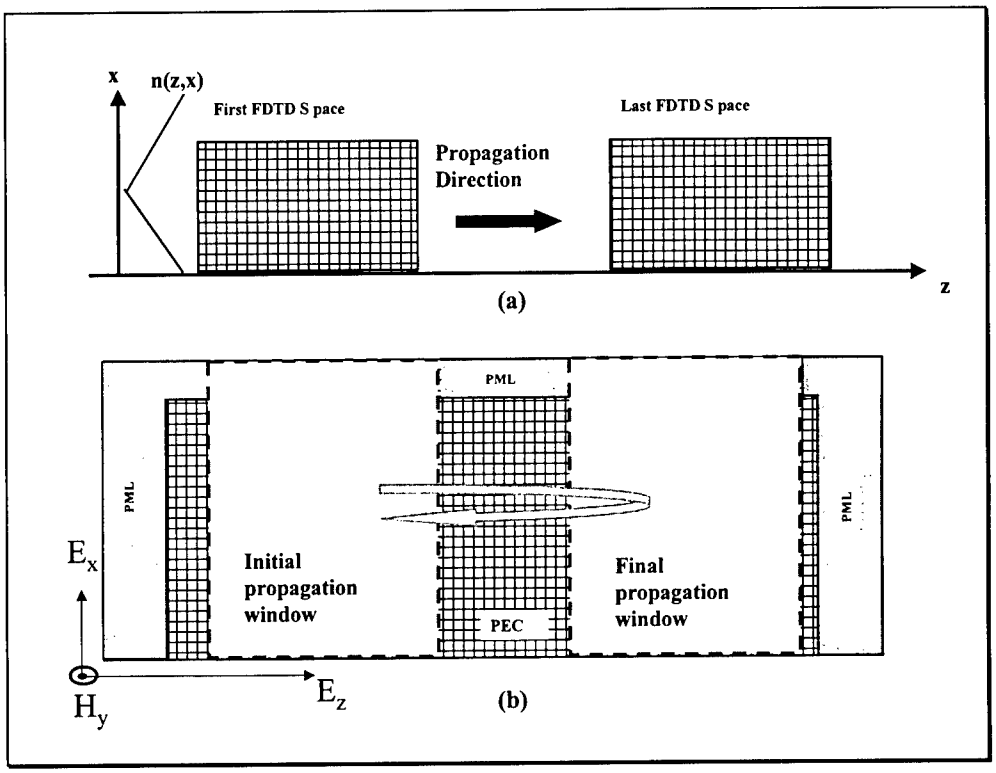


**Figure 1: (a)** The 2D propagation space. Here, x and z are the transverse and longitudinal coordinates, respectively. A finite-sized FDTD computation space is used as if this region is covered by multi FDTD computation spaces. **(b)** Detailed sketch of one FDTD computation space. Left, right and top boundaries are terminated by PML blocks to simulate an open propagation region. The bottom is shown to be PEC in this example. A virtual propagation window, which is adjusted to contain the propagation of the initial pulse, slides from left-to-right inside this FDTD computation space. The final window of the current FDTD computation space will be the initial window of the next FDTD space.

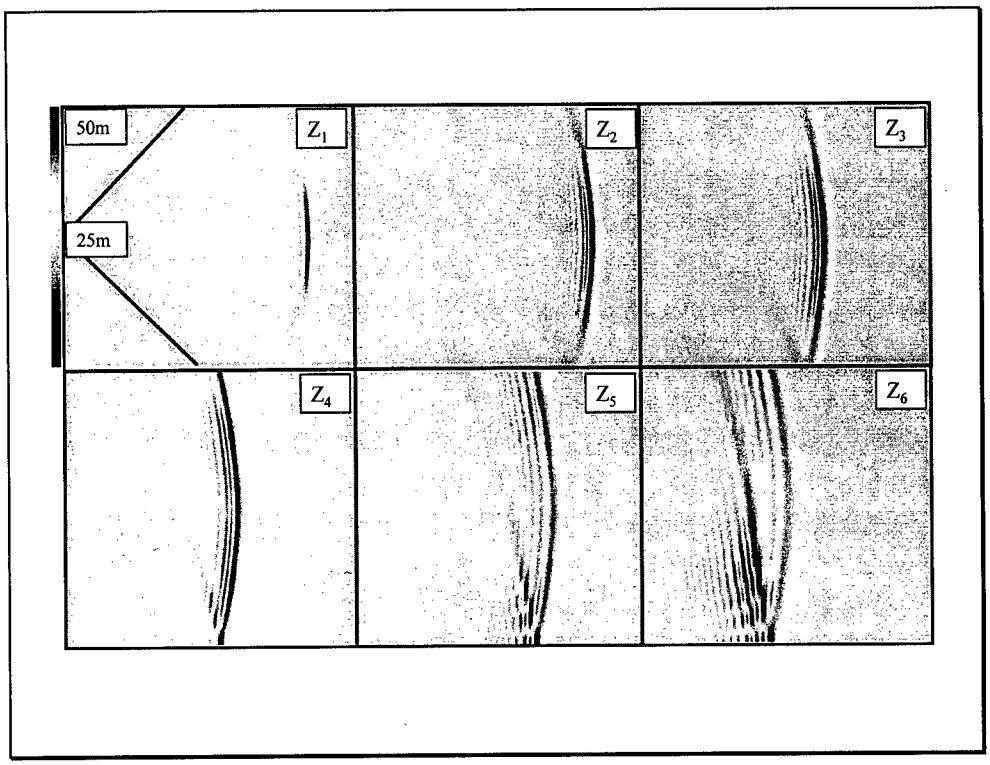


**Figure 2:** Time-domain pulse propagation inside the sliding window at propagation ranges $Z_1$, $Z_2$, …, $Z_6$. $Z_1$: $670^{th}$ time step ≈50m range; $Z_2$: $1570^{th}$ time step ≈110m range; $Z_3$: $2250^{th}$ time step ≈155m range; $Z_4$: $2580^{th}$ time step ≈180m range; $Z_5$: $3070^{th}$ time step ≈215m range; $Z_6$: $4330^{th}$ time step ≈305m range. The propagation region is characterized by a longitudinally homogeneous, bi-linear vertical refractive index profile with $dn/dx=10^{-3}$ [n unit/m]. The vertical distribution of the source is Gaussian with spatial extent ≈15m and maximum at 25m height. The temporal distribution is a differentiated Gaussian pulse with 200MHz bandwidth centered at 200MHz.

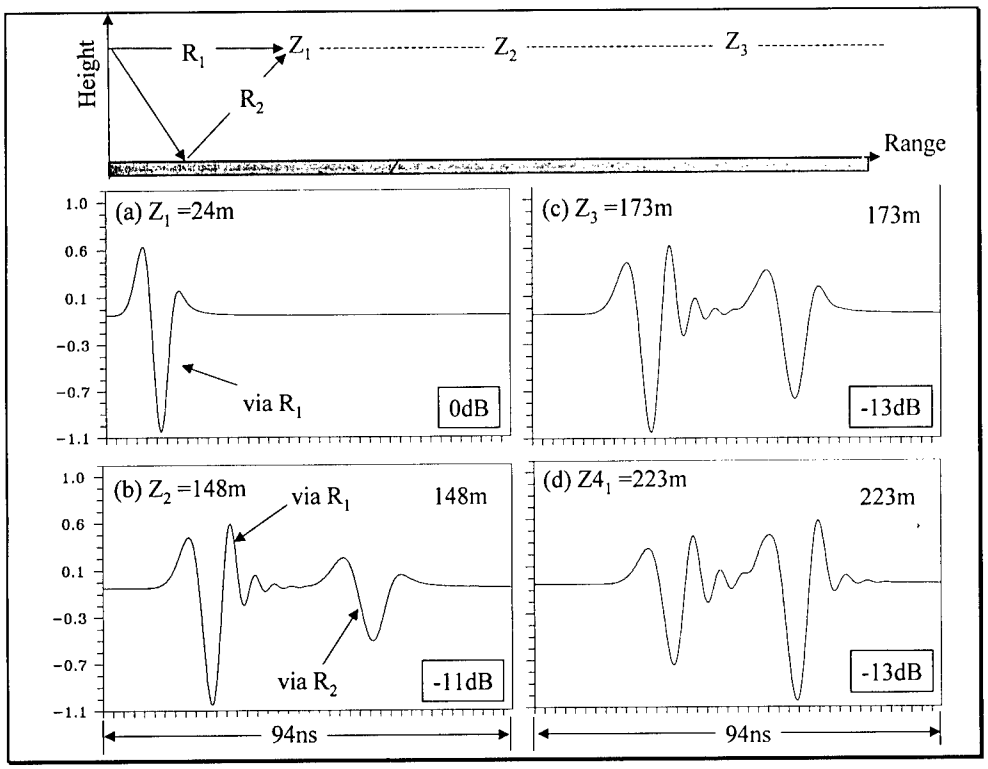


**Figure 3:** Time histories of the pulse in Fig.2 observed at different ranges along the source height 25m above the surface. Four plots (from top to bottom, left to right) correspond to the FDTD propagation windows (signal vs. time) at four different ranges (indicated at the top right of each plot). The temporal extent of the FDTD window is 94ns. Each plot is normalized to its maximum signal strength and the relative dB levels are given inside the boxes.

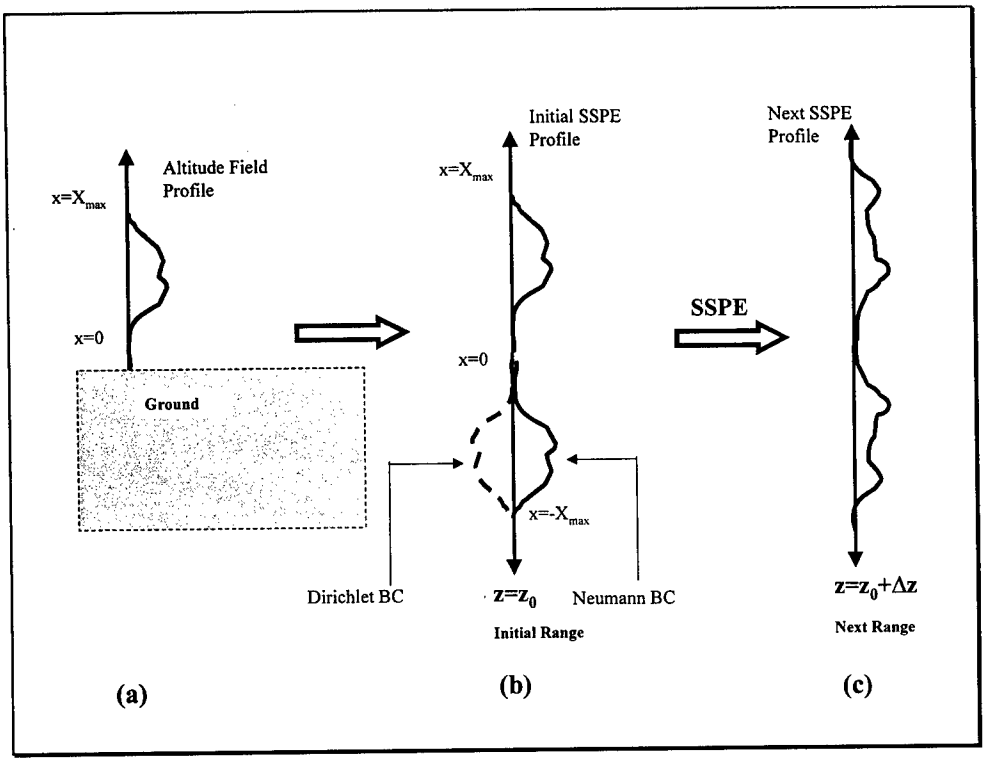


**Figure 4: (a)** The 2D propagation space that extends from x=0 to $x=X_{max}$ vertically and from $z\rightarrow -\infty$ to $z\rightarrow \infty$ horizontally. **(b)** Initial altitude profile of SSPE wave propagator at the range of $z=z_0$. The Dirichlet or Neumann type boundary condition at the surface is satisfied by extending vertical profile odd or even symmetric with respect to x=0 axis. The initial field profile at $z=z_0$ is $u(z_0,x)$. **(c)** The next altitude profile at $z=z_0+\Delta z$ is $u(z_0+\Delta z,x)$ and is obtained via a single SSPE run. Using $u(z_0+\Delta z,x)$ at $z=z_0+\Delta z$ as a new initial profile will give the profile $u(z_0+2\Delta z,x)$ at $z=z_0+2\Delta z$ via the second SSPE run. The desired altitude profile at $z=z_{last}$ ($z_{last}=z_0+N\Delta z$, N number of consecutive SSPE runs) is $u(z_0+N\Delta z,x)$ and is obtained after N consecutive SSPE runs.

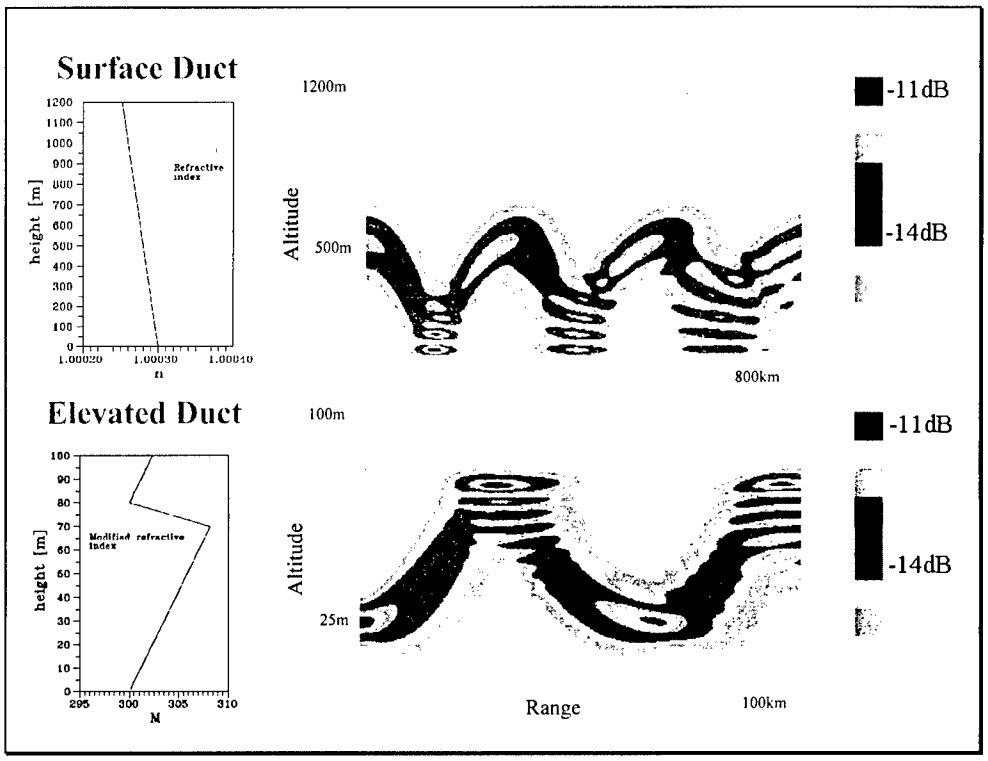


**Figure 5:** Two typical SSPE simulations; **(top)** propagation through a surface duct formed by the standard atmosphere (i.e., linearly decreasing vertical refractivity) **(bottom)** propagation through an elevated duct formed by a tri-linear vertical refractivity profile.

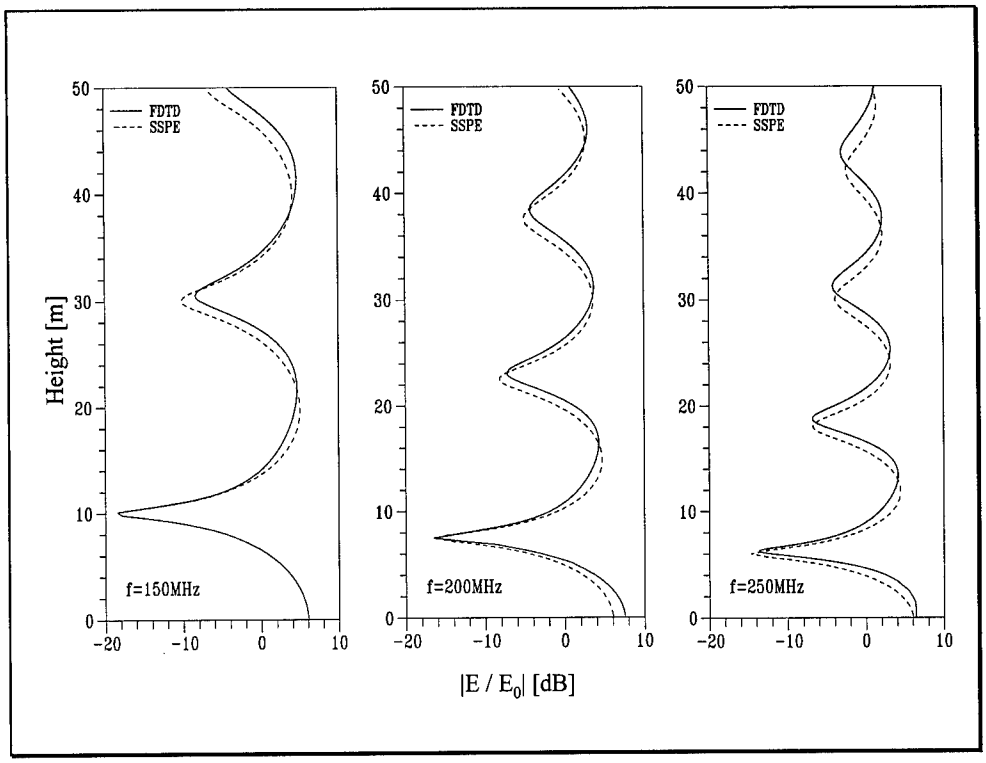


**Figure 6:** Propagation factor $|E/E_0|$ vs. height computed via both TDWP and SSPE propagators at 500m away from the source (corresponding to the ranges of 250λ, 330λ, 415λ at 150MHz, 200MHz and 250MHz, respectively). The vertical distribution of the source is Gaussian with spatial extent ≈15m and maximum at 25m height. The TDWP initial profile is a once-differentiated Gaussian pulse with bandwidth 200 MHz at center frequency 200 MHz; the SSPE propagator is run separately for each frequency. The propagation region is characterized by longitudinally homogeneous, linear vertical refractive index with $dn/dx = -10^{-7}$ [n unit/m].

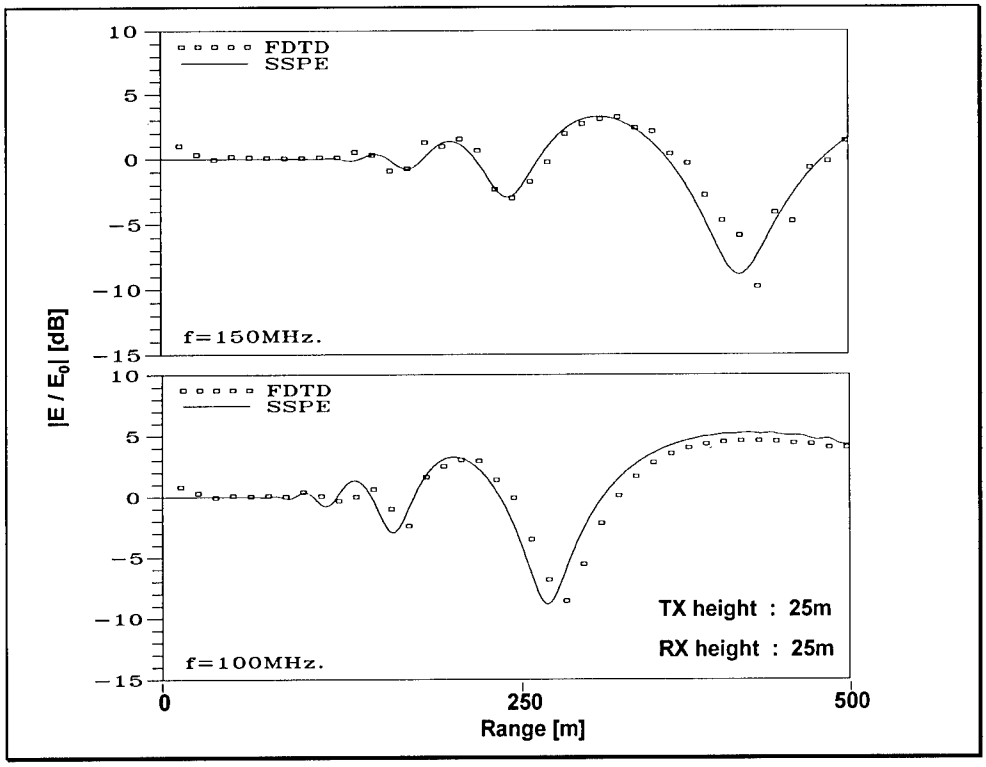


**Figure 7:** Propagation factor $|E/E_0|$ vs. range computed via both TDWP and SSPE at fixed altitude, for the same scenario explained in Fig. 6. Both the transmitter and observation altitudes are same and are equal to 25m. Top: 150MHz, bottom:100MHz.

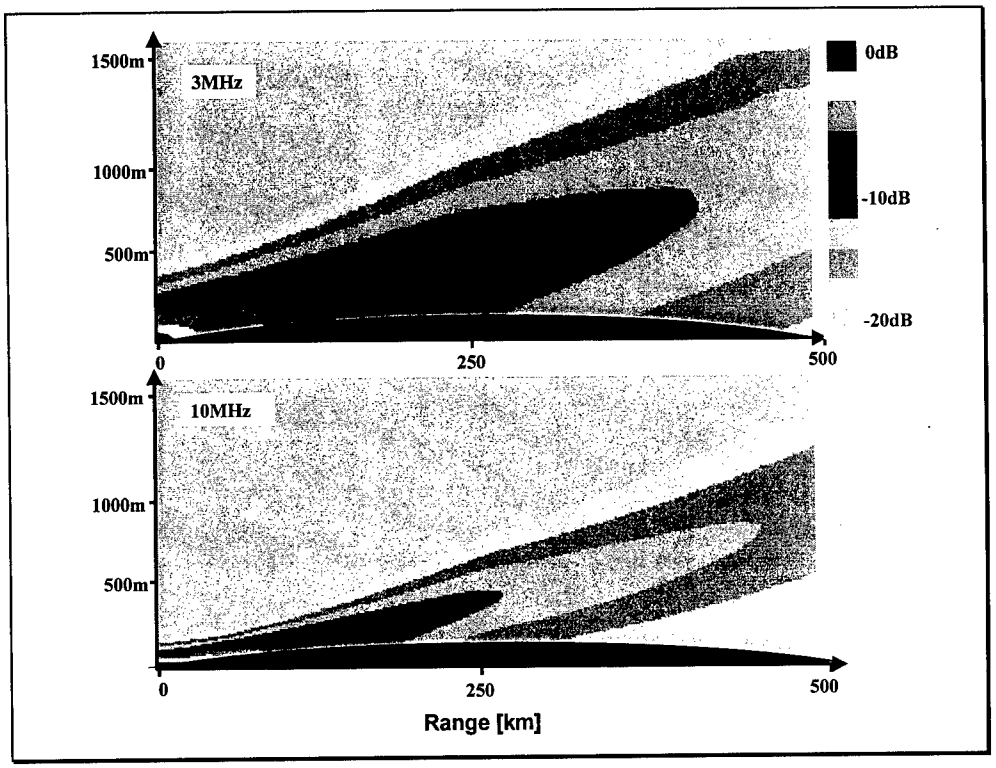


**Figure 8:** Wave detachment over earth's surface, under standard atmosphere approximation when earth's curvature is included (SSPE results). Top: 3MHz, bottom: 10MHz.

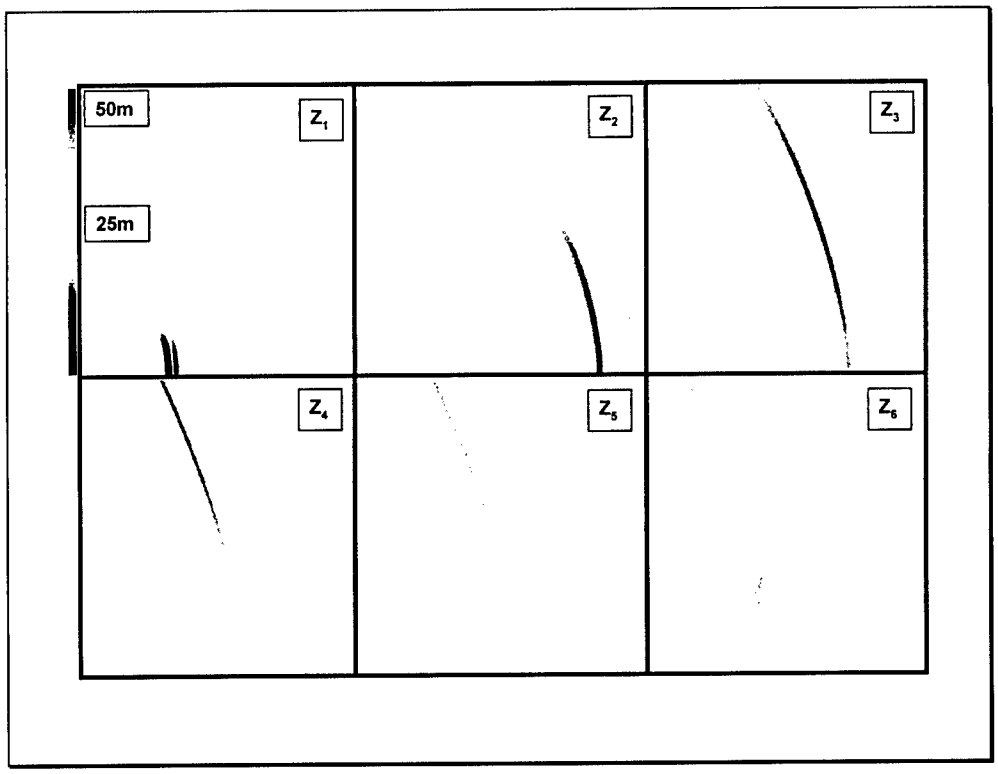


**Figure 9:** Wave detachment over earth's surface, under standard atmosphere approximation when earth's curvature is included (TDWP results with fictitious refractivity and curvature; the on-surface source is Gaussian with spatial extent of ≈15m and a once-differentiated Gaussian temporal profile with 200MHz bandwidth at 200MHz center frequency. The propagation region is characterized by longitudinally homogeneous, linear vertical refractive index with $dn/dx = 10^{-3}$ [n unit/m]

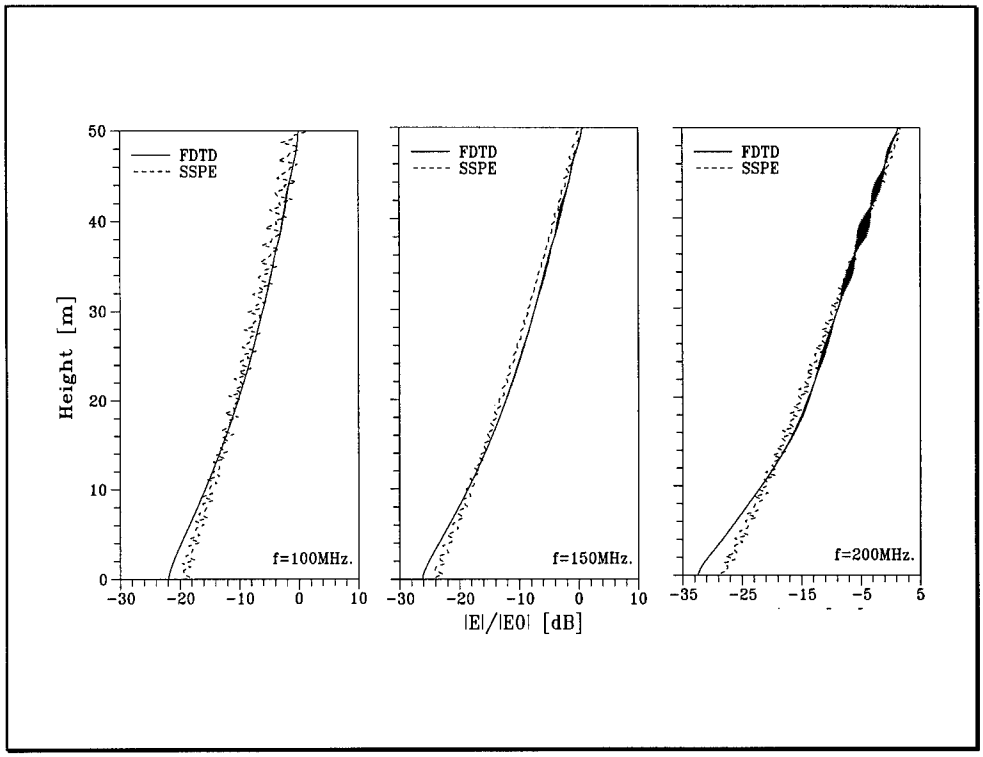


**Figure 10:** Propagation factor $|E/E_0|$ vs. height computed via both TDWP and SSPE propagators at 500m away from the source (corresponding to the ranges of 166λ, 250λ and 333λ at 100MHz, 150MHz and 200MHz, respectively). On-surface source is Gaussian with spatial extent of ≈15m. In TDWP, a once-differentiated Gaussian temporal profile with 200MHz bandwidth at 200MHz center frequency is used. The SSPE propagator is run separately for each frequency. The propagation region is characterized by longitudinally homogeneous, linear vertical refractive index with $dn/dx = 10^{-3}$ [n unit/m].

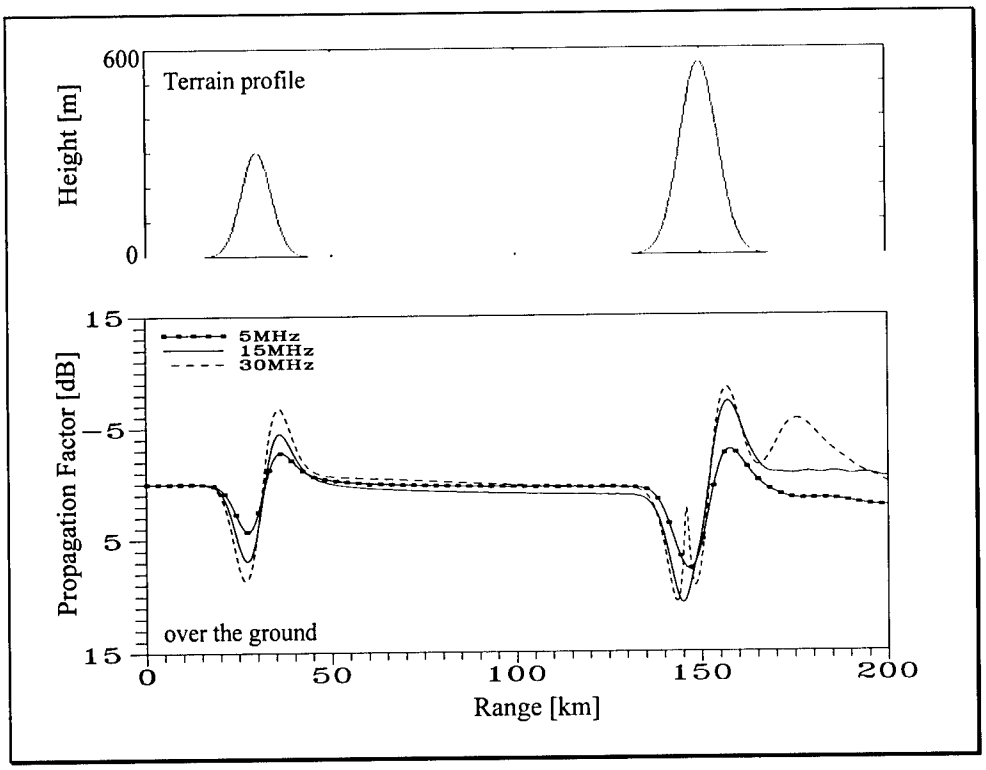


**Figure 11: (Top)** A typical terrain model with two mountains and a valley lying between them. **(Bottom)** Propagation factor results for three frequencies 5,15 and 30MHz for this terrain type. Refractivity index for standard atmosphere that includes earth's curvature is used.

# RAY-TRACING TECHNIQUES FOR MOBILE COMMUNICATIONS.

O. Gutiérrez, F. Saez de Adana, I. González, J. Pérez, M. F. Cátedra

Dprt. de Teoría de la Señal y Comunicaciones.

Escuela Politéctica, Universidad de Alcalá

28806 Alcalá de Henares (Spain)

Tel: +34918856724, Fax: +34918856724

e-mail: felipe.catedra@uah.es

## ABSTRACT

**In this paper an application for mobile communication of several ray-tracing techniques is presented. The techniques work in combination with deterministic propagation models based on GTD/UTD techniques. Several ray-tracing techniques are reviewed and some results applying one of them, the Angular Zeta Buffer (AZB) method for urban and indoor scenarios are shown, obtaining in all the cases good results comparing with measurements.**

## 1. INTRODUCTION

For mobile communication, traditionally, propagation models based on empirical and semi-empirical models have been used. Several models for urban and rural environments have been developed and largely used [1]. However, when the traffic had increased the size of the cells has decreased (microcells, picocells) and these methods do not provide good predictions and deterministic models should be used.

A model based on Geometric Optics (GO), on Geometrical Theory of Diffraction (GTD) and on Uniform Theory of Diffraction (UTD) is presented. This is a ray-based method, the electric field at the observation points is calculated as the coherent sum of the fields associated with the rays that reach the points.

The propagation model requires a detailed information about the environment, which includes geometric and electromagnetic information of the obstacles, that are modeled by means of flat facets, each one of them with its own electromagnetic properties. In complex environments, like mobile communications scenarios, the principal difficulty of the GTD application is to solve ray-tracing. It consumes most of the simulation time. The shadowing problem is the most critical part of the ray tracing from a computational point of view. The problem is to determine if any facet of the model shadows a ray, that is the so-called intersection test.

The ray tracing techniques have been developed in the last 30 year in the world of computer graphics for visualization of complex scenarios [2-3]. Some of the acceleration ray-tracing techniques used for computer graphics can be used in combination with UHF propagation models for the reduction of the number of intersection tests in mobile communications environments. They are the Space Volumetric Partitioning (SVP), the Binary Space Partitioning (BSP) and the Angular Z-Buffer (AZB).

Some computer codes have been developed, using the propagation model and the AZB technique, for different environments. Computer codes FASPRO [4] and FASPRI [5] have been developed for the analysis of urban and indoor environments, respectively. This paper presents the electromagnetic basis of the application of GTD/UTD to the prediction of propagation in mobile communications implemented in those codes (Section 2) and a survey of the main ray-tracing acceleration techniques mentioned above showing the advantages of the AZB technique for our purposes (Section 3), whereas in [4] only the comparison between two ray tracing techniques were presented. Also, in Section 4, a validation of the results of both codes, compared with measurements is shown. Finally, the conclusions are outlined in Section 5

1054-4887 © 2000 ACES

## 2. GTD/UTD APPROACH

The electric field $\vec{E}_T$ created at an observation point by a source will be approximated by:

$$\vec{E}_T = \sum_{i=1}^{N} \vec{E}_i \tag{1}$$

where $\vec{E}_i$ represents the electric field due to each one of the ray-paths which connect the source with the observation: direct ray, reflected rays, diffracted rays, transmitted rays, reflected-diffracted rays, double-reflected rays, etc.

Each $\vec{E}_i$ term can be computed using the ray-tube formulation of GTD/UTD [6]:

$$\vec{E}(s) = \vec{E}(s=0)\sqrt{\frac{\rho_1 \rho_2}{(\rho_1 + s)(\rho_2 + s)}}\exp(-j\beta s) \tag{2}$$

where $s$ is distance to the reference point ($s=0$), $\vec{E}(s=0)$ is the electric field at the reference point and $\rho_1, \rho_2$ are the principal radii of curvature of the wavefront associated with the ray at the reference point. $\beta$ is the free-space wavenumber.

The GTD/UTD expression is valid for a finite number of rays that pass through the observation point. When $s=-\rho_1$ or $s=-\rho_2$ the number of rays is infinite and the GTD does not give valid results. They are the caustics (see Figure 1).

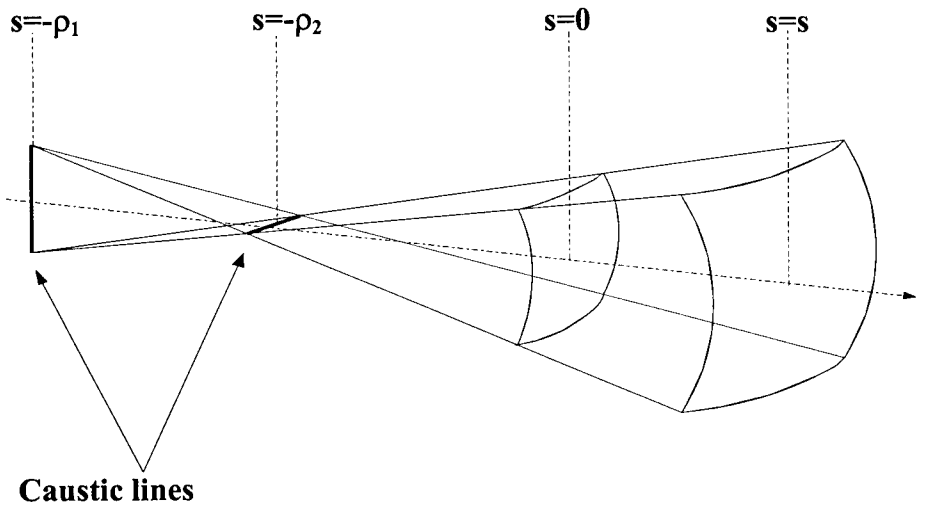


**Figure 1.** Astigmatic wavefront.

To apply the expression seen above the incident field shall be ray-optical [6]. In the mobile communication context, the above condition is satisfied except in certain special cases.

### 2.1. DIRECT FIELD

The electric field due to the direct ray is evaluated considering that the caustic lines degenerate at the same point, so the wavefront is spherical, and this point is taken as the reference point. Then applying the expression (2) the direct field is given by:

$$\vec{E}(r,\theta,\phi) = \vec{E}_t(\theta,\phi)\frac{\exp(-j\beta r)}{r} \tag{3}$$

where $\vec{E}_t(\theta,\phi)$ can be obtained from the radiation pattern of the transmitter antenna $\vec{E}_0(\theta,\phi)$:

$$\vec{E}_t(\theta,\phi) = \sqrt{\frac{\eta P_r G}{2\pi}}\vec{E}_o(\theta,\phi) \tag{4}$$

- $\eta$ is the free space impedance
- $P_r$ is the power radiated by the transmitter
- $G$ is the gain of the transmitter antenna

These expressions can be used when the observation point is in the far-field from the antenna, as is usual in mobile communications.

## 2.2. REFLECTED FIELD

When the environmental obstacles are flat facets and the GO is applicable, a more efficient way to compute the field contribution of the reflected rays can be used instead of the general expression of GTD for the reflected field calculation. The method consists in applying the Image Theory and the Fresnel reflection coefficients.

Figure 2 shows a reflection case. The facet belongs to a body whose permittivity, conductance and permeability are defined by parameter $\varepsilon$, $\sigma$ and $\mu$ respectively.

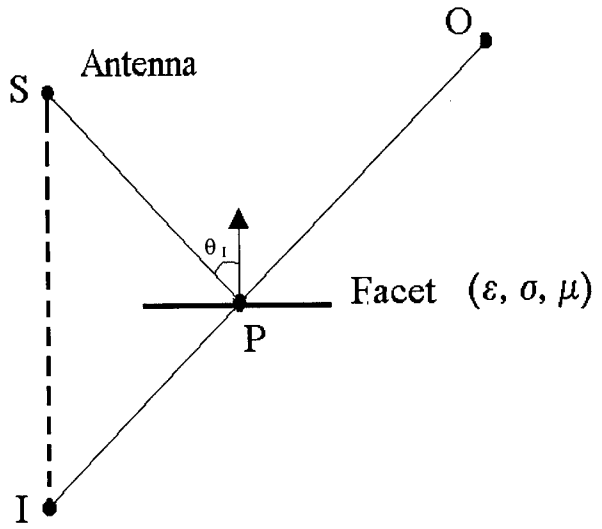


**Figure 2.** Transmitter antenna in front of a flat facet and definition of the image point, the reflection point and the incident angle.

According to the Snell's law the incident ray is reflected in the specular direction. It can be observed that point P can be also obtained as the intersection between the straight line IO and the facet, being the Image of the source point S.

The reflected field at point P can be obtained from the incident field using the Fresnel reflection matrix $\overline{\Gamma}$

$$\vec{E}^r = \overline{\Gamma}\vec{E}^i \tag{5}$$

where $\vec{E}^i$ can be obtained from the radiation pattern of the antenna considering an equivalent antenna at the image point I [7]. This expression can only be applied when $\vec{E}^i$ and $\vec{E}^r$ are resolved into their parallel and perpendicular components to the planes of incidence and reflection respectively. In this situation, expression (5) can be written as follows

$$\begin{bmatrix} E_{||}^r \\ E_{\perp}^r \end{bmatrix} = \begin{bmatrix} \Gamma_h & 0 \\ 0 & \Gamma_s \end{bmatrix} \begin{bmatrix} E_{||}^i \\ E_{\perp}^i \end{bmatrix} \tag{6}$$

where $\Gamma_s$ and $\Gamma_h$ are the so-called soft and hard reflection Fresnel coefficients [8] respectively.

The Fresnel coefficients are given by:

$$\Gamma_s(\theta) = \frac{\cos(\theta) - \sqrt{\varepsilon_r - sin^2(\theta)}}{\cos(\theta) + \sqrt{\varepsilon_r - sin^2(\theta)}} \tag{7}$$

$$\Gamma_h(\theta) = \frac{\varepsilon_r \cos(\theta) - \sqrt{\varepsilon_r - sin^2(\theta)}}{\varepsilon_r \cos(\theta) + \sqrt{\varepsilon_r - sin^2(\theta)}} \tag{8}$$

where $\theta$ is the angle of incidence formed by the incident ray and the normal vector to the facet (see Figure 2). $\varepsilon_r$ is the complex relative dielectric constant

Thus it can be stated that the reflected field is equivalent to the direct field of an antenna whose radiation pattern is calculated as the image of the pattern of the transmitter antenna.

## 2.3. EDGE-DIFFRACTED FIELD

The field diffracted by an edge is given by [8]

$$\vec{E}^d(s) = \vec{E}^i(Q_d)\, \overline{D} \sqrt{\frac{\rho_e^i}{s(\rho_e^i + s)}}\, e^{-j\beta s} \tag{9}$$

where $\vec{E}^i(Q_d)$ is the incident field at the diffraction point $Q_d$, $\overline{D}$ is the diffraction coefficients matrix, and s is the distance between the observation point and the diffraction point.

When the field is resolved into the parallel and the perpendicular components, the dyadic form of the diffraction coefficients can be expressed as:

$$\overline{D} = \begin{bmatrix} -D_s & 0 \\ 0 & -D_h \end{bmatrix} \tag{10}$$

where $D_s$ and $D_h$ are the soft and hard diffraction coefficients, which can be obtained from the reflection coefficients given by:

$$D_{s,h} = D_1 + D_2 + R_{s,h}(D_3 + D_4) \tag{11}$$

where $D_1$, $D_2$, $D_3$ and $D_4$ are the components of the diffraction coefficients [9].

## 2.4. MULTIPLE-EFFECTS

In complex environments such as urban and indoor scenarios, multiple effects must be included to give an accurate estimation of the field at the observation points. In microcells and picocells two or three interactions are sufficient to provide a good prediction, but in large cells, sometimes it is necessary to consider higher order field contributions. A multiple effect contribution can be obtained as a combination of simple effects.

## 3. RAY TRACING TECHNIQUES

In a mobile communications problem, the field is calculated at a large number of observation points (thousands or even greater). Considering a faceted model for an urban environment with $N_f$ facets, $N_e$ edges and $N_o$ observation points, if a "brute force" method is used, the number of intersection tests are proportional to $N_0 N_f (N_f+N_e)^X$ where $X$ is the order prediction.

A typical microcell can be modeled by a number of facets and edges of the order of magnitude of several hundreds, so the number of intersection tests required for the ray-tracing are incommensurate. For these cases, it is necessary to reduce this number using ray-tracing acceleration techniques. The efficiency of a GTD based tool depends highly on the ray tracing simulator.

## 3.1. SPACE VOLUMETRIC PARTITIONING (SVP).

One of the earliest techniques used to speed up the ray tracing was the Space Volumetric Partitioning (SVP). This technique is based on dividing the space in volumes called voxels. The voxels are cubes in the three directions of the space. A 2D example is shown in Figure 3.

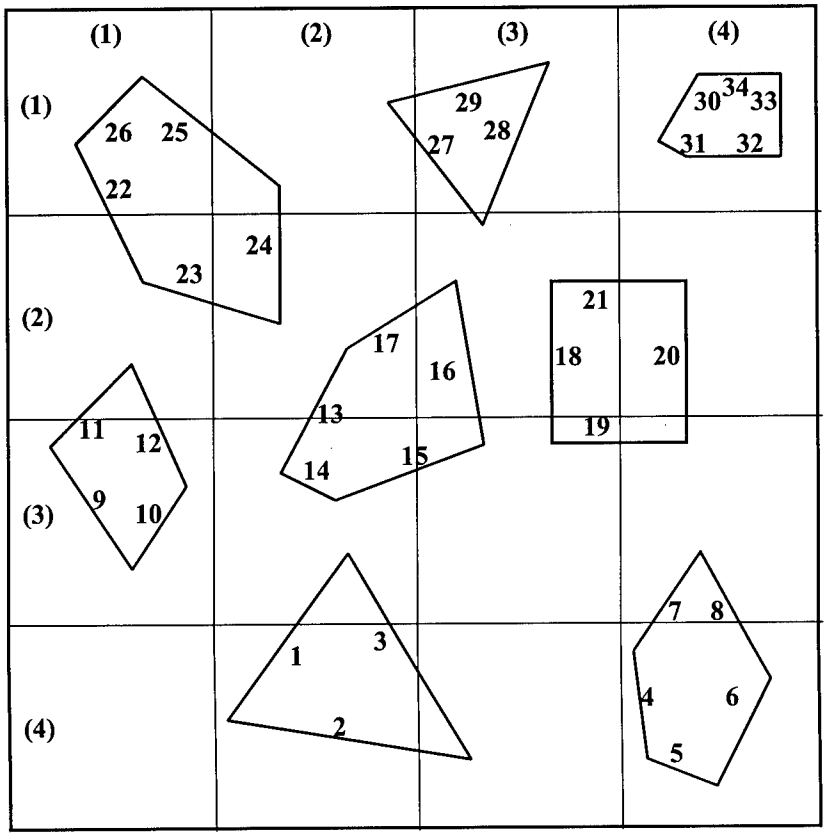


**Figure 3.** Example of space volumetric partitioning.

Once the space is divided, the facets that belong to each voxel are obtained, which are those that are totally or partially inside the volume. This information is loaded in the SVP matrix. The SVP matrix for the example of Figure 3 is shown in Table 1.

| Voxel | Facets |
|---|---|
| (1,1) | 22,25,26 |
| (1,2) | 24,25,27,29 |
| (1,3) | 27,28,29 |
| (1,4) | 30,31,32,33,34 |
| (2,1) | 11,12,22,23 |
| (2,2) | 13,17,23,24 |
| (2,3) | 16,17,18,21,27,28 |
| (2,4) | 20,21 |
| (3,1) | 9,10,11,12 |
| (3,2) | 1,3,13,14,15 |
| (3,3) | 15,16,18,19 |
| (3,4) | 7,8,19,20 |
| (4,1) | |
| (4,2) | 1,2,3 |
| (4,3) | 2,3 |
| (4,4) | 4,5,6,7,8 |

**Table 1.** Voxels distribution of the facets of the model.

When a shadowing test for a ray path source-observer is achieved, the voxel where the source lies is determined and all the facets loaded in the SVP matrix for this voxel are interrogated. If none of them shadows the ray, the facets contained in the next voxel that the ray crosses are considered for the intersection test. The procedure is repeated until a facet of the model shadows the ray or until the observation point is reached (in this case the ray is not shadowed and contributes to the total field).

In Figure 4, two examples of rays are shown, one shadowed and the other not. The ray from the source (S) to the first observation point ($O_1$) crosses the voxels (3,2), (3,3) and (3,4). Therefore, the facets loaded in these voxels must be interrogated, that is to say, the facets 1, 3, 13, 14, 15, 16, 18, 19, 7, 8 and 20 in that order. On the other hand, the ray which goes from S to the second observation point ($O_2$) crosses the voxels (3,2), (2,2), (2,1) and (1,1) and the facets 1, 3, 13, 14, 15, 17 and 23 should not be interrogated because this the ray is shadowed by facet number 23

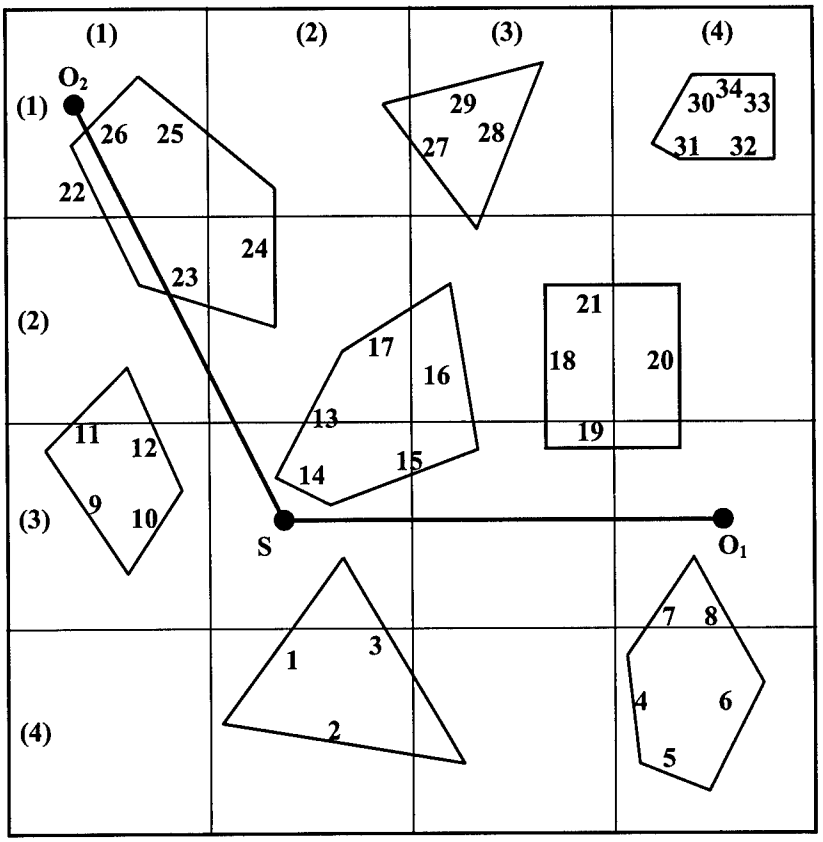


**Figure 4.** Example of ray tracing for two observation point.

The SVP algorithm is applied in the same way independently of the effect considered, because the source can be the transmitter antenna or a reflection, transmission or diffraction point and the observer can be an observation point or also a reflection, transmission or diffraction point. In this way the division in voxels is the same for all the effects. The only thing different is the number of paths to analyze: two if it is a simple effect, three if it is a double effect and so on. For example, for a reflection-diffraction, one starts from the transmitter antenna and questions the facets of all the voxels that the ray passes through until the reflection point is reached. Then the process is repeated from the reflection point to the diffraction point and finally from the diffraction point to the observation point. The SVP matrix only depends on the geometrical model not on the source position and the effect considered.

## 3.2. BINARY SPACE PARTITIONING (BSP).

The Binary Space Partitioning (BSP) [10] is a very effective technique, which takes into account the relationships between the facets of the model. For that, a BSP tree of the scene is generated: this is a binary tree, independent of the source and observer positions, which simplifies the number of facets to be interrogated to determine if the ray is or is not shadowed.

To generate the BSP tree of the model a facet of it is chosen as root and the space is divided in two regions: one formed by all the facets behind the root and the other by all which are in front of it. Each half-space will correspond with a tree branch. After that, the procedure is repeated for each branch, choosing any facet, dividing the space in two and forming other two tree branches. This procedure is repeated successively until only one facet hangs from each branch.

As an example, the BSP tree of the 2D scenario of Figure 5 is going to be generated. The procedure is the following: facet 1 is taken as root, so the plane which contains this facet, divides the space in two halves, which correspond with the tree branches. The half in front of facet 1 (according to the outward normal vector) will be on the left of the tree and the half behind on the right. The process is repeated for the facets 5 and 4 in such way that each one of the previous branches is divided again. Following the procedure recursively the binary tree is built. Figure 6 shows graphically the process.

Depending on the facet chosen, different trees of the same scene can be created. The algorithm efficiency will depend on the tree structure. The optimum tree is that which uses the least number of divided facets and tree levels. Figure 7 shows another example of BSP tree for the scenario of Figure 5. Although the number of tree levels is 5 as in the previous one, this is a better tree than the other, because it does not divide any facet. The minimum number of tree levels in a scenario is $\text{int}(\log_2 N) + 1$ where $N$ is the number of facets. In the example the minimum number of levels would be 4.

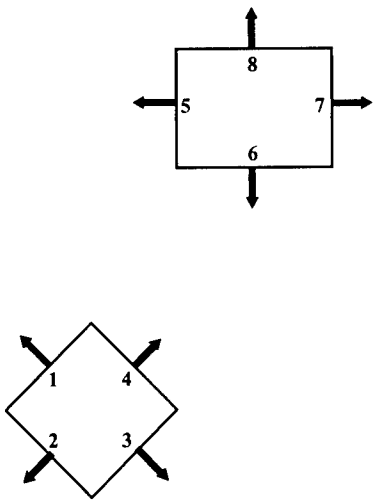


**Figure 5.** Scenario analysed.

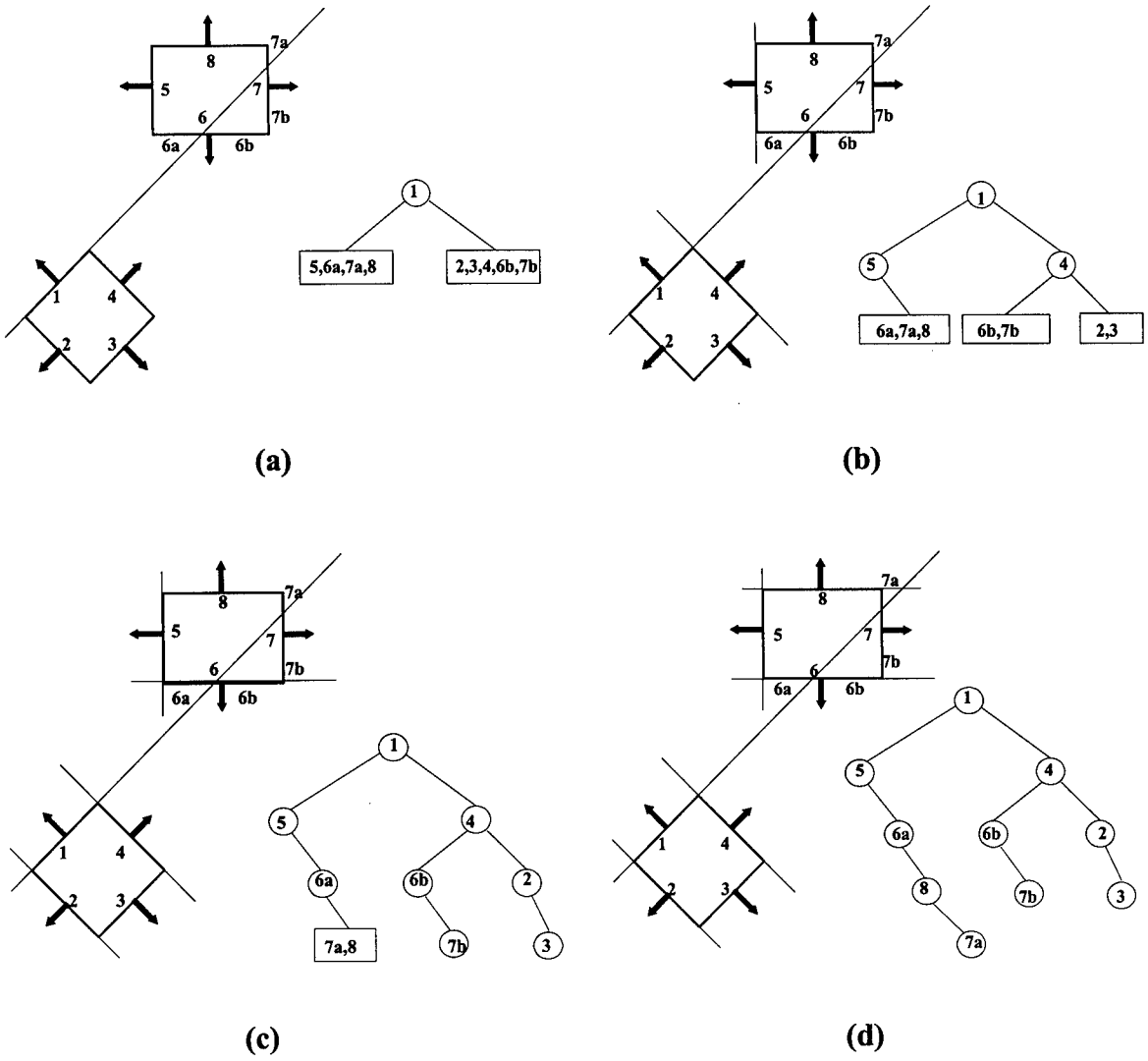


**Figure 6.** Binary tree generation.

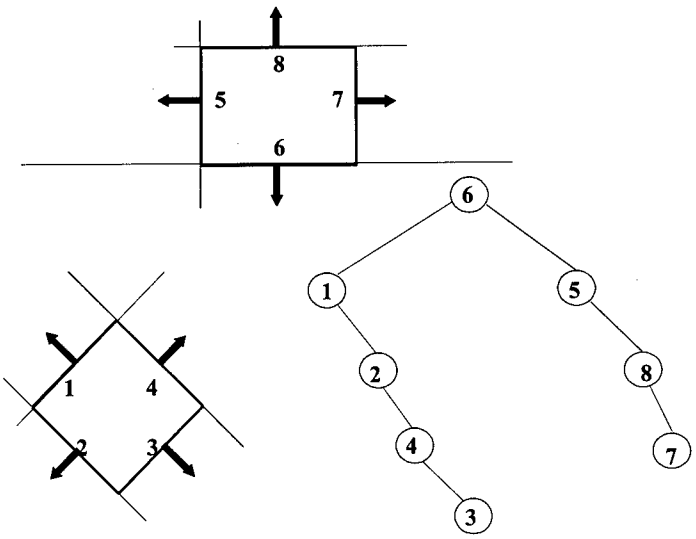


**Figure 7.** Binary tree from facet 6.

To interrogate the tree, one starts from the source to the observation point and there are three possible situations:

1) The source and the observation point are in front of the root facet: in this case the root facet and those which are behind it (right branch in the example) can not hide the ray.

2) The source and the observation point are behind the root facet: in this case the root facet and the facets which are in front of it (left branch in the example) can't hide the ray.

3) The source and the observation point are in different half-spaces: then the root facet can hide the ray and the intersection test must be done rigorously.

In cases 1 and 2 all the facets placed in a half-space of the model are discarded and the analysis must be continued for other branch of the tree.

As in the SVP algorithm, the BSP tree creation does not depend on the effect considered, only change the number of times that the tree must be questioned which will depend on the number of stretches of the ray, or, what is the same, on the effect is being treated.

## 3.3. THE ANGULAR ZETA BUFFER (AZB) ALGORITHM

The AZB technique has been developed by the authors. It is based on the Light Buffer technique [11] used for computer graphic design. The AZB has a lot of particular features that make it especially well suited for the UHF propagation problem, especially for the treatment of diffraction. The application of the algorithm is different for each coupling mechanism considered, as discussed in the following subsections.

### 3.3.1 Application to direct rays

For the direct ray case, the space is divided into spherical sectors from the source point called anxels. They are defined by the spherical coordinates theta ($\theta$) and phi ($\phi$) of a fixed coordinate system located on the source (see Figure 8).

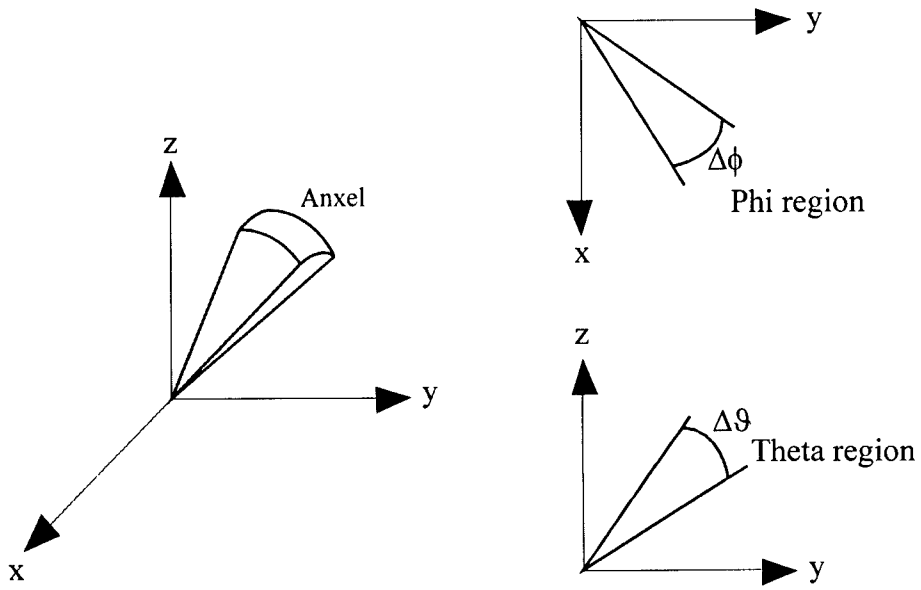


**Figure 8.** Anxel definition.

The anxel where each facet belongs is computed from the spherical coordinates of its vertices. Figure 9 shows a representation of the anxels in the $\theta\phi$ plane (AZB plane), with an example of facets that lie in each anxel

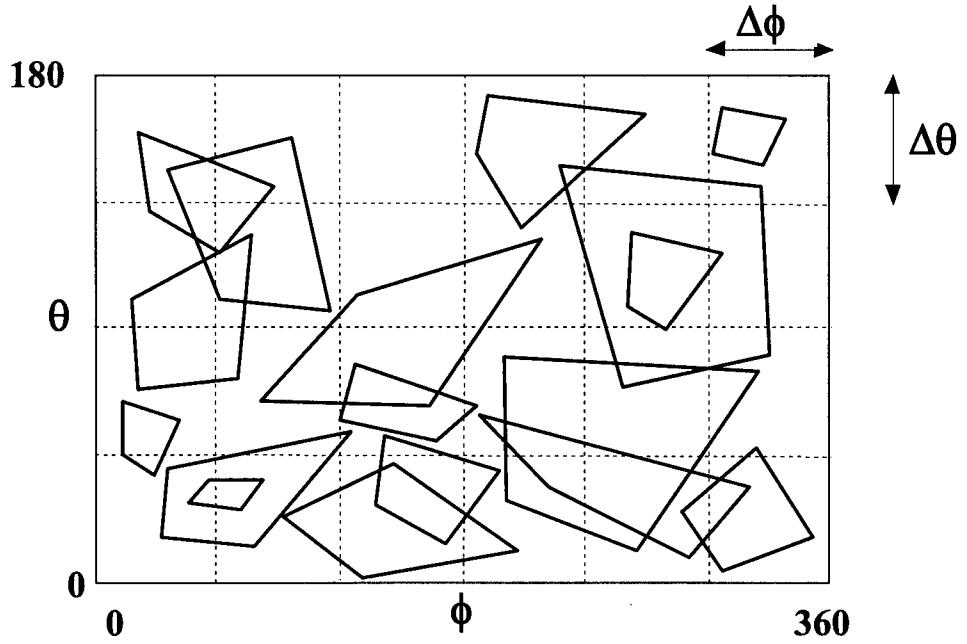


**Figure 9**. Facets' storage in the AZB plane.

This information is stored in the so-called AZB matrix. It depends, exclusively, on the source point and on the environmental model. For each anxel the facets are arranged according to the distance to S. As an example, Figure 10 shows the simple 2-D outdoor scene of Figure 3 where a space partitioning in 12 anxels has been accomplished. Table 2 shows the storage of the facets in the AZB matrix.

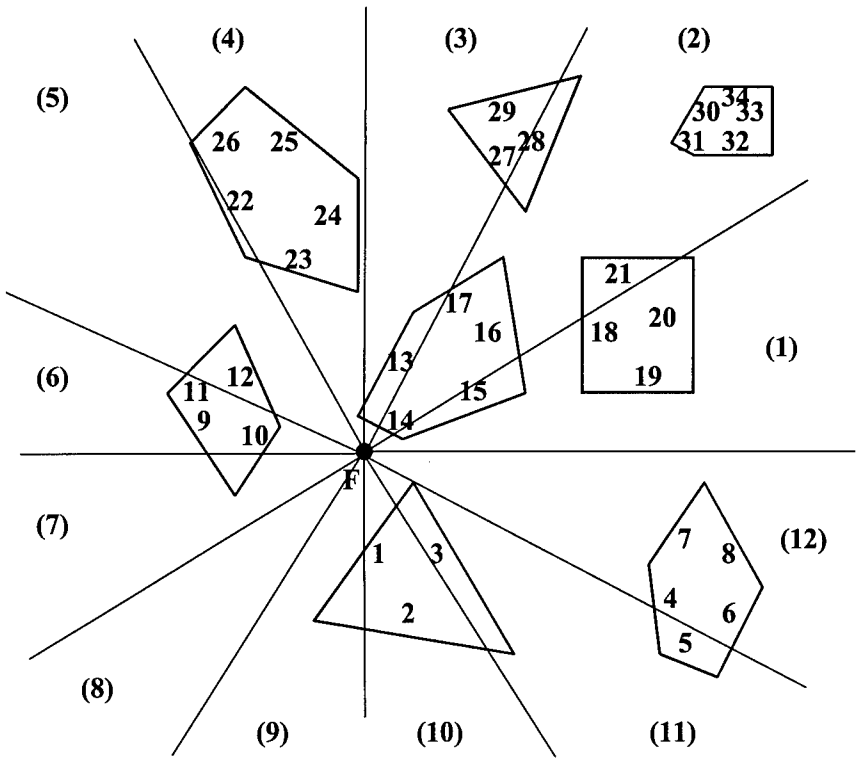


**Figure 10**. Example of a 2-D outdoor scene divided in 12 "anxels".

| Anxel | Facets |
|---|---|
| 1 | 14,15,16,18,19,20,21 |
| 2 | 14,16,17,27,28,18,21,31,32,30,33,34 |
| 3 | 14,13,17,27,29 |
| 4 | 14,13,23,24,25,26 |
| 5 | 12,11,23,22,26 |
| 6 | 10,12,9,11 |
| 7 | 10,9 |
| 8 | |
| 9 | 1,2 |
| 10 | 1,2 |
| 11 | 1,3,2,4,5,6 |
| 12 | 4,7,8,6 |

**Table 2.** Facets storage in the AZB of the scene of Figure 14

In outdoor scenes, only illuminated facets from the source are taken into account. To know if a facet is illuminated, the backface culling test is applied (see Figure 11) and the facets which are not illuminated are removed of the AZB matrix. For example, in anxel 1, facets 16, 20 and 21 can be removed. Also, there can be facets shadowed by others closer to the source (eclipse shadowing). All the facets totally shadowed are removed from the AZB matrix. For example in anxel 2 facets 18, 21, 27, 28, 31, 32, 30, 33 and 34 are totally shadowed by facet 14.

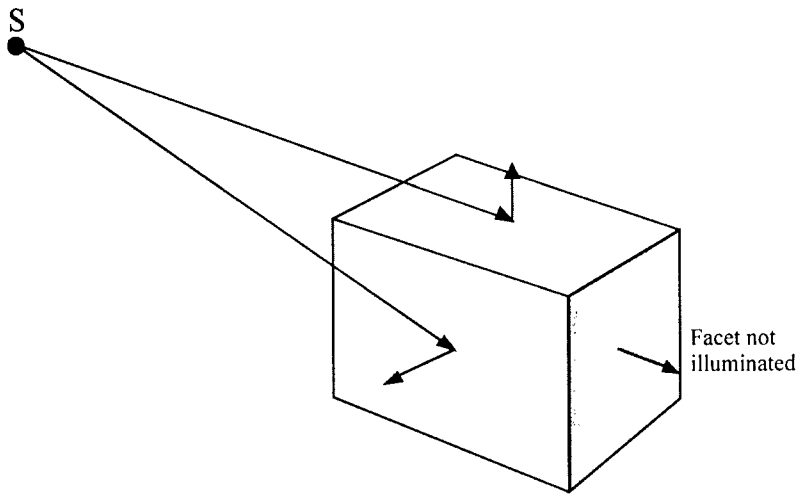


**Figure 11.** Application of the backface culling test.

To make the shadowing test for a given observation point (O), this is located in the corresponding anxel by means of their spherical coordinates. Then the facets placed in the anxel with distance to S less than the distance S-O are required. Figure 12 shows a case with two observation points. The point $O_1$ is in anxel 1 and only the facets 14, 15, 18 and 19 are interrogated, because the others are not illuminated. In this case any facet does not obstruct the ray. The point $O_2$ is in anxel 4, the intersection

test is made with facets 23 and 24 (the only ones illuminated in the anxel). It can be observed that the ray is shadowed by facet 23

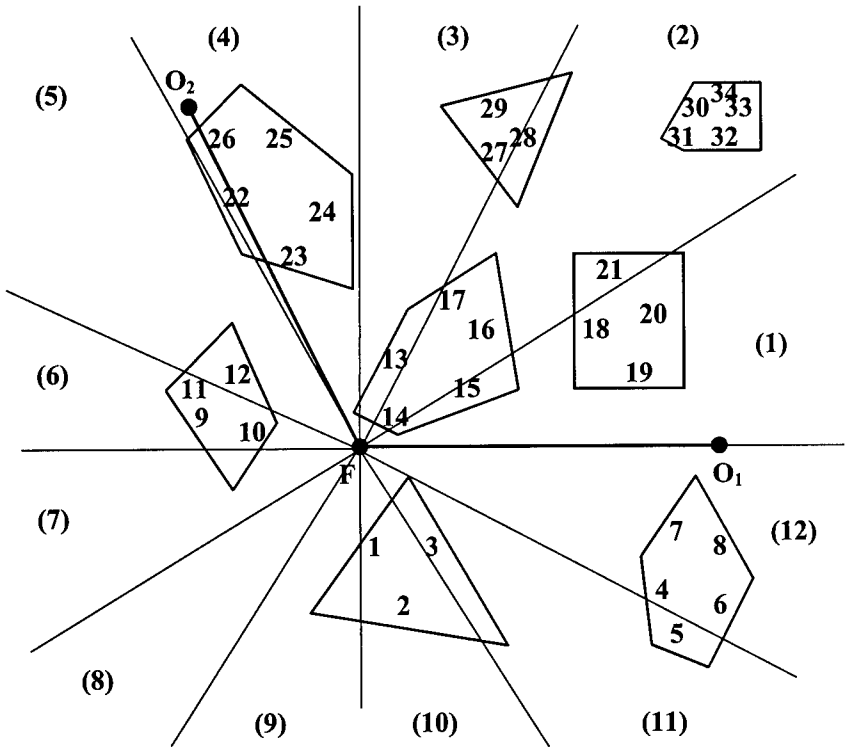


**Figure 12**. The shadowing test for two observation points.

The reduction in the number of facets tested decreases with the number of anxels, that is to say, it depends on the values of $\Delta\theta$ and $\Delta\phi$. On the other hand, the number of regions is limited by the memory size available.

### 3.3.2 Application to reflected rays

The algorithm application is similar to the direct ray case taking, in this case, as sources the images (I) of the transmitter antenna (S) with respect to the directly illuminated facets. It is taking into account that each image only radiates in the reflection space (RS) (see Figure 13). Therefore, the space to divide in anxels is limited by the highest and lowest values of the spherical coordinates ($\theta$, $\phi$) of the reflecting facet vertices.

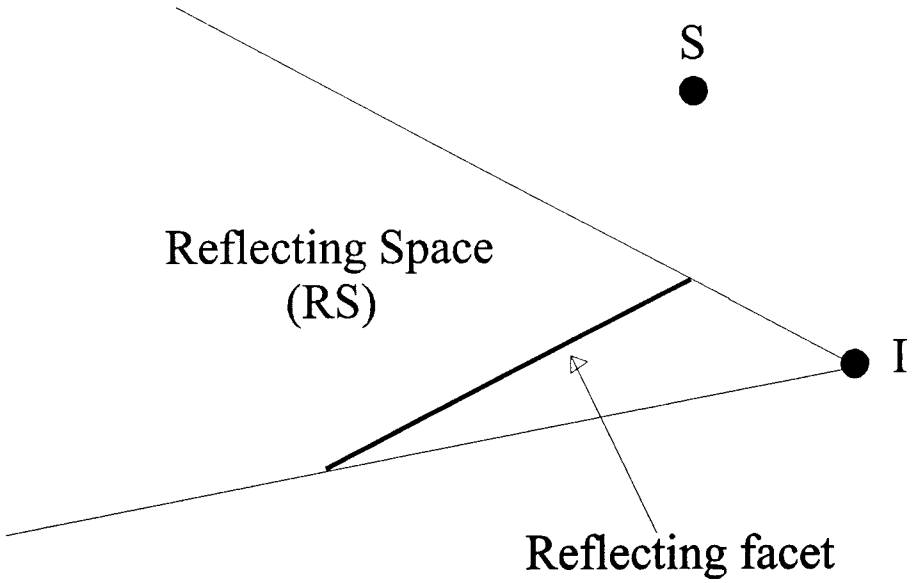


**Figure 13.** Reflection space (RS)

For the shadowing test, the first thing is to calculate if the observation point (O) is into the reflection space. If this condition is satisfied, it is found the anxel where this point is placed. Finally, the facets located on the anxel are tested orderly, following the same procedure as in the direct ray. The analysis of the incident ray (from S to the reflection point) is done using the AZB matrix of the direct field, taking the reflection point as the observation point.

### 3.3.3. Application to edge diffracted rays

Given a source (S) and an edge, the coordinates $\beta, \alpha$ are used instead of the spherical coordinates $\theta, \phi$. These coordinates are defined as follows: $\beta$ is the angle of the Keller's cone for a diffraction point and $\alpha$ is the angle formed by the diffracted ray and the first facet of the wedge (see Figure 14). So, the facet arrangement is accomplished in terms of these coordinates. For each source-edge pair the space where diffracted rays can exist is limited by the edge coordinates ( $\beta_{max}$ , $\beta_{min}$ , $\alpha_{max}$ , $\alpha_{min}$ ) which fix the margins of the so-called AZB rectangle of diffraction. This rectangle is divided into anxels.

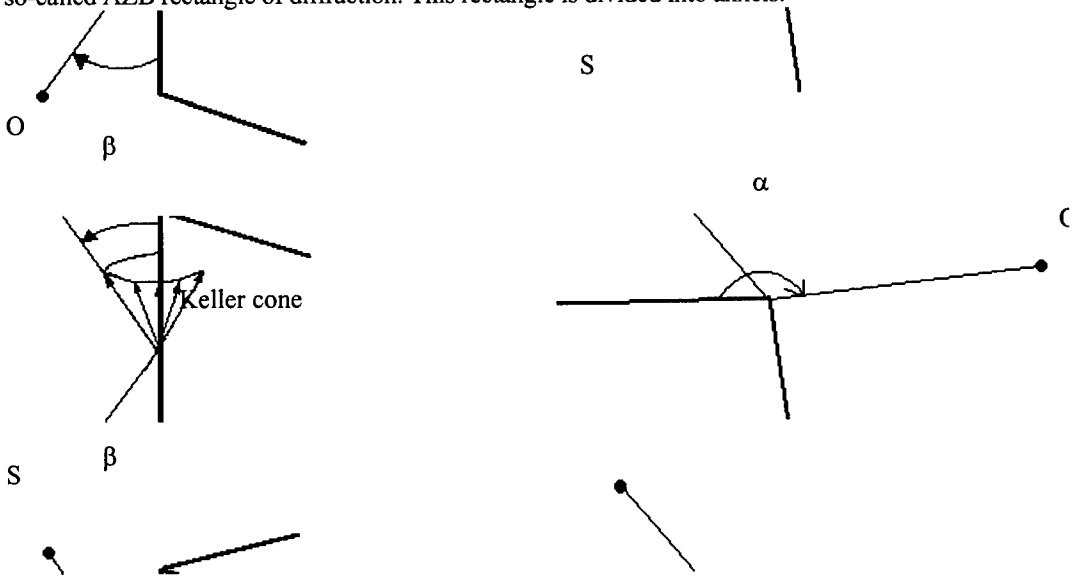


**Figure 14.** Definition of the β and α angular parameters for the AZB of edge-diffraction

The facets of the environment are located in the anxels of the AZB rectangle by means of the edge coordinates of their vertices. This information is stored in the so-called AZB matrix of diffraction. Given an edge and an observation point, its edge coordinates ( $\beta_o, \alpha_o$ ) are computed and, if they are into the rectangle margins, the anxel where the point lies is determined. Only the facets stored in the cell are considered in the test of the diffracted ray shadowing. If the diffracted ray is not hidden, the incident ray (source-diffraction point) is analyzed. To complete this task, the AZB matrix of the direct field is used, taking the diffraction point as the observation point.

### 3.3.4 Application to multiple effects

For multiple effects, the ray-tracing is made as a combination of the effects involved using the information of the corresponding AZB matrices. For instance, for reflection-diffraction, first the reflection and diffraction points are computed, and after this the intersection test for every path is made. For the diffraction the AZB matrices created from the edge are employed, for the reflection the AZB matrices of reflection are used, and, finally, for the incident ray the AZB matrices of direct ray are considered.

## 3.4. COMPARISON BETWEEN THE DIFFERENT ACCELERATION RAY-TRACING TECHNIQUES.

The BSP technique is very efficient for 2D scenes where making the BSP tree is relatively easy. However for 3D scenarios this task is more complex, it being difficult to find an optimum tree. Often, the trees are very long and with lots of broken facets, resulting trees which are not useful for efficient analysis.

The SVP method, for large scenes, needs a large number of voxels in order to load a low amount of facets per voxel. Also, when the source is far away from the observation point, the number of voxels that cross the ray is very high and, therefore, the amount of facets that are considered in the intersection test is enormous. In the example of Figure 3, it can be observed that the number of interrogated facets is, on average, less in the AZB method than in the SVP method.

The SVP method has the advantage of the memory size required, because it only needs a matrix that depends only on the scene, whereas the AZB technique has to make a matrix by source (antenna, image, edge, etc). For high order effects, when the number of sources is very large and the number of observation points involved in the effect is very low, it is not efficient to create the AZB matrices. In these cases the SVP method can be combined with the AZB.

The AZB technique has the advantage, with respect to the other methods, that it only load the facets not shadowed by illumination or by eclipse, because the space is divided taking the source as reference. This allows a reduction in the number of facets stored in each matrix.

## 4. RESULTS

In this section, validation of GTD/UTD approach using the AZB technique, is presented for two kinds of scenarios: an urban environment and an indoor environment.

For the urban environment, a Manhattan scenario has been analyzed, as shown in Figure 15. For this case, three paths along three streets have been simulated and compared with measurements [12]. In Figure 15 the antenna position and the three paths can be observed. Path 1 is along 51$^{st}$ Street (1200 m), path 2 is along Lexington Avenue (1300 m) and path 3 is along Third Avenue (1300 m).

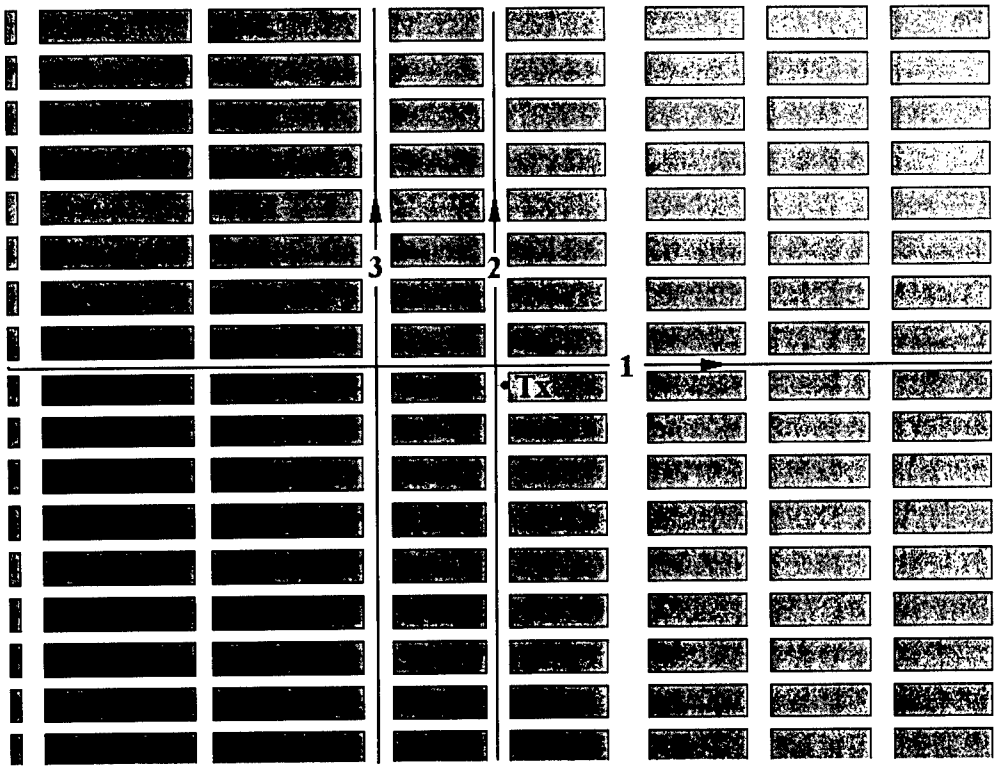


**Figure 15.** Plant view of Manhattan scenario with antenna position (Tx) and paths 1,2 and 3 analyzed (taken from [7]).

This scenario has been modeled with 680 facets and 1,888 edges. The electric properties of the facets are: $\varepsilon_r$=15, $\mu_r$=1, and $\sigma$=7 S/m. This environment has been simulated using a code called FASPRO, which has been developed by the authors. This code, based on GTD and on the AZB acceleration ray-tracing technique, allows analysis of propagation in outdoor environments. Prediction path loss results, compared with measurements, are shown in Figures 16 to 18. In the x-axis the distance in meters is represented, taking the source as reference. The mechanisms considered are first-order effects, second-order effects (except double diffractions), and third-order effects, which involve a ground reflection and do not involve more than one diffraction.

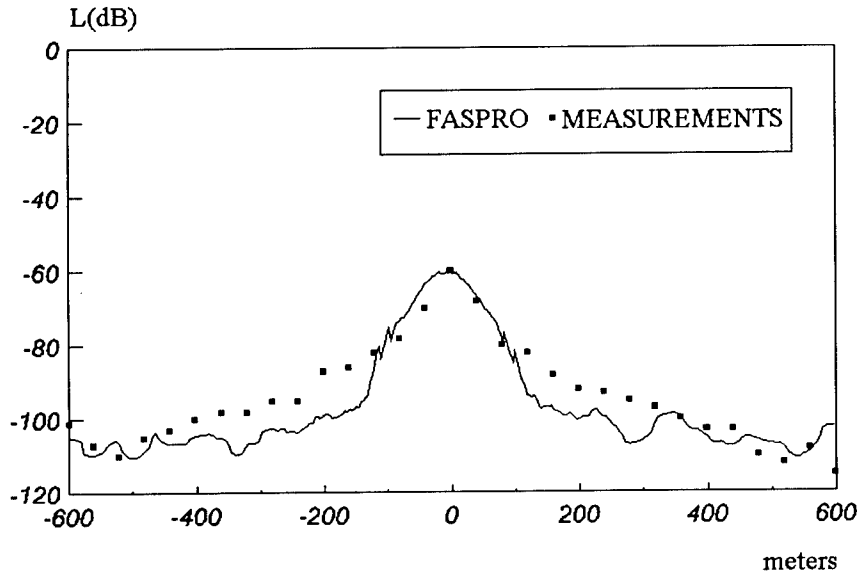


**Figure 16.** Comparison between measurements and computations of path 1 (taken from [7]).

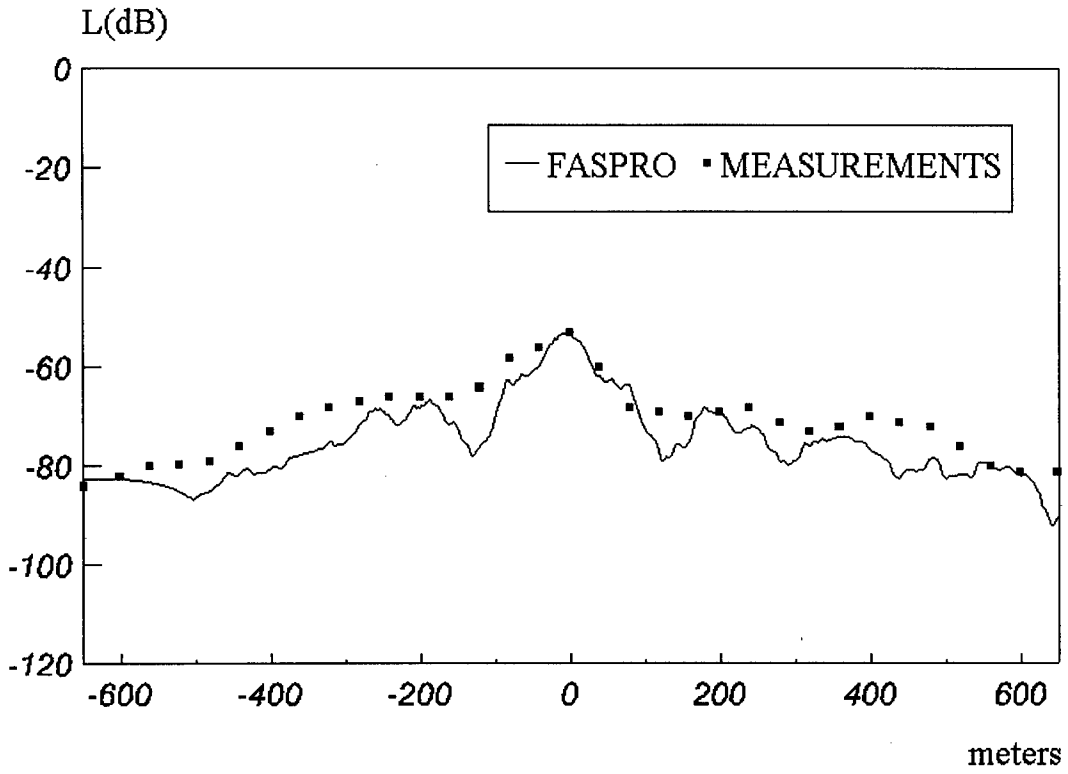


**Figure 17**. Comparison between measurements and computations of path 2 (taken from [7]).

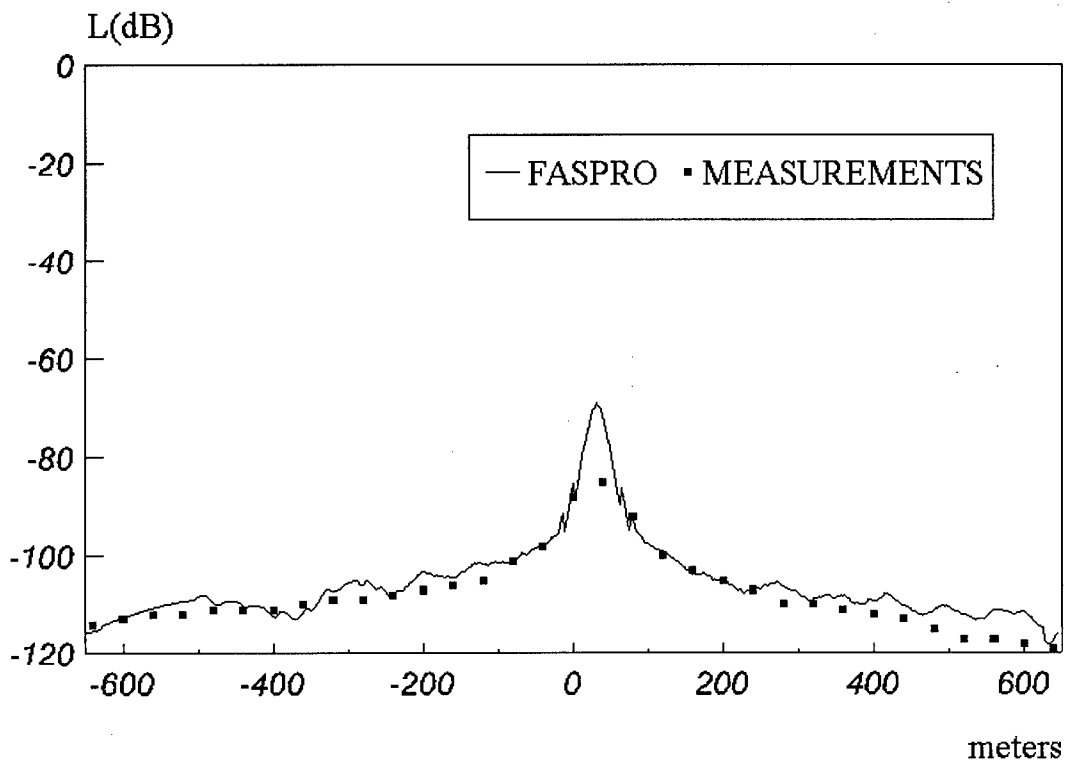


**Figure 18**. Comparison between measurements and computations of path 3 (taken from [7]).

It can be observed that the agreement between measurements and simulation results is good for engineering purposes. Table 3 shows the CPU time necessary to analyze each path on a Pentium 333 MHz with 128 MB of RAM. It can be seen the high efficiency of the method.

| Caption Path | Distance (m) | Number of points | Time |
|---|---|---|---|
| 1 | 1200 | 1200 | 5'44" |
| 2 | 1300 | 1300 | 5'58" |
| 3 | 1300 | 1300 | 6'01" |

**Table 3.** CPU time for the three paths in Manhattan.

For the indoor environment, the office scenario shown in Figure 19 has been analyzed. Measurements were made and compared with simulation results. A code, called FASPRI, which has also been developed by the authors, has been used for the simulation. This code is based on GTD and on the AZB acceleration ray-tracing technique and has been designed to analyze the indoor propagation. The antenna position and orientation and the paths analyzed are shown in Figure 19. In the first path the measurements were made at 48 points. The path length is 20.1 m. The second path is 28.3m long and the measurements were done at 74 points. Path 3 is 20.3 m long and the measurements were made at 48 points.

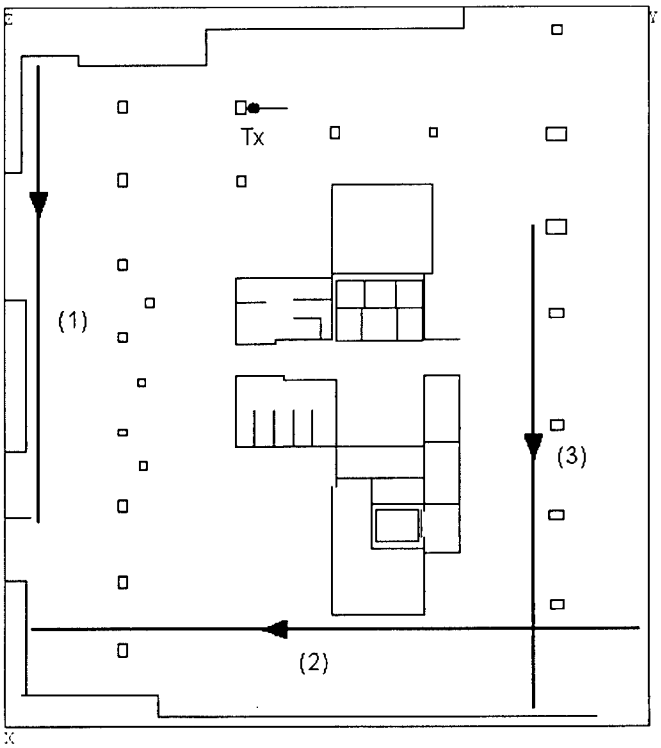


**Figure 19.** Plan view of the indoor scenario analyzed with the antenna position and the paths to simulate.

This scenario has been modeled with 175 facets. In the simulation all the facets have the same electric properties: $\varepsilon_r$=4.44, $\mu_r$=1.0, $\sigma$ =0,08 S/m and the same width: 0.1m. The mechanisms considered were: simple effects, double effects, triple reflections, third-order effects involving one, two or three

transmissions and fourth-order effects involving two, three or four transmissions. Predictions compared with measurements are shown in Figures 20 to 22 (paths 1 to 3).

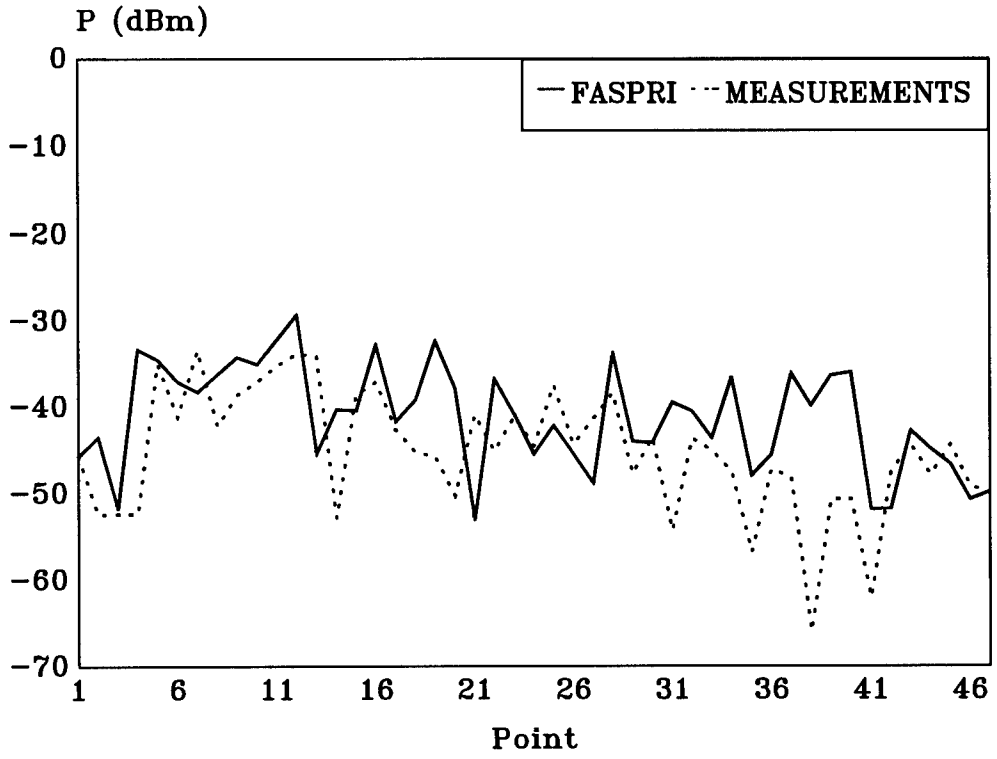


**Figure 20**. Comparison between measurements and computations of path 1

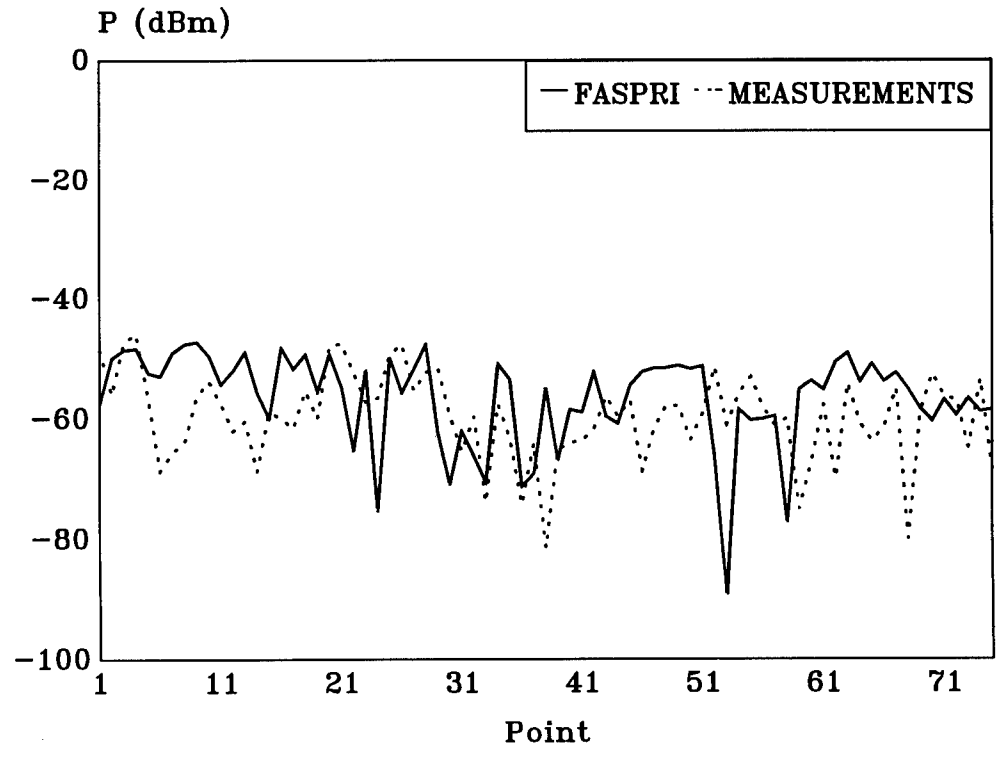


**Figure 21**. Comparison between measurements and computations of path 2

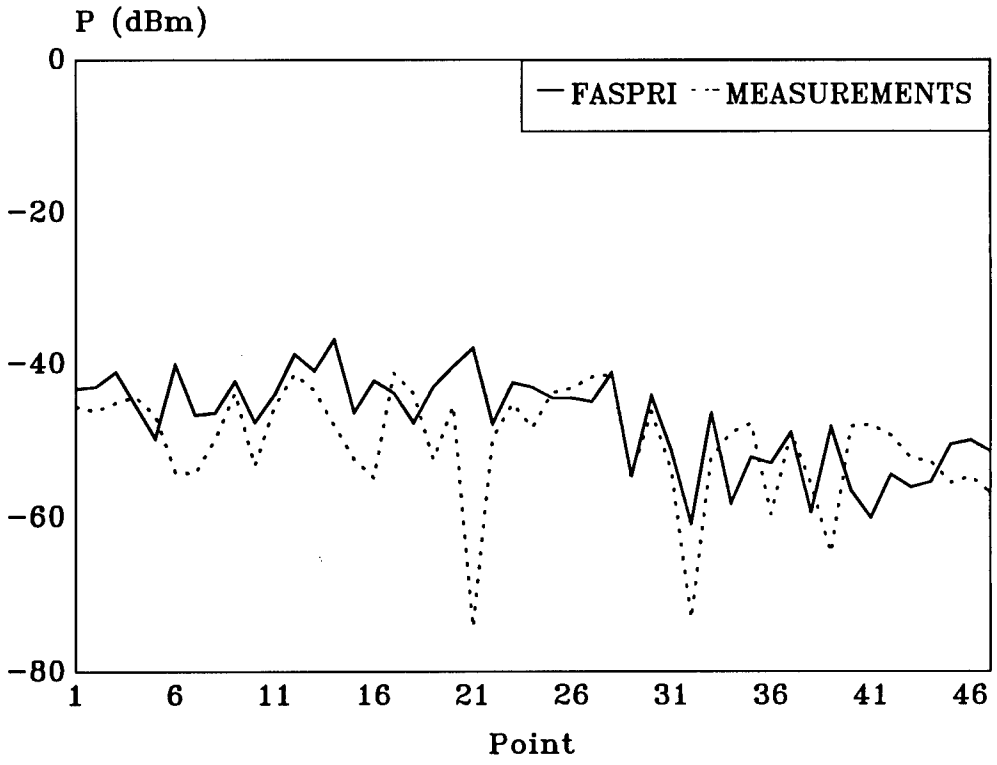


**Figure 22.** Comparison between measurements and computations of path 3

Other measurements were made with the same antenna placed on the ceiling pointing to the floor. Figure 23 shows the new antenna position and the paths analyzed. Path 4 is 25.7 m long and the measurements were made at 68 points, whereas path 5 is 14.8 m long and the measurements were made at 21 points. The same mechanisms were considered. Figures 24 (path 4) and 25 (path 5) show the comparison between these measurements and simulation results

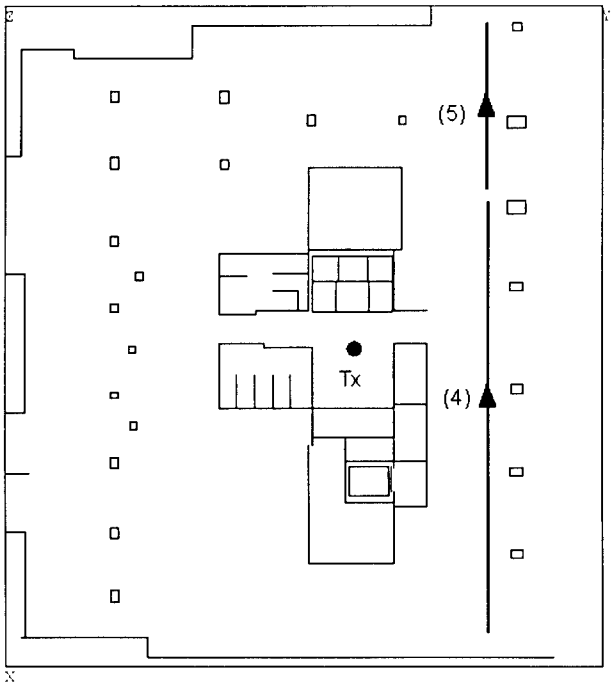


**Figure 23.** Plan view of the indoor scenario analyzed with the antenna position and the paths to simulate.

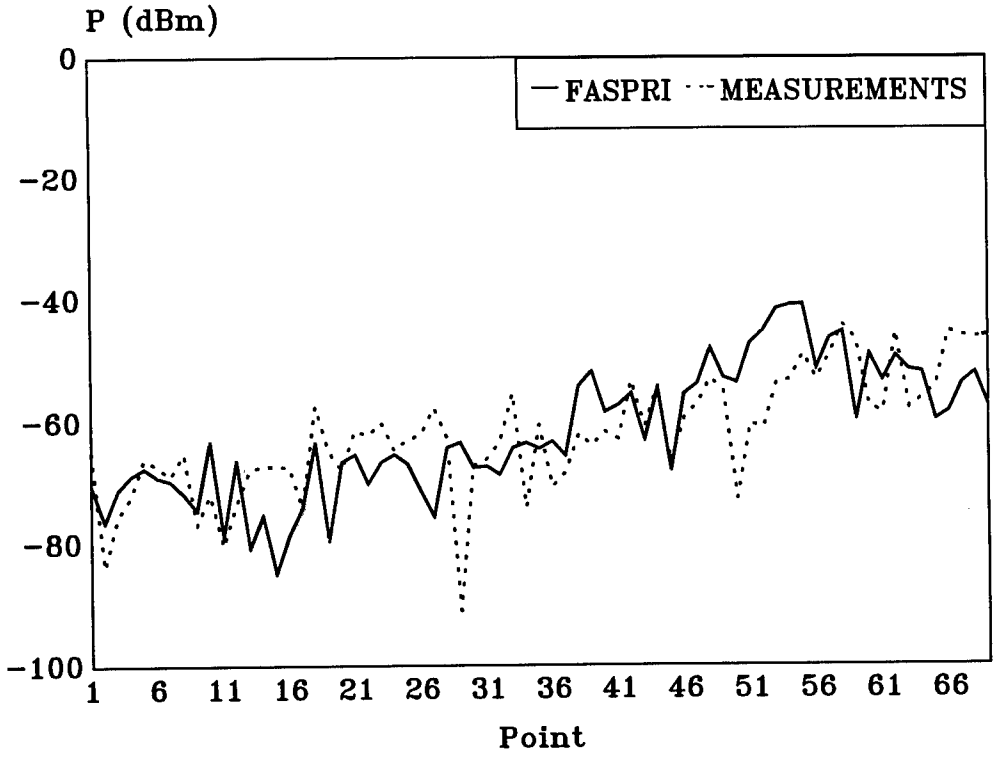


**Figure 24**. Comparison between measurements and computations of path 4

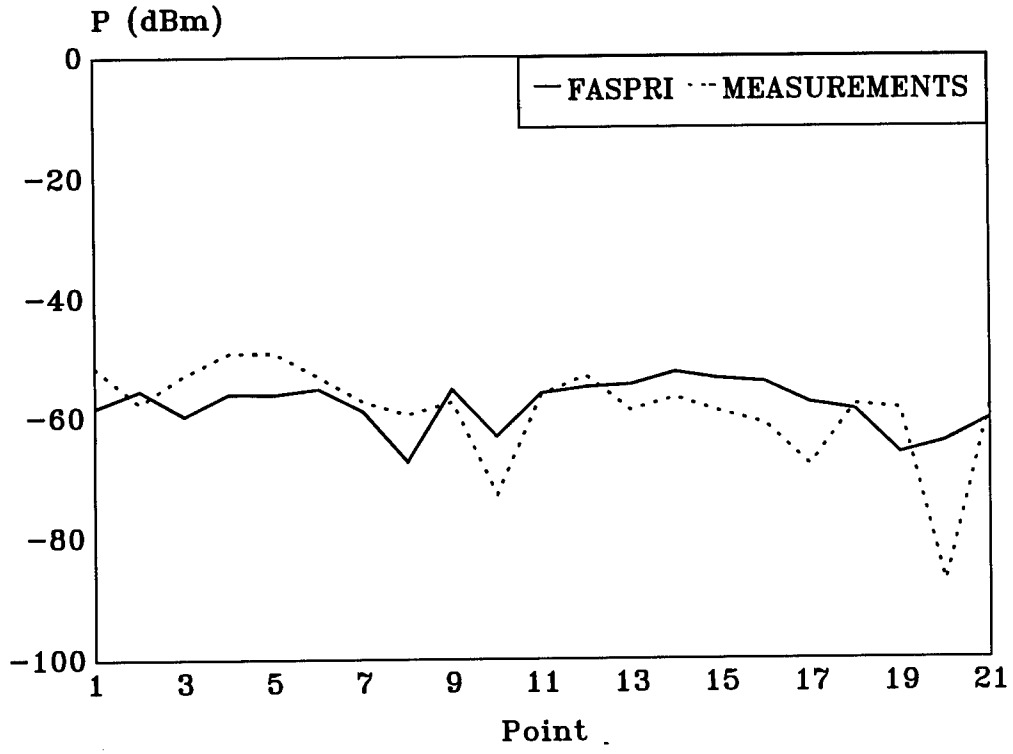


**Figure 25**. Comparison between measurements and computations of path 5

As in the outdoor case, predicted values are deemed reliable for engineering design. Table 4 shows the computation time necessary to obtain the results of each path in the same computer described above. It can be noticed that, on average, this method consumes 8" of CPU time for each point analyzed, what proves its efficiency.

| Caption Path | Distance (m) | Number of points | Time |
|---|---|---|---|
| 1 | 20.1 | 48 | 5'45'' |
| 2 | 34.7 | 74 | 9'34'' |
| 3 | 20.3 | 48 | 5'51'' |
| 4 | 25.7 | 68 | 8'42'' |
| 5 | 14.8 | 21 | 2'33'' |

**Table 4.** Computation time of the different paths in the indoor environment.

## 5. CONCLUSIONS

Some acceleration ray-tracing techniques have been presented for a propagation model based on GTD/UTD techniques for mobile communications. The Angular Z-Buffer method has been implemented, which allows the realization of the propagation model in a PC with low cost in time. This method has been validated with measurements for urban and indoor scenarios, obtaining good accuracy.

## 6. REFERENCES

[1] D. Parsons, *"The mobile Radio Propagation Channel"*, London, Pentech Press Limited, 1992

[2] Glassner, A. S. (Ed.) *" An Introduction to Ray Tracing"*, San Diego, CA: Academic Press, 1989.

[3] Foley, J. D., A. Van Dam, S. K. Feiner, and J. F. Hughes, *"Computer Graphics. Principles and Practice"*, 2nd ed., New York: Addison-Wesley, 1995.

[4] M. F. Cátedra, J. Pérez, F. Saez de Adana, and O. Gutiérrez *"Efficient Ray-Tracing Techniques for Three-Dimensional Analyses of Propagation in Mobile Communications: Application to Picocell and Microcell Scenarios"*, IEEE Antennas and Propagation Magazine, Volume 40, N° 2, April 1998, pp 15-28.

[5] M. F. Cátedra, J. Pérez, F. Saez de Adana, O. Gutiérrez, J. Cantalapiedra, I. González *"Fast Ray-Tracing Method for Calculating the Propagation in Indoor Environments"*, IEEE Antennas and Propagation Society Intenational Symposium, Atlanta, Georgia June 21-26, Volume 3, pp 1656-1659.

[6] Mc Namara, D. A., C. W. I. Pistorious, and J. A. G. Maherbe, *"Introduction to the Uniform Geometric Theory of Diffraction"*, Norwood, MA: Artech House, 1990.

[7] M. Felipe Cátedra, Jesús Pérez, *"Cell Planning for Wireless Communications"*, Artech House, 1999.

[8] C.A.Balanis. "Advanced Engineering Electromagnetics". John Wiley and Sons, 1989.

[9] Kouyoumjian, R. G., and P. H. Pathak, *"A Uniform Geometrical Theory of Diffraction for an Edge in a Perfectly Conducting Surface", Proc* IEEE, Volume 62, N° 11, Nov. 1974, pp 1448-1461.

[10] Fuchs, H., *"On Visibility Surface Generation by a priori Tree Structures,"*, Computer Graphics, Vol. 14, N° 3, July 1980, pp 124-133.

[11] Hines, E. A., and D. P. Greenberg, *"The Light Buffer: A Shadow-Testing Accelerator"*, IEEE Computer Graphics and Animation, September 1986, pp. 6-16.

[12] A.J.Rustako, N.Amitay, G.J.Owens, R.S.Roman. *"Radio propagation at microwave frequencies for line-of-sight microcellular mobile and personal communications"*. IEEE Transactions on Vehicular Technology, vol. 40, 1991, pp. 203-210.

# On the Feasibility of the Multipath Fingerprint Method for Location Finding in Urban Environments

Ivy Y. Kelly, Hai Deng and Hao Ling

Department of Electrical and Computer Engineering
The University of Texas at Austin
Austin, TX 78712-1084

**Abstract**

The feasibility of the multipath fingerprint method for wireless location finding in urban environments is examined using computational electromagnetics simulation. Fingerprints composed of time and angle of arrival data in urban environments are created using electromagnetic ray tracing. The fingerprints at specific locations within a simple four-by-four building model are studied to address issues including uniqueness of the fingerprints, repeatability due to environmental changes, and bandwidth limitations. A classifier based on template matching is also constructed using the simulation data from a 1-km city area of downtown Austin, Texas. Angle of Arrival (AOA) is found to be a stronger identifier than Time of Arrival (TOA). The classifier results demonstrate that good location-finding performance is achievable using both time of arrival and angle of arrival features.

## 1. Introduction

By October 2001, wireless callers to the emergency number 911 must be located within 125 meters of their actual positions, according to regulations contained in the Federal Communications Commission (FCC) Docket 94-102 [1, 2]. There are many other uses for wireless location finding including location-sensitive billing, intelligent transport systems (ITS), and electronic yellow pages [3 - 5]. However, the Docket 94-102 regulations have been the major impetus behind the strong recent interest in location finding.

The best-known location finding methods are GPS (Global Position System), AOA, and TDOA (Time Difference of Arrival). Each of these solutions has advantages and disadvantages. GPS is a handset solution (i.e., modifications are made to the handset) that is well-tested and very accurate except in urban canyons where one or more of the necessary satellites are blocked [4, 6]. AOA and TDOA are network solutions (i.e., modifications are needed at the base stations only) that require two or three base stations to identify a location [6]. However, a direct line of sight (LOS) signal is needed at all base stations to properly locate a caller. Similar to the GPS solution, urban environments pose a problem to these methods since LOS is very uncommon and the propagation channels are dominated by multipath.

One proposed method that can potentially work well in an urban setting is the multipath fingerprint method [7]. It is a network-based solution that actually takes advantage of the multipath information in the incoming signal to identify the location of the mobile user. It does not require a LOS signal and only uses one base station. The basic idea of the method is to extract the features of the multipath signals contained in the incoming call, including the parameters of angle of arrival ($\theta$), time delay ($\tau$), and signal strength ($\gamma$). The bandwidth of the incoming signal is used to extract time delay. Angle of arrival is extracted by using an antenna array at the base station. The three parameters from all the multipath components of the signal are used to create a fingerprint that is compared to a database of fingerprints previously cataloged. Each fingerprint in the database corresponds to a known location. Thus, when a matching fingerprint is found in the database, the correct location is found as well (Figure 1).

In this paper, we carry out a study to examine the feasibility of the multipath fingerprint method. The data for our study is based on channel data simulated by applying electromagnetic ray tracing to urban CAD models [8]. The ray-based simulation allows us to accurately extract the required parameters and to pinpoint the cause-and-

effect between the physical propagation mechanisms and the resulting features. We study the fingerprints in the database at specific locations within the urban environment to address issues including the uniqueness of the fingerprints, repeatability due to environmental changes, and bandwidth limitations. In addition, we construct a classifier based on template matching using the simulation data from a 1-km city area to more closely investigate the location-finding performance of the fingerprinting approach.

This paper is organized as follows. Section 2 describes the ray tracing simulation used to generate the channel data and the methodology used to construct the simulation database. Section 3 describes results and findings from a simple four-by-four building model. In Section 4, we construct a classifier based on the simulation results generated using a CAD model of downtown Austin, Texas and evaluate the performance of the multipath fingerprint scheme. Discussions and conclusions are given in Section 5.

## 2. Ray Tracing Simulation for Fingerprint Generation

We first generate the necessary channel data for this study using a code called CPATCH, which is an electromagnetic ray tracer designed for telecommunications applications [9]. It calculates the coupling between transmitting and receiving antennas in a complex environment by using the shooting and bouncing ray (SBR) technique [10, 11]. Rays are shot in all angular directions from the transmitter location and traced according to the laws of geometrical optics as they bounce around in a CAD model description of the environment. The phase of the field along each ray is calculated by tracking the total distance traveled by the ray as well as the phase change due to reflections. The amplitude is computed by taking into consideration the antenna pattern, the divergence of the ray tube, field polarization and the materials used in the model. The field at the receiving antenna is then computed by summing the contributions from all the ray tubes that illuminate the receiver location.

In actual implementation, a grid of receiver locations is first defined and each receiver location is updated as each ray is traced. Since only the receiver points within the ray tube are updated for each ray, the total computation time is essentially independent of the number of receiver points. The majority of the computation time is the ray tracing time. For a CAD model of an $8 \times 10$ block area of a city containing over 21,000 triangular facets, the simulation time is less than 10 minutes on a typical workstation. Channel characteristics simulated using this approach have been compared against measurement data in Austin, Texas and the results showed fairly good agreement between simulation and measurement [12].

The CPATCH methodology described above is well suited for calculating the channel data from a fixed transmitter to a large number of receiver locations. However, the problem at hand is to simulate the multipath fingerprints from handset transmission at multiple locations to a fixed base station receiver. In order to effectively simulate the fingerprint data needed in this study, we invoke reciprocity [13]. We first perform ray tracing from the base station assuming it is the transmitter. For each handset location, we find all the rays that contribute to that particular location. Then based on reciprocity, we assume those rays are also the ones that will reach the base station receiver if the handset is used as the transmitter. Next, the parameters needed to form a fingerprint are readily extracted from the information for each ray. The time of arrival is directly proportional to the total disance travel by the ray. The signal strength is proportional to the field strength of the ray. The angle of arrival at the base station is obtained from the ray direction with respect to the base station. Therefore, using only a one-time ray trace, we can obtain the needed multipath fingerprint information for all possible handset locations.

## 3. Phenomenology Study of a Simple Model

We first investigate the characteristic features of the fingerprints using a simple model consisting of 16 buildings in a symmetrical four-by-four arrangement. The center frequency is chosen at 1.0 GHz. The buildings are identical with 30 meters in height, width, and length, and are placed 30 meters apart on a square grid (Figure 2a). All surfaces are assumed to be perfectly conducting. A base station antenna is placed in the middle of the model at a height of 15 meters above ground. Fingerprints are examined for each 30-meters-by-30-meters sector, located between each of the buildings (Figure 2b). To form the fingerprints within each sector, we collect 9 fingerprints from 9 mobile locations, each 10 meters apart. Fingerprints are formed from the angle of arrival, time delay, and signal strength data as calculated by CPATCH. The individual fingerprints from each of the 9 mobile locations are summed to form a fingerprint template (called Mx) for that sector. Data for a total of 65 sectors are generated.

Figure 3 shows the fingerprint templates from Sectors 5, 12, 19, and 26, which make up half of a typical LOS street. Each template on a LOS street has a unique feature, an arc from the LOS rays. The arc is centered around 90° in each of the four fingerprint templates shown. The arc gets narrower and is located at a larger time of arrival (TOA) as the location of the sector gets farther from the base station. Although not shown, the arc is shifted by 180° on the other side of the base station on the same street. In fact, it is found that angle of arrival (AOA) is the main distinguishing feature between different quadrants of the model. Although the model is perfectly symmetrical, each of the four quadrants has features that are 90° shifted from the quadrant next to it.

The fingerprint templates from Sectors 3, 11, 17, and 25 are shown in Figure 4. These sectors make up half of the street immediately parallel to the LOS street from Figure 3. Sector 3 is the farthest from the base station. Each of the three most prominent features in Sector 3 can be seen in the other three sectors at the same AOA. The TOA, of course, decreases as the location of the sector gets closer to the base station. Finally, fingerprint templates from Sectors 1, 10, 15 and 24 (i.e., the street parallel to the previous two streets and farthest from the base station) have fewer features. This is due to the limitation of the simulation, as we have chosen to terminate the ray tracing for any ray that exceeds 5 bounces. For this reason, the outermost sectors have few features. In a larger environment (e.g. Austin, TX, which will be studied next), more bounces are included in the calculations to provide features in sectors farther from the base station.

In order to examine the uniqueness of the fingerprints at different locations in this model, we calculate the correlation coefficient between the fingerprint templates from different sectors. For this calculation, we assume that the AOA is known on an absolute angular scale, while the time origin of the TOA is not known. In practice, the AOA will be extracted from an antenna array at the base station. Therefore, it is reasonable to assume that absolute AOA can be determined (e.g., using a circular array). However, the time origin of the TOA will not in general be known since the handset and base station are not synchronized with the precise time of call origination. We implement the correlation calculation using a one-dimensional Fourier transform along the TOA axis and use the peak value to give a measure of how well one fingerprint correlates with another.

Figure 5a shows the correlation coefficient matrix for each fingerprint template with every other fingerprint template in the database. The correlation coefficient is normalized to take on a value between zero and one. The diagonal values of the correlation coefficient matrix are '1', since each fingerprint correlates perfectly with itself. The off-diagonal terms represent the possible confusion amongst the fingerprints. Figure 5b shows the center 9x9 portion of the correlation matrix that corresponds to Sectors 29-37 along the horizontal LOS street. The block-diagonal structure can be understood since the templates along each side of the LOS street share the same arc feature shown in Figure 3a. Since the features on opposite sides of the LOS street are 180° off from each other, fingerprints on the same side of the street have a stronger correlation. The TOA information becomes the main distinguishing features in the templates for these sectors. Figure 5c shows the portion of the correlation matrix that corresponds to Sectors 15-23 along the next parallel street. The fingerprints farthest from the base station are most highly correlated since they contain the least amount of features and those features have similar AOA.

Next, we study the effect of finite frequency bandwidth and array size on the correlation matrix. Contrary to the present simulation data, there are resolution limits due to frequency bandwidth and array size on how well the fingerprint features can be extracted in practice. The smaller the frequency bandwidth and the array size, the more difficult it is to resolve the TOA and AOA. Figure 6a is the correlation coefficient matrix of ten of the sectors (Sectors 34, 35, 36, 37, 41, 48, 49, 50, 51 and 55) in the lower right quadrant formed from the original simulation data. These ten fingerprint templates are low-pass filtered to correspond to a frequency bandwidth of 2.9MHz and an array size of 0.6m. Figure 6b is the correlation coefficient matrix of these ten templates after the low pass. As expected, the cross correlation levels increase, making the correct identification of fingerprints more difficult.

Finally, we consider the fluctuation of the fingerprints due to changes in the environment. For this study, we examine the fingerprints with the addition of cars on the streets. The car CAD model is designed with specifications from a Ford Mustang Coupe and a Ford Escort Sedan [14]. Sixty-five fingerprint templates are created in the four-by-four model in the same locations as before, but by including 190 cars in the lower right-hand quadrant. The cars are placed in Sectors 34, 36, 41, 42, 48, 50, 55, and 56 to simulate parked cars along the buildings as well as traffic in the streets (Figure 7). A new set of correlation coefficients is calculated by comparing the new fingerprint templates with cars to the original template database without cars. Figures 8a to 8c show three examples of this comparison between the new correlation and the original correlation values for Sectors 34, 41 and

48, respectively. The dotted line is the new correlation between the fingerprint template with cars and the 65 original fingerprint templates without cars. The solid line shows the original correlation values with no cars. These three sectors (34, 41 and 48) contain the most noticeable differences in the correlation coefficients. As can be seen, the addition of traffic causes very little change in the correlation.

## 4. Classifying Results in an Urban Setting

To more directly investigate the location-finding performance of the multipath fingerprint approach, we construct a classifier based on template matching by using the simulation data at 1.0 GHz from a 1-km city area. We set out to determine the probability of correctly identifying the unknown handset location using its AOA-TOA fingerprint, when a database of known fingerprints is available. The urban area examined is based on a CAD model of the city of Austin, Texas, obtained from a local architectural firm (Figure 9). This model is significantly more complex than the four-by-four model studied in the last section. Since the requirement for wireless E-911 location finding is 125 meters, the downtown area is first divided into 7x8=56 sectors, as shown in Figure 10. Each sector is a square of size 125 m x 125 m. The base station is located at the intersection of Congress Avenue and 7$^{th}$ Street, in Sector 25. Fingerprints are calculated using CPATCH at multiple handset locations on the streets within each sector. On average, there are about 180 such locations within each sector. We denote each sample fingerprint by a 2-D intensity image, $R_k(m,n)$, where $m$ is the TOA index and $n$ is the AOA index. The resolution interval in the TOA dimension is chosen to be 800ns. This corresponds to a frequency bandwidth of 1.25 MHz, which is typical of a channel in a CDMA system. The resolution interval in the AOA dimension is chosen to be 5°. This corresponds to an array of dimension 12 wavelengths. The size of the resulting fingerprint images is 100×72.

We randomly choose $L$=40 locations in a sector and form a template for the classification database by averaging the individual fingerprints. The template for sector $j$ is constructed simply as an average of the individual fingerprints:

$$T_j(m,n) = \frac{1}{L}\sum_{k\in j} R_k(m,n) \tag{1}$$

Next, we define the match score between an individual fingerprint image $R(m,n)$, and the template for sector $j$, $T_j(m,n)$. Since the received signal amplitude changes dramatically with propagation distance, a correlation score is chosen instead of the mean squared error criterion. Our match score definition is [15-17]:

$$\text{Match Score}_j = \max_p \frac{\sum_m \sum_n R^l(m,n) T_j^l(p-m,-n)}{\sqrt{\sum_m \sum_n R^{2l}(m,n) \sum_m \sum_n T_j^{2l}(p-m,-n)}} \tag{2}$$

This match score is normalized by the signal energy so that it takes on values between zero and one. As has been discussed in the last section, the correlation process is only carried out in the TOA dimension due to the lack of a time reference. Note also that we apply a power transform (where $l$ is the power transform parameter) to both the individual fingerprint and the template. Usually we choose $l$ to be a small number (0.02) to emphasize the weaker features that might be important in the matching process.

With the templates computed using in (1) and the correlation match score defined in (2), we set out to find the correct location-finding probability, $P_{lf}$, for the fingerprints generated in each sector. We experimentally determine $P_{lf}$ for each sector by feeding a large number of test fingerprints to the template-matching process in (2). For each fingerprint tested, the sector with the highest match score is identified as the location of the handset. The forced decision rule is used, i.e., the sector with the highest match score is chosen no matter how low the score. Finally, after all the test fingerprints have been identified, we tally up the number of correct identifications relative to the total number of test fingerprints to arrive at $P_{lf}$.

Table 1 shows the results of the location finding for all 56 sectors in the downtown Austin area. Each block in the table denotes a sector. The first number is the index of the sector. The second number is the correct sector location-finding probability ($P_{lf}$). We observe that for most of the sectors, $P_{lf}$ is greater than 70%. The

average $P_{lf}$ for all sectors is 76%. However, for a few sectors it is below 30% (Sectors 48, 51, 55). Closer examination of the fingerprints in these sectors reveals that either there are fewer features within these sectors, or the features are similar to the adjacent sectors. We also compute the probability of successfully identifying either the correct sector or the sectors immediately adjacent to the correct sector. For those interior sectors, this includes 8 adjacent sectors. For the border sectors, this includes either 5 or 3 (corners) adjacent sectors. This probability, $P_{alf}$, is shown as the third number in each sector in Table 1. We observe that $P_{alf}$ is in general much higher than $P_{lf}$, especially for those sectors where $P_{lf}$ is low. The average $P_{alf}$ is found to be 92%. Therefore, when misidentifications occur in the classification process, the fingerprint locations tend to be misidentified in an adjacent sector. In practice, this is certainly not as detrimental as when the handset location is misidentified in a sector very far away from its true location.

Next we investigate the relative importance of the AOA features and the TOA features. Table 2 shows the correct location finding probabilities obtained using AOA information only. For AOA-only processing, the 1-D fingerprints are matched against the 1-D templates, with the same set of parameters as the 2-D processing. The average probabilities of correct identification are found to be $P_{lf}$ = 60% and $P_{alf}$ = 80%. Table 3 shows the correct location finding probabilities obtained using TOA information only. In this case, a 1-D correlation operation with time-shift is applied in the matching process. The average probabilities of correct identification are found to be $P_{lf}$ = 24% and $P_{alf}$ = 40%. Clearly, due to the lack of a time reference, the performance of the TOA-only classifier is much worse than that of the AOA-only classifier. The 2-D fingerprint processing results are significantly improved compared with 1-D processing results in either case.

Lastly, we consider the effect of inaccuracies in the AOA and TOA positions on the performance of location finding. While in this simulation study we have assumed that the fingerprint features are readily available, in the actual implementation, the 2-D features must be extracted from the incoming handset signal prior to the classification process. The accuracy with which the AOA and TOA positions can be extracted from the incoming handset signal depends on, respectively, the size of the base station array and the frequency bandwidth of the signal. We simulate the inaccuracies by adding Gaussian jitters with standard deviation of one fourth of the resolution cell to the AOA and TOA positions of the individual test fingerprints. The templates in the database remain unperturbed. Table 4 shows the performance of the 2-D fingerprint classifier with corrupted features. The average probabilities of correct identification are found to be $P_{lf}$ = 71% and $P_{alf}$ = 88%. Compared to the results from Table 1 ($P_{lf}$ = 76% and $P_{alf}$ = 92%), the performance of the corrupted data is only slightly worse than that of the uncorrupted data. This implies that the needed accuracy for the feature extraction algorithm should be on the order of one-half the Fourier resolution. This appears to be within the reach of parameter estimation algorithms such as MUSIC.

## 5. Conclusions

In this paper, we have applied computational electromagnetics simulation to examine the feasibility of the multipath fingerprint method as a wireless location-finding tool in urban areas. The electromagnetics simulation was carried out using ray tracing, which allowed us to accurately extract the time of arrival and angle of arrival features used to form the fingerprints. Results from a four-by-four building model showed that fingerprints are quite unique at various locations even in such a highly symmetrical environment. Repeatability was examined by simulating traffic in the simple model. Bandwidth effects were studied to show the effect due to frequency bandwidth and finite array size. In addition, we have constructed a classifier based on template matching using the simulation data from a 1-km city area of downtown Austin, Texas to more directly investigate the location-finding performance of the fingerprinting approach. AOA was shown to be a stronger identifier than TOA. The classifier results demonstrated that good location finding performance is achievable using both AOA and TOA features. Also studied was the effect of errors in the AOA and TOA features on the classifier performance. We believe that the main challenge in the implementation of such a system is how to reliably and accurately extract the AOA and TOA features from noisy, band-limited data.

## 6. Acknowledgments

The authors would like to thank Drs. Arthur Giordano and Samuel Rescheff, and the Wireless Access Technologies Department in the Network Infrastructure Lab at GTE Laboratories, Inc. for their support and assistance in this research. The authors would also like to thank SAIC-Demaco of Champaign, IL for supplying the

CPATCH code used in this study. This work is supported in part by the Texas Higher Education Coordinating Board under the Texas Advanced Technology Program.

## 7. References

[1] "FCC Adopts Rules to Implement Enhanced 911 for Wireless Service," FCC News, CC docket no. 94-102, June 12, 1996

[2] FCC Docket 94-102, "Report and Order and Further Notice of Proposed Rulemaking in the Matter of Revision of the Commission's Rules to Ensure Compatibility with Enhanced 911 Emergency Calling Systems," stated June 12, 1996; published July 26, 1996.

[3] C. Drane, M. Macnaughtan and C. Scott, "Positioning GSM Telephones," *IEEE Communications Magazine,* vol. 36, no. 4, pp. 46-59, Apr. 1998.

[4] M. Licht, "Tracking Emergency Calls," WB&T, p 29-30, Apr. 1998.

[5] J.Caffery, Jr. and G. Stuber, "Overview of Radiolocation in CDMA Cellular Systems," *IEEE Communications Magazine,* vol. 36, no. 4, pp. 38-45, Apr. 1998.

[6] J. Reed, K. Krizman, B. Worener and T. Rappaport, "An Overview of the Challenges and Progress in Meeting the E-911 Requirement for Location Service," *IEEE Communications Magazine,* vol. 36, no. 4, pp. 30-37, Apr. 1998.

[7] M.Wax and A. Leshem, "Joint Estimation of Time Delays and Directions of Arrival of Multiple Reflections of a Known Signal," *IEEE Transactions on Signal Processing*, vol. 45, no. 10, p. 2477-2484, Oct. 1997.

[8] I.Y. Kelly, H. Ling, and W.J. Vogel, "Urban Channel Propagation Modeling Using the Shooting and Bouncing Ray Technique," to appear in *Microwave and Optical Technology Letters*, Mar. 2000.

[9] S.W. Lee, J.E. Baldauf and R. A. Kipp, "CPATCH: Antenna Coupling in Complex Environments," DEMACO Tech. Rep., Champaign, IL, Oct. 1994.

[10] H. Ling, R. Chou and S.W. Lee, "Shooting and Bouncing Rays: Calculating the RCS of an Arbitrarily Shaped Cavity," *IEEE Transactions on Antennas and Propagation*, vol. 37, no. 2, pp. 194-205, Feb. 1989.

[11] S.W. Lee, H. Ling and R. Chou, "Ray-Tube Integration in Shooting and Bouncing Ray Method," *Microwave and Optical Technology Letters*, vol. 1, no. 8, pp. 286-289, Oct. 1988.

[12] G. Benavides, "A Fast Algorithm to Calculate Channel Characteristics of an Urban Environment," masters thesis, University of Texas at Austin, Austin, TX, 1998.

[13] C. Balanis, *Antenna Theory Analysis and Design*, New York: John Wiley & Sons, 1982.

[14] Web site for Ford Motor Company, http://www.ford.com

[15] R. Duda and P. Hart, *Pattern Classification and Scene analysis,* New York: John Wiley & Sons, 1973.S.

[16] Hudson, "Correlation Filters for Aircraft Identification from Radar Range Profiles," *IEEE Transactions on Aerospace and Electronic Systems*, vol. 29, no. 3, pp. 741-749, July 1997.

[17] T. D. Ross, S. W. Worrell, V. J. Velten, J. C. Mossing and M. L. Bryant, "Standard SAR ATR Evaluation Experiments Using the MSTAR Public Release Data Set," *Proceedings of SPIE*, Algorithm for SAR Imagery V, vol. 3370, pp. 566-573, April 1998.

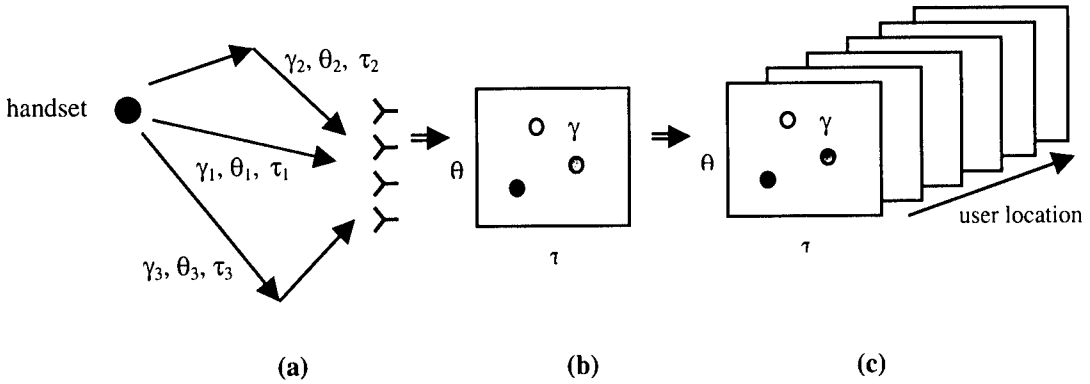


**Figure 1. Multipath Fingerprint System.**
**(a) Multipath components of the handset signal arriving at the base station.**
**(b) Fingerprint created from parameters extracted from the incoming signal.**
**(c) Existing fingerprint database – each fingerprint is associated with a specific mobile location. The extracted fingerprint from the handset signal is compared to the database to find the best fingerprint match and thus the handset location.**

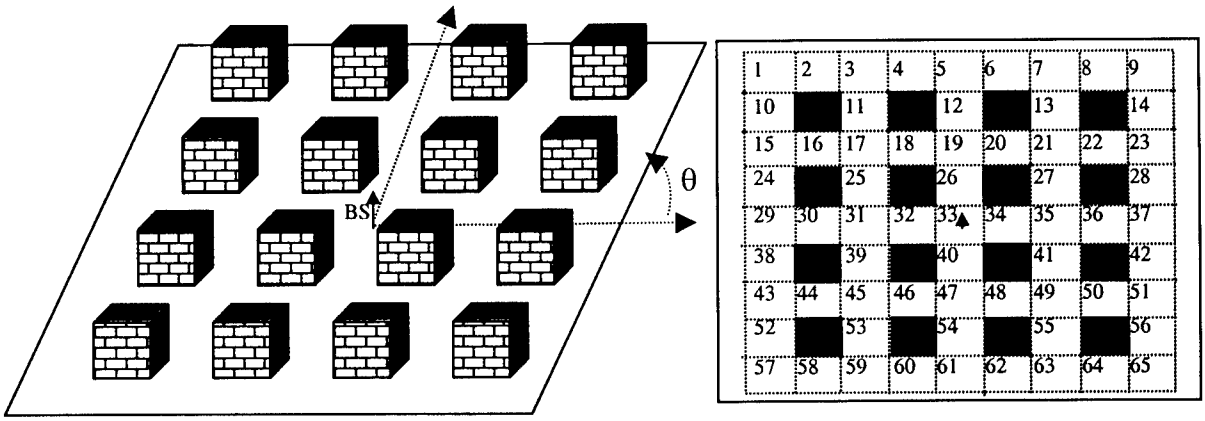


**Figure 2. Four-by-four symmetrical building model.**

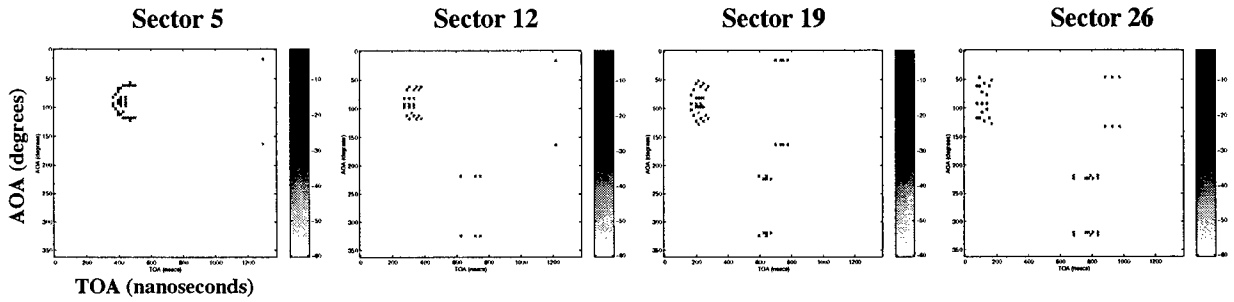


**Figure 3. Fingerprints for the sectors along the LOS street in the four-by-four symmetrical model.**

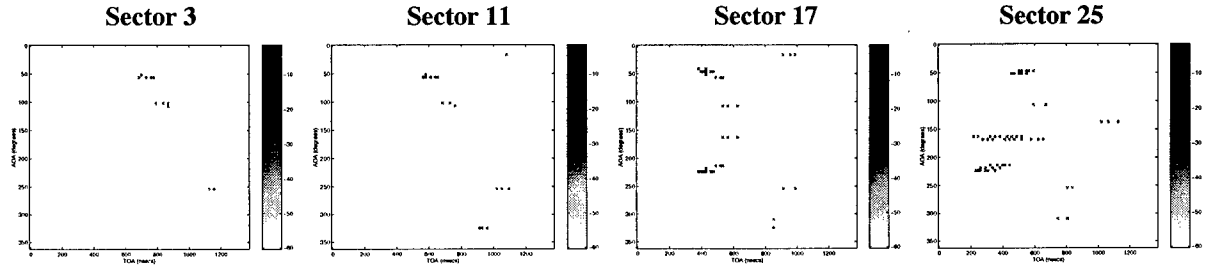


**Figure 4. Fingerprints for the sectors along the non-LOS parallel street in the four-by-four symmetrical model.**

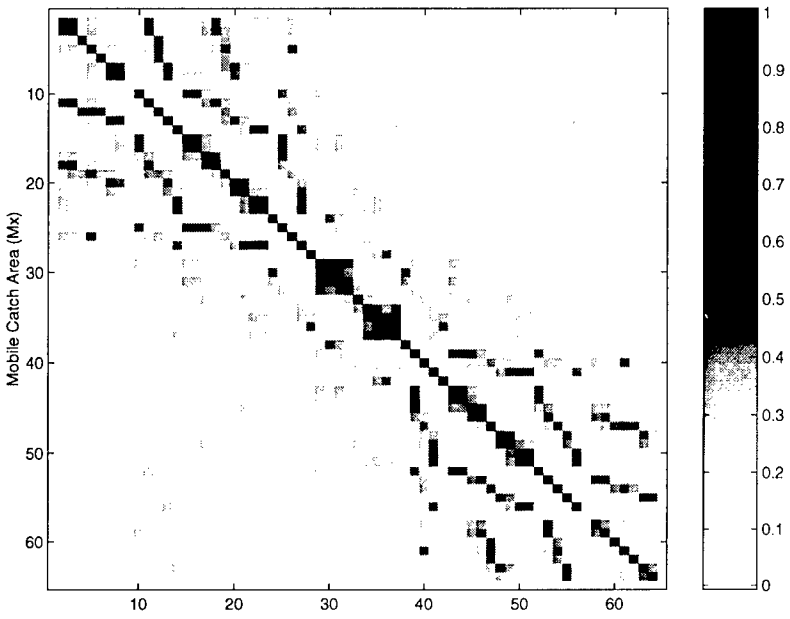


**Figure 5a. Correlation coefficient matrix for all the fingerprints in the four-by-four model.**

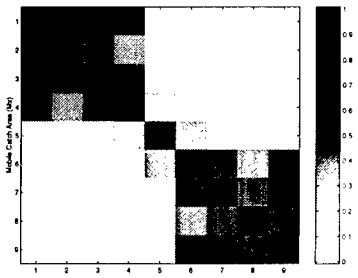

**Figure 5b. LOS street, Sectors 29-37**

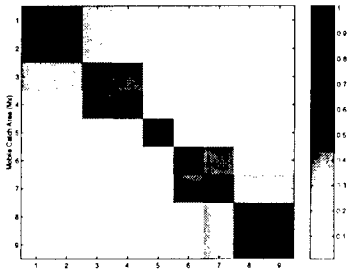

**Figure 5c. Parallel Street, Sectors 15-23**

**Figure 5. Correlation coefficient matrix for the four-by-four model.**

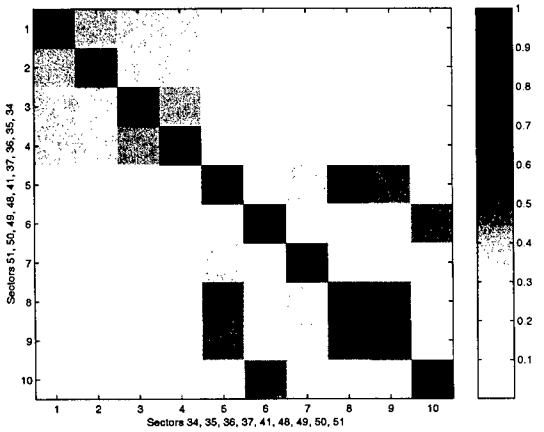


Figure 6a. Correlation Coefficient Matrix for Mx34, 35, 36, 37, 41, 48, 49, 50, 51, 55 assuming infinite AOA and TOA resolution

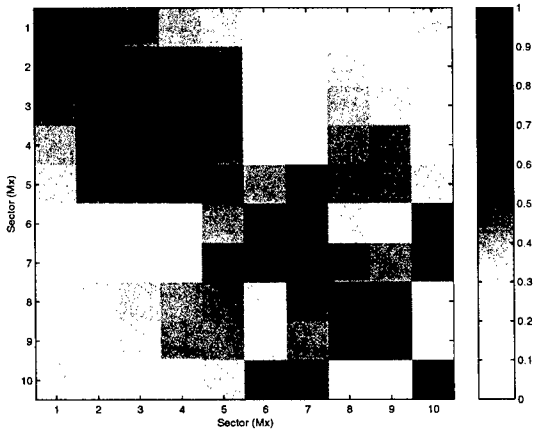


Figure 6b. Correlation Coefficient Matrix with 2.9 MHz bandwidth and array size 2λ

**Figure 6. Correlation coefficient matrix for the lower right-hand quadrant showing the effect of limited bandwidth and array size.**

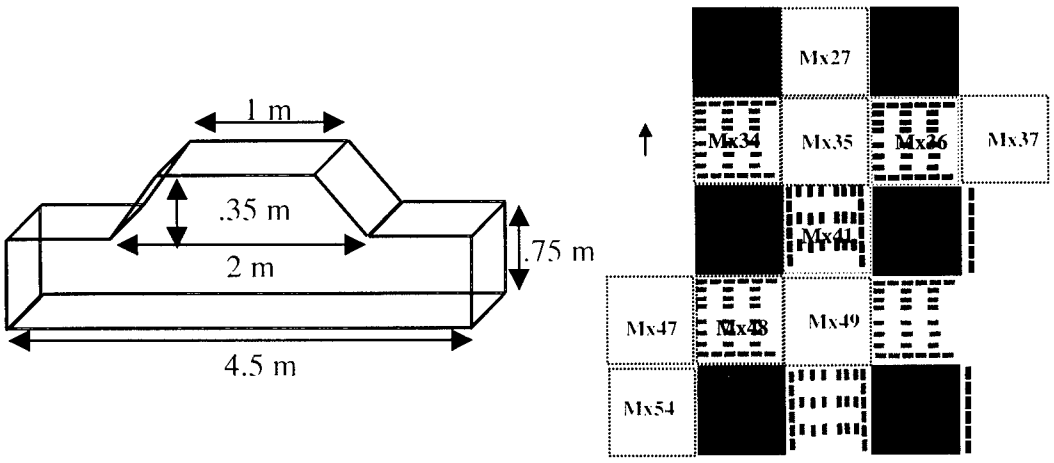


**Figure 7. Car model and location of cars placed in the four-by-four model.**

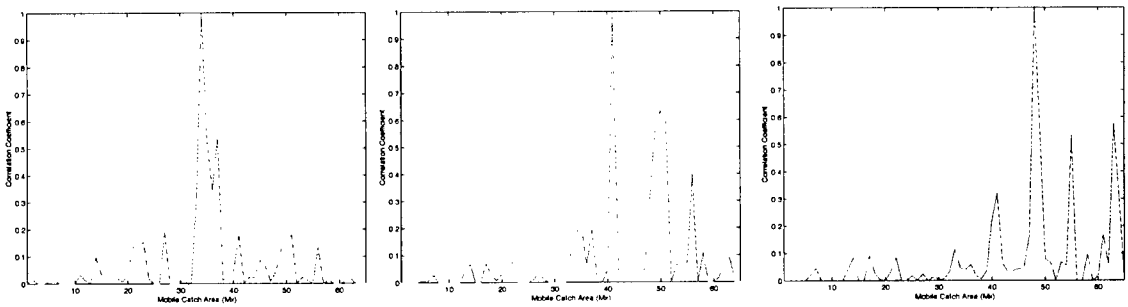

Figure 8a. Mx34 Figure 8b. Mx41 Figure 8c. Mx48

**Figure 8. Effect of cars on the correlation coefficient.**
**Solid, Blue - original template without cars compared to database.**
**Dotted Red - template with cars compared to database**

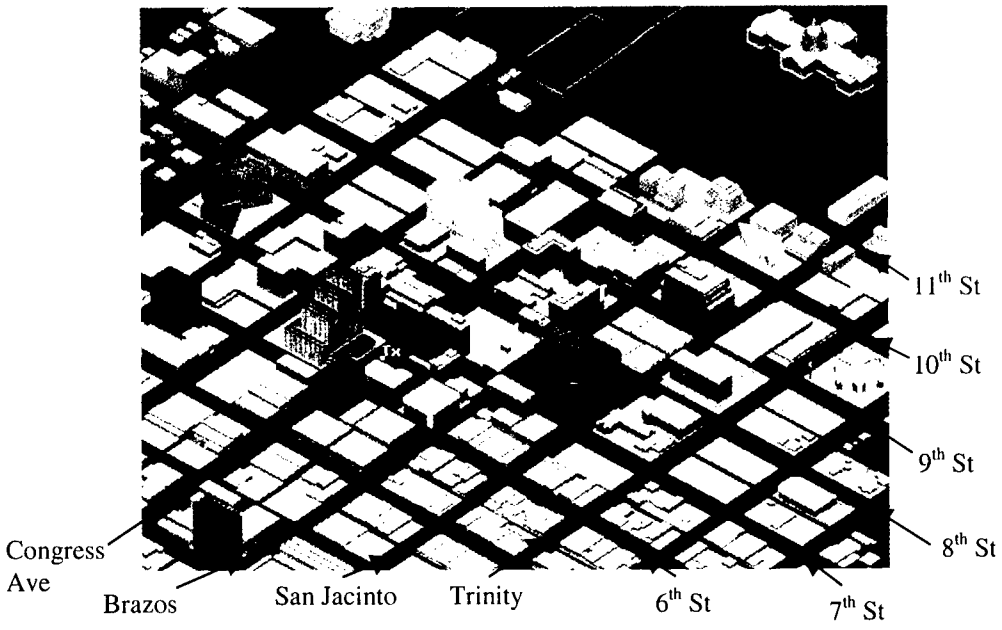


**Figure 9. CAD model of dowtown Austin, Texas.**

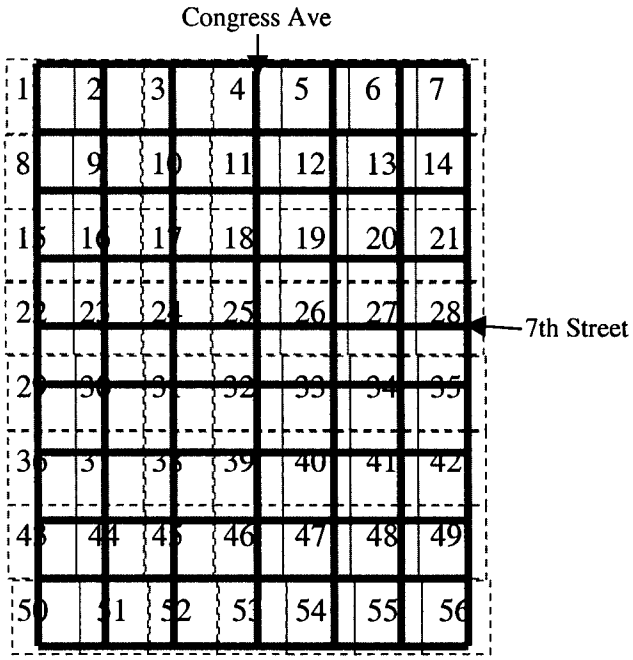


**Figure 10. Sectorization of dowtown Austin, Texas.**

| | | | | | | |
|---|---|---|---|---|---|---|
| 1 | 2 | 3 | 4 | 5 | 6 | 7 |
| 0.95 | 0.73 | 0.82 | 0.86 | 0.78 | 0.82 | 0.88 |
| 0.95 | 0.88 | 0.95 | 0.98 | 0.98 | 0.91 | 0.89 |
| 8 | 9 | 10 | 11 | 12 | 13 | 14 |
| 0.84 | 0.67 | 0.87 | 0.92 | 0.95 | 0.89 | 0.91 |
| 0.85 | 1 | 0.97 | 1 | 0.97 | 1 | 0.91 |
| 15 | 16 | 17 | 18 | 19 | 20 | 21 |
| 0.92 | 0.76 | 0.82 | 0.69 | 0.97 | 0.82 | 0.83 |
| 0.99 | 0.93 | 0.9 | 0.98 | 1 | 0.92 | 0.87 |
| 22 | 23 | 24 | 25 | 26 | 27 | 28 |
| 0.99 | 0.57 | 0.62 | 0.68 | 0.9 | 0.88 | 1 |
| 0.99 | 0.96 | 0.81 | 0.84 | 0.96 | 1 | 1 |
| 29 | 30 | 31 | 32 | 33 | 34 | 35 |
| 0.85 | 0.81 | 0.74 | 0.82 | 0.76 | 0.79 | 0.87 |
| 0.9 | 0.96 | 0.82 | 0.86 | 0.82 | 0.94 | 0.99 |
| 36 | 37 | 38 | 39 | 40 | 41 | 42 |
| 0.54 | 0.65 | 0.62 | 0.63 | 0.7 | 0.62 | 0.9 |
| 0.81 | 0.93 | 0.83 | 0.88 | 0.88 | 0.91 | 0.96 |
| 43 | 44 | 45 | 46 | 47 | 48 | 49 |
| 1 | 0.35 | 0.52 | 0.7 | 0.56 | 0.22 | 0.89 |
| 1 | 0.94 | 0.85 | 0.94 | 0.88 | 1 | 1 |
| 50 | 51 | 52 | 53 | 54 | 55 | 56 |
| 0.87 | 0.24 | 0.53 | 0.87 | 0.6 | 0.25 | 1 |
| 1 | 0.87 | .0.89 | 0.95 | 0.9 | 0.81 | 1 |

Table 1. Correct Location Finding Probability Using both TOA and AOA Information. The average values over all sectors are: $P_{lf}$=76%, $P_{alf}$=92%.

| | | | | | | |
|---|---|---|---|---|---|---|
| 1 | 2 | 3 | 4 | 5 | 6 | 7 |
| 0.77 | 0.69 | 0.64 | 0.67 | 0.81 | 0.74 | 0.75 |
| 0.82 | 0.78 | 0.78 | 0.82 | 0.86 | 0.91 | 0.78 |
| 8 | 9 | 10 | 11 | 12 | 13 | 14 |
| 0.54 | 0.87 | 0.78 | 0.73 | 0.69 | 0.68 | 0.87 |
| 0.71 | 0.91 | 0.87 | 0.88 | 0.94 | 0.9 | 0.88 |
| 15 | 16 | 17 | 18 | 19 | 20 | 21 |
| 0.81 | 0.5 | 0.7 | 0.5 | 0.82 | 0.5 | 0.64 |
| 0.92 | 0.66 | 0.75 | 0.72 | 0.84 | 0.57 | 0.73 |
| 22 | 23 | 24 | 25 | 26 | 27 | 28 |
| 0.23 | 0.59 | 0.39 | 0.55 | 0.7 | 0.76 | 0.83 |
| 0.69 | 0.78 | 0.64 | 0.73 | 0.95 | 0.86 | 0.95 |
| 29 | 30 | 31 | 32 | 33 | 34 | 35 |
| 0.66 | 0.58 | 0.58 | 0.55 | 0.69 | 0.78 | 0.59 |
| 0.87 | 0.91 | 0.69 | 0.79 | 0.91 | 0.88 | 0.71 |
| 36 | 37 | 38 | 39 | 40 | 41 | 42 |
| 0.46 | 0.53 | 0.6 | 0.41 | 0.43 | 0.52 | 0.4 |
| 0.62 | 0.67 | 0.71 | 0.72 | 0.73 | 0.88 | 0.62 |
| 43 | 44 | 45 | 46 | 47 | 48 | 49 |
| 0.65 | 0.15 | 0.58 | 0.65 | 0.73 | 0.16 | 0.49 |
| 0.68 | 0.9 | 0.83 | 0.98 | 0.9 | 0.77 | 0.6 |
| 50 | 51 | 52 | 53 | 54 | 55 | 56 |
| 0.39 | 0.67 | 0.64 | 0.58 | 0.51 | 0.49 | 0.78 |
| 0.73 | 0.93 | 0.76 | 0.91 | 0.88 | 0.76 | 1 |

Table 2. Correct Location Finding Probability Using AOA Information Only.
The average values over all sectors are: $P_{lf}$=60%, $P_{alf}$=80%.

| | | | | | | |
|---|---|---|---|---|---|---|
| 1 | 2 | 3 | 4 | 5 | 6 | 7 |
| 0.1 | 0.03 | 0.02 | 0.15 | 0.2 | 0.24 | 0.23 |
| 0.1 | 0.11 | 0.09 | 0.15 | 0.34 | 0.3 | 0.25 |
| 8 | 9 | 10 | 11 | 12 | 13 | 14 |
| 0.22 | 0.24 | 0.12 | 0.02 | 0.52 | 0.18 | 0.21 |
| 0.41 | 0.42 | 0.18 | 0.08 | 0.65 | 0.28 | 0.24 |
| 15 | 16 | 17 | 18 | 19 | 20 | 21 |
| 0.19 | 0.09 | 0.37 | 0.33 | 0.3 | 0.36 | 0.26 |
| 0.29 | 0.31 | 0.42 | 0.45 | 0.49 | 0.4 | 0.39 |
| 22 | 23 | 24 | 25 | 26 | 27 | 28 |
| 0.33 | 0.06 | 0.09 | 0.51 | 0.41 | 0.3 | 0.52 |
| 0.37 | 0.24 | 0.16 | 0.54 | 0.59 | 0.51 | 0.53 |
| 29 | 30 | 31 | 32 | 33 | 34 | 35 |
| 0.54 | 0.53 | 0.32 | 0.62 | 0.63 | 0.41 | 0.58 |
| 0.59 | 0.61 | 0.42 | 0.67 | 0.7 | 0.6 | 0.67 |
| 36 | 37 | 38 | 39 | 40 | 41 | 42 |
| 0.07 | 0.12 | 0.24 | 0.08 | 0.37 | 0.21 | 0.26 |
| 0.13 | 0.28 | 0.32 | 0.28 | 0.72 | 0.49 | 0.54 |
| 43 | 44 | 45 | 46 | 47 | 48 | 49 |
| 0.12 | 0.26 | 0.17 | 0.34 | 0.03 | 0.86 | 0.11 |
| 0.15 | 0.52 | 0.32 | 0.36 | 0.51 | 0.87 | 0.76 |
| 50 | 51 | 52 | 53 | 54 | 55 | 56 |
| 0.06 | 0 | 0 | 0 | 0.09 | 0 | 0 |
| 0.18 | 0.22 | 0.01 | 0 | 0.51 | 0.79 | 0.85 |

Table 3. Correct Location Finding Probability Using TOA Information Only.
The average values over all sectors are: $P_{lf}$=24%, $P_{alf}$=40%.

| 1 | 2 | 3 | 4 | 5 | 6 | 7 |
|---|---|---|---|---|---|---|
| 0.93 | 0.68 | 0.70 | 0.81 | 0.82 | 0.81 | 0.75 |
| 0.93 | 0.81 | 0.90 | 0.92 | 0.95 | 0.91 | 0.8 |
| 8 | 9 | 10 | 11 | 12 | 13 | 14 |
| 0.84 | 0.66 | 0.92 | 0.9 | 0.89 | 0.73 | 0.8 |
| 0.92 | 0.94 | 0.99 | 0.97 | 0.93 | 0.99 | 0.84 |
| 15 | 16 | 17 | 18 | 19 | 20 | 21 |
| 0.87 | 0.74 | 0.8 | 0.79 | 0.87 | 0.69 | 0.74 |
| 0.94 | 0.87 | 0.88 | 0.97 | 0.96 | 0.82 | 0.79 |
| 22 | 23 | 24 | 25 | 26 | 27 | 28 |
| 0.89 | 0.5 | 0.61 | 0.65 | 0.89 | 0.87 | 0.97 |
| 0.94 | 0.91 | 0.75 | 0.75 | 0.94 | 0.99 | 0.99 |
| 29 | 30 | 31 | 32 | 33 | 34 | 35 |
| 0.83 | 0.68 | 0.65 | 0.78 | 0.84 | 0.76 | 0.85 |
| 0.93 | 0.94 | 0.76 | 0.88 | 0.91 | 0.91 | 1 |
| 36 | 37 | 38 | 39 | 40 | 41 | 42 |
| 0.43 | 0.54 | 0.53 | 0.57 | 0.74 | 0.65 | 0.89 |
| 0.57 | 0.86 | 0.77 | 0.73 | 0.79 | 0.89 | 0.92 |
| 43 | 44 | 45 | 46 | 47 | 48 | 49 |
| 0.95 | 0.32 | 0.48 | 0.57 | 0.43 | 0.21 | 0.89 |
| 0.98 | 0.94 | 0.78 | 0.88 | 0.77 | 0.95 | 1 |
| 50 | 51 | 52 | 53 | 54 | 55 | 56 |
| 0.8 | 0.19 | 0.78 | 0.83 | 0.59 | 0.18 | 0.88 |
| 0.92 | 0.72 | 0.79 | 0.92 | 0.89 | 0.72 | 0.93 |

Table 4. Correct Location Finding Probability with Gaussian Random Jitter Applied to TOA and AOA Features in Measured Fingerprints.
The average values over all sectors are: $P_{lf}$=71%, $P_{alf}$=88%.

# NEW DESIGNS FOR DUAL BAND ANTENNAS FOR SATELLITE-MOBILE COMMUNICATIONS HANDSETS

S. M. Daddish, R. A. Abd-Alhameed and P.S. Excell
Department of Electronic and Electrical Engineering,
University of Bradford, UK

*ABSTRACT:*

The design of dual-band antennas for hand-held terminals (HHT) to be used in personal communications via a satellite network (SPCN) is investigated. The quadrifilar helical antenna (QHA) is selected as the optimum design for further study and a new design for a QHA is derived and optimized using a standard Moment-Method program. A dual L-S band design with an input VSWR in its two operating bands of between 1 and 2 was developed, incorporating external shorted turns to achieve the desired passbands. The design of the required hybrid feed phasing network is derived. Experiments with physical realizations of the optimum designs showed good performance and confirmed the computational predictions.

## *1. INTRODUCTION*

The Quadrifilar Helical Antenna (QHA) is *an ingenious* antenna invented by Kilgus [1] in the 1970s. It consists of four coaxial helices rotated 90° with respect to each other (Fig. 1). The four helical elements are connected by short radial arms and are fed with identical signals, differing only by sequential 90° phase shifts (i.e. 0°, 90°, 180°, 270°). The analysis by Kilgus [1] for the resonant QHA (RQHA) is based on the assumption that the QHA consists of four helical and four radial parts. The analysis approach to the RQHA is based on the viewpoint that a QHA consists of two bifilar helices (BH) placed at 90° angular displacement and fed in phase quadrature. The radial segments at the distant end can be shorted or open circuited, giving only changes to the input impedance.

*This antenna has the useful property of producing a single main lobe from a structure of modest electrical size (i.e. that fits in an electrically small envelope). It is thus attractive for application in mobile satellite terminals.*

One of the major disadvantages of the QHA is the complex feed network that it requires. One approach is to feed each BH with the assistance of a balun, most configurations also needing a 90° phase shifter. The exceptions to this are the self-phased configuration and the Keen balun [2], which can provide the phase difference without a hybrid and with the use of only one balun. The other way is to feed each of the four helical elements separately, with appropriate phases, using three hybrids. This method does not require a balun to feed the QHA.

## *2. DESIGN PROCEDURE OF QHA AND HYBRID FEEDING NETWORK*

A quadrifilar helix that requires a separate phasing network at the input is known as an externally phased quadrifilar helix. Fig. 1 shows a quadrifilar helix fed from the bottom. This type of antenna requires a network creating the appropriate phases and matching the impedance of the elements to the coaxial feed line. A simple phasing network of 3 dB hybrids can be used to produce equal amplitude signals with quadrature phasing to the radiating elements.

The radiating helical elements determine the pattern characteristics and the shape. The element dimensions have been empirically determined by many authors *[3-5]* to accord with satellite system specifications. The feeding direction relative to the main lobe can be arranged to be either forward-fire or backfire by changing the phase sequence of the elements. The axial ratio of the main beam radiation is controlled by the length and diameter of the helix, and the symmetry of the elements. The phasing circuit plays an important role in generating a shaped conical pattern, which is required for many mobile satellite system applications. The sense of the polarization is controlled by the winding direction of the helices.

### *2.1 DUAL BAND DESIGN*

For dual-frequency operation, a single QHA is not feasible, because it is a resonant-type antenna and is inherently too narrow-band. Therefore, dual-band operation can only be achieved through the incorporation of two antennas into one structure by coaxially mounting them in either an enclosed (QHA-1 inside QHA-2) or a piggyback (QHA-1 on top of QHA-2) fashion [4,5]. For ease of manufacture and minimized antenna cross-section, the piggyback design was chosen. In addition, a third short external set of helices (QHA-3) was introduced to optimize the VSWR for the second operating frequency band by acting as a set of tapping windings. Table 1 shows the data for the forward-fire QHAs found to be optimal.

Table 1: Dimensional Data for dual-band end-fire QHA.

| *QH no.* | *Spacing between turns (m)* | *Wire Radius (m)* | *Helix Radius (m)* | *Number of Turns (N)* | *Axial Length (m)* | *Length of one Element (m)* |
|---|---|---|---|---|---|---|
| 1 | 0.028 | 0.00089 | 0.007 | 1.25 | 0.035 | 0.0652 |
| 2 | 0.068 | 0.00089 | 0·007 | 1.25 | 0.085 | 0.1012 |
| 3 | 0.068 | 0.00089 | 0.007 top<br>0.0105 bottom | 0.25 | 0.017 | 0.0217 |

All the QHAs were designed for minimum VSWR (between 1 and 2) over the dual L and S band satellite-mobile frequency ranges (approximately 1.61-1.63 GHz and 2.47-2.5 GHz for SPCN services). The objectives were to achieve maximum power gain (greater than 5 dB [3]) and an axial ratio close to unity over elevation angles from zenith to ±60°. *The handset is box-shaped and its height was kept constant at 14 cm (a typical value for current satellite-mobile handsets*). To ease installation of the phasing network and subsequent testing, the dimensions of the top plate were taken to be 6cm × 6cm and the antenna was optimized with this.

The hybrid phasing networks for the QHA was constructed on high permittivity ($\varepsilon_r$ = 10.2) substrate for operation at 1.62 GHz and 2.48 GHz. The design was optimized *for both bands subject to a VSWR ≤ 2.*

The simulation of the forward-fire QHA and handset for dual L/S bands was performed using NEC-WIN Pro [6], while the hybrid phasing network was designed using the Libra package [7]. A wire grid representation of the design is shown in Fig. 2. The handset box was represented by a mesh of 18 × 8 × 8 wires, each being a single NEC segment; the radius of the wires was chosen in accordance with the equal-area rule. The QHAs were represented using the NEC GH (Geometry – Helix) command, the number of segments per single helix being 30, 30 and 3 for QHA-1, 2 and 3 respectively. *Four voltage sources are used for excitation; each one of them is placed at the attachment mode of each helix to the top of the box.* The simulations were stable *for two values of grid size in the handset box model and segment size in the helices* and the run times were a few minutes per frequency when using a 400MHz Pentium-II computer with 256 Mbyte RAM.

*Although it is known that modeling of helices can sometimes cause stability problems with MoM programs, no such problems were experienced in this case. This is presumed to be due the relatively large pitch of the helices used, which thus avoided large values of mutual coupling between turns.*

## *3. RESULTS*

The computed axial ratio and power gain (at 1.620 GHz and 2.480 GHz) of the proposed antenna are shown in Figs. 3 and 4 respectively. The attenuation of the main beam (relative to boresight) at ±60° is seen to be about 3dB at 1.620GHz and 7dB at 2.480GHz: the latter figure is rather high but manageable within a typical link budget. The axial ratio remains greater than 0.9 over the ±60° range at both frequencies.

The prototype antenna was manufactured from copper wire, supported on acrylic struts distributed radially, at each turn, from a central acrylic rod (Fig. 5). The wires entered the copper case through separate SMA connectors. The hybrid phase networks were fabricated within the two bands of interest on substrate having $\varepsilon_r$ = 10.2 and a thickness of 1.27 mm. The prototypes of the hybrids are shown in Fig. 5, with the dummy handset and prototype antenna. The measured performance of the hybrid phasing networks at 1.620 GHz and 2.480 GHz are given in Tables 2 and 3 respectively.

Table 2: Measurement results for hybrid phasing network at 1.62 GHz.

| *Port Number* | *Target phase (degrees)* | *Measured phase (degrees)* | *Insertion Loss (dB)* | *Return Loss (dB)* |
|---|---|---|---|---|
| 1 | 0 | 0 | -6.27 | -17.0 |
| 2 | 90 | 88.9 | -6.74 | -18.2 |
| 3 | 180 | 178.1 | -6.09 | -18.2 |
| 4 | 270 | 268.2 | -6.63 | -18.5 |

Table 3: Measurement results for hybrid phasing network at 2.48 GHz.

| *Port Number* | *Target phase (degrees)* | *Measured phase (degrees)* | *Insertion Loss (dB)* | *Return Loss (dB)* |
|---|---|---|---|---|
| 1 | 0 | 0 | -6.05 | -14.2 |
| 2 | 90 | 89.2 | -6.96 | -15.5 |
| 3 | 180 | 178.1 | -6.38 | -14.5 |
| 4 | 270 | 268.8 | -6.69 | -15.4 |

The results agree well with the desired values *required for feeding*. The small size of the hybrid phasing networks allowed them to be inserted easily inside the handset. The measured VSWR and the input impedance as a function of the frequency at the input of the hybrid networks when connected to the antenna within the handset are shown in Figs. 6 and 7 respectively. The results are quite encouraging and in line with the expected VSWR pass-bands.

An initial measurement of axial ratios (Fig. 8) showed a degree of agreement with the predictions (Fig. 3), although there was some degradation, believed to be due to deficiencies in the test facility.

## *CONCLUSIONS*

A dual-band quadrifilar helical antenna (QHA) was designed and analyzed. It consists of two sets of four coaxial helixes, each helix rotated 90° with respect to its neighbors in each set. The realization adopted in the present work used a bottom-fed (end fire) version for convenience in feeding. The helices were fed with a sequential phase difference of 90 degrees, with the sense of the phasing relative to the helix senses controlling whether the antenna radiates in forward-fire (end-fire) or back-fire mode. By using two sets of QH groups, combined in 'piggyback' fashion, plus a small additional set of QH matching stubs, it was possible to achieve good matching over the two desired operating bands (satellite-mobile allocations in the L and S bands). The computed results showed end-fire (zenith-directed) patterns for the two operating frequencies, having the desired beamwidth of around 120° and an axial ratio close to unity across the beam. The measured results showed good agreement with the theoretical predictions in the sense of minimum VSWR and matching to a 50Ω source in the two operating bands. A preliminary measurement of axial ratio showed an encouraging degree of agreement with the predictions.

*MoM modeling using NEC was found to operate stably and reliably in this case, despite the adoption of multifilar helical antennas. This gives confidence in the use of this method for other electrically-small helical antennas, as are now popular in mobile communications handsets. However, incorporation of the interaction with the human head would be desirable, but thus would require a hybrid formulation with a differential-equation method, since use of MoM for large inhomogeneous dielectric volumes is not feasible. This has already been implemented for single helical antennas [8] and work on its extension to QHA handsets is in progress.*

## *References*

[1] C. C. Kilgus, 'Resonant Quadrifilar Helix', IEEE Transactions on Antennas and Propagation, Vol. AP-17, No. 3, pp. 349-351, 1969.

[2] K.M. Keen, D Smith and B.S. Lee, 'Improved form of backfire bifilar helix conical beam antenna', Microwave and Optical Technology Letters, vol. 14, Iss 5, pp. 278-280, 1997.

[3] A. Gregory and J. O'Neill, 'Dual Frequency Band Quadrifilar Helix Antenna Systems and Methods', United States Patent No. 5,909,196, 1999.

[4] V. C. Smith, 'Dual-Frequency Circularly Polarized Spiral Antenna for Satellite Navigation', United States Patent No. 4,008,479, 1977.

[5] A. A. Agius, M. S. Mahmoud, R. Tafazolli and B. G. Evans, 'Quadrifilar Helical Antenna for Handheld Terminal in Satellite Personal Communication Networks (SPCN)', IEE Conference Publication No. 424 'Antennas and Propagation', pp.76-79, London, 1996.

[6] 'NEC-WIN Pro – Antenna Analysis Software', USA: Nittany Scientific Inc., Version 1.1.

[7] 'Libra – High-Frequency Design Solutions Software', Series 4, USA: Agilent Technologies (Hewlett Packard).

[8] *Mangoud, M.A., Abd-Alhameed, R.A. and Excell, P.S.: 'Simulation of Human Interaction with Mobile Telephones using Hybrid Techniques over Coupled Domains', IEEE Trans. on Microwave Theory and Techniques, 2000, in press.*

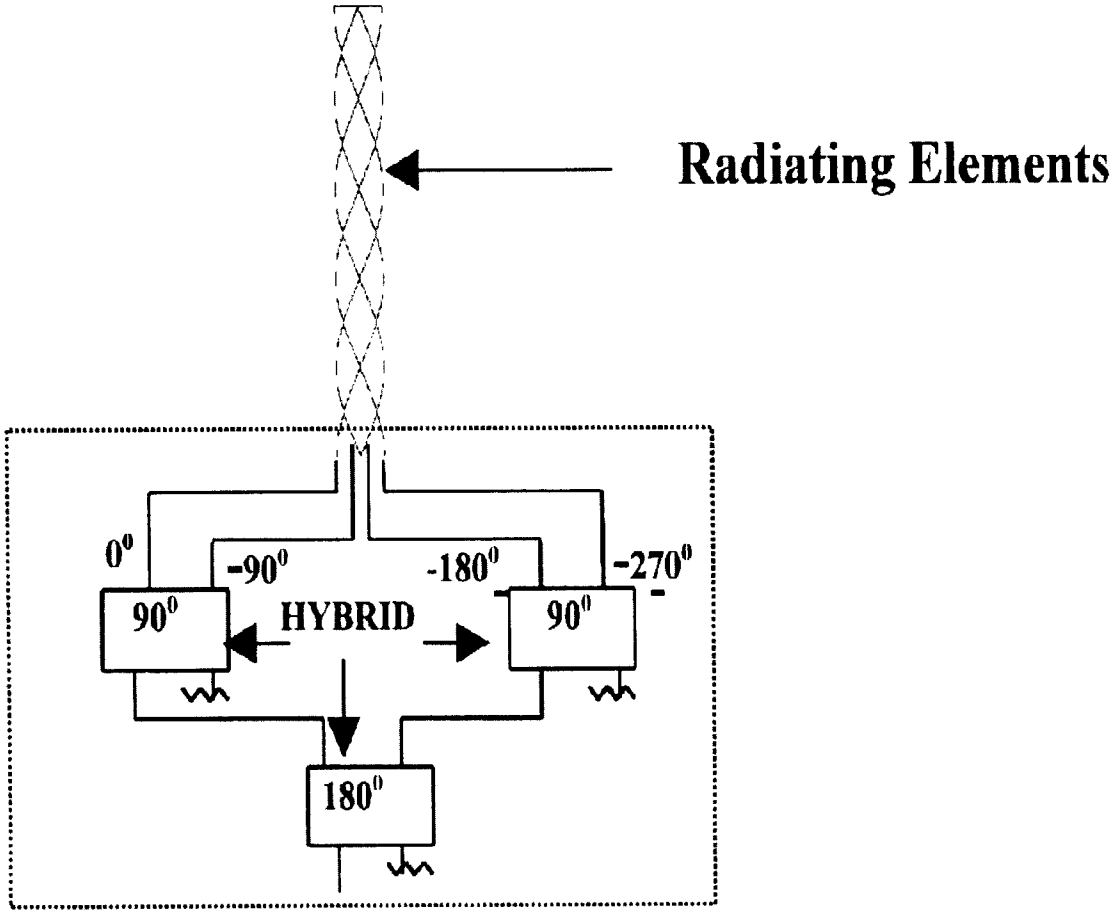


Fig. 1 Conceptual phasing network for an end-fire QHA.

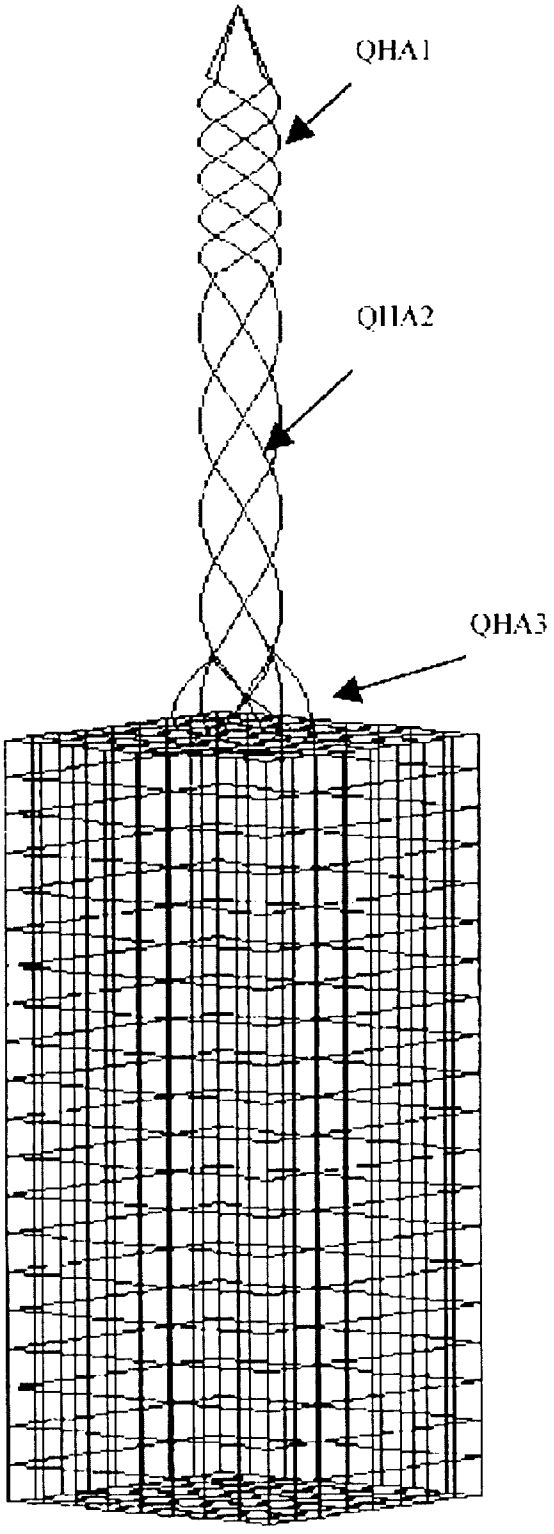


Fig. 2 Wire grid geometry model of dual band QHA and dummy handset, as used in NEC-WIN Pro.

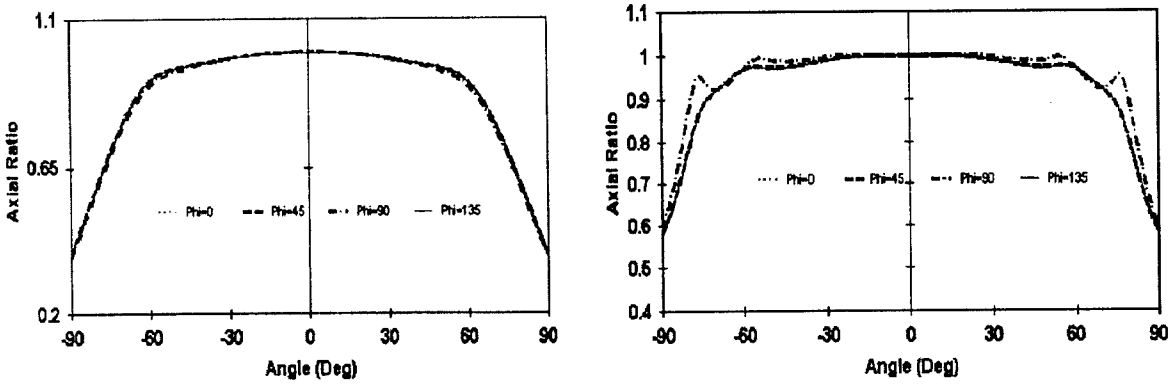


(a) (b)

Fig. 3 Axial Ratio over main beam (a) at 1.62 GHz; (b) at 2.48 GHz.

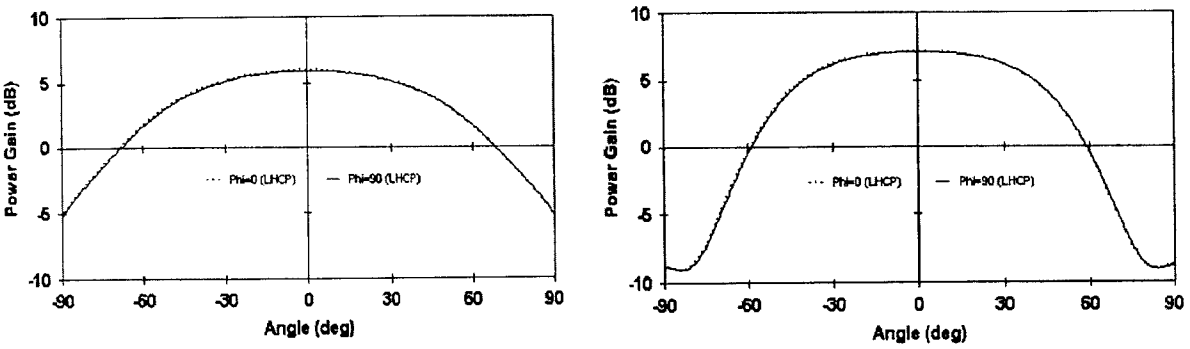


(a) (b)

Fig. 4 Radiation Pattern Power Gain (a) at 1.62 GHz; (b) at 2.48 GHz.

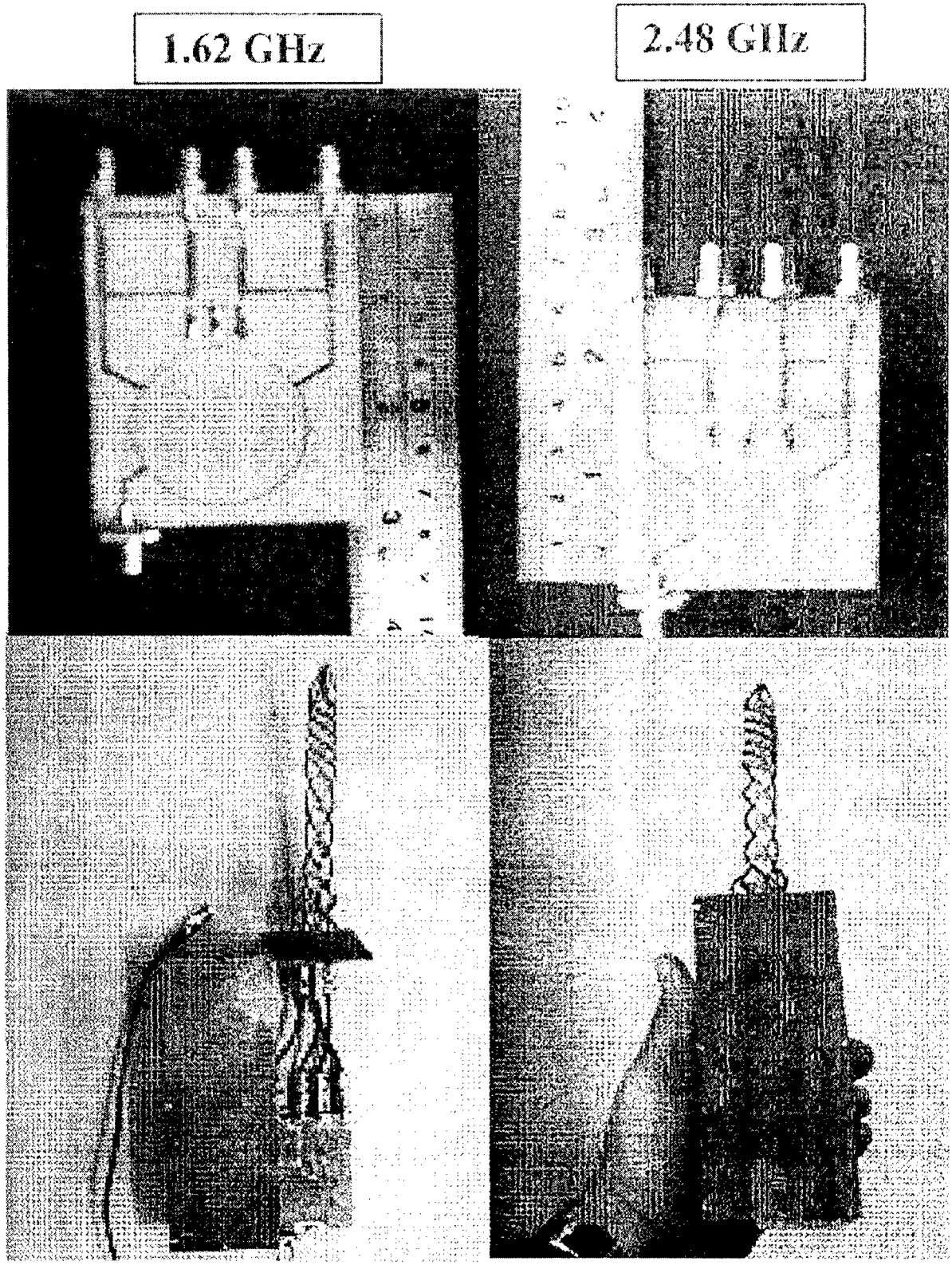


Fig. 5 Photographs of the QHA for dual L-S band, with dummy handset and hybrids.

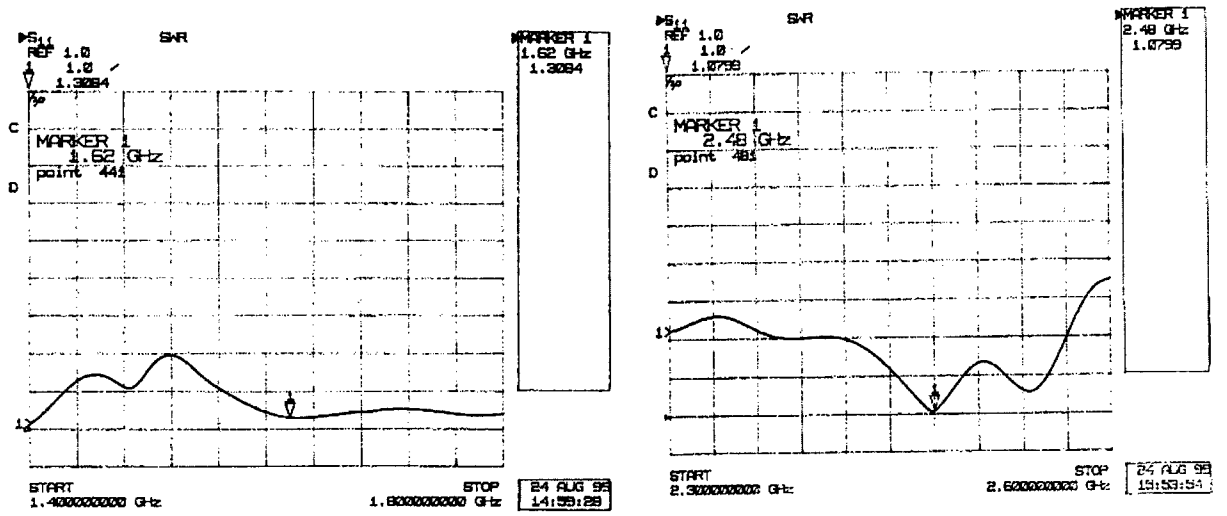


(a) (b)

Fig. 6 The measured VSWR as a function of the frequency at the input of the hybrid network (a) at 1.62 GHz; (b) at 2.48 GHz.

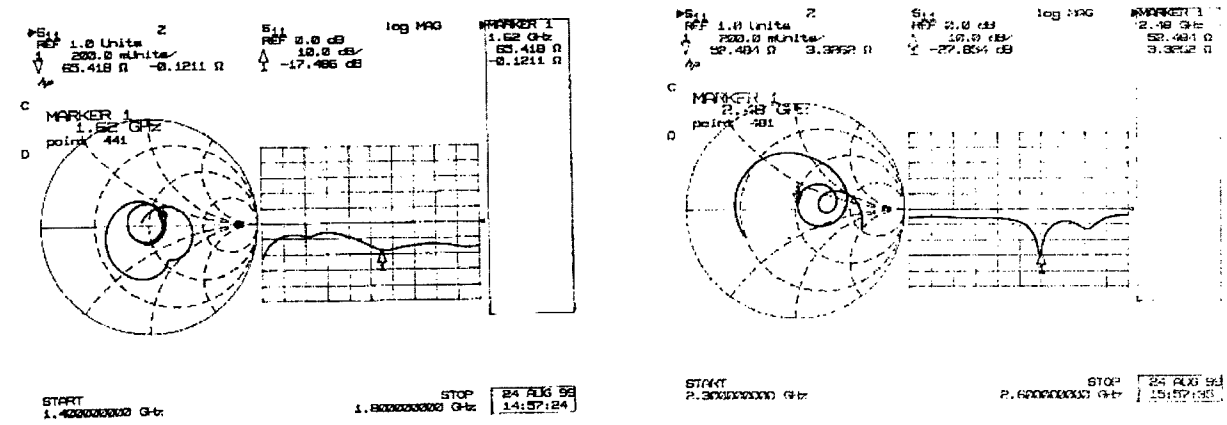


(a) (b)

Fig. 7 Smith chart for the input impedance and return loss of the antenna located at the input of a hybrid network (a) at 1.62 GHz; (b) at 2.48 GHz.

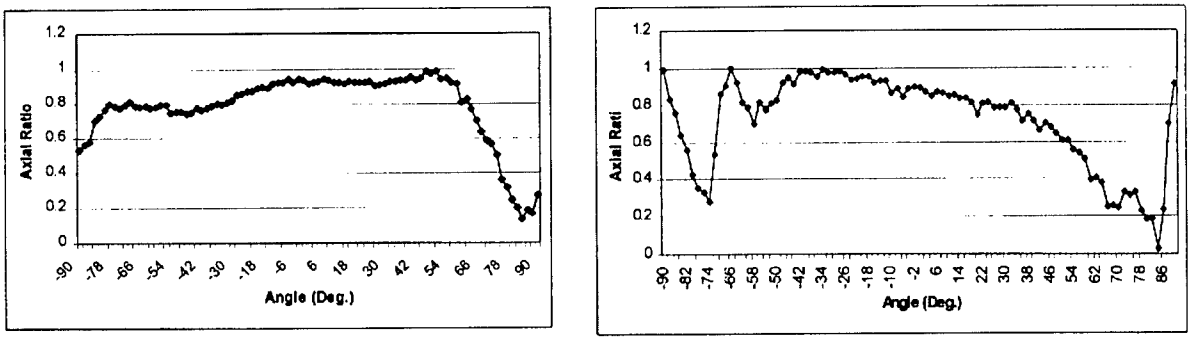


(a) (b)

Fig. 8 Preliminary test results for axial ratios (a) at 1.62 GHz; (b) at 2.48 GHz.

# 2000 INSTITUTIONAL MEMBERS

ADVANSIS, INC.
20370 Town Center
Cupertino, CA 95014

ALGON MOBILE COMM.
Nasvagen 17
Akersberga, SWEDEN S-18425

AUSTRALIAN DEFENCE LIB.
Northcott Drive
Campbell, A.C.T. AUSTRALIA 2600

BAE SYSTEMS
Gunnelswood Road
Stevenage, HERTS, SG1 2DB UK

BOEING CO, RENTON TECH LIB
PO Box 3707
Seattle, WA 98124-2207

BOEING NORTH AMERICAN SVCS
1745 Jefferson Davis Hwy
Arlington, VA 22202

BPLUS
100 University Court, PO Box 1428
Blackwood, NJ 08012

BRITISH AEROSPACE
Newport Road
Isle of Wight, PO 318 PF UK

BRITISH AEROSPACE
FPC 267 PO Box 5
Filton, BRISTOL, BS12 7QW UK

CENTER HP COMPUTING
PO Box 830657
Birmingham, AL 35283-0657

CHALMERS UNIV of TECHNOLOGY
Dept of Microwave Technology
Gothenburg, S 41296 SWEDEN

CHIHUAHUA UNIVERSITY
P.O. Box 830657
Birmingham, AL 35283-0657

CULHAM SCIENCE LAB
UK Atomic Energy Authority
Abingdon, OXFORD, OX14 3DB UK

DARTMOUTH COLL-FELDBERG LIB
6193 Murdough Center
Hanover, NH 03755-3560

DEFENCE TECH & PROCUREMNT
NEMP LAB
SPIEZ, CH 3700 SWITZERLAND

DEFENSE RESEARCH ESTAB. LIB.
3701 Carling Avenue
Ottowa, ON, K1A 0Z4 CANADA

DEUTSCHE TELEKOM AG
PO Box 10-00-03
Darmstadt, D-64 276 GERMANY

EASTWOOD BOOKS
3250 Wilshire Blvd
Los Angeles, CA 90010

ELECTRICAL COMM LIBRARY
1-1 Hikarinooka
Kanagawa, Ken, 239-0847 JAPAN

ERA TECHNOLOGY
Cleve Road
Leatherhead, SU, KT22 7SA UK

ERICSSON SAAB
Gelbgjutaregat
Linkoping, SE 58188 SWEDEN

E.T.S.E. TELECOMMUNICATION
BIBLIOTECA, Campus Logas
Vigo 36200 SPAIN

FACOLTA INGEGNERIA
Library, Via G Duranti 89
Perugia, 06125 ITALY

FANFIELD LTD
Braxted Park
Witham, Essex, CM8 3XB UK

FUNDACAO CPqD, BIBLIOTECA
Rod. Campinas M
Campinas, SP, 13083-970 BRAZIL

GEC MARCONI RES. CTR. LIB.
W. Hanningfield Road, Gt. Baddow
Chelmsford, ESSEX, CM2 8HN UK

GEORGIA TECH LIBRARY
225 North Avenue, NW
Atlanta, GA 30332-0001

HKUST, UNIVERSITY LIBRARY
Clear Water Bay Road
Kowloon, HONG KONG

HUNTING ENGINEERING LTD.
Reddings Wood, Ampthill
Bedford, MK45 2HD UK

IABG MBH
Einsteinstrasse
Ottobrunn, D-85521 GERMANY

IIT RESEARCH INSTITUTE
185 Admiral Cochrane Drive
Annapolis, MD 21401-7396

IMAGINEERING LTD.
1090 Don Mills Road
Toronto, M3C 3R6, CANADA

INFO & LIBRARY SERVICE
Private Bag 37
Clayton, Vic, 3168 AUSTRALIA

IPS RADIO & SPACE SVC/LIBRARY
PO Box 5606
W. Chatswood, 2057 AUSTRALIA

KATHREIN-WERKE
PO Box 100 444
Rosenheim, D-83004 GERMANY

LINDA HALL LIBRARY
5109 Cherry Street
Kansas City, MO 64110-2498

MISSISSIPPI STATE UNIV LIBRARY
PO Box 9570
Mississippi State, MS 39762

MITRE CORPORATION LIBRARY
202 Burlington Road
Bedford, MA 01730-1407

MYERS ENGINEERING INTL.
PO Box 15908, 5425 NW 24th St.
Margate, FL 33063

NATIONAL AEROSPACE LAB, NLR
Anthony Fokkerweg 2
Emmeloord, 8300 NETHERLANDS

NATL GROUND INTELLIGENCE
220 7th Street N.E.
Charlottesville, VA 22902-5307

NATL RADIOLOGICAL PROT. BD.
Chilton, Didcot, OXON,
OX11 0RG UK

NAVAL RESEARCH LABORATORY
C. Office
Washington, DC 20375

NEMP –LABOR SPIEZ LABS
Nemp Laboratory
Spiez, CH 3700 SWITZERLAND

NNR AIR CARGO SERVICE
Hook Creed Blvd. & 145th Avenue
Valley Stream, NY 11581

PENN STATE UNIVERSITY
126 Paterno Library
University Park, PA 16802

PHILIPS RESEARCH LAB LIBRARY
Cross Oak Lane, Salfords
Redhill, , RH1 5HA SURREY UK

QUEENSLAND CENTER, LIBRARY
2643 Moggill Road
Brisbane, QLD, 4069 AUSTRALIA

RADIO FREQUENCY
36 Garden Street
Kilsyth, VIC 3137 AUSTRALIA

READMORE ACADEMIC LIBRARY
901 Route 168
Turnersville, NY 08012

RENTON TECH LIB – BOEING
PO Box 3707
Seattle, WA 98124-2207

SALISBURY DSTO
PO Box 830701
Birmingham, AL 35283-0701

SESTRA STRADA,CRS4 BIBLIOTEC
Casella Postale
Uta, 09010 ITALY

SOFTWARE TECHNOLOGY
5535 Fillmore Avenue
Alexandria, VA 22311

SONY CORPORATION
174 Fujitsukacho, Hodogaya Ku
Yokohama MZ, 240 JAPAN

SOUTHWEST RESEARCH INST.
6220 Culebra Road
San Antonio, TX 78238

SPIKE TECH
1 Chestnut Street
Nashua, NH 03060

SWETS SUBSCRIPTION SERVICE
440 Creamery Way, Suite A
Exton, PA 19341

T NOVA DEUTSCHE
Am Kavalleriesa
Darmstadt, 64295 GERMANY

TASC LIBRARY
55 Walker Brook
Reading MA 01867-3238

TECHNISCHE UNIV. DELFT
Mekelweg 4, Delft, HOLLAND
2628 CD NETHERLANDS

TELSTRA RES. LABS LIBRARY
770 Blackburn Road
Clayton, VIC, 3168 AUSTRALIA

UNIV OF CENTRAL FLORIDA LIB.
PO Box 162440
Orlando, FL 32816-2440

UNIV OF COLORADO LIBRARY
Campus Box 184
Boulder, CO 80309-0184

UNIV OF MISSOURI-ROLLA LIB.
1870 Miner Circle
Rolla, MO 65409-0001

US ARMY COLD REGION RES, LIB.
72 Lyme Road
Hanover, NH 03775-1290

UNIV SAO PAULO, USP/SIBI
Av Prof. Luciano
Sao Paulo 05508-900 BRAZIL

VTT, TECHNICAL RES. CTR.
PO Box 1202
Espoo, FIN-02044 FINLAND

# ACES COPYRIGHT FORM

This form is intended for original, previously unpublished manuscripts submitted to ACES periodicals and conference publications. The signed form, appropriately completed, MUST ACCOMPANY any paper in order to be published by ACES. PLEASE READ REVERSE SIDE OF THIS FORM FOR FURTHER DETAILS.

TITLE OF PAPER:

AUTHORS(S)

PUBLICATION TITLE/DATE:

RETURN FORM TO:
Dr. Richard W. Adler
Naval Postgraduate School
Code EC/AB
833 Dyer Road, Room 437
Monterey, CA 93943-5121 USA

## PART A - COPYRIGHT TRANSFER FORM

(NOTE: Company or other forms may not be substituted for this form. U.S. Government employees whose work is not subject to copyright may so certify by signing Part B below. Authors whose work is subject to Crown Copyright may sign Part C overleaf).

The undersigned, desiring to publish the above paper in a publication of ACES, hereby transfer their copyrights in the above paper to The Applied Computational Electromagnetics Society (ACES). The undersigned hereby represents and warrants that the paper is original and that he/she is the author of the paper or otherwise has the power and authority to make and execute this assignment.

**Returned Rights**: In return for these rights, ACES hereby grants to the above authors, and the employers for whom the work was performed, royalty-free permission to:

1. Retain all proprietary rights other than copyright, such as patent rights.
2. Reuse all or portions of the above paper in other works.
3. Reproduce, or have reproduced, the above paper for the author's personal use or for internal company use provided that (a) the source and ACES copyright are indicated, (b) the copies are not used in a way that implies ACES endorsement of a product or service of an employer, and (c) the copies per se are not offered for sale.
4. Make limited distribution of all or portions of the above paper prior to publication.
5. In the case of work performed under U.S. Government contract, ACES grants the U.S. Government royalty-free permission to reproduce all or portions of the above paper, and to authorize others to do so, for U.S. Government purposes only.

**ACES Obligations**: In exercising its rights under copyright, ACES will make all reasonable efforts to act in the interests of the authors and employers as well as in its own interest. In particular, ACES REQUIRES that:

1. The consent of the first-named author be sought as a condition in granting re-publication permission to others.
2. The consent of the undersigned employer be obtained as a condition in granting permission to others to reuse all or portions of the paper for promotion or marketing purposes.

In the event the above paper is not accepted and published by ACES or is withdrawn by the author(s) before acceptance by ACES, this agreement becomes null and void.

AUTHORIZED SIGNATURE — TITLE (IF NOT AUTHOR)

EMPLOYER FOR WHOM WORK WAS PERFORMED — DATE FORM SIGNED

## PART B - U.S. GOVERNMENT EMPLOYEE CERTIFICATION

(NOTE: If your work was performed under Government contract but you are not a Government employee, sign transfer form above and see item 5 under Returned Rights).

This certifies that all authors of the above paper are employees of the U.S. Government and performed this work as part of their employment and that the paper is therefore not subject to U.S. copyright protection.

AUTHORIZED SIGNATURE — TITLE (IF NOT AUTHOR)

NAME OF GOVERNMENT ORGANIZATION — DATE FORM SIGNED

## PART C - CROWN COPYRIGHT

(Note: ACES recognizes and will honor Crown Copyright as it does U.S. Copyright. It is understood that, in asserting Crown Copyright, ACES in no way diminishes its rights as publisher. Sign only if *ALL* authors are subject to Crown Copyright.

This certifies that all authors of the above Paper are subject to Crown Copyright. (Appropriate documentation and instructions regarding form of Crown Copyright notice may be attached).

AUTHORIZED SIGNATURE TITLE OF SIGNEE

NAME OF GOVERNMENT BRANCH DATE FORM SIGNED

### Information to Authors

**ACES POLICY**

ACES distributes its technical publications throughout the world, and it may be necessary to translate and abstract its publications, and articles contained therein, for inclusion in various compendiums and similar publications, etc. When an article is submitted for publication by ACES, acceptance of the article implies that ACES has the rights to do all of the things it normally does with such an article.

In connection with its publishing activities, it is the policy of ACES to own the copyrights in its technical publications, and to the contributions contained therein, in order to protect the interests of ACES, its authors and their employers, and at the same time to facilitate the appropriate re-use of this material by others.

The new United States copyright law requires that the transfer of copyrights in each contribution from the author to ACES be confirmed in writing. It is therefore necessary that you execute either Part A-Copyright Transfer Form or Part B-U.S. Government Employee Certification or Part C-Crown Copyright on this sheet and return it to the Managing Editor (or person who supplied this sheet) as promptly as possible.

**CLEARANCE OF PAPERS**

ACES must of necessity assume that materials presented at its meetings or submitted to its publications is properly available for general dissemination to the audiences these activities are organized to serve. It is the responsibility of the authors, not ACES, to determine whether disclosure of their material requires the prior consent of other parties and if so, to obtain it. Furthermore, ACES must assume that, if an author uses within his/her article previously published and/or copyrighted material that permission has been obtained for such use and that any required credit lines, copyright notices, etc. are duly noted.

**AUTHOR/COMPANY RIGHTS**

If you are employed and you prepared your paper as a part of your job, the rights to your paper initially rest with your employer. In that case, when you sign the copyright form, we assume you are authorized to do so by your employer and that your employer has consented to all of the terms and conditions of this form. If not, it should be signed by someone so authorized.

**NOTE RE RETURNED RIGHTS**: Just as ACES now requires a signed copyright transfer form in order to do "business as usual", it is the intent of this form to return rights to the author and employer so that they too may do "business as usual". If further clarification is required, please contact: The Managing Editor, R.W. Adler, Naval Postgraduate School, Code EC/AB, Monterey, CA, 93943, USA (408)656-2352.

Please note that, although authors are permitted to re-use all or portions of their ACES copyrighted material in other works, this does not include granting third party requests for reprinting, republishing, or other types of re-use.

**JOINT AUTHORSHIP**

For jointly authored papers, only one signature is required, but we assume all authors have been advised and have consented to the terms of this form.

**U.S. GOVERNMENT EMPLOYEES**

Authors who are U.S. Government employees are not required to sign the Copyright Transfer Form (Part A), but any co-authors outside the Government are.

Part B of the form is to be used instead of Part A only if all authors are U.S. Government employees and prepared the paper as part of their job.

**NOTE RE GOVERNMENT CONTRACT WORK:** Authors whose work was performed under a U.S Government contract but who are not Government employees are required to sign Part A-Copyright Transfer Form. However, item 5 of the form returns reproduction rights to the U.S. Government when required, even though ACES copyright policy is in effect with respect to the reuse of material by the general public.

# APPLIED COMPUTATIONAL ELECTROMAGNETICS SOCIETY JOURNAL

## INFORMATION FOR AUTHORS

### PUBLICATION CRITERIA

Each paper is required to manifest some relation to applied computational electromagnetics. **Papers may address general issues in applied computational electromagnetics, or they may focus on specific applications, techniques, codes, or computational issues.** While the following list is not exhaustive, each paper will generally relate to at least one of these areas:

**1. Code validation.** This is done using internal checks or experimental, analytical or other computational data. Measured data of potential utility to code validation efforts will also be considered for publication.

**2. Code performance analysis.** This usually involves identification of numerical accuracy or other limitations, solution convergence, numerical and physical modeling error, and parameter tradeoffs. However, it is also permissible to address issues such as ease-of-use, set-up time, run time, special outputs, or other special features.

**3. Computational studies of basic physics.** This involves using a code, algorithm, or computational technique to simulate reality in such a way that better or new physical insight or understanding is achieved.

**4. New computational techniques**, or new applications for existing computational techniques or codes.

**5. "Tricks of the trade"** in selecting and applying codes and techniques.

**6. New codes, algorithms, code enhancement, and code fixes.** This category is self-explanatory but includes significant changes to existing codes, such as applicability extensions, algorithm optimization, problem correction, limitation removal, or other performance improvement. **Note: Code (or algorithm) capability descriptions are not acceptable, unless they contain sufficient technical material to justify consideration.**

**7. Code input/output issues.** This normally involves innovations in input (such as input geometry standardization, automatic mesh generation, or computer-aided design) or in output (whether it be tabular, graphical, statistical, Fourier-transformed, or otherwise signal-processed). Material dealing with input/output database management, output interpretation, or other input/output issues will also be considered for publication.

**8. Computer hardware issues.** This is the category for analysis of hardware capabilities and limitations in meeting various types of electromagnetics computational requirements. Vector and parallel computational techniques and implementation are of particular interest.

Applications of interest include, but are not limited to, antennas (and their electromagnetic environments), networks, static fields, radar cross section, shielding, radiation hazards, biological effects, electromagnetic pulse (EMP), electromagnetic interference (EMI), electromagnetic compatibility (EMC), power transmission, charge transport, dielectric and magnetic materials, microwave components, MMIC technology, remote sensing and geophysics, communications systems, fiber optics, plasmas, particle accelerators, generators and motors, electromagnetic wave propagation, non-destructive evaluation, eddy currents, and inverse scattering.

Techniques of interest include frequency-domain and time-domain techniques, integral equation and differential equation techniques, diffraction theories, physical optics, moment methods, finite differences and finite element techniques, modal expansions, perturbation methods, and hybrid methods. This list is not exhaustive.

A unique feature of the Journal is the publication of unsuccessful efforts in applied computational electromagnetics. Publication of such material provides a means to discuss problem areas in electromagnetic modeling. Material representing an unsuccessful application or negative results in computational electromagnetics will be considered for publication only if a reasonable expectation of success (and a reasonable effort) are reflected. Moreover, such material must represent a problem area of potential interest to the ACES membership.

Where possible and appropriate, authors are required to provide statements of quantitative accuracy for measured and/or computed data. This issue is discussed in "Accuracy & Publication: Requiring quantitative accuracy statements to accompany data", by E.K. Miller, *ACES Newsletter*, Vol. 9, No. 3, pp. 23-29, 1994, ISBN 1056-9170.

### EDITORIAL REVIEW

In order to ensure an appropriate level of quality control, papers are refereed. They are reviewed both for technical correctness and for adherence to the listed guidelines regarding information content. Authors should submit the initial manuscript in draft form so that any suggested changes can be made before the photo-ready copy is prepared for publication.

### JOURNAL COPY INFORMATION

| | |
|---|---|
| March issue | Copy deadline 13 January |
| July issue | Copy deadline 25 May |
| November issue | Copy deadline 25 September |

## STYLE FOR CAMERA-READY COPY

The ACES Journal is flexible, within reason, in regard to style. However, certain requirements are in effect:

1. The paper title should NOT be placed on a separate page. The title, author(s), abstract, and (space permitting) beginning of the paper itself should all be on the first page. The title, author(s), and author affiliations should be centered (center-justified) on the first page.

2. An abstract is REQUIRED. The abstract should state the computer codes, computational techniques, and applications discussed in the paper (as applicable) and should otherwise be usable by technical abstracting and indexing services.

3. Either British English or American English spellings may be used, provided that each word is spelled consistently throughout the paper.

4. Any commonly-accepted format for referencing is permitted, provided that internal consistency of format is maintained. As a guideline for authors who have no other preference, we recommend that references be given by author(s) name and year in the body of the paper (with alphabetical listing of all references at the end of the paper). Titles of Journals, monographs, and similar publications should be in boldface or italic font or should be underlined. Titles of papers or articles should be in quotation marks.

5. Internal consistency shall also be maintained for other elements of style, such as equation numbering. As a guideline for authors who have no other preference, we suggest that equation numbers be placed in parentheses at the right column margin.

6. The intent and meaning of all text must be clear. For authors who are NOT masters of the English language, the ACES Editorial Staff will provide assistance with grammar (subject to clarity of intent and meaning).

7. Unused space should be minimized. Sections and subsections should not normally begin on a new page.

## MATERIAL, SUBMITTAL FORMAT AND PROCEDURE

The preferred format for submission and subsequent review, is 12 point font or 12 cpi, double line spacing and single column per page. Four copies of all submissions should be sent to the Editor-in-Chief (see inside front cover). Each submission must be accompanied by a covering letter. The letter should include the name, address, and telephone and/or fax number and/or e-mail address of at least one of the authors.

Only camera-ready original copies are accepted for publication. The term **"camera-ready" means that the material is neat, legible, and reproducible**. The preferred font style is Times Roman 10 point (or equivalent) such as that used in this text. A double column format similar to that used here is preferred. **No author's work will be turned down once it has been accepted because of an inability to meet the requirements concerning fonts and format.** Full details are sent to the author(s) with the letter of acceptance.

There is NO requirement for India ink or for special paper; any plain white paper may be used. However, faded lines on figures and white streaks along fold lines should be avoided. Original figures - even paste-ups - are preferred over "nth-generation" photocopies. These original figures will be returned if you so request.

While ACES reserves the right to re-type any submitted material, this is not generally done.

## PUBLICATION CHARGES

ACES members are allowed 12 pages per paper without charge; non-members are allowed 8 pages per paper without charge. Mandatory page charges of $75 a page apply to all pages in excess of 12 for members or 8 for non-members. Voluntary page charges are requested for the free (12 or 8) pages, but are NOT mandatory or required for publication. A priority courtesy guideline, which favors members, applies to paper backlogs. Full details are available from the Editor-in-Chief.

## COPYRIGHTS AND RELEASES

Each primary author must sign a copyright form and obtain a release from his/her organization vesting the copyright with ACES. Forms will be provided by ACES. Both the author and his/her organization are allowed to use the copyrighted material freely for their own private purposes.

Permission is granted to quote short passages and reproduce figures and tables from an ACES Journal issue provided the source is cited. Copies of ACES Journal articles may be made in accordance with usage permitted by Sections 107 or 108 of the U.S. Copyright Law. This consent does not extend to other kinds of copying, such as for general distribution, for advertising or promotional purposes, for creating new collective works, or for resale. The reproduction of multiple copies and the use of articles or extracts for commercial purposes require the consent of the author and specific permission from ACES. Institutional members are allowed to copy any ACES Journal issue for their internal distribution only.